UNDERSTANDING C-H OXIDATION AND AMINATION REACTIONS PERFORMED BY LATE FIRST-ROW TRANSITION METALS: TRAPPING HIGH-VALENT METAL-O/N SPECIES

Teresa Corona Prieto

Universitat de Girona

DOCTORAL THESIS

Understanding C-H oxidation and amination reactions performed by late first-row transition metals: trapping high-valent metal-O/N species

Teresa Corona Prieto

2017

Doctoral programme in Chemistry

Supervised by: Dr. Anna Company Casadevall

Tutor: Dr. Xavi Ribas Salamaña

Presented in partial fulfilment of the requirements for a doctoral degree from the University of Girona

Universitat de Girona

Dr. Anna Company Casadevall and Dr. Xavi Ribas Salamaña from Universitat de Girona,

WE DECLARE:

That the thesis entitled “Understanding C-H oxidation and amination reactions performed by late first-row transition metals: trapping high-valent metal-O/N species”, presented by Teresa Corona Prieto to obtain a doctoral degree, has been completed under our supervision and meets the requirements to opt for an International Doctorate.

For all intents and purposes, we hereby sign this document.

Director: Dr. Anna Company Casadevall Tutor: Dr. Xavi Ribas Salamaña

Girona, 9th of January, 2017

“La ciencia se compone de errores, que a su vez, son los pasos hacia la verdad”

Jules Verne

Als meus pares i als meus germans

a l’Òscar, la llum que il·lumina el meu camí

FULL LIST OF PUBLICATIONS

This thesis is based on a compendium of the following publications:

Chapter III

"Reactivity of a nickel(II) bis(amidate) complex with meta-chloroperbenzoic acid: formation of a potent oxidizing species" Teresa Corona, Florian F. Pfaff, Ferran Acuña-Parés, Apparao Draksharapu, Christopher J. Whiteoak, Vlad Martin-Diaconescu, Julio Lloret-Fillol, Wesley R. Browne, Kallol Ray, and Anna Company in *Chem. Eur. J.* **2015**, *21*, 15029–15038. (Impact factor: 5.771, position 24/163 in Chemistry, Multidisciplinary, 1st quartile).

Chapter IV

"Rapid hydrogen and oxygen atom transfer by a high-valent nickel-oxygen species" Teresa Corona, Apparao Draksharapu, Sandeep K. Padamati, Ilaria Gamba, Vlad Martin-Diaconescu, Ferran Acuña-Parés, Wesley R. Browne, and Anna Company in *J. Am. Chem. Soc.* **2016**, *138*, 12987−12996. (Impact factor: 13.038, position 10/163 in Chemistry, Multidisciplinary, 1st quartile).

Chapter V

"Nitrous oxide activation by a cobalt(II) complex for aldehyde oxidation under mild conditions" Teresa Corona and Anna Company in *Dalton Trans.* **2016**, *45*, 14530−14533. (Impact factor: 4.177, position 10/46 in Chemistry, Inorganic & Nuclear, 1st quartile).

Chapter VI

"Characterization and reactivity studies of a terminal copper-nitrene species" Teresa Corona, Lídia Ribas, Mireia Rovira, Erik Farquhar, Xavi Ribas, Kallol Ray, and Anna Company in *Angew. Chem. Int. Ed.* **2016**, *55*, 14005−14008. (Impact factor: 11.709, position 11/163 in Chemistry, Multidisciplinary, 1st quartile).

All these papers have been published in journals that belong to the first quartile according to JCR.

Publications not included in this thesis

“Assessing the impact of electronic and steric tuning of the ligand in the spin state and catalytic oxidation ability of the Fe^{II}(Pytacn) family of complexes” Irene Prat, Anna Company, Teresa Corona, Teodor Parella, Xavi Ribas, and Miquel Costas in *Inorg. Chem.* **2013**, *52*, 9229−9244.

“Migration of components from cork stoppers to food: Challenges in determining inorganic elements in food simulants” Teresa Corona, Mònica Iglesias, and Enriqueta Anticó in J*. Agric. Food Chem.* **2014**, *62*, 5690−5698.

“Spectroscopically trapped synthetic mononuclear nickel-oxygen species” Teresa Corona, and Anna Company in *Chem. Eur. J.* **2016**, *22*, 13422−13429.

“Activation of O_2 at Lewis acidic nickel(II) complex – characterization of a metastable organoperoxide complex” Patrick Holze, Teresa Corona, Nicolas Frank, Beatrice Braun-Cula, Christian Herwig, Anna Company, and Christian Limberg, in *Angew. Chem. Int. Ed.* **2016**, DOI: 10.1002/anie.201609526R1.

“Trapping a reversible cobalt-peroxo and cobalt-superoxo species” Teresa Corona, Sandeep K. Padamati, Ferran Acuña-Parés, Wesley R. Browne, and Anna Company. In preparation

LIST OF ABBREVIATIONS

^{o}C	Celsius degrees
μ_B	bohr magneton
μ_{eff}	effective moment
δ	chemical shift (units: ppm)
ρ	spin density
σ_p	hammett parameter
v	frequency (units: cm^{-1})
ΔE_{ZPE}	electronic energy
ΔGº	Gibbs free energy
50% ^{15}N-labeled	singly terminal labelled azide, ^{15}N-^{14}N-^{14}N
^{1}H-NMR	proton nuclear magnetic resonance
^{13}C-NMR	^{13}Carbon nuclear magnetic resonance
^{31}P-NMR	^{31}Phosphorous nuclear magnetic resonance
1-D	monodimensional
2-D	bidimensional
Å	Angstrom
Abs	absorbance
acac	acetylacetonate
AcOH	acetic acid
Ad	adamantane
Ar	argon
atm	atmosphere
BDE	bond dissociation energy
br s	broad singlet
CCA	cyclohexanecarboxaldehyde
CHD	1,4-cyclohexadiene
CID	collision induced dissociation
COSY	correlation spectroscopy 2-D
CSI-MS	cryospray ionization mass spectrometry
CV	cyclic voltammetry
d	doublet
d	deuterated
DFT	density functional theory
DHA	9,10-dihydroanthracene
Dipp	2,6-diisopropylphenyl
ε	extinction coefficient
e^-	electrons

$E_{1/2}$	redox potential
EPR	electron paramagnetic resonance
equiv.	equivalents
ESI-MS	electrospray ionization mass spectrometry
Et	ethyl
eV	electronvolt
EXAFS	extended X-ray absorption fine structure
FT-IR	fourier transform infrared spectroscopy
GC-FID	gas chromatography-flame ionization detector
GC-MS	gas chromatography-mass spectrometry
GC-TCD	gas chromatography-thermal conductivity detector
h	hours
HAT	hydrogen atom transfer
HSQC	heteronuclear single quantum coherence
*i*Pr	*iso*-propyl
J	coupling constant
K	Kelvin
k	second order rate constant
k'	second order rate constant corrected by the number of C-H bonds
kcal	kilocalories
KIE	kinetic isotope effect
k_{obs}	observed rate constant
M	metal
*m*CBA	*meta*-chlorobenzoic acid
*m*CPBA	*meta*-chloroperbenzoic acid
Me	methyl
Mes	mesyl
min	minutes
mL	milliliter
mM	millimolar
m/z	mass to charge ratio
MW	molecular weight
MS/MS	tandem mass spectrometry
N_2	molecular nitrogen
N_2O	nitrous oxide
n.d.	not-detected
nm	nanometer
NMR	nuclear magnetic resonance
O_2	molecular oxygen
OAT	oxygen atom transfer

OTf	CF_3SO_3 anion
Ox	oxidant
p	*para*
p.	page
Ph	phenyl
Porph	porphyrin
PPh_3	triphenylphosphine
ppm	part per million
py	pyridine
RC	retention of configuration
Ref.	reference
rRaman	resonance Raman
r.t.	room temperature
S	spin state
s	singlet
SCE	saturated calomel electrode
SNOs	spin natural orbitals
T	temperature
t	triplet
$t_{1/2}$	half-life time
*t*Bu	*tert*-butyl
THF	tetrahydrofuran
Ts	tosyl
UV-vis	ultraviolet-visible spectroscopy
XANES	X-ray absorption near edge structure
XAS	X-ray absorption spectroscopy
XRD	X-ray diffraction
V	volts

LIST OF FIGURES

LIST OF TABLES

LIST OF SCHEMES

AGRAÏMENTS

Ja han passat gairebé 4 anys des que vaig començar al QBIS. En aquest temps he viscut grans moments i m'emporto una experiència inoblidable. M'agradaria començar agraint a l'Anna, qui m'ha supervisat al llarg d'aquest temps, i qui va confiar i creure en mi donant-me l'oportunitat de fer el doctorat. M'has ensenyat a fer ciència, a fer-me preguntes, a fer les coses de manera acurada i gràcies a la teva dedicació i paciència he pogut créixer tant a nivell personal com acadèmic. Sempre t'estaré agraida per l'entusiasme vers la química que desprens i contagies, i per creure que juntes podrien arribar a bon port projectes difícils com el del níquel o el de l'N_2O, dels quals n'estic molt contenta dels resultats obtinguts. Al final hem fet gairebé tot el que escrivia a les famoses llistes! També vull agrair a en Miquel, Xavi i Julio per també ser una part important durant el doctorat, donant-me el vostre suport, aportant idees i ganes de fer ciència.

Pel que fa als membres del grup QBIS, volia començar amb els que ja no hi són: la Irene (qui em va iniciar al laboratori), la Mercè (primera companya de despatx i a qui consultava els dubtes), en Zoel (l'expert informàtic amb qui vaig compartir els inicis als tallers), en David Font (qui et resolia qualsevol dubte d'orgànica, gràcies pel revelador!), l'Arnau (espero que et vagi molt bé el post-doc al Japó i gràcies pel complex de cobalt!), en Ferran (que m'ha ajudat en el "lado oscuro" de la ciència) i la Carla (una gran amiga que es troba a faltar per Girona, tant les seves converses com les seves rialles).

Vull agrair especialment als meus companys actuals de laboratori. M'agradaria agrair-los el dia a dia, les converses i els bon moments que fan més amé les a vegades feixugues hores del laboratori i que sempre animen quan hi ha alguna cosa que no surt: la Michela (qui amb el seu bon humor i la música italiana li dóna alegria al laboratori), en Diego (qui sempre està superactiu i fent supercolumnes però que sempre està superatent a com vas) i en Marco (a qui no se li acaben mai les abraçades).

També vull agrair a les matineres que animen a començar el dia amb energia: la Mònica (una gran amiga amb qui explicar-li qualsevol problema tant del lab com de fora i està allà per animar-te i tirar endavant), la Carlota (ja fa 9 anys que ens coneixem i sempre estàs per posar una mica d'ordre al laboratori i organitzar coses, gràcies!) i la Mago (qui sempre ens sorprèn portant alguna cosa per menjar, molta sort amb el doctorat!). I també vull donar les gràcies als altres dels tallers: a l'Olaf (sempre de broma), en Giorgio (qui et proposa solucions quan estàs encallada), la Valeria (qui et contagia el seu somriure) i la Raquel (sense la qual hi hauria un caos al laboratori). Als meus companys d'UV: en Gerard (sempre disposat a ajudar-te) i la Ilaria (amb qui hem solucionat més d'un problema amb l'UV), els quals a partir d'ara ja no tindran problemes de calendari!

I també els del QBIS4 amb qui també he compartit menjars, excursions, seminaris i congressos. La Cristina (la *crack* de les caixes), en Joan (sort en el post-doc a Suïssa!), la Mireia (ens ha fet plorar el lligand però hem aconseguit un coure-nitrè!), l'Uri (qui sempre té bones idees, amunt el cobalt!), en Jordi i en Carles (sort amb el doctorat!) i en Màrius (gràcies per les teves malles...).

Finalment als nous estudiants: la Carla (ànims amb el cobalt!), la Lorena, en Cristian, en Pau i la Laia us desitjo bona sort en el futur.

Moltes gràcies a tots QBISencs pel bon ambient de treball que ha estat imprescindible aquests anys de doctorat.

També vull agrair al professor Kallol Ray per donar-me la oportunitat de poder fer una estada de quatre mesos al seu grup a Berlín, i també als membres del seu grup, especialment a l'Inés i a la Xenia que em van acollir amb els braços oberts en el laboratori i em feien sentir com a casa.

Per acabar, m'agradaria agrair als meus pares i als meus germans els seus consells i sobretot que sempre estigui al meu costat.

I finalment, no podia acabar sense agrarir a la persona més important i qui sempre ha cregut en mi, l'Òscar. Sense ell aquesta tesi no seria el que és, gràcies per la teva paciència infinita!

Moltes gràcies a tots!

TERESA

ACKNOWLEDGEMENTS

This work would have not been possible without the following collaborations:

- Serveis Tècnics de Recerca (STR) from University of Girona for technical support, with especial remark to Dr. Laura Gómez.

- Dr. Ferran Acuña-Parés and Dr. Julio Lloret-Fillol from University of Girona and Institut Català d'Investigació Química (ICIQ) for guidance in DFT calculations.

- Prof. Dr. Kallol Ray from Humboldt Universität zu Berlin for hosting a scientific visit and the collaborative research in the high-valent copper-nitrene project.

- Dr. Wesley Browne from University of Groningen for all the collaborative research in the high-valent nickel-oxygen species and his supervision during my scientific visit.

- Financial support from European Commission 2011-CIG-303522 to Dr. Anna Company.

- Financial support from COST Action CM1305 (ECOSTBio) for STSM grants STSM-CM1305-21541 and STSM-CM1305-32120.

- Financial support from Clara Immerwahr award of UniCat to Dr. Anna Company.

GRAPHICAL ABSTRACT

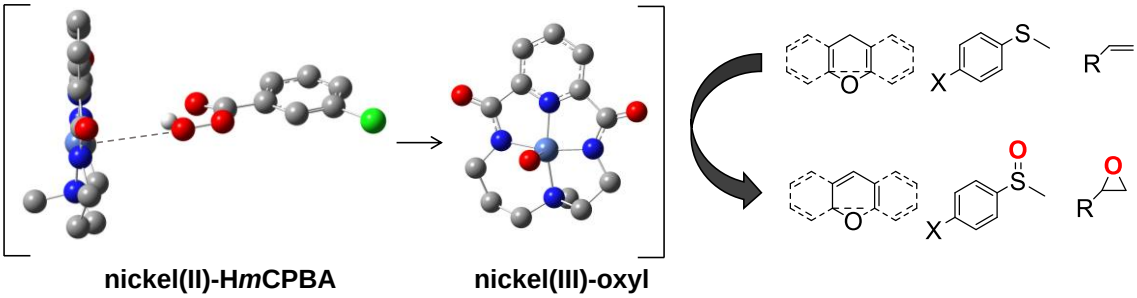

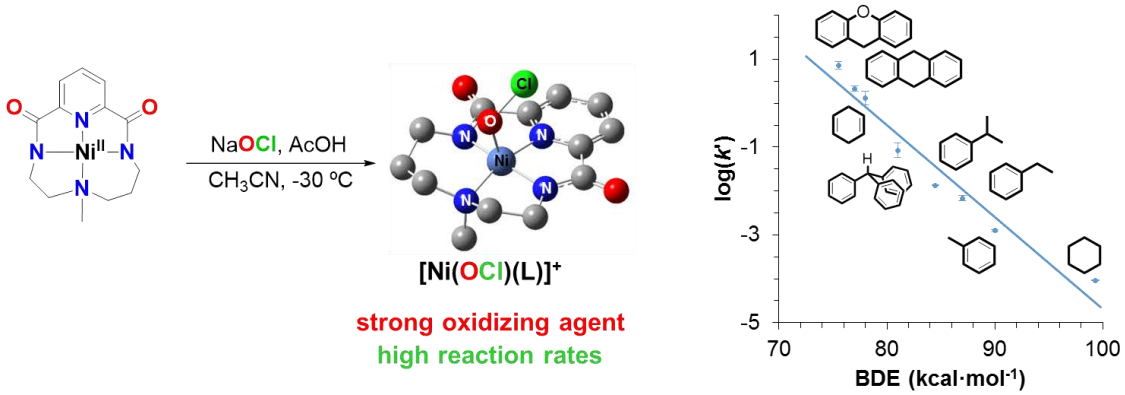

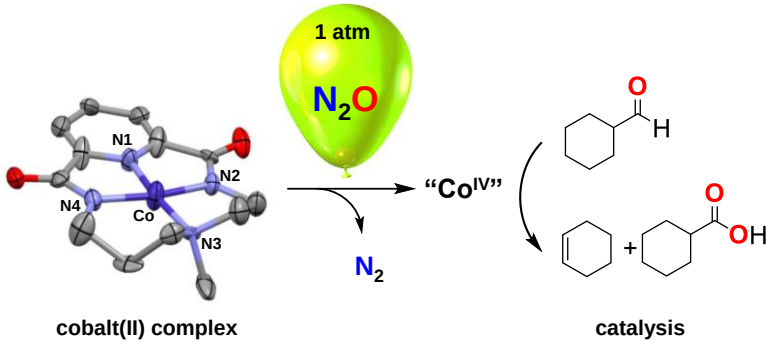

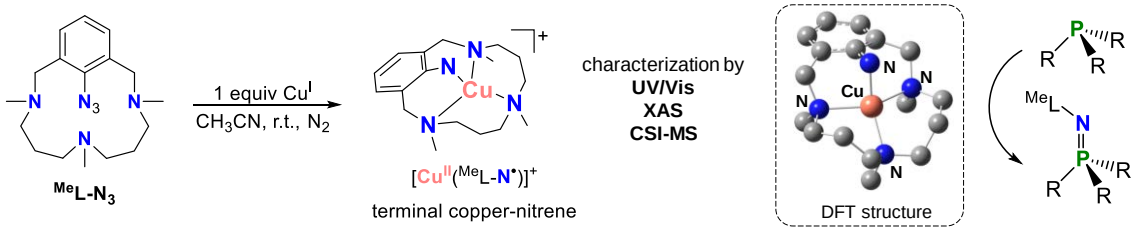

TABLE OF CONTENTS

SUMMARY

The transformation of C-H bonds into functional groups such as C-O or C-N bonds is a process of general interest in organic synthesis, but controlling the reactivity and selectivity among the multiple C-H bonds existing in most molecules is a very challenging task. Traditional methodologies usually rely on the use of stoichiometric reagents that generate high amounts of often toxic waste and relatively harsh reaction conditions are required. A sustainable alternative to these traditional methods is the use of catalysts, which enable the performance of these transformations under milder reaction conditions, with improved selectivities and using less hazardous reagents. However, finding good catalysts inevitably means that intimate details about the reaction mechanism need to be unraveled. Otherwise, rational advance in this field would be impossible. For these reasons, this thesis aims at obtaining mechanistic insight into these transformations by trapping the corresponding active species, that is the high-valent metal-oxygen or metal-nitrogen species based on late first-row transition metals.

This thesis starts with the design and synthesis of a new dianionic unsymmetric tetradentate macrocylic ligand that contains a 2,6-pyridinecarboxamidate motif, as a platform for the stabilization of the prospective high-valent metal species. We found that the corresponding nickel(II) complex reacted with *meta*-chloroperbenzoic acid or NaOCl at low temperature giving rise to the formation of two nickel-oxygen species, described as high-valent nickel(III)-oxyl and nickel(III)-hypochlorite radical species on the basis of spectroscopic and computational data. Interestingly both compounds were much more reactive towards organic substrates than previously reported well-defined nickel–oxygen species, which suggest that they might be relevant in nickel catalyzed oxidation reactions for the conversion of C-H into C-O bonds.

In a subsequent section of this thesis we turned our interest towards the use of green oxidants, and in particular we focused on the activation of nitrous oxide using first-row transition metals under mild conditions. This topic is of special relevance taking into account that the concentration of this gas is increasing every year due to anthropogenic sources with important consequences in ozone layer depletion and global warming. Thus, finding an application for this waste gas would be highly desirable. In this line, N_2O is potentially a very attractive green oxidant as it only generates N_2 as by-product, but due to its kinetic inertness reductive activation is needed. Remarkably, we found that the cobalt(II) complex containing the above-mentioned macrocyclic ligand was highly reactive towards N_2O under mild conditions (0 ºC, 1 atm). Mechanistic studies suggested that a cobalt(IV) species was formed along this process and that this species was involved in the observed catalytic deformylation of aldehydes with N_2O.

In the final part of this thesis, we focused our attention on the entrapment of imidocopper (copper-nitrene) species that have been long postulated as active species in copper catalyzed C-N bond formation reactions. Reaction of a copper(I) salt with an azide-containing macrocyclic ligand afforded the stabilization of an imidylcopper(II) (copper(II)-nitrene radical) species as established by several spectroscopic techniques. Reactivity studies showed that this compound interacted with weak C-H bonds and phosphines to perform nitrene-transfer reactions.

RESUM

La transformació d'enllaços C-H en grups funcionals com ara enllaços C-N o C-O és un procés molt interessant en síntesi orgànica, però avui en dia encara és un repte controlar la reactivitat i selectivitat entre els diferents enllaços C-H presents en les molècules. Les metodologies tradicionals solen estar basades en l'ús de reactius en quantitats estequiomètriques, generant importants quantitats de residus tòxics, i en condicions de reacció agressives. Una alternativa sostenible és l'ús de catalitzadors, els quals permeten dur a terme aquestes transformacions en condicions de reacció més suaus, millorant les selectivitats, i utilitzant reactius menys perillosos. Tot i així, trobar nous catalitzadors implica conèixer en detall el mecanisme de les reaccions. Sense aquest coneixement, el progrés en aquest camp no seria possible. Per això, aquesta tesi té com a objectiu estudiar els mecanismes d'aquestes transformacions a través de la detecció i l'estudi de les espècies actives, corresponents a compostos metall-O o metall-N en alt estat d'oxidació basats en metalls de la primera sèrie de transició.

El punt de partida d'aquesta tesi és el disseny i la síntesi d'un nou lligand macrocíclic tetradentat asimètric dianiònic basat en una estructura de 2,6-piridinacarboxamidat, la qual té la capacitat d'estabilitzar espècies metàl·liques en alt estat d'oxidació. S'ha trobat que el complex de níquel(II) amb aquest lligand reacciona amb àcid *meta*-cloroperbenzoic o hipoclorit de sodi a baixa temperatura generant la formació de dues espècies de níquel-oxigen, descrites com a níquel(III)-oxil i níquel(III)-radical hipoclorit. Aquestes espècies han estat estudiades mitjançant tècniques espectroscòpiques i càlculs computacionals. Cal destacar que ambdós compostos reaccionen molt més ràpidament amb substrats orgànics que altres espècies de níquel-oxigen prèviament descrites i caracteritzades, la qual cosa suggereix que podrien ser rellevants en processos catalítics d'oxidació d'enllaços C-H per donar enllaços C-O.

El segon objectiu d'aquesta tesi va ser l'ús d'oxidants benignes, en particular, l'activació en condicions suaus de l'òxid nitrós (N_2O) utilitzant metalls de la primera sèrie de transició. Cal destacar que aquesta línia de recerca és especialment rellevant, tenint en compte que la concentració d'aquest gas està augmentant cada any a causa de fonts antropogèniques, amb importants conseqüències pel que fa a la destrucció de la capa d'ozó i l'escalfament global. Per tant, trobar una manera de consumir aquest gas de rebuig seria d'un gran interès. En aquesta línia, l'N_2O és un oxidant molt interessant, ja que només genera N_2 com a subproducte. L'inconvenient és que necessita ser activatat mitjançant una reducció ja que és cinèticament inert. En aquesta tesi es descriu com el complex de cobalt(II) del lligand macrocíclic esmentat anteriorment és altament reactiu vers N_2O en condicions suaus (T= 0 ºC, P= 1 atm). Estudis mecanístics suggereixen que aquest procés es té lloc a través de la formació d'una espècie de cobalt(IV), la qual és capaç de deformilar aldehids de manera catalítica.

La part final d'aquesta tesi se centra en la detecció d'espècies imidocoure, les quals s'han postulat com a espècies actives en la formació d'enllaços C-N. Així doncs, la reacció d'una sal de coure(I) amb un lligand macrocíclic que conté un grup azida permet l'estabilització d'una espècie d'imidilcoure(II), caracteritzada per diverses tècniques espectroscòpiques. Estudis de reactivitat mostren que aquest compost és capaç d'interactuar amb enllaços C-H febles i fosfines per dur a terme reaccions de transferència del grup nitrè.

RESUMEN

La transformación de enlaces C-H en grupos funcionales tales como C-N o C-O es un proceso de interés en la síntesis orgánica, pero todavía es un reto controlar la reactividad y selectividad entre los distintos enlaces C-H presentes en las moléculas. Las metodologías tradicionales suelen estar basadas en el uso de reactivos en cantidades estequiométricas, generando importantes cantidades de residuos tóxicos, requiriendo condiciones de reacción agresivas. Una alternativa sostenible es el uso de catalizadores, los cuales permiten estas transformaciones en condiciones de reacción más suaves, mejorando las selectividades, y utilizando reactivos menos peligrosos. A pesar de ello, la búsqueda de nuevos catalizadores implica el conocimiento de los mecanismos de reacción. Sin este conocimiento, el progreso en este campo no sería posible. Por esto, esta tesis tiene como objetivo el estudio de los mecanismos de estas transformaciones a través de la detección y estudio de las especies activas, correspondientes a especies de metal-oxígeno o metal-nitrógeno en altos estados de oxidación y basadas en metales de la primera serie de transición.

El punto de inicio de esta tesis es el diseño y la síntesis de un nuevo ligando macrocíclico tetradentado asimétrico y dianiónico basado en una estructura 2,6-pridinacarboxamidato, la cual estabiliza especies metálicas en elevados estados de oxidación. Se ha encontrado que el complejo de níquel(II) reacciona con ácido *meta*-cloroperbenzoico o hipoclorito de sodio a baja temperatura generando dos especies de níquel-oxígeno, descritas como níquel(III)-oxilo y níquel(III)-radical hipoclorito, las cuales han sido estudiadas mediante técnicas espectroscópicas y cálculos computacionales. Cabe destacar que ambos compuestos resultaron mucho más reactivos frente a sustratos orgánicos que las especies de níquel-oxígeno previamente descritas, lo cual sugiere que podrían ser relevantes en la oxidación catalítica de enlaces C-H para dar enlaces C-O.

El segundo objetivo de esta tesis fue el uso de oxidantes benignos, en particular, la activación bajo condiciones suaves de óxido nitroso (N_2O) mediante el uso de metales de la primera serie de transición. Esta línea de investigación es especialmente importante si consideramos que la concentración de este gas está aumentando cada año debido a fuentes antropogénicas, con importantes consecuencias en la destrucción de la capa de ozono y en el calentamiento global. Por lo tanto, hallar una manera de consumir este gas residual sería de gran interés. En este sentido, el N_2O es un oxidante muy interesante ya que sólo genera N_2 como subproducto. El inconveniente es que necesita ser activado mediante reducción ya que es cinéticamente inerte. En esta tesis se describe como el complejo de cobalto(II) con el ligando macrocíclico antes mencionado, es altamente reactivo frente a N_2O en condiciones suaves (T= 0 ºC, P= 1 atm). Estudios mecanísticos sugieren que esta reacción da lugar a la formación de una especie de cobalto(IV) capaz de deformilar aldehídos de manera catalítica.

La parte final de esta tesis se centra en la detección de especies imidocobre, las cuales se han postulado como especies activas en la formación de enlaces C-N. La reacción de una sal de cobre(I) con un ligando azida ha permitido la estabilización de una especie imidilcobre(II), caracterizada mediante diversas técnicas espectroscópicas. Estudios de reactividad muestran que este compuesto es capaz de reaccionar con enlaces C-H débiles y fosfinas para llevar a cabo reacciones de transferencia del grupo nitreno.

Chapter I.

General Introduction

I. GENERAL INTRODUCTION

I.1. C-H functionalization in organic synthesis

The selective transformation of ubiquitous but inert C-H bonds into functional groups, such as C-O or C-N, is a process of general interest and significance in organic synthesis as it allows the increase in molecular complexity of simpler reagents.[1] At the extreme end of this idea such transformations are unavoidable to convert current petrochemical feedstocks into useful raw materials for the preparation of valuable commodities for everyday life, but these methodologies are also at the core for the synthesis of fine chemicals including pharmaceuticals.[2] Thus, C-H bond activation is considered to be one of the key steps for the future development of organic synthesis.

Controlling the reactivity and selectivity among the multiple C-H bonds existing in most molecules is one of the most difficult challenges in chemistry because it demands the use of concurrently highly reactive but also selective reagents.[3] These reagents must also align to sustainability criteria. Traditional methodologies usually rely on the use of stoichiometric reagents that generate important amounts of often toxic waste and relatively harsh reaction conditions are required, which often translates into poor selectivities. In this line, the use of transition metal catalysts has represented a tremendous step forward in the field as more sustainable and selective processes have been developed under milder reaction conditions with minimal waste production. Despite the fact that catalysis is considered to be superior to stoichiometric procedures as far as sustainability issues are concerned (9th principle of Green Chemistry: “Use of catalytic instead of stoichiometric reagents in reactions”)[4], the use of first-row transition metals instead of their second and third-row counterparts is highly desirable because the former are less toxic, more abundant and cheaper. Thus, many research groups are focusing on the development of C-H activation reactions using first-row transition metals for both environmental and economic reasons.[5] Finding successful catalysts for these transformations and improving their efficiency or selectivity inevitably means that intimate details about the mechanism operating in catalysis need to be unraveled.

Two different approaches can be used from the perspective of metal-based catalysis to achieve the functionalization of C-H bonds into C-O or C-N bonds (Scheme I.1). The first one consists in oxidative cross-coupling reactions involving the formation of metal-carbon bonds in organometallic catalytic cycles. The second approach, instead, affords C-H oxidation or amination by the mediation of high-valent metal-oxygen or metal-nitrogen species. In this case, reactions usually involve an initial hydrogen-atom abstraction from the targeted C-H bond by the high-valent metal species.

For the purposes of this thesis, we will exclusively focus on the second approach entailing high-valent metal-O/N species with special attention to late first-row transition metals such as cobalt, nickel or copper which have emerged as interesting alternatives to heavier elements.

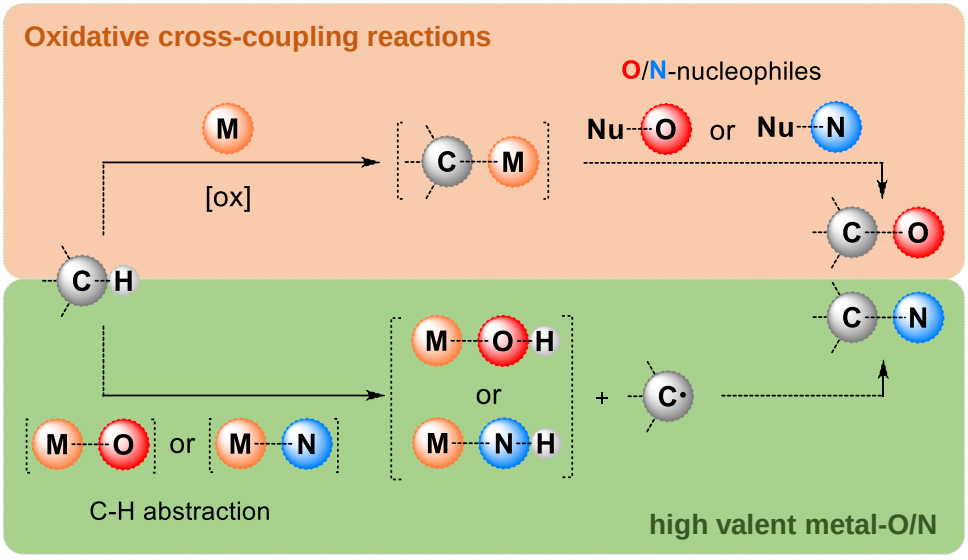

Scheme I.1. Schematic representation of the two possible pathways (oxidative cross-coupling reaction or mediation of high-valent metal-O/N) to achieve the functionalization of C-H bonds.

I.2. High-valent metal-oxygen species

The oxidation of C-H bonds, which affords the formation of C-O bonds, is a very interesting transformation as it allows the preparation of compounds with new functionalities, with applications in bulk and fine chemistry but also in the synthesis of pharmaceuticals and value-added products.[6] Despite the fact that the oxidation of C-H groups is thermodynamically feasible, large activation barriers limit these transformations due to the high energy of the C-H bonds and its lack of polarization and delocalization.[7] Indeed, several research groups have tried to tackle these limitations, but metal-based C-H activation is still far from being efficient, selective and environmentally sustainable for large scale production processes.[8] Due to the sensitivity of other functional groups that might be present in the substrate, trying to avoid the use of harsh conditions in terms of temperature, pressure and long reaction times would also be highly desirable.[9]

In this section we will review the importance of choosing an appropriate oxidant in these transformations and the relevance of iron-oxygen and copper-oxygen species in biological and bioinspired C-H oxidations. Then, we will turn our attention into the less studied mononuclear cobalt-oxygen and nickel-oxygen species preceded by an explanation of why oxometal species for these two metals are so uncommon.

I.2.1. Oxidants

The sustainability of oxidation reactions is dictated in large part by the choice of an appropriate oxidant. The ideal reagent should be readily available, environmentally sustainable, and inexpensive and have a high percentage of active oxygen content (high atom economy). However, traditional stoichiometric oxidants used in industrial processes (such as chromate[10] or permanganate[11]) are obsolete because they are very toxic, require high temperatures and

extended reaction times. In addition, these reactions are rather inefficient, barely selective and produce an unacceptable amount of, often toxic, inorganic salts as waste. On the basis of economic and environmental costs, such methodologies are being discarded in favor of catalytic processes involving a transition-metal-based catalyst together with cheaper and much less toxic oxidants (Table I.1).[12]

NaOCl, *m*CPBA or PhIO are nowadays common oxidants in organic synthesis but they present important drawbacks such as their high production costs and the formation of undesired by-products during the oxidation processes. Thus, most research efforts in the field are devoted to the use of molecular oxygen (O_2) or hydrogen peroxide (H_2O_2) which are readily available, have higher atom efficiencies (100% in the case of O_2) and do not generate toxic by-products (only water in the case of H_2O_2). Nitrous oxide (N_2O) also constitutes a very attractive oxidant as it only generates innocuous N_2 as by-product. However, activation of this recalcitrant reagent is still unsolved. Limitations, perspectives and applications of N_2O will be discussed in section I.2.6. In the following section, the mechanisms of O_2 activation and its coordination modes to metal centers will be described.

Table I.1. Active oxygen content and by-products of some oxidants.

oxidant	% active oxygen	by-products
O_2	100	-
H_2O_2	47.0	H_2O
N_2O	36.4	N_2
NaOCl	21.6	NaCl
CH_3CO_3H	21.1	CH_3COOH
*m*CPBA[a]	10.2	ClC_6H_4COOH
PhIO[b]	7.3	C_5H_5I

[a]*meta*-chloroperbenzoic acid [b]Iodosobenzene

- **Molecular O_2**

Dioxygen is an abundant, inexpensive and clean oxidant. However, its triplet ground state ($S = 1$) does not enable its reaction with most organic molecules (closed-shell) from a kinetic point of view, despite being potentially reactive from a thermodynamic standpoint. Thus, molecular oxygen presents a diradical configuration bearing two unpaired electrons that reside in the two degenerated antibonding π_{2px}* and π_{2py}* orbitals, leaving O_2 with a formal bond order of two (Figure I.1). Despite of its inherent lack of kinetic reactivity, dioxygen can interact with molecules that carry out single-electron transfer reactions or that contain unpaired electrons (radicals, photochemically produced triplet excited states or transition metal centers). For example, nature has mainly chosen the use of metal centers (generally Cu and Fe, but also Mn) located in the active site of oxidase and oxygenase enzymes to activate dioxygen to reactive singlet or doublet species (superoxide O_2^-, peroxide O_2^{2-} or oxide O^{2-}) (Scheme I.2).

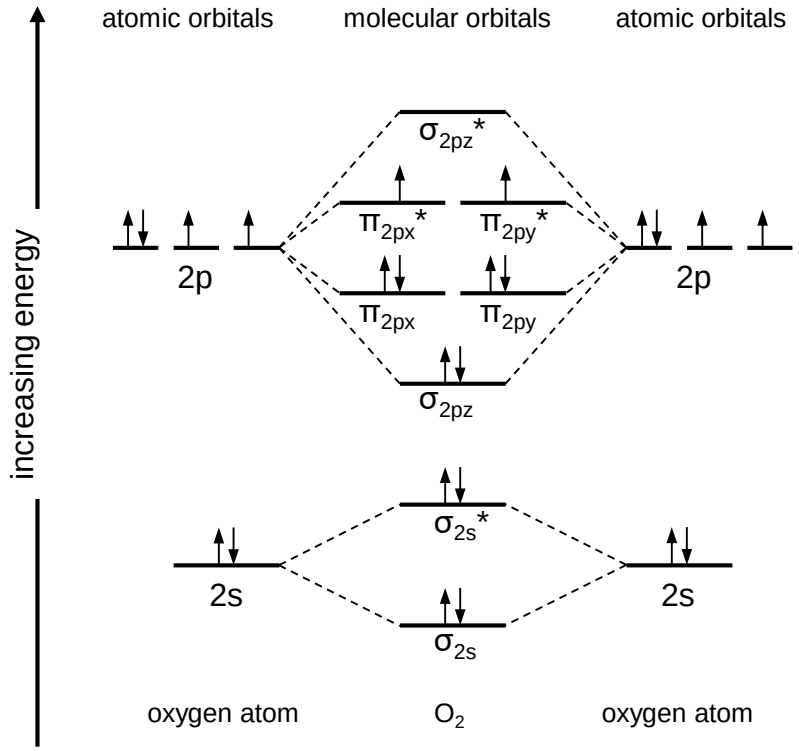

Figure I.1. Molecular orbitals energy diagram for O_2.

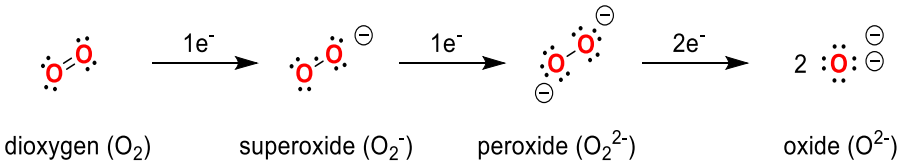

Scheme I.2. Activation of dioxygen to give its reduced active forms.

The binding mode of the dioxygen activated form to the metal is usually determined by several factors such as the availability of d orbitals in the metal and also the steric hindrance from the spectator ligands. The interaction with the metal can be classified according to the hapticity as end-on (η^1, one oxygen atom bound to the metal center) or side-on (η^2, both oxygen atoms bound to the metal center). Moreover, activated forms of dioxygen can form dimeric species (2:1 M:O_2) by bridging to an additional metal through a second interaction. Once these metal-dioxygen species are formed they can either react directly with an organic substrate or undergo O-O cleavage to form high-valent oxometal species (M=O) (Figure I.2).[13]

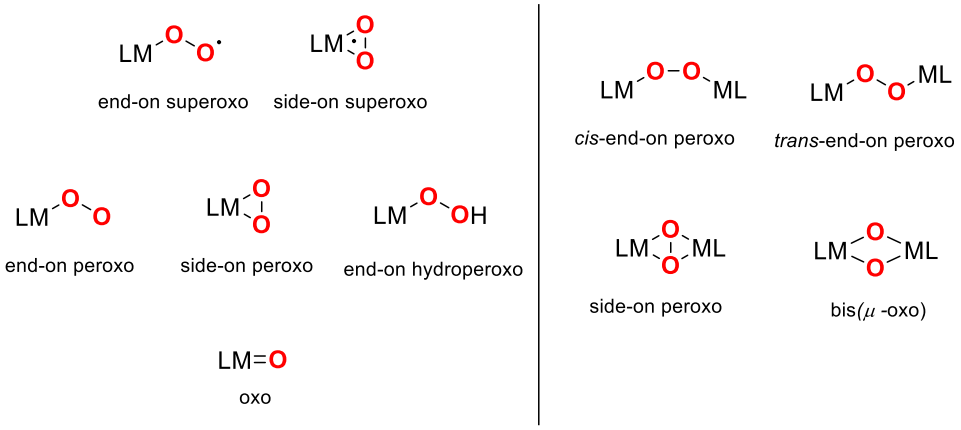

Figure I.2. Different binding modes of metal-oxygen species.

I.2.2. Metal-oxygen species in nature and bioinspired systems: predominance of Fe and Cu

The challenging selective oxidation of C-H bonds under mild conditions has been successfully solved by nature using metalloenzymes. The metal, which constitutes less than 1% of the protein weight, is located in the protein active site and it is essential for the enzyme function. During the last decades, many efforts have been dedicated to the elucidation of metalloprotein active sites using spectroscopic techniques, crystallography, site-directed mutagenesis, mechanistic enzymology or theoretical calculations. An added benefit of knowing the metalloenzyme structure and function is its potential application in the design of synthetic catalysts. These “bioinspired” or “biomimetic” catalysts may expand the substrate scope with respect to enzymes or tune selectivity or specificity. At the same time these synthetic model systems constitute an attractive approach for gaining knowledge about the protein chemistry, providing mechanistic, structural and spectroscopic data of the active species involved in the natural enzymes (e.g. high-valent metal-oxygen species) (Figure I.3).[14] The first step in biomimetic design starts with the preparation of suitable ligands that reproduce the environment found in the enzyme active site and it continues through several steps towards the ultimate goal of achieving catalytic activity.

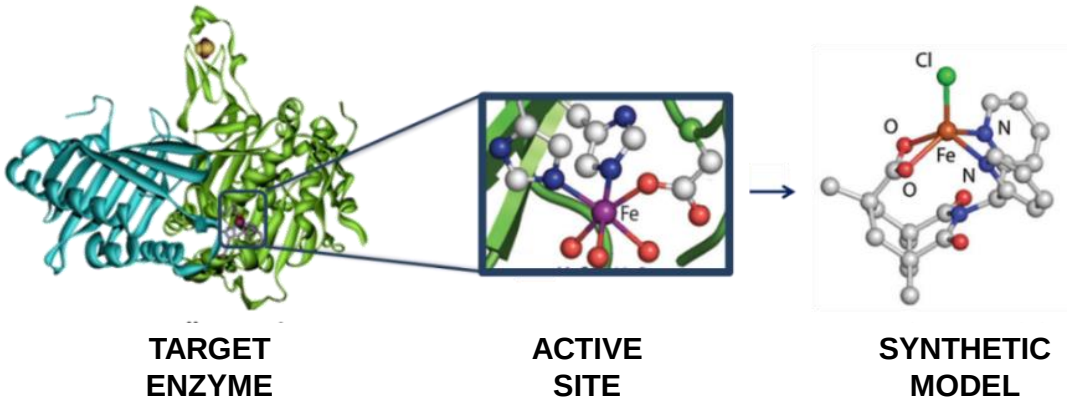

Figure I.3. Bioinspired approach from the active site of enzymes to designed functional models.

Iron and copper are the metals of choice in many biological oxidations due to their abundance, inherent electronic properties and accessible redox potentials. Due to the predominance of these two metals, many research groups have devoted their efforts to understand how these biological systems work and to develop model systems that can reproduce the activity of these enzymes. These O_2-activating enzymes behave as either oxidases (oxidation of a substrate) or oxygenases (substrate oxidation is coupled with oxygen atom incorporation) and the presence of metal-oxygen species as key reaction intermediates is a common feature (Scheme I.3). Indeed, important parallelisms exist between the O_2 activation carried out by copper and iron metalloproteins.[15]

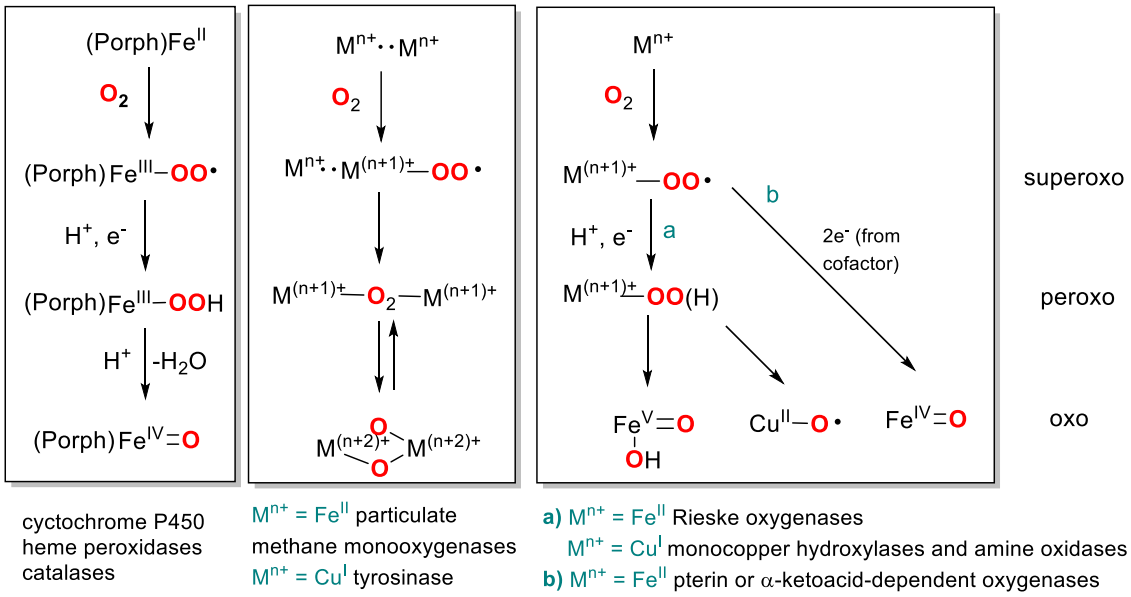

Scheme I.3. Mechanisms of O_2 activation by heme, non-heme, and copper-based metalloenzymes. This scheme is reproduced from Que, L.; Tolman, W. B., *Nature*, **2008**, *455*, 333.[15]

Iron-contain metalloenzymes are throughout the natural world and they participate in vital oxidative processes involving the activation of O_2. Thanks to the efforts carried out by many research groups the structure of many of these enzymes is now well established. The structural diversity that has arisen from these studies has led to the classification of iron O_2-activating enzymes in three different categories: heme (e.g. cytochrome P450), mononuclear non-heme (e.g. Rieske dioxygenases) and dinuclear non-heme oxygenases (e.g. soluble methane monooxygenase). Interestingly, most of the knowledge about iron enzymes involved in oxygen activation originates from the pioneer studies on the mechanism of action of heme enzymes and in particular of cytochrome P450.

Cytochrome P450 enzymes constitute a large family of heme proteins, which are present in all forms of life: plants, bacteria and mammals.[16] Cytochrome P450s carry out the oxidation of non-activated organic substrates, such as hydroxylation of aliphatic C-H bonds, epoxidation of C=C bonds, N-, S- and O-dealkylation, N-oxidation, sulfoxidation and dehalogenation with high regioselectivity and steroselectivity.[17] For these oxidations, cytochrome P450 enzymes use O_2 as both oxidant and oxygen source and they act as monooxygenases: they insert one oxygen atom

into a wide variety of biological substrates, concomitantly with a two-electron reduction of the other oxygen atom to form a water molecule (Scheme I.4).

The active center of cytochrome P450 consists of an iron center coordinated to a porphyrin ring attached to the protein through coordination of a cysteine residue at one of the axial positions of the metal. The other axial position is occupied by a water molecule in the resting state (Scheme I.4b).[18] In the initial step, O_2 coordinates to the reduced iron center and it becomes progressively reduced to superoxo and peroxo forms until O-O cleavage occurs to form an oxoiron(IV)-porphyrin radical species that carries out the oxidation of the substrate.

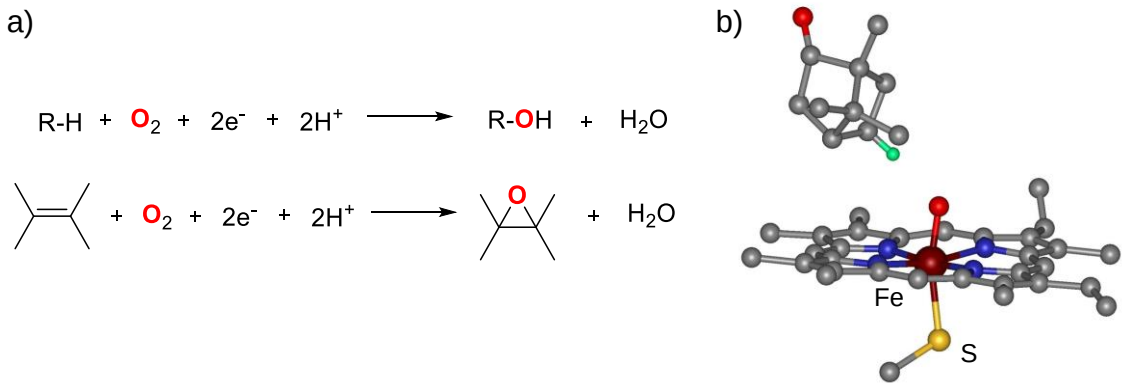

Scheme I.4. a) Hydroxylation and epoxidation reactions catalyzed by cytochrome P450. b) Active site of cyctochrome P450-camphor hydroxylase.[18]

The proposed mechanism of action of non-heme iron enzymes generally follows the heme paradigm, and evidence for peroxoiron(III) and high-valent oxoiron species has been obtained for some of these enzymes.[19] For example, the dinuclear iron enzyme soluble methane monooxygenase (Smmo), which catalyzes the oxidation of methane to methanol, activates O_2 via a peroxodiiron(III) and bis(μ-oxo)diiron(IV) species.[20] In the case of the mononculear non-heme Rieske dioxygenases, C-H hydroxylation and C=C *cis*-dihydroxylation occurs by the mediation of an oxoiron(V) species formed after O-O heterolytic cleavage of a peroxoiron(III) precursor.[21]

Taking inspiration form nature, selected non-heme iron complexes have been developed that oxidize C-H bonds by reaction with H_2O_2. Selectivity and stereospecificity exhibited by these catalysts convert them as good models of enzymes. However, due to their high reactivity, the active species do not accumulate in solution, and it is challenging to establish their nature. For instance, Chen and White used an iron(II) complex with an aminopyridine tetradentate ligand that reacted with H_2O_2 and acetic acid for the hydroxylation of unactivated secondary C-H bonds to afford products in useful yields and predictable selectivities (Scheme I.5a).[22] Then, Cussó *et al.* used a similar iron(II) complex with H_2O_2 in the presence of carboxylic acids to obtain excellent enatioselectivities in synthetically valuable yields for the oxidation of different olefins (Scheme I.5b).[23] In this line, Che and co-workers showed that an iron(III) catalyst was able to catalyze in less than 10 min the *cis*-dihydroxyaltion of olefins at 10 g scale using Oxone® as oxidant[24] (Scheme I.5c).

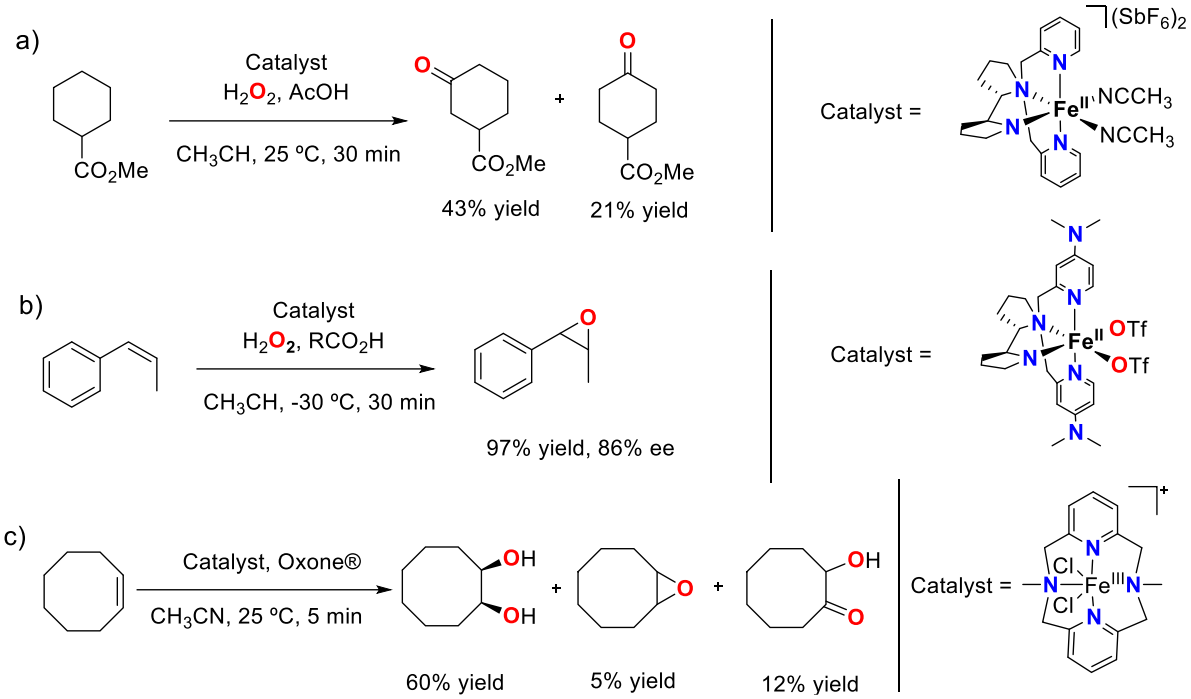

Scheme I.5. Selected examples of hydroxylation[22] (a) epoxidation[23] (b) and *cis*-dihydroxilation[24] (c) of olefins by bioinspired iron catalysts.

Oxidases and oxygenases based on copper present a wide range of active site configurations, from mononuclear (e.g. amine oxidase, galactose oxidase), dinuclear (e.g. peptidylglycine α-hydroxylating monooxygenase, tyrosinase), trinuclear (e.g. laccase) or polymetallic configurations (e.g. superoxide dismutase).

One of the best studied copper oxygenases is tyrosinase which catalyzes the oxidation of phenols to *ortho*-catechols and *ortho*-quinones towards the final synthesis of melanines (Scheme I.6a). XRD studies have enabled the unequivocal identification of the active site of tyrosinase, which in the reduced form is constituted by two copper(I) centers bound to three histidine residues in a trigonal planar distorted coordination geometry. Reversible reaction with O_2 gives rise to the formation of a (μ-η^2:η^2-O_2) peroxocopper(II) center, in which the O_2 has suffered a $2e^-$ reduction, $1e^-$ coming from each Cu^I atom (Scheme I.6b).[25,26] Despite not being observed in biological systems, synthetic models have shown that the (μ-η^2:η^2-O_2) peroxocopper(II) unit can interconvert with its bis(μ-oxo)dicopper(III) isomer, suggesting that this core might be responsible for substrate attack occurring during catalysis in tyrosinase.[27]

Another important copper-based enzyme is particulate methane monooxygenase (pMMO) which catalyzes the oxidation of methane to methanol. According to recent crystallographic studies, this enzyme operates with a dicopper active site but further studies are needed to unequivocally establish the nature of the active species.[28]

a) b)

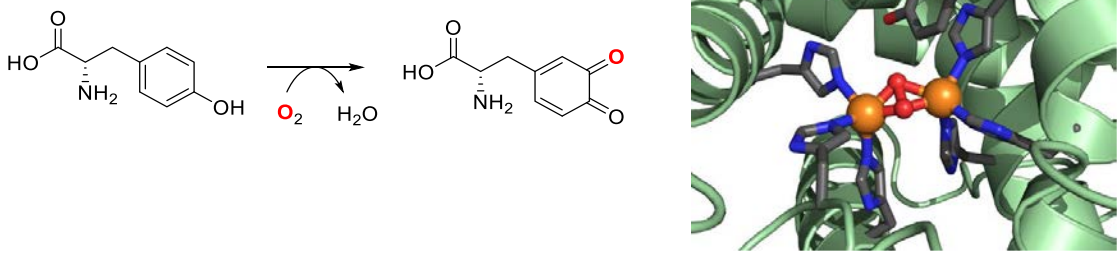

Scheme I.6. a) *Ortho*-hydroxylation of phenols catalyzed by tryrosinase. b) XRD structure of the substrate-bound tyrosinase.[29]

Dopamine β-hydroxylase and peptidylglycine α-hydroxylating monooxygenase represent another class of copper oxygenases which contain a mononuclear copper center capable of hydroxylating weak C-H bonds using a second reducing equivalent from a distant copper center. The reduced form of the enzyme reacts with O_2 to form a superoxocopper(II) intermediate which is further reduced to a hydroperoxocopper(II) species that either attacks the substrate directly or after forming an oxylcopper(II) species. The latter still lacks conclusive identification in an enzyme or synthetic model and thus, its role remains controversial.

Over the last decades an extensive library of synthetic models of copper-dioxygen adducts have been reported.[30] For example, in 2006, Sundermeyer and Schindler provided the only crystallographically characterized mononuclear superoxocopper(II) complex, $[Cu^{II}(O_2)(TMG_3tren)]$ using a bulky tripodal tetradentate ligand by reaction of the copper(I) precursor and O_2 (Scheme I.7b).[31] In 1992, Kitajima, Moro-oka, Kitagawa, Tatsumi, and co-workers reported the first crystal structure of Cu_2O_2 species (Scheme I.7a).[32]

a) b)

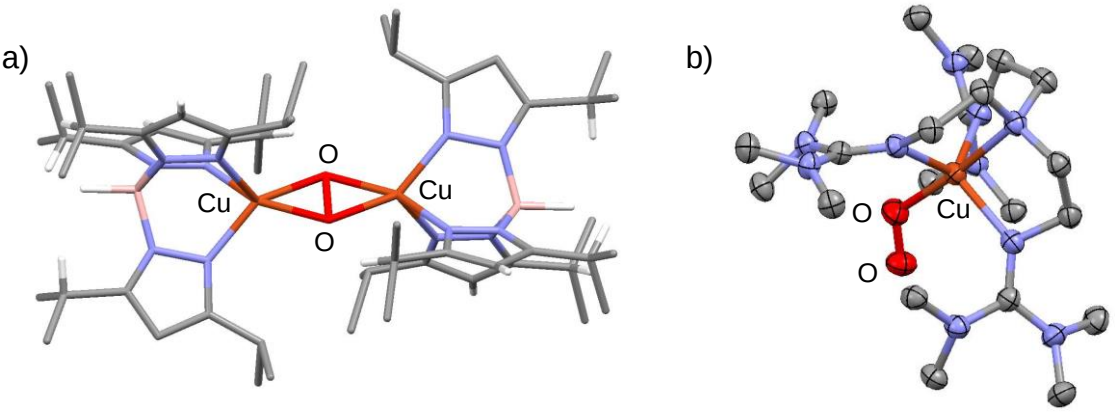

Scheme I.7. a) XRD structure of the first example of a peroxodicopper(II) species bound in a side-on fashion.[32] b) XRD structure of $[Cu^{II}(O_2)(TMG_3tren)]$ (ellipsoids drawn at 50% probability and hydrogen atoms omitted for clarity).[31]

Overall, iron and copper centers play key roles in oxygenases and bioinspired oxidation systems. As a consequence, a variety of studies have led to the detection and characterization of a series of biologically and synthetically relevant copper-oxygen and iron-oxygen species including oxometal, peroxometal or superoxometal species in both mononuclear and dinuclear systems.

These species are invoked as key reaction intermediates along the catalytic cycle and they are either directly responsible for the substrate oxidation event or they precede the formation of the active species. In contrast to iron and copper, and despite some efforts, detection of metal-oxygen species involved into the mode of action of enzymes and oxidation catalysts based on other transition metals such as nickel and cobalt are much scarcer but they constitute interesting species with important implications in oxidation catalysis.

I.2.3. The "Oxo-wall" concept: unstablity of oxometal species based on late first-row transition metals

The stability of terminal high-valent oxometal compounds can be derived from simple ligand field.[33] For late transition metals (groups 9-11, e.g. Co, Cu and Ni), multiple oxometal bonds cannot be supported in tetragonal (C_{4v}) geometries and the usual convention is to describe them as oxylmetal species. Thus, the "*Oxo-wall"* concept predicts that oxometals are stabilized at metal centers with an oxidation state of no less than +4 and no more than 4 d electrons in C_{4v} environments. Consequently, oxo complexes of the early transition elements (groups 3−6) are extremely stable and abundant. Those of the mid-transition elements (groups 7−8) are generally more reactive and intensely investigated, and those of the late transition metal (groups 9−11) are rarely reported.[34] For this reason, detection of terminal high-valent oxometal species based on cobalt, nickel or copper and postulated in the mechanism of action of highly efficient oxidation catalysts are relatively scarce.

As stated above, in C_{4v} environments the oxo moiety is typically found in metals with a d electron count of 4 or less. The first two electrons populate the non-bonding d_{xy} orbital (e.g. d^2: oxomanganese(V)), but the subsequent addition of electrons populates the degenerated M-O π^* orbital (d_{xz} and d_{yz}) (Figure I.4). For this reason, in octahedral geometries terminal triple bonded oxometal complexes are very rare. However, there are many terminal oxometal complexes with a bond order of less than 3 through the population of the M-O π^* orbitals with one electron (e.g. d^3: oxoiron(V)) or two electrons (e.g. d^4:oxoiron(IV)). However, addition of more electrons causes a destabilization of the oxometal unit due to further population of antibonding orbitals. A similar situation is found in square-pyramidal geometries because removal of the apical ligand *trans* to the oxo unit in octahedral geometries has a minimal effect on the overall splitting pattern of molecular orbitals.

Changing the geometry about the M-O to C_{3v} affords a different criterion for the stabilization of a terminal oxometal bond. For a trigonal bipyramidal geometry, the two lowest orbitals are the M-O π^* (d_{xz} and d_{yz}) (Figure I.4). In this case, an oxometal species is only possible for d^0, d^1 or d^2 metal centers. On the other hand, in pseudotetrahedral geometries oxometal compounds are possible for up to 6 d electrons (Figure I.4). In this geometry late transition metal with terminal oxo ligands are known (e.g. d^4 oxoiridium(V)[35], d^6 oxocobalt(III).[36]).

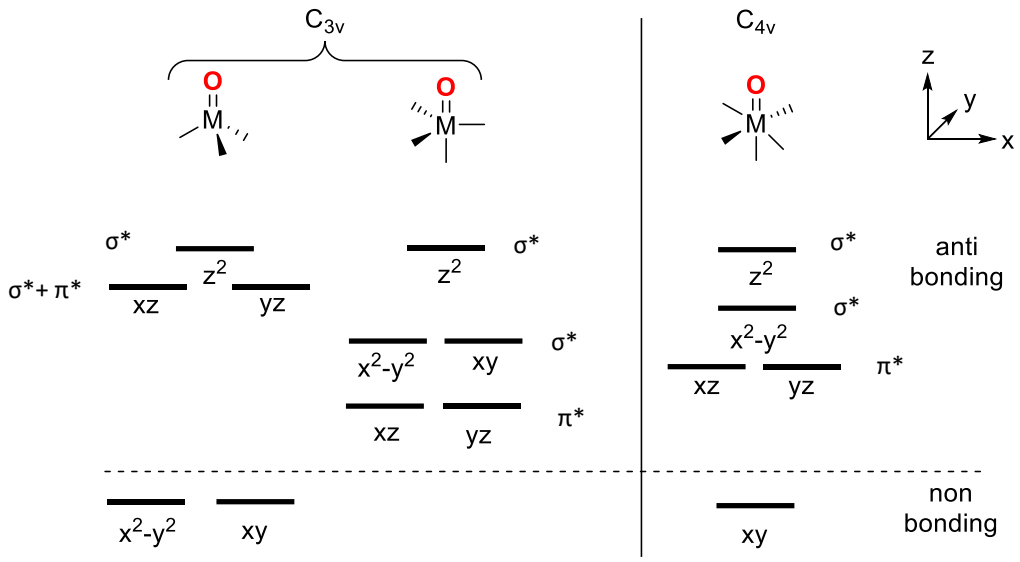

Figure I.4. Qualitative d orbital splitting diagrams for oxometal cores residing in pseudotetrahedral (C_{3v}), trigonal bipyramidal (C_{3v}), and octahedral/square-pyramidal (C_{4v}) ligand fields. M=O π antibonding orbitals and the σ antibonding orbitals are represented as π* and σ*, respectively.

I.2.4. Mononuclear cobalt-oxygen species

Cobalt has been used in the oxidation of alkanes as a catalyst for important industrial processes such as the Mid-Century/Amoco process (synthesis of terephthalic acid by oxidation of *p*-xylene)[37] and DuPont process (cyclohexane oxidation for the synthesis of adipic acid) using air or pure O_2 as oxidants.[38] Both reactions are mediated by alkylperoxocobalt(III) intermediates and they proceed at high temperatures and pressures.[39] Apart from these rather harsh oxidation reactions, cobalt catalysts have also found application in the oxidation of strong C-H bonds under mild conditions. In this line, *N*-hydroxyphthalimide (NHPI) and $Co(acac)_2$ can be efficiently used in the oxidation of alkanes and alkylbenzenes at ambient conditions (room temperature, 1 atm O_2).[40,41,42] This system enables the conversion of cyclohexane to cyclohexanone and adipic acid, adamantane can be oxidized to a mixture of alcohol and ketone products with conversions up to 93%, and toluene is efficiently transformed to benzaldehyde and benzoic acid (Scheme I.8).[43]

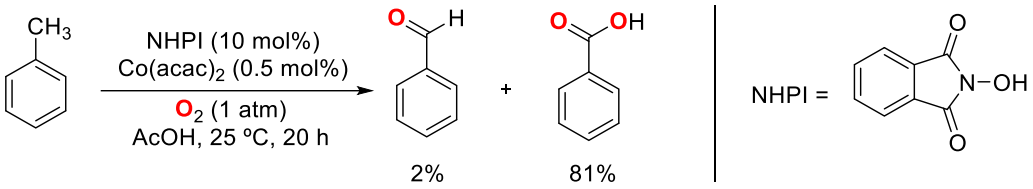

Scheme I.8. Oxidation of toluene by $Co(acac)_2$/NHPI using O_2 as the oxidant. The yield (%) of each product is based on the amount of reacted substrate (74% conversion).

Thus, highly reactive cobalt-oxygen species are involved in the cobalt-catalyzed transformations described above. Indeed, well-defined mononuclear cobalt-oxygen species have been known for decades, which is in part due to the fact that cobalt(III) complexes are thermodynamically and kinetically very stable complexes (low spin d^6 configuration) and so the corresponding cobalt(III)-

oxygen adducts are easier to study compared to other metal-oxygen compounds. Thus, in early biomimetic investigations, the relative stability of Co^{III}-dioxygen complexes provided a lot of information on the structure and physicochemical properties of transition metal-dioxygen intermediates. For instance, coboglobin, an enzyme analogue of hemoglobin in which the iron center has been replaced by cobalt, was used in the 70s to structurally mimic the biologically relevant O_2 transporter (Scheme I.9).[44] This substitution allowed the formation of a very stable superoxocobalt(III) complex through the reductive activation of molecular oxygen by the cobalt(II) starting material. The structure and electronic properties of this species could be studied in detail and the results could be extrapolated to hemoglobin, for which the O_2 binding mode was not understood at that time.

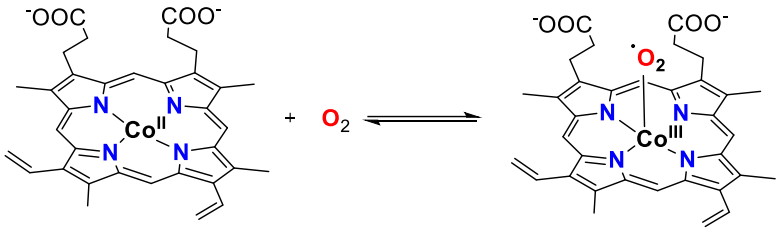

Scheme I.9. Schematic representation of coboglobin active site.

Despite the fact that cobalt is found in most living organisms as part of the vitamin B12 structure, there are to date no Co-enzymes known that are directly involved in O_2 activation. For this reason, in the following section we will focus our attention to the most important cobalt-oxygen species that have been synthesized to date and that might be relevant in cobalt-catalyzed C-H oxidation reactions. For the purposes of this thesis, only mononuclear cobalt-oxygen species will be reviewed.

Among the different metals used in the synthesis of metal-dioxygen complexes, cobalt was the first one for which a metal-dioxygen species could be unequivocally synthesized and characterized. It was back in 1966 when the dinuclear superoxocobalt(III) species $[(NH_3)_5Co^{III}(\mu\text{-}O_2)Co^{III}(NH_3)_5]^{5+}$ was reported by Schaefer and Marsh.[45] Due to its remarkable stability, in most of the reported cobalt-oxygen species the metal center is found in the +3 oxidation state. Usually these complexes exhibit poor oxidation capability because further electron donation to the bound dioxygen moiety in order to cleave the O-O bond is difficult in comparison with iron and copper counterparts. In the particular case of mononuclear cobalt-oxygen species, several well-defined compounds have been reported. In the following section these species are overviewed and they are classified into different categories depending on their structure and the degree of reduction of the O_2 moiety. Tables I.2 summarizes the spectroscopic features of the mononuclear cobalt-oxygen species described in this section.

I.2.4.1. Superoxocobalt species

In the 1970s a wide number of mononuclear superoxocobalt(III) species were reported to be formed by reaction of cobalt(II) precursors bearing Schiff base or porphyrins ligands with O_2

(Figure I.5). However, their characterization was rather poor and limited to EPR spectroscopy and FT-IR.[46]

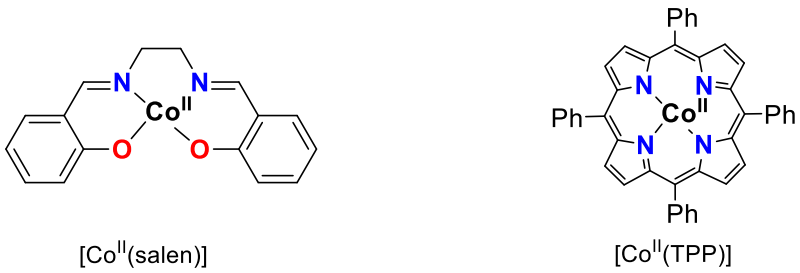

[Co^{II}(salen)] [Co^{II}(TPP)]

Figure I.5. Schematic representation of cobalt(II) salen and cobalt(II) porhyrin complexes for the preparation of superoxocobalt(III) compounds.

Better characterization of superoxocobalt species was achieved in the 90s. At that time Theopold and co-workers could synthesize a superoxocobalt(II) compound, which was obtained upon reaction of [Co^{I}(Tp^{tBu,Me})(N$_2$)] with O$_2$ at room temperature (Figure I.6).[47] FT-IR analysis showed a O-O stretching frequency of 961 cm^{-1} which was between those reported for superoxo (1200-1070 cm^{-1}) and peroxo units (930-740 cm^{-1}). The ambiguity was solved after crystallographic XRD analysis, which indicated that the O-O bond length in the [Co^{II}(O$_2$)(Tp^{tBu,Me})] complex was 1.262 Å. The observed distance fits well with a cobalt center in a +2 oxidation state bearing a superoxo moiety. This assignment was further corroborated by a temperature independent magnetic moment (μ_{eff}) of 3.88 μ_B, indicative of an antiferromagnetic coupling between the cobalt(II) center (S = 3/2) and the superoxo ligand (S = 1/2). Furthermore, it was observed that this complex could abstract hydrogen atoms from the ligand C-H bonds.[47]

In 2004, Goldberg and co-workers could in situ generate the superoxocobalt(III) species [Co^{III}(TBP$_8$Cz)(O$_2$)(py)]$^-$ species using a corrole system as ligand by reaction of the cobalt(II) precursor with oxygen at -78 ºC (Figure I.6).[48] Interestingly, reversible O$_2$ binding occurred at 25 ºC under argon as determined by EPR spectroscopy.

Very recently, Berry and co-workers characterized a superoxocobalt(II) complex with a ligand-centered radical [Co^{II}(•N(PhNCO*i*Pr)$_2$)(O$_2$)]$^-$ which was formed by reaction of the cobalt(II) precursor with O$_2$ resulting in O$_2$ reduction by an electron originating from the redox non-innocent ligand (Figure I.6).[49] Spectroscopic characterization was performed by FT-IR with a characteristic band at 1248 cm^{-1} that shifted to 1203 cm^{-1} with ^{18}O$_2$. XAS, EPR and DFT studies further supported this assignment. Interestingly, [Co^{II}(•N(PhNCO*i*Pr)$_2$)(O$_2$)]$^-$ reacted with both electrophilic and nucleophilic substrates: triphenylphosphine was oxidized to the corresponding oxide but also 2-phenylpropionaldehyde formed acetophenone by a deformylation reaction. This divergent reactivity was attributed to the electronic structure which showed that the d_{xy} orbital could behave as either a donor or acceptor orbital.

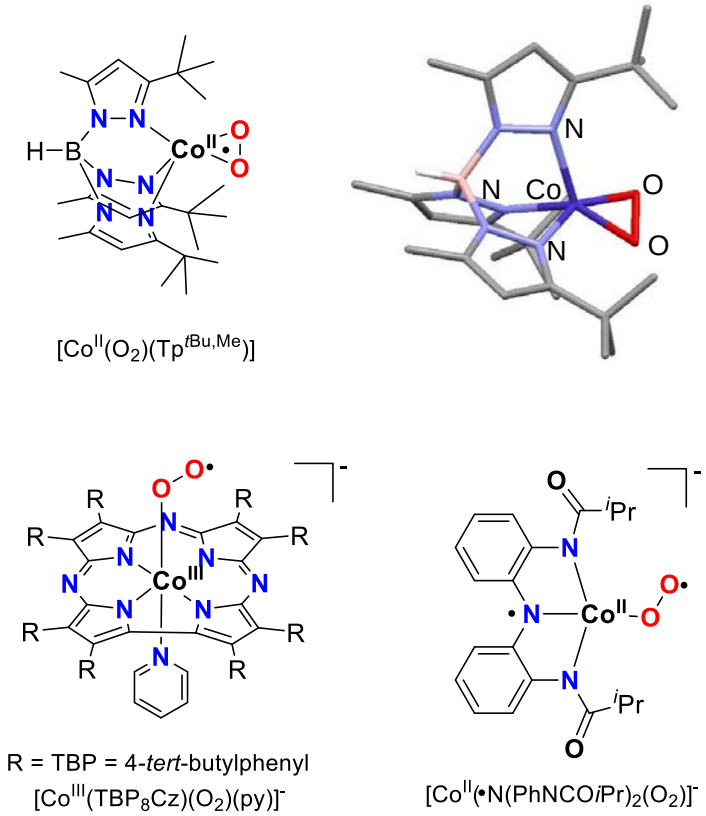

Figure I.6. Schematic representation of spectroscopically characterized superoxocobalt(II/III) species together with the XRD structure of $[Co^{II}(O_2)(Tp^{tBu,Me})]$ (hydrogen atoms omitted for clarity).

I.2.4.2. (Hydro)peroxocobalt species

In 2004, Meyer and co-workers reported the formation of the diamagnetic peroxocobalt(III) $[Co^{III}(O_2)(TIMEN)]^+$ bearing a carbene-based tripodal ligand, which was formed by the reaction of a cobalt(I) complex with O_2 at room temperature (Figure I.7). Vibrational studies showed a characteristic O-O frequency at 890 cm^{-1} which shifted by -50 cm^{-1} when ^{18}O-labeled O_2 was used for its generation. Furthermore, XRD analysis of the structure of $[Co^{III}(O_2)(TIMEN)]^+$ showed a six-coordinate cobalt center with four positions occupied by the TIMEN ligand and the other two corresponding to the side-on bound peroxide ligand with a characteristic O-O distance of 1.429 Å. This compound was able to carry out oxygen-atom transfer to benzoyl chloride to form phenyl benzoate, but no reaction occurred with alkenes, styrene, cyclohexene or triphenylphospine.[50]

Peroxocobalt(III) species can also be generated by reaction of cobalt(II) precursors with hydrogen peroxide. This is the case of $[Co^{III}(O_2)(TMEN)_2]^+$ reported by Willis, Jackson and co-workers[51] or compound $[Co^{III}(O_2)(12\text{-TMC})]^+$ and $[Co^{III}(O_2)(13\text{-TMC})]^+$ described by Nam and co-workers in 2010 (Figure I.7).[52,53] These compounds were fully characterized by spectroscopic techniques (rRaman spectroscopy, EPR and X-ray diffraction). Compounds $[Co^{III}(O_2)(12\text{-TMC})]^+$ and $[Co^{III}(O_2)(13\text{-TMC})]^+$ were found to be reactive in the oxidation/deformylation of aldehydes. The nucleophilic reactivity of peroxocobalt(III) complexes was found to depend significantly on the ring size of the macrocyclic ligands, and $[Co^{III}(O_2)(12\text{-TMC})]^+$ was a poorer oxidant compared to $[Co^{III}(O_2)(13\text{-TMC})]^+$. Very recently, the same group could generate and characterize (both

spectroscopically and computationally) the hydroperoxocobalt(III) species $[Co^{III}(OOH)(12\text{-}TMC)]^{2+}$ formed upon addition of trific acid to $[Co^{III}(O_2)(12\text{-}TMC)]^{+}$ at low temperature (Figure I.7). Reactivity studies on this hydroperoxocobalt(III) compound showed an amphoteric reactivity and reaction occurred with both nucleophilic and electrophilic substrates.[54]

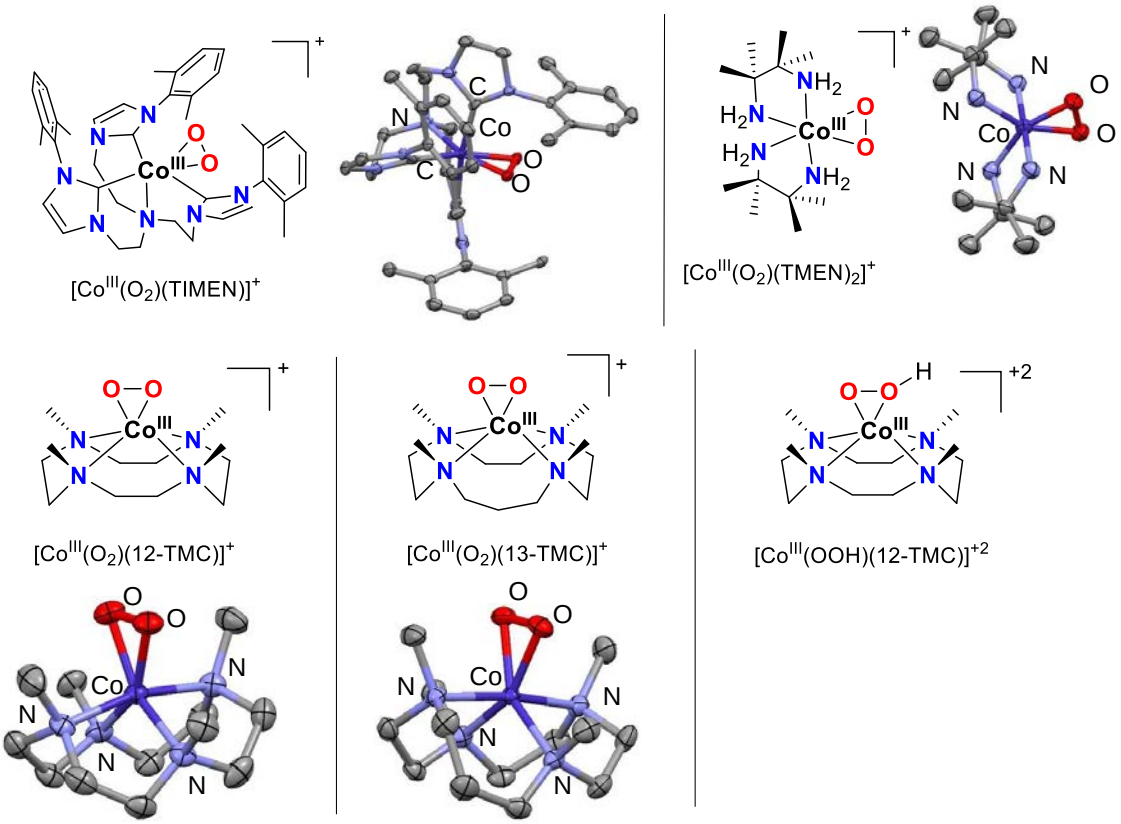

Figure I.7. Schematic representation of spectroscopically characterized (hydro)peroxocobalt(III) species and XRD structures of $[Co^{III}(O_2)(TIMEN)]^{+}$, $[Co^{III}(O_2)(TMEN)_2]^{+}$, $[Co^{III}(O_2)(12\text{-}TMC)]^{+}$, and $[Co^{III}(O_2)(13\text{-}TMC)]^{+}$ (ellipsoids drawn at 50% probability and hydrogen atoms and counterions omitted for clarity).

I.2.4.3. Alkylperoxocobalt species

Experimental evidences point towards the involvement of alkylperoxocobalt species in some of the industrially relevant cobalt-catalyzed oxidation processes (see above).[55] A few studies have been published on the preparation of such species and most systems require the use of anionic ligands bearing hard donor centers such as deprotonated carboxamido groups, carboxylates, phenolates, oximates, or β-diketonates. Synthesis of these octahedral $[LCo^{III}(OOR)]$ complexes has been achieved by different strategies: a) addition of excess ROOH to a Co^{II} precursor, b) dioxygen insertion into a cobalt-alkyl bond or into metal-ligand bond promoted by irradiation, and c) reaction of a hydroxo precursor with the corresponding alkylhydroperoxide (ROOH).

The first examples of alkylperoxocobalt(III) species were reported back in the 70s and 80s and the XRD structures of $[Co^{III}(dmgH)_2(OOCm)(py)]$[56], $[Co^{III}(Salpr)(4\text{-}OO\text{-}(2,4,6\text{-}t\text{Bu-}C_6H_2O))]$[57], $[Co^{III}(TPP)(OO\text{-}CH_2CH{=}CH_2)(py)]$[58] and $[Co^{III}(BPI)(OCOPh)(OOt\text{Bu})]$[59] were described (Figure I.8). For the latter, catalytic hydroxylation of alkanes was observed and they were converted into alcohols, ketones, or the *tert*-butylperoxy product.

Afterwards, in the late 90s Mascharak and co-workers could isolate other new alkylperoxocobalt(III) compounds: [$Co^{III}(Py_3P)(OOR)$] (R = OO*i*Pr, OO*t*Bu, OOCy, OOCm),[60,62] [$Co^{III}(PyPz_2P)(OOCy)$][61] and [Co^{III}(β-diketonate)$_2$(L)(OO*t*Bu)] (L= py, 1-MeIm) (Figure I.8).[62] The structures were unequivocally established by XRD crystallography and reactivity studies showed that these compounds were competent to perform catalytic oxidation of hydrocarbons (e.g. cyclohexane to generate cyclohexanol, cyclohexanone, and cyclohexyl chloride as products).

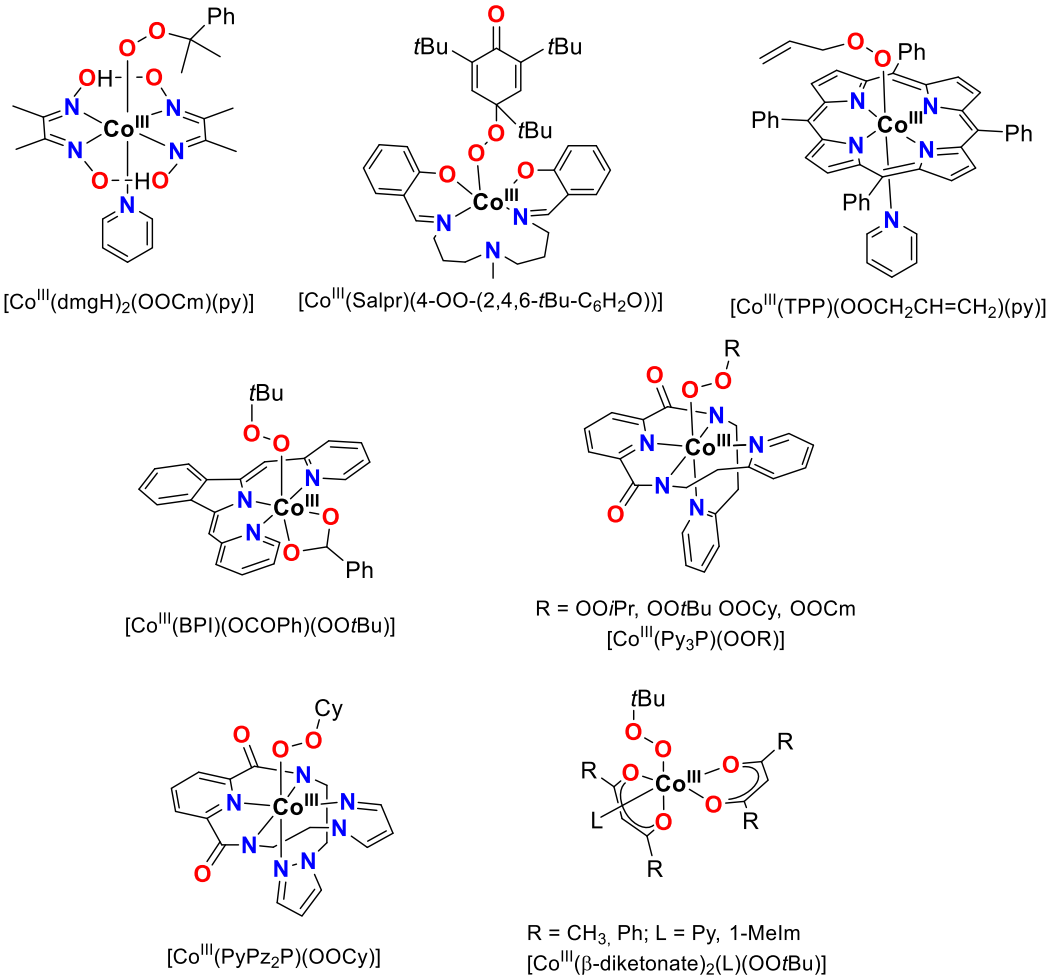

Figure I.8. Schematic representation of structurally characterized alkyperoxocobalt(III) species.

I.2.4.4. Oxyl/oxocobalt species

Oxocobalt species (best described as oxylcobalt species, see section I.1.2.3 the "Oxo-wall") are proposed to be responsible in a number of oxidation reactions catalyzed by cobalt complexes such as hydroxylation reactions. However, there is only indirect evidence of their existence and they have never been directly observed.[63]

Only recently, Ray and co-workers could isolate a Lewis acid adduct of an oxocobalt(IV) species, which provided the first direct evidence for the existence of such species with $Sc(OTf)_3$ (Tf = trifluoromethanesulfonyl) (Figure I.9). The synthesis was carried out by reaction of a cobalt(II) complex of the tetradentate tripodal ligand TMG_3tren with iodosobenzene in the presence of Sc^{3+}. The Lewis acid oxocobalt adduct could be characterized by XAS and EPR. These data together

with DFT studies agreed with the formulation of this species as {[Co^{IV}(O)(TMG$_3$tren)]-Sc(OTf)$_3$}$^{2+}$. The Lewis acid stabilized species was further reacted with substrates at –60 ºC, showing the ability to perform H-atom abstraction and O-atom transfer reactivities.[64] Recently, Borovik and co-workers provided a different formulation for Ray's system and they assigned it as a hydroxocobalt(III) species.[65] The use of Lewis acids was also used in 2014 by Ray, Nam and co-workers to spectroscopically characterize by EPR and XAS an oxocobalt(IV) using a tetraamido macrocyclic ligand with the general formula {[Co^{IV}(O)(TAML)]-Sc(OTf)$_3$}$^{+}$ (Figure I.9). This complex was able to react with weak C-H bonds and thioanisole to perform H-atom abstraction and O-atom transfer, respectively. [66]

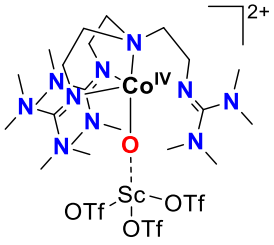

{[Co^{IV}(O)(TMG$_3$tren)]-Sc(OTf)$_3$}$^{2+}$

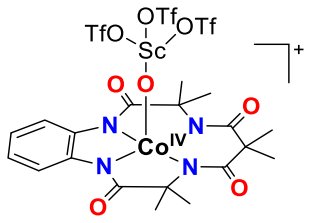

{[Co^{IV}(O)(TAML)]-Sc(OTf)$_3$}$^{+}$

Figure I.9. Schematic representation of spectroscopically characterized oxocobalt(IV) adducts stabilized with Sc^{3+}.

Overall, there are different types of well-defined mononuclear cobalt-oxygen species specially bearing the kinetically stable cobalt(III) center. However, due to the remarkable stability of these complexes, reactivity studies are still relatively scarce. Specially interesting would be the detection and characterization of oxo/oxylcobalt species without the need of stabilization with Lewis acids. Surely these will be strong oxidizing species with relevance in oxidation catalysis.

Table I.2. Selected spectroscopic features of synthetic mononuclear superoxo, peroxo, alkylperoxo and oxo/oxyl cobalt species.

	S	*r*(O-O), Å[a]	ν(O-O), cm^{-1} (Δ[^{18}O], cm^{-1})[b]	μ_{eff} (μB)	*g* values[c]	ref
Superoxocobalt						
$[Co^{II}(O_2)(Tp^{tBu,Me})]$	3/2 + 1/2	1.262	961	3.88		47
$[Co^{III}(TBP_8Cz)(O_2)(py)]^-$	1/2	-	-	-	1.996, 2.011, 2.075	48
$[Co^{II}(•N(o\text{-}PhNC(O)iPr)_2)(O_2)]^-$	1/2	-	1248 (1203)	2.13	2.20,2.00,1.975	49
(Hydro)peroxocobalt						
$[Co^{III}(O_2)(TIMEN)]^+$	0	1.429	890 (840)	-	-	50
$[Co^{III}(O_2)(TMEN)_2]^+$	0	1.457	861	-	-	51
$[Co^{III}(O_2)(12\text{-}TMC)]^+$	0	1.4389	902 (845)	-	Silent	52-53
$[Co^{III}(O_2)(13\text{-}TMC)]^+$	0	1.438	902 (846)	-	Silent	52-53
$[Co^{III}(OOH)(12\text{-}TMC)]^{2+}$	0	-	-	-	Silent	54
Alkyperoxocobalt						
$[Co^{III}(dmgH)_2(OOCm)(py)]$	0	1.455	-	-	-	56
$[Co^{III}(Salpr)(4\text{-}OO\text{-}(2,4,6\text{-}tBu\text{-}C_6H_2O))]$	0	1.50	-	-	-	57
$[Co^{III}(TPP)(OO\text{-}CH_2CH{=}CH_2)(py)]$	0	1.40	-	-	-	58
$[Co^{III}(BPI)(OCOPh)(OOtBu)]$	0	1.444	880	-	-	59
$[Co^{III}(Py_3P)(OOtBu)]$	0	1.49	879	-	-	60,62
$[Co^{III}(PyPz_2P)(OOCy)]$	0	1.456	-	-	-	61
$[Co^{III}(\beta\text{-diketonate})_2(L)(OOtBu)]$	0	1.466		-	-	62
Oxo/oxylcobalt						
$\{[Co^{IV}(O)(TMG_3tren)]\text{-}Sc(OTf)_3\}^{2+}$	3/2	-	-	-	2.33, 2.10	64
$\{[Co^{IV}(O)(TAML]\text{-}Sc(OTf)_3\}^+$	1/2	-	-	-	2.57, 2.16, 2.03	66

[a] Bond distances are determined by XRD.
[b] Frequency of the Ni-O and O-O vibrations and the corresponding shifts upon labeling with ^{18}O determined by Raman or IR.
[c] *g* values determined by EPR.

I.2.5. Mononuclear nickel-oxygen species

Despite being much less spread than iron or copper, nickel has also been found in enzymes involved in oxidation processes. For example, nickel superoxide dismutase catalyzes the disproportionation of superoxide in a process in which superoxonickel(II) and superoxonickel(III) species play a key role (Figure I.10 left).[67] Similarly, a nickel-dioxygen adduct has been crystallographically detected in the active site of quercetin 2,4-dioxygenase, during the oxidative cleavage of the flavonol quercetin (Figure I.10 right).[68] Acireductone dioxygenase also employs nickel to catalyze the conversion of acireductone to 3-(methylthio)propionate, formate and carbon monoxide.[69] However, in this enzyme the metal activates the substrate towards reaction with O_2 by acting as a Lewis acid and no evidence for metal-centered redox chemistry involving nickel-O_2 species exists.

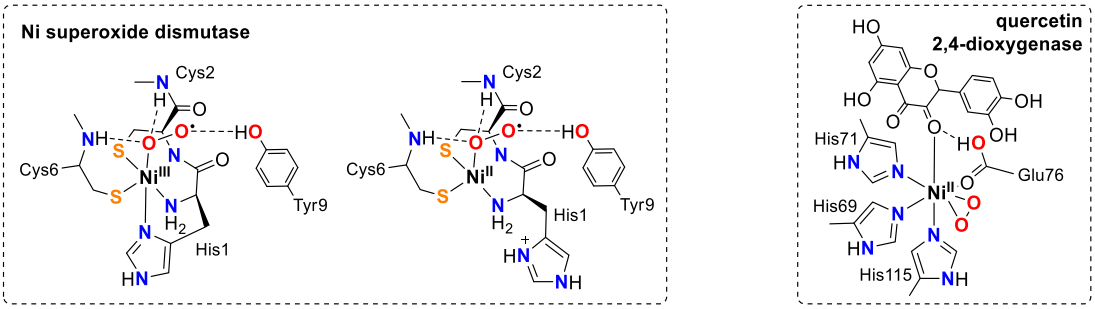

Figure I.10. Schematic representation of the terminal nickel-oxygen species in Ni superoxide dismutase and Ni dependent quercetin 2,4-dioxygenase.

On the other hand, in the field of synthetic chemistry, nickel catalysts have been proven to be efficient in the oxidation of alkanes and alkenes. In 1987, Kochi and Koola reported that $[Ni^{II}(cyclam)]^{2+}$ (cyclam = 1,4,8,11-tetraazacyclotetradecane) complex was a highly active catalyst for the epoxidation of olefins by iodosylbenzene.[70] Prior to this, there were no examples of nickel-catalyzed olefins epoxidation. Other compounds such as $[Ni^{II}(OAc)(tpa)(H_2O)]^+$ (tpa = tris(2-pyridylmethyl)amine) and related systems[71,72,73] were reported to catalyze the oxidation of alkanes or aromatics with *m*CPBA or H_2O_2 as oxidants (Scheme I.10), while Ni-salen complexes (salen = N,N'-bis(salicylidene)ethylenediamine)[74,75] and Ni^{II} salts[76] have been successfully applied as catalysts in alkene epoxidation in combination with NaOCl. In most of these transformations, mononuclear nickel-oxygen compounds are postulated to be the active species directly responsible for the oxidation event.

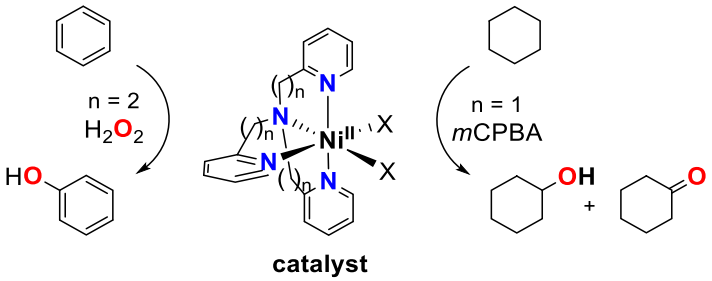

Scheme I.10. Tpa-derived nickel complexes as catalysts for the oxidation of benzene and cyclohexane using H_2O_2 and *m*CPBA as oxidants, respectively.

Thus, it is clear that nickel-oxygen species are emerging as a new class of metal-oxygen compounds with relevance both in biology and catalysis. As it will be shown in the following sections, nickel is a very versatile metal for the activation of O_2, which results in structurally and electronically diverse nickel-oxygen species. The synthesis of these compounds entails either direct reaction of a low-valent nickel(I) complex with O_2 or the interaction of a nickel(II) compound with activated forms such as superoxides or peroxides, which, in some cases, may undergo O-O bond cleavage. Extensive spectroscopic studies have enabled the characterization of these species which are described below. For the purposes of the present thesis, only mononuclear species are described. Table I.3 summarizes the spectroscopic features of the mononuclear cobalt-oxygen species described in this section.

I.2.5.1. Hydroxonickel and related carbonatonickel species

Terminal hydroxometal units are relevant species in the catalytic cycle of enzymes. However, their involvement in the oxidation event is limited as they are usually the species formed prior or after substrate oxidation occurs. Preparation of monomeric hydroxonickel compounds is generally challenging because the OH ligand tends to bridge between metal centers in middle and late transition metals. Frequently, bulky ancillary ligands are needed to prevent formation of multi-nuclear species.

In 2004, Riordan and co-workers reported the crystal structure of a mononuclear terminal hydroxonickel(II) complex using the macrocyclic tetradentate ligand 14-TMC (Figure I.11).[77] Compound $[Ni^{II}(OH)(14\text{-}TMC)]^+$ showed a square pyramidal geometry, which was responsible for the high-spin $S = 1$ character of this compound. More common are diamagnetic hydroxonickel(II) species with the metal center in a square planar environment typical for d^8 metals, such as diphosphine-based systems including $[Ni^{II}(OH)(PNP)]$[78] and the organometallic complexes $[Ni^{II}(OH)(PCP)]$ and $[Ni^{II}(OH)(dippe)(Me)]$ (Figure I.11).[79,80] A distorted square planar geometry was observed in $[Ni^{II}(Mebuea)(OH)]^-$ (Figure I.11).[81] In this case, a network of intramolecular hydrogen-bonding interactions was established between the hydroxo ligand and the amide NH groups of the Mebuea ligand. Finally, no structural information has been gathered for hydroxonickel(III) species, but EPR and vibrational characterization of such compounds has been achieved in a few cases.[82,83]

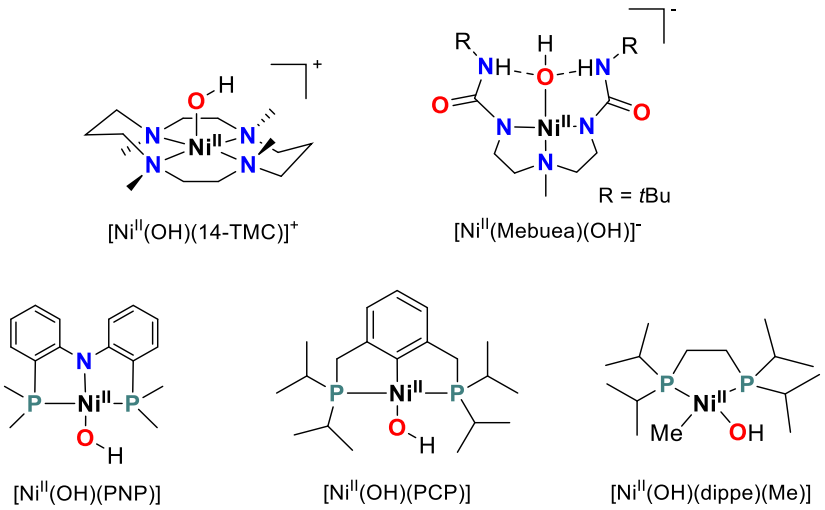

Figure I.11. Schematic representation of spectroscopically characterized hydroxonickel(II) species.

The square planar hydroxonickel(II) species described by Holm and co-workers with pincer type 2,6-pyridinedicarboxamidate ligand deserve special consideration. Bulky R groups in $[Ni^{II}(pyN_2^{R2})(OH)]^-$ were necessary to prevent the formation of octahedral bis-ligand complexes (Scheme I.11).[84] Such compounds reacted with ethyl formate and CO_2 to form $[Ni^{II}(pyN_2^{R2})(HCO_2)]^-$ and $[Ni^{II}(pyN_2^{R2})(HCO_3)]^-$ products, respectively.[85] Interestingly, rate constants for the reaction with CO_2 were directly affected by the bulkiness of the R group, being faster for less sterically hindered systems (Me > Et > *i*Pr > *i*Bu > Ph) and they were in the range of those determined by carbonic anhydrase, the most efficient enzyme for CO_2 fixation reactions.[86]

One-electron oxidation of the bicarbonate complex $[Ni^{II}(pyN_2^{Me2})(HCO_3)]^-$ using *tris*(4-bromophenyl)ammoniumyl hexachloroantimonate (magic blue) as oxidant at low temperature afforded the corresponding nickel(III) species as described by McDonald and co-workers (Scheme I.11).[87a] No crystal structure was reported but the nature of this species could be unambiguously determined by UV-vis, XAS, EPR and DFT calculations. Reactivity studies showed that $[Ni^{III}(pyN_2^{Me2})(HCO_3)]$ carried out hydrogen-atom abstraction of O-H and weak C-H bonds (e.g. 1-benzyl-1,4-dihydronicotinamide) and oxygen-atom transfer to triphenylphospine. Very recently, the same group reported two structurally related metastable Ni^{III}-oxygen complexes bearing different oxygen donors, that is $[Ni^{III}(pyN_2^{Me2})(OAc)]$ and $[Ni^{III}(pyN_2^{Me2})(ONO_2)]$ formed by one-electron oxidation of their Ni^{II} precursors (Scheme I.11).[87b] Compound $[Ni^{III}(pyN_2^{Me2})(ONO_2)]$ was specially active in the oxidation of phenols, while $[Ni^{III}(pyN_2^{Me2})(OAc)]$ was the strongest oxidant in the series in hydrogen-atom abstraction from C-H bonds (including strong ones such as those of toluene). These results not only demonstrate that late transition metals can behave as strong oxidants, but also that their reactivity can be easily tuned by manipulating the nature of the oxygen substituents.

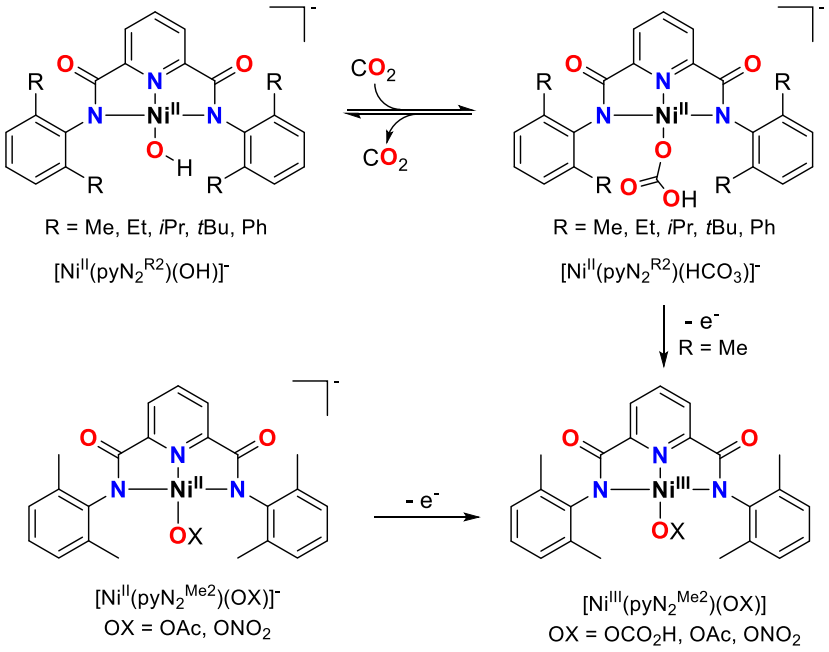

Scheme I.11. Fast and reversible CO_2 coordination to $[Ni^{II}(pyN_2^{R2})(OH)]^-$ and $1e^-$ oxidation of $[Ni^{II}(pyN_2^{Me2})(OX)]^-$ species (OX= HCO_3, OAc, ONO_2) to form $[Ni^{III}(pyN_2^{Me2})(OX)]$.

I.2.5.2. Superoxonickel species

Superoxonickel species are proposed to be key reaction intermediates in the catalytic cycle of nickel superoxide dismutase.[88,89] This is also a plausible formulation for the nickel-dioxygen species which has been recently crystallographically characterized in nickel-dependent quercetin 2,4-dioxygenase (Figure I.10).

In 2004, Riordan and co-workers reported the formation of a side-on superoxonickel(II) species by reaction of the nickel(I) complex $[Ni^{I}(PhTt^{Ad})(CO)]$ with O_2 (Figure I.12).[90] Compound $[Ni^{II}(O_2)(PhTt^{Ad})]$ was a precursor of a bis(μ-oxo)dinickel(III) species previously characterized by the same group.[91] ^{1}H-NMR showed paramagnetically shifted signals and EPR analysis displayed a S = 1/2 signal (g = 2.24, 2.19, 2.01). Finally, a complete XAS study confirmed the +2 oxidation state of the metal center and suggested a side-on coordination of the O_2 molecule. Unfortunately, no vibrational analysis could be performed and information about the O-O and Ni-O stretching frequencies was missing. According to DFT calculations, the single unpaired electron resided in the Ni d_{z2} orbital, in accordance with the measured EPR spectrum. $[Ni^{II}(O_2)(PhTt^{Ad})]$ oxidized PPh_3 to $OPPh_3$ and also nitric oxide to nitrate. ^{18}O-labeling experiments confirmed O_2 as the oxygen source.

In 2006, the same group described the formation of another superoxonickel(II) but in this case the O_2 was bound in an end-on fashion (Figure I.12).[92] $[Ni^{II}(O_2)(14\text{-TMC})]^+$ was also generated by reaction of the nickel(I) precursor with O_2 in THF, which preceded the formation of a (μ-1,2-peroxo)dinickel(II) species.[93] Apart from UV-vis, XAS and EPR, spectroscopic analysis of $[Ni^{II}(O_2)(14\text{-TMC})]^+$ also included resonance Raman which exhibited bands at 1131 and 437 cm$^-$

[1] which downshifted to 1067 and 416 cm^{-1}, respectively, in samples prepared from ^{18}O-labeled O_2. The more intense, higher-energy feature was assigned to a ν(O-O) mode, while the low-energy band was associated to a Ni-O vibration. The frequency of the O-O vibration was in full agreement with that expected for a superoxide ligand (1070–1200 cm^{-1}). An end-on superoxide coordination was proposed on the basis of EXAFS data and theoretical calculations. An analogous species was obtained using the structurally related 13-TMC ligand (Figure I.12).[94] Similarly to [$Ni^{II}(O_2)(PhTt^{Ad})$], these species were poorly reactive and oxygen-atom transfer was limited to triphenylphosphine.

The first and, so far, the only crystallographically characterized superoxonickel species was reported by Driess and co-workers in 2008 (Figure I.12).[95] This green compound with the general formula [$Ni^{II}(^{Dipp}Nacnac)(O_2)$] was stable at room temperature and could be obtained in 84% isolated yield by reaction of the β-diketiminato(toluene)nickel(I) precursor with O_2 in toluene. Single crystals suitable for XRD analysis revealed that the nickel atom was planar tetracoordinated and thus, the O_2 moiety was bound in a side-on fashion. The measured O-O distance of 1.34 Å was fully consistent with a superoxo character of the O_2 ligand. In contrast to [$Ni^{II}(O_2)(PhTt^{Ad})$], the unpaired electron in [$Ni^{II}(^{Dipp}Nacnac)(O_2)$] resided in the superoxide ligand. Apart from oxygen-atom transfer to triphenylphosphine, this compound could perform hydrogen-atom abstraction from O-H and N-H groups.[96]

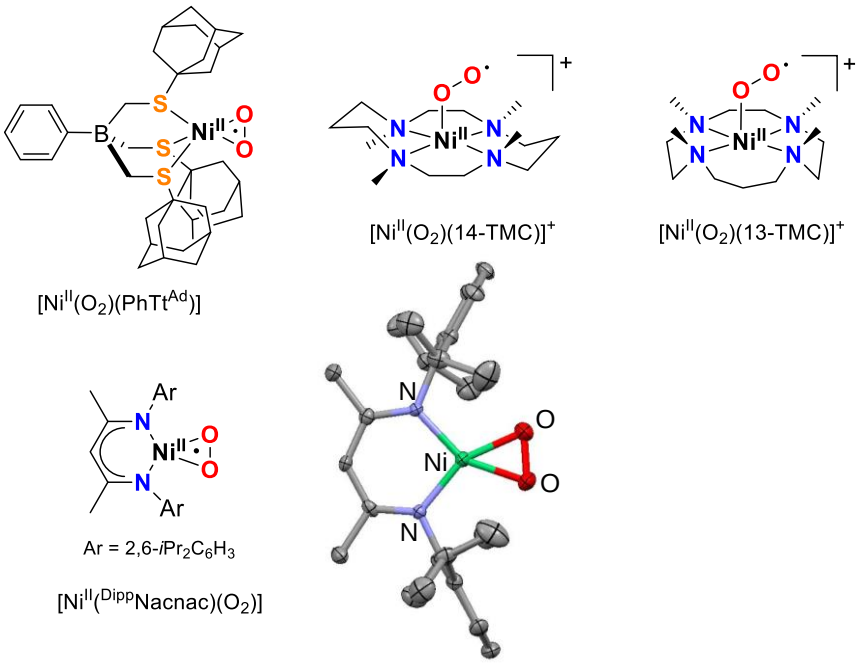

Figure I.12. Schematic representation of spectroscopically characterized superoxonickel(II) species along with the XRD structure of [$Ni^{II}(^{Dipp}Nacnac)(O_2)$] (ellipsoids drawn at 50% probability and hydrogen atoms omitted for clarity).

I.2.5.3. (Hydro)peroxonickel species

Back in 1969, the first mononuclear peroxonickel(II) complex was prepared by reaction of zero-valent nickel [$Ni^0(RNC)_4$] (R = *t*Bu or cyclohexyl) with O_2 at -20 ºC.[97] The side-on coordination mode of the peroxide ligand in the resulting [$Ni^{II}(O_2)(RNC)_2$] complexes was proved by FT-IR

analysis (Figure I.13),[98] which was further confirmed by single crystal X-ray diffraction of $[Ni^{II}(O_2)(tBuNC)_2]$.[99] This compound could oxygenate alkyl isocyanides or triphenylphosphine to afford the corresponding isocyanates or phosphine oxides.

More recently, Limberg, Driess and co-workers reported the synthesis of a thermally stable peroxonickel(II) complex $[Ni^{II}(^{Dipp}Nacnac)(O_2)K(solv)]$ obtained by one-electron reduction of the superoxide precursor $[Ni^{II}(^{Dipp}Nacnac)(O_2)]$ using elemental potassium as reducing agent (Figure I.13).[100] The crystal structure showed an uncommon $[Ni(\mu,\eta^2{:}\eta^2\text{-}O_2)K]$ core in which the K^+ atom was weakly coordinated to the peroxide ligand (average K-O distance of 2.7 Å). Recently, the group of Gade reported the structure of a diamagnetic square planar hydroperoxonickel(II) species with the general formula $[Ni^{II}(iso\text{-}pmbox)(OOH)]$ obtained by reaction of a nickel(II) species with H_2O_2 (Figure I.13). In this case, a tridentate anionic ligand occupied three of the coordination positions of the square planar nickel center and the coordination sphere was completed by a hydroperoxide ligand in an end-on coordination mode.[101] In both cases, O-O bond distances of ~1.48 Å determined by XRD analysis were clearly indicative of a peroxide ligand.

Preparation and characterization of two structurally related peroxonickel(III) species was reported by Nam and co-workers using *N*-tetramethylated cyclam derivatives.[102] Compounds $[Ni^{III}(O_2)(12\text{-}TMC)]^+$ and $[Ni^{III}(O_2)(13\text{-}TMC)]^+$ were obtained by reaction of the corresponding nickel(II) precursors with H_2O_2 in the presence of triethylamine at low temperature (Figure I.13). Interestingly, both the measured O-O bond distances (~1.38 Å, determined by XRD) and the O-O vibrations (~1005 cm^{-1}, determined by rRaman) fell between those measured for peroxometal (~1.4-1.5 Å, ~900 cm^{-1}) and superoxometal (~1.2-1.3 Å, ~1130 cm^{-1}) ligands but DFT calculations tipped the scales in favor of their formulation as a peroxonickel(III) species. Reactivity studies demonstrated that these two species were nucleophilic in nature and they could nucleophilically deformylate aldehydes such as 2-phenylpropionaldehyde or cyclohexanecarboxaldehyde.

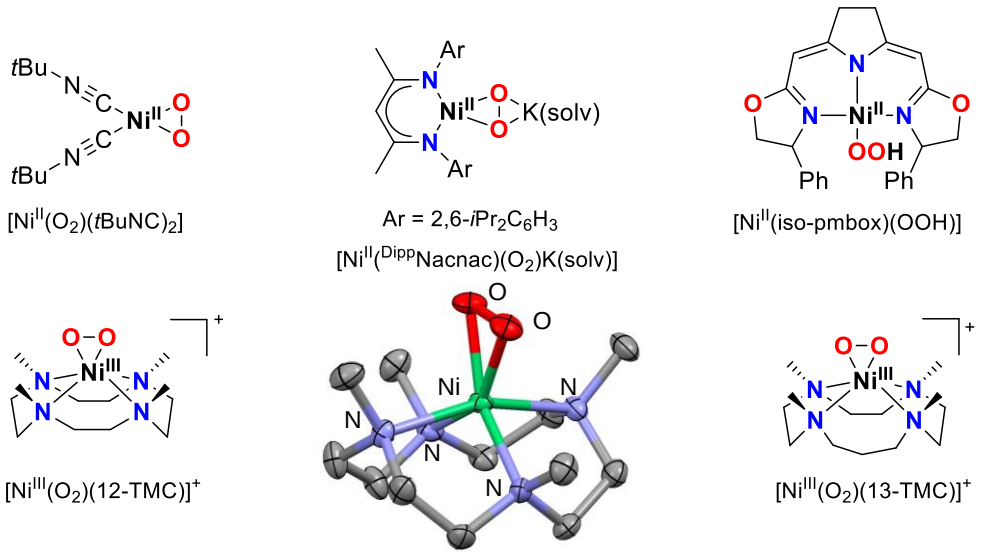

Figure I.13. Schematic representation of spectroscopically characterized (hydro)peroxonickel(II/III) species along with the XRD structure of $[Ni^{III}(O_2)(12\text{-}TMC)]^+$ (ellipsoids drawn at 30% probability; hydrogen atoms and ClO_4^- counterion omitted for clarity).

I.2.5.4. Alkylperoxonickel species

To date, the only structurally characterized alkylperoxonickel species was reported back in 2009.[103] A bis(μ-hydroxo)dinickel(II) species reacted stoichiometrically at 0 ºC with *tert*-butylhydroperoxide to give the corresponding mononuclear alkylperoxonickel(II), [Ni^{II}(OO*t*Bu)(Tp^{iPr})] (Figure I.14). This complex was relatively thermally stable ($t_{1/2}$ of 2.5 h at 25 ºC) but spectroscopic analyses were limited to UV-vis spectroscopy and ^{1}H-NMR, which showed a paramagnetically shifted spectrum consistent with a high-spin *S* = 1 nickel center. XRD analysis revealed a nickel(II) center coordinated to the three nitrogen donor atoms of Tp^{iPr} and to the OO*t*Bu ligand in a non-square planar fashion. Interestingly, the coordination mode of OO*t*Bu was intermediate between end-on and side-on. An in-depth study of the reactivity properties of [Ni^{II}(OO*t*Bu)(Tp^{iPr})] indicated that it behaved as a weak electrophilic oxidant that could react with triphenylphosphine to afford the corresponding phosphine oxide and also with carbon monoxide to yield a μ-carbonatodinickel(II) complex. Nucleophilic reactivity against aldehydes was also proved and reaction with benzaldehyde afforded the corresponding benzoatonickel(II) complex. Measurement of the reaction rates of [Ni^{II}(OO*t*Bu)(Tp^{iPr})] with a series of *para*-substituted benzaldehydes afforded a Hammett plot with a positive slope in agreement with its nucleophilic character.

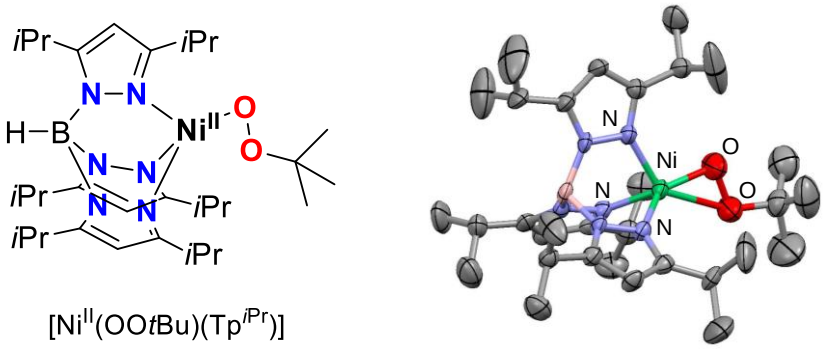

[Ni^{II}(OO*t*Bu)(Tp^{iPr})]

Figure I.14. Schematic representation of [Ni^{II}(OO*t*Bu)(Tp^{iPr})] along with its XRD crystal structure (ellipsoids drawn at 25% probability and hydrogen atoms omitted for clarity).

I.2.5.5. Acylperoxonickel species

Despite the fact that the combination of nickel(II) complexes and peracids affords efficient catalytic systems for the oxidation of unactivated alkanes, the exact nature of the species involved in these processes is not known. It is commonly postulated that acylperoxonickel species can either act directly as the oxidant or serve as precursors for the real active species after O-O homolytic or heterolytic cleavage.[104,105] In this line, Hikichi and co-workers reported a series of acylperoxonickel(II) complexes bearing trispyrazolyl borate ligands that were relevant to catalytic alkane hydroxylation.[106] These compounds were prepared by reaction of the bis(μ-hydroxo)dinickel(II) species with *meta*-chloroperbenzoic acid (*m*CPBA) at -40 ºC. The authors found that the introduction of electronwithdrawing and bulky groups in the pyrazole rings significantly increased the stability of the resulting acylperoxonickel(II) species. Therefore, the inclusion of CF_3 and methyl groups in the pyrazole rings led to the preparation of the thermally

robust [Ni^{II}(OOCOC$_6$H$_4$Cl)(Tp^{CF3Me})], which structure could be unequivocally established by XRD analysis (Figure I.15).[107] The distorted five-coordinate nickel(II) center was coordinated to Tp^{CF3Me} and to a bidentate acylperoxide ligand. This geometry was in accordance with the paramagnetism of the sample determined by ^{1}H-NMR, indicative of a *S* = 1 nickel(II) center. Compound [Ni^{II}(OOCOC$_6$H$_4$Cl)(Tp^{CF3Me})] could oxidize sulfides and olefins as well as perform hydrogen-atom abstraction of hydrocarbons with activated methylene C−H bonds.

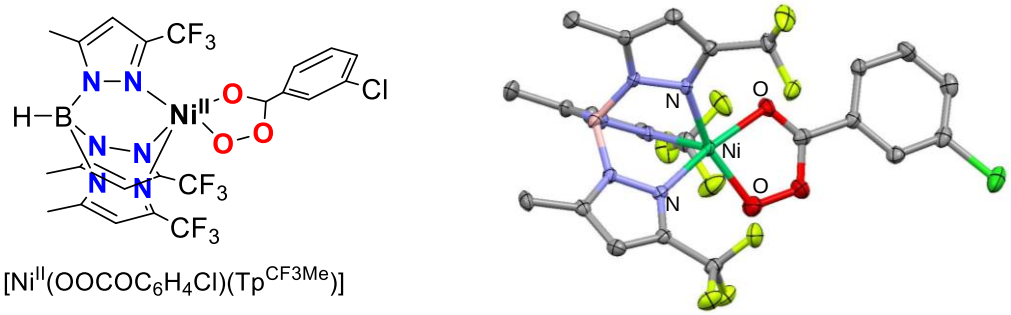

Figure I.15. Schematic representation of [Ni^{II}(OOCOC$_6$H$_4$Cl)(Tp^{CF3Me})] along with its XRD crystal structure (ellipsoids drawn at 50% probability and hydrogen atoms omitted for clarity).

I.2.5.6. Oxo/oxylnickel species

The involvement of oxometal species in the oxidation of organic compounds in chemical and biochemical processes is beyond any doubt. Both in enzymes and in catalysis oxometal compounds are frequently invoked as the species directly responsible for the oxidation event. Interestingly, the ability of a series of bare transition metal oxide cations MO^+ to oxidize organic compounds in the gas phase has been a matter of intense study. In particular, NiO^+ proved to be a potent oxidant that could even oxidize methane to methanol in the gas phase.[108,109]

Despite the fact that in oxidation catalysis the involvement of oxonickel species has frequently been invoked, little success has been achieved in the detection of such species. In 2012, Ray and co-workers postulated the formation of an oxo/hydroxonickel(III) species by reaction of [Ni^{II}(CF$_3$SO$_3$)(TMG$_3$tren)] with *m*CPBA at -30 ºC (Figure I.16). The authors proposed that the resulting [Ni^{III}(O)(TMG$_3$tren)]$^+$ (or [Ni^{III}(OH)(TMG$_3$tren)]$^{2+}$) species was formed after homolytic O-O bond cleavage of a putative acylperoxonickel(II) precursor that could not be trapped.[110] EPR analysis showed that this species accounted for only 15% of the sample but the authors unequivocally proved that it was kinetically competent to perform oxygen-atom transfer to triphenylphosphine and hydrogen-atom abstraction of weak C-H bonds.

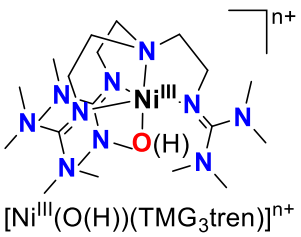

Figure I.16. Schematic representation of the spectroscopically characterized oxo/oxylnickel species [Ni^{III}(O(H))(TMG$_3$tren)]$^{n+}$.

Table I.3. Selected spectroscopic features of synthetic mononuclear superoxo, (hydro)peroxo, alkylperoxo, acylperoxo and oxo/oxylnickel species.

	S	*r*(Ni-O), Å[a]	*r*(O-O), Å[a]	ν(Ni-O), cm^{-1} (Δ[^{18}O], cm^{-1})[c]	ν(O-O), cm^{-1} (Δ[^{18}O], cm^{-1})[c]	λ_{max}, nm (ε, $M^{-1}cm^{-1}$)[d]	*g* values[e]	ref
Superoxonickel								
$[Ni^{II}(O_2)(PhTt^{Ad})]$	1/2	1.85[b]	-	-		310 (5900), 386 (2900), 450 (2500), 845 (350)	2.24, 2.19, 2.01	90
$[Ni^{II}(O_2)(14\text{-TMC})]^+$	1/2	1.98[b]	-	437 (-21)	1131 (-64)	345 (1500), 328 (sh)	2.29, 2.21, 2.09	92
$[Ni^{II}(O_2)(13\text{-TMC})]^+$	1/2	1.91[b]	-	-	1130 (-60)	339 (800), 416 (130), 684 (60)	2.25, 2.21, 2.06	94
$[Ni^{II}(^{Dipp}Nacnac)(O_2)]$	1/2	1.817(2), 1.840(2)	1.347(2)		971 (-52)	360 (1500), 590 (170), 980 (430)	2.14, 2.12, 2.07	95
(hydro)peroxonickel								
$[Ni^{II}(O_2)(t\text{BuNC})_2]$	0	1.902(7), 1.808(8)	1.45(1)	-	898 (-50)	380 (316), 600 (38)	-	97-99
$[Ni^{II}(^{Dipp}Nacnac)(O_2)K(solv)]$	0	1.820(2), 1.820(2)	1.468(2)	-	829 (-47)	-	-	100
$[Ni^{II}$(iso-pmbox)(OOH)]	0	1.8456(16)	1.492(2)	-	-	-	-	101
$[Ni^{III}(O_2)(12\text{-TMC})]^+$	1/2	1.884(3), 1.894(3)	1.386(4)	-	1002 (-57)	350 (300), 400 (280), 650 (100), 900 (80)	2.2, 2.17, 2.06	102
$[Ni^{III}(O_2)(13\text{-TMC})]^+$	1/2	1.897(3), 1.898(3)	1.383(4)	-	1008 (-58)	400 (150), 700 (80), 900 (50)	2.19, 2.07	102
alkylperoxonickel								
$[Ni^{II}(OOt\text{Bu})(Tp^{iPr})]$	1	1.854(7), 2.467(7)	1.440(7)	-	-	370 (1400)	-	103
acylperoxonickel								
$[Ni^{II}(OOCOC_6H_4Cl)(Tp^{CF3Me})]$	1	1.914(2), 2.040(2)	1.443(3)	-	-	375 (300), 630 (60)	-	107
oxo/oxyl nickel								
$[Ni^{III}(O(H))(TMG_3tren)]^{n+}$	1/2	-	-	-	-	464, 520, 794	2.05, 2.16, 2.31 2.13, 2.17, 2.26	109

[a] Unless otherwise stated, bond distances are determined by XRD.
[b] Bond distance determined by XAS.
[c] Frequency of the Ni-O and O-O vibrations and the corresponding shifts upon labeling with ^{18}O determined by Raman or IR.
[d] UV-vis absorption features determined in solution.
[e] *g* values determined by EPR.

In summary, despite the variety of mononuclear nickel-oxygen species reported to date, reactivity studies towards exogenous substrates indicate that, with a few exceptions, these compounds are poorly reactive and their relevance in nickel-catalyzed oxidation reactions is questioned. Thus, in the forthcoming years, stronger efforts will be needed to unravel the real nature of the active species involved in these transformations, with special emphasis on the detection and characterization of oxo/oxylnickel species, which, according to gas phase experiments should be very potent oxidants. In comparison to analogous compounds with other first-row transition metals such as iron, manganese or copper, nickel-oxygen species are still largely unexplored. However, the significant advances in the recent years set the basis for future development. Surely, the oxidation chemistry of nickel will provide interesting chemical surprises in the future.

I.2.6. Relevance of metal-oxygen species in N_2O activation

Nitrous oxide (N_2O) is a minor component of the Earth's atmosphere (319 ppb). However, it has been identified as a major environmental concern because it is approximately 300 times more potent as greenhouse gas than CO_2 and it is involved in the depletion of the stratospheric ozone layer. Despite being naturally generated in biological systems (as part of the nitrogen cycle), the concentration of N_2O is increasing every year in large part due to anthropogenic sources, including manufacturing, fossil fuel and agricultural activities. For example, N_2O is produced as a by-product in multimillion kg/year worldwide during the synthesis of adipic acid (Scheme I.12), the precursor for the manufacture of nylon.[111]

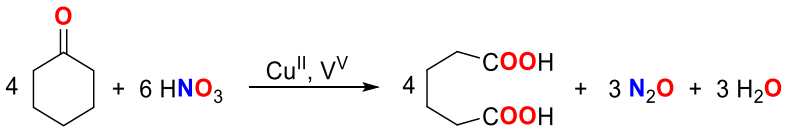

Scheme I.12. Industrial synthesis of adipic acid.

In recognition of these facts, extensive research and development of remediation methods have been pursued. However, this goal has proven highly challenging because N_2O itself, despite being thermodynamically a potent oxidant (its decomposition is energetically driven by N_2 formation), it is kinetically recalcitrant both towards decomposition and reduction. In biological systems these kinetic barriers are overcome by binding and activation to metal ions. That is, decomposition of N_2O into innocuous N_2 and O_2 (or H_2O) is carried out by the metalloenzyme nitrous oxide reductase (N_2OR)[112] (Figure I.17). The active site of N_2OR contains four copper ions coordinated to histidine residues and to a bridging sulfide ligand in a unique cluster geometry.

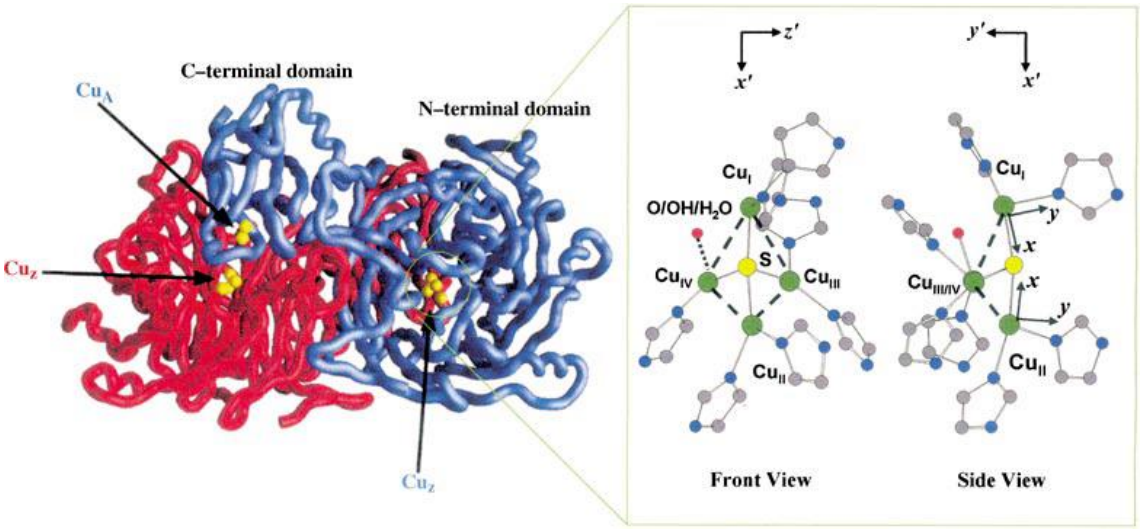

Figure I.17. Respesentation of the metalloenzyme nitrous oxide reductase (N_2OR) and its active site.[112]

However, there is an increasing interest in the use of nitrous oxide as an oxidizing reagent.[113] This reagent would constitute a clean alternative to the polluting oxidation processes used in industry as it only generates N_2 as waste.[114] Actually, selected works show that N_2O can be directly used as oxidant in the oxidation of phosphines or alkenes but, due to the inertness of nitrous oxide, these processes require harsh conditions to succeed (T > 100 ºC, P > 10 atm).[115] Inspired by biological systems, an interesting strategy to perform these reactions under milder reaction conditions is by the mediation of metal ions. If nitrous oxide is to be applied as oxidant, an oxo-transfer mechanism involving $2e^-$ reduction, N-O breakage and N_2 release is desirable. In this process, the N_2O molecule gets reduced by two electrons from the metal center. This redox process causes the cleavage of the N-O bond giving a high-valent oxometal species which is potentially capable of oxidizing an organic substrate (Scheme I.13).

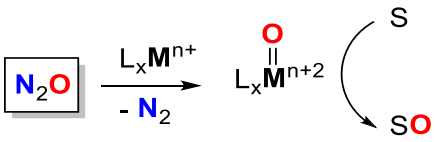

Scheme I.13. Schematic representation of the reaction of N_2O with a metal center to form high-valent oxometal and N_2.

- **Formation of oxometal compounds by N_2O activation**

Groves and co-workers in 1995 were the first to use N_2O for the preparation of oxometal species. Thus, they synthesized a dioxoruthenium(VI) species by efficient oxidation of $[Ru^{II}(TMP)(THF)_2]$ with N_2O under mild conditions (Scheme I.14a).[116] Afterwards, Yamada and co-workers used this compound as catalyst in combination with N_2O to afford alkene epoxidation[117] and alcohol oxidation.[118] Despite these pioneering works, reactions required high temperatures (100–200 ºC) and often elevated pressures achieving only very modest turnover numbers (4-14 turnovers).

In 2007, Harman and Chang synthesized an iron(II) complex based on a tripodal trianionic ligand with three pyrrole groups that could react with N_2O under mild conditions to give the corresponding iron(III) complex bearing a terminal hydroxyl ligand (Scheme I.14b)[119]. The authors postulated that this reaction took place through an oxoiron(IV) which was capable of carrying out the abstraction of a hydrogen atom from the solvent or an exogenous substrate such as 1,4-cyclohexadiene.

Successful N_2O activation has also been achieved with metal complexes based on nickel,[120] cobalt[121] or copper. On the one hand, the nickel(I) complex [Ni^{I}(β-diketiminate)(tol)] reacted with N_2O to afford a well-defined bis(hydroxo)dinickel(II) complex through the putative formation of an oxonickel intermediate (Scheme I.14c).[120] On the other hand, the catalytic oxidation of triphenylphosphine to triphenylphosphine oxide was achieved using a mononuclear cobalt(I) complex that activates nitrous oxide, in a Co^{I}/Co^{III} catalytic cycle.[121] Recently, Ménage and co-workers isolated a dissymmetric mixed-valent dicopper(II,I) containing a {Cu_2S} core with labile triflate and water molecules at the copper centers that could react with N_2O to from doubly bridged (μ-thiophenolato)(μ-hydroxo)dicopper(II) species derived from a transient oxo-bridged dicopper species (Scheme I.14d).[122]

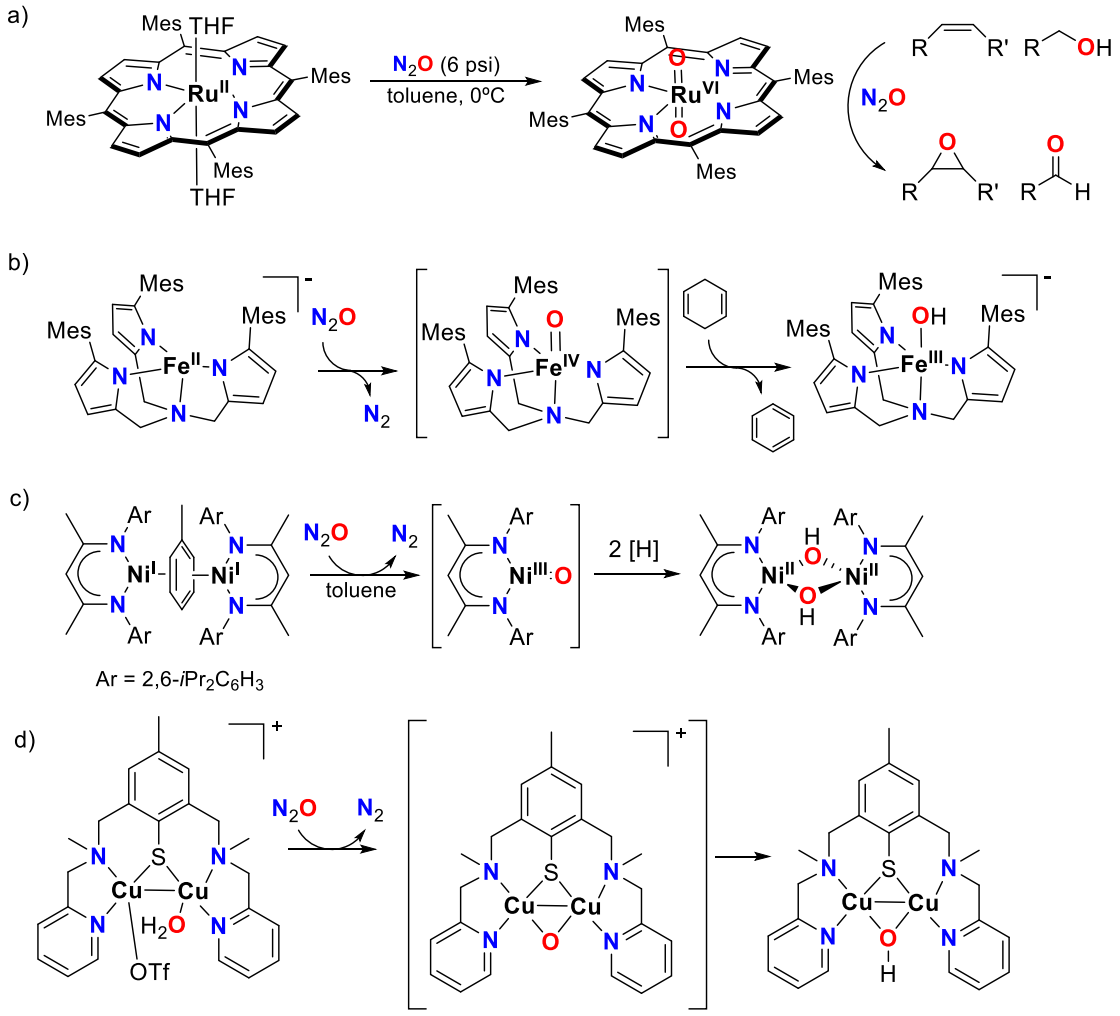

Scheme I.14. Oxometal species formed upon activation of N_2O by ruthenium (a), iron (b), nickel (c) and copper (d) complexes.

- **Application of N_2O in oxidation catalysis**

In 1993, Sobolev and co-workers used an iron-substituted zeolite (Fe/ZSM-5) as catalyst for selective oxidation reactions using N_2O as oxidant. In particular, hydroxylation of benzene to phenol was achieved with 25-30% conversion at 300-500 ºC.[123,124] Panov and co-workers also reported that the combination of Fe/ZSM-5 and nitrous oxide could perform single-turnover cycles of methane oxidation to methanol at room temperature.[125] Finally, Long and co-workers found that a metal-organic framework, Fe_2(dobdc) (dobdc = 2,5-dioxido-1,4-benzenedicarboxylate), could activate the C-H bonds of ethane and convert it into ethanol using nitrous oxide as oxidant. The authors postulated that this reaction took place through the mediation of an oxoiron(IV) as active species.[126]

Neumann and co-workers have successfully applied polyoxometalates as catalysts in oxidation reactions using N_2O as oxidant (Scheme I.15). Oxidation of alcohols or conversion of alkyl aromatics to ketones was achieved with a simple Keggin-type polyoxomolybdate, $[PV_2Mo_{10}O_{40}]^{5-}$ (Scheme I.15a).[127] Wacker-type oxidation of terminal alkenes to methyl ketones was performed with an hybrid metallorganic polyoxometalate, Pd^{II}(15-crown-5-phen)Cl_2-$H_5PV_2Mo_{10}O_{40}$ (Scheme I.15b)[128] while a manganese-substituted polyoxometalate $[Mn^{III}_2ZnW(Zn_2W_9O_{34})_2]^{10-}$ afforded alkene epoxidation (Scheme I.15c).[129] Catalyst loadings of 1-2 mol% were used with maximum turnover numbers of 25 for alkene epoxidation and 99 for the other transformations. While only 1 atm N_2O was used in most cases, high temperatures (150 ºC) and extended reaction times (8-18 hours) were necessary to obtain good results.

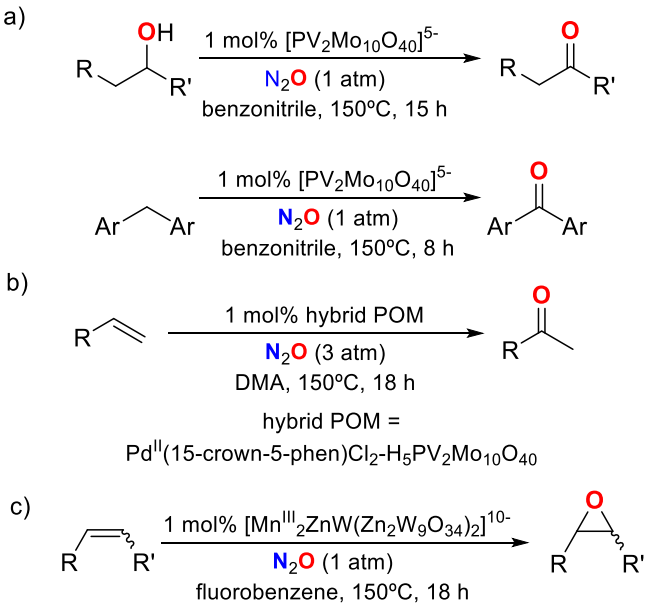

Scheme I.15. Polyoxometalates as catalysts in different oxidation reactions using N_2O as oxidant.

In the literature the use of N_2O in oxidative C–C coupling reactions is also described. Severin and co-workers showed that N_2O could be used as oxidant for the oxidative coupling reactions of Grignard reagents with good selectivity and unprecedented turnover numbers (Scheme I.16).[130]

These reactions were performed using different transition metal salts as potential catalysts (Li_2CuCl_4, Li_2MnCl_4, $CoCl_2$, $FeCl_3$, $Fe(acac)_3$) under mild conditions (1 atm N_2O, room temperature, 1 h) in THF as solvent. The same transformations were also tested with O_2 as oxidant, affording lower yields compared to N_2O.

R	X
p-MePh	Cl
o-MePh	Br
p-FPh	Cl
p-CNPh	Cl
p-(CO_2Et)Ph	Cl

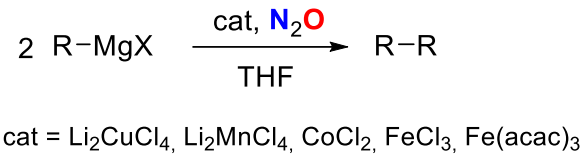

Scheme I.16. Oxidative homocoupling of aryl Grignard reagents with N_2O as oxidant.

All these catalytic systems are still far from being applicable in useful chemical transformations, but they constitute the proof-of-concept that N_2O can turn out to be a green alternative to the oxidants commonly used nowadays in most industrial processes.

I.3 High-valent metal-nitrogen species

The introduction of nitrogen moieties in organic frameworks is a very interesting topic in organic synthesis due to the presence of C-N bonds in natural products, synthetic intermediates as well as in pharmaceutical agents.[131] Analogously to C-H bond oxidation, traditionally the selective functionalization of C-H bonds with nitrogen-containing groups also requires several steps. Recently, new methodologies based on cross-coupling reactions involving metal-mediated catalysis have demonstrated improved reactivity and selectivity for the formation of C-N bonds (Scheme I.17a).[132] However, these methodologies usually require a prefunctionalized starting material (aryl halides or pseudohalides) that reacts with the amino source by mediation of a metal catalyst to produce the desired product with the new C-N bond together with stoichiometric amounts of the halogenated by-products. In this context, direct C-H amination has emerged as an alternative method to cross-coupling reactions with high atom economy and avoiding the substrate prefunctionalization. C-H amination proceeds either by metal C-H activation to form a carbon-metal species that reacts with amination reagents giving the C-N bond (Scheme I.17b) or via the formation of imidometal species (high-valent metal-nitrogen) that inserts into the C-H bond (Scheme I.17c).[133] However, the former is usually restricted to substrates containing directing groups to form metallacyclic intermediates upon C-H activation and employs oxidants to facilitate the reaction generating stoichiometric by-products. In this section we will focus on the latter approach, in which high-valent imidometal species are responsible for the C-H activation and amination event.

Among the several catalysts that have been reported to mediate C-H amination by imidometal species, those based on non-abundant Rh, Ru and Pd metals are the most successful ones.[134]

Cost, sustainability and toxicity concerns have strongly motivated the development of selective catalysts based on earth-abundant metals. Iron is the first-row transition metal that has been more extensively used in these transformations and several mechanistic studies have been carried out. This is in large part due to its biological relevance. However, late first-row transition metals such as cobalt, nickel or copper are becoming interesting alternatives.

In this section, we will first look at the most common nitrogen sources employed, and after a general overview on the biological relevance of high-valent metal-nitrogen species, we will focus our attention on metal-catalyzed C-H amination reactions based on late first-row late transition metals (e.g. cobalt, nickel and copper). For the purposes of this thesis, special focus will be given to imidocopper species.

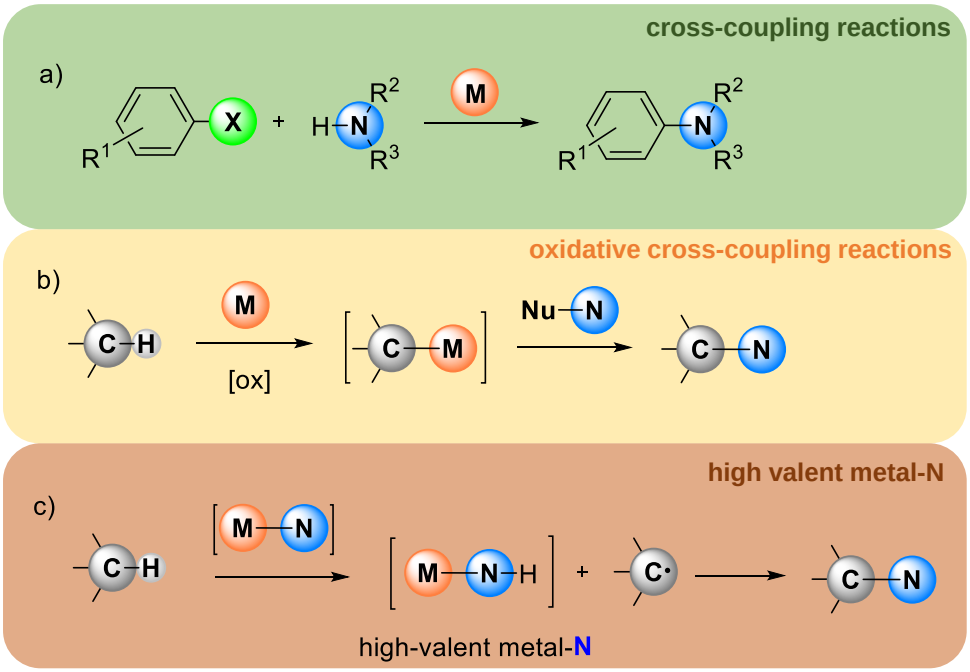

Scheme I.17. Schematic representation of the three possible pathways (cross-coupling reaction, mediation of high-valent metal-nitrogen and oxidative cross-coupling) to form C-N bonds.

I.3.1. Nitrogen sources

The nitrogen source is one important aspect to take into account in direct C-H amination reactions mediated by imidometal species. These nitrogen sources provide the metal with a nitrene group (the nitrogen analogue of carbene). Typically these nitrene sources are imidoiodanes (e.g. PhI=NTs), or haloamine-T (e.g. chloroamine-T) (Figure I.18). However, these compounds generate phenyl halides or other halogen-containing compounds as stoichiometric by-products. The other disadvantage of using iminoiodanes is their poor solubility and the fact that there are not many possibilities to change the pre-existing functionality on the nitrogen atom (R^1), which limits their interest from the perspective of green chemistry. On the other hand, organic azides (N_3R) have been reported to be an efficient and green source of nitrene groups by the thermodynamic release of N_2.[135]

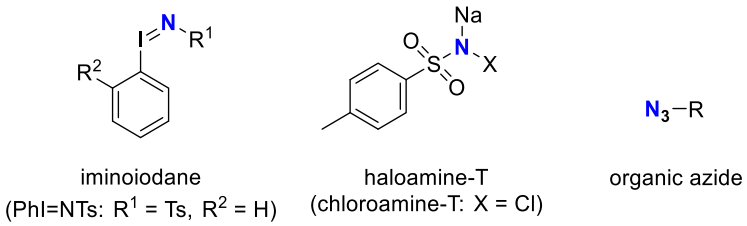

Figure I.18. Schematic representation of the different nitrene sources for direct C-H amination reactions mediated by imidometal species.

All these nitrene sources provide the formation of imidometal species (also known as metal-nitrene) which are responsible for the C-H amination reaction (Scheme I.18a). Such monosubstituted nitrogen ligands should not be confused with amido and nitrido ligands derived from disubstituted and unsubstituted nitrogen moieties respectively (Scheme I.18b-c)[136]

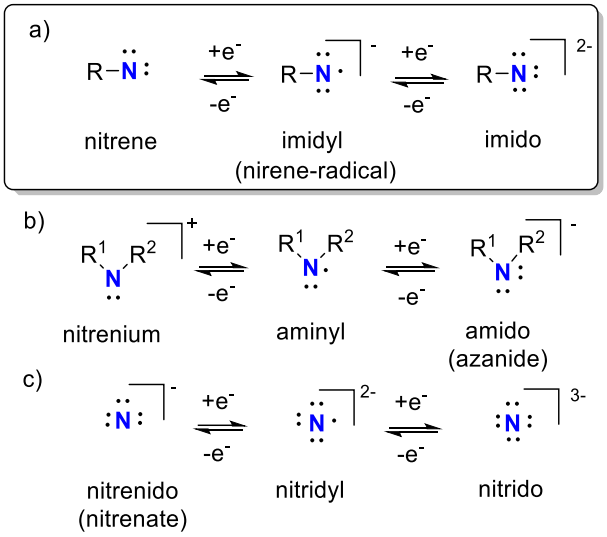

Scheme I.18. Lewis structures and nomenclature of a) monosubstituted b) disubstituted, and c) unsubstituted nitrogen ligands.

I.3.2. Imidometal species in nature and bioinspired systems: predominance of Fe

Iron is by far the most studied first-row transition metal forming imido (Fe=NR) and nitrido (Fe≡N) complexes, including characterization of the +4, +5, and +6 oxidation states.[137] This interest is in part due to the biological relevance of such compounds. Despite not being directly detected in nature, nitridoiron(IV) species and related imidoiron compounds are postulated to be involved in the catalytic cycle of nitrogenases. Thus, the FeMo cofactor in nitrogenase contains seven Fe centers and a single Mo center held together by nine bridging sulphides and a carbide atom, but dinitrogen reduction is proposed to occur at a single iron site (Scheme I.19a).[138] Dinitrogen binds and is heterolytically cleaved at this iron site in a stepwise manner, which results in the generation of imidoiron species (Fe^{III}=N-NH_2) and finally to a nitridoiron(IV) compound (Fe^{IV}≡N). Moreover, a related imidoiron(IV) porphyrin species was postulated to be the reactive intermediate for cytochrome-P450-LM-3,4 catalyzed N-atom transfer reactions (Scheme I.19b).[139]

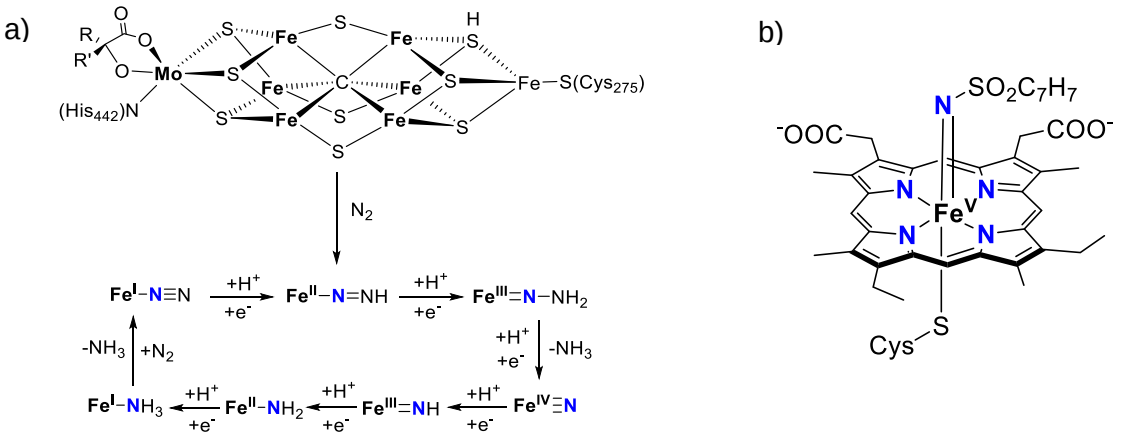

Scheme I.19. Proposed structures of biological intermediates with iron-nitrogen multiple bonds. a) The FeMo cofactor of the nitrogenase enzyme and the proposed intermediates of the dinitrogen activation process. b) Structure of the imidoiron(IV) porphyrin intermediate that has been invoked for cytochrome-P450 catalyzed nitrogen group transfer reaction.

To probe the possibility of the involvement of nitridoiron and imidoiron species in biological dinitrongen-reduction and atom-transfer reactions, bioinorganic chemists became interested in the synthesis and reactivity of model compounds involving nitridoiron and imidoiron compounds. As a result of these studies, several examples of the catalytic amination of C-H bonds (e.g. cyclohexane, toluene)[140] and olefin aziridiantion (e.g. styrene) [141] have been reported using iron-based catalysts (Scheme I.20a). The interest to study this kind of systems has grown during the last 15 years and very recently, Betley and co-workers reported the synthesis of an imidoiron complex by reaction of an iron dimer and an organic azide at -40 ºC.[142] The complex was characterized by ^{57}Fe Mössbauer spectroscopy and XRD showing a Fe-N distance of 1.768 Å (Scheme I.20b).

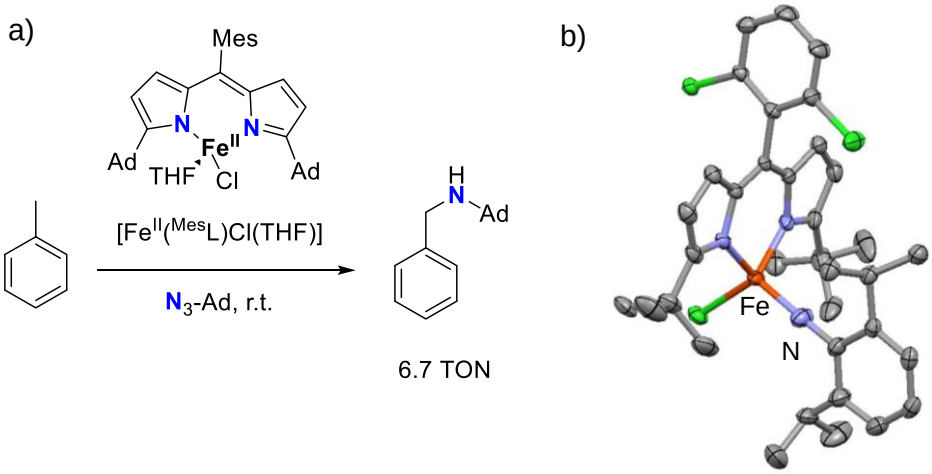

Scheme I.20 a) Catalytic C-H bond amination of toluene catalyzed by an iron(II) complex through the mediation of an imidoiron species.[141] b) XRD structure of the imidoiron compound characterized by Betley (ellipsoids drawn at 50% probability and hydrogen atoms omitted for clarity).[142]

I.3.3. High-valent imidocobalt- and imidonickel species

Late transition metals such as cobalt and nickel have been successfully used for the preparation of catalytically relevant imidometal compounds.

In the case of cobalt, cobalt(II)-porphyrin complexes have extensively been used as catalysts in C-H amination and olefin aziridination reactions including amination of alkylic, allylic and benzylic C-H bonds (Scheme I.21a).[143] Recent spectroscopic and theoretical studies by Zhang, de Bruin and co-workers have disclosed the involvement of an imidylcobalt(III) complex [Co^{III}(porphyrin)($^{\bullet}$NR)] as the key species responsible for the benzylic C-H bond amination of ethylbenzene or toluene using organic azides as the nitrene source and a cobalt(II)-porphyrin catalyst (Scheme 21b).

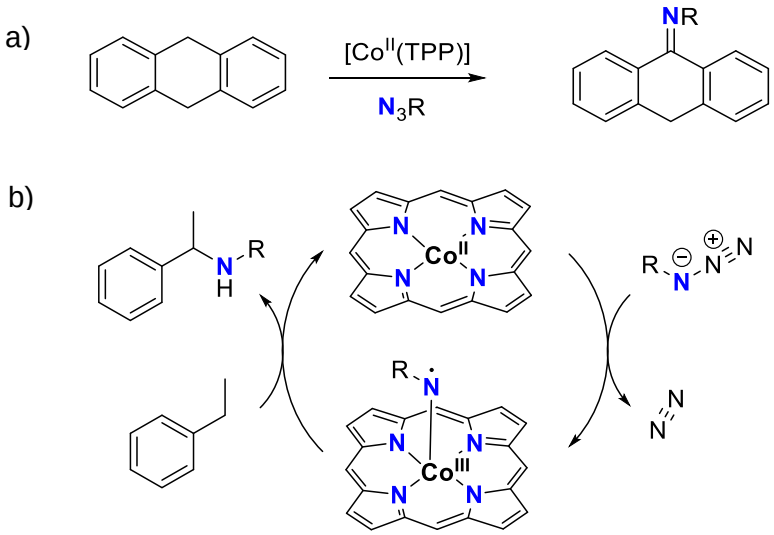

Scheme I.21. a) Example of catalytic C-H amination of 9,10-dihydroanthracene catalyzed by a cobalt(II)-porphyrin complex. TPP = tetraphenylporphyrin b) Catalytic cycle for [Co(porphyrin)]-catalyzed C-H aminations with azides.

Analogous imidocobalt complexes have been characterized using non-porphyrinic ligands. Their synthesis usually entails the reaction of a cobalt(I) precursor with a nitrene source (see section I.3.1). Using this strategy several well-defined and stable imidocobalt(III) species have been isolated with different geometries including tetrahedral, three-coordinate and two-coordinate.[144] Some examples of these structures are shown in Figure I.19. However, in most cases these species have proven to be sluggish oxidants and at best they perform nitrene group transfer to easily oxidizable substrates or they activate weak benzylic C-H bonds. Importantly, the two-coordinate imidocobalt(II) compound [Co^{II}(Ndmp)(IPr)] was able to react with CO and ethylene to form isocyanide and imine, respectively.[145]

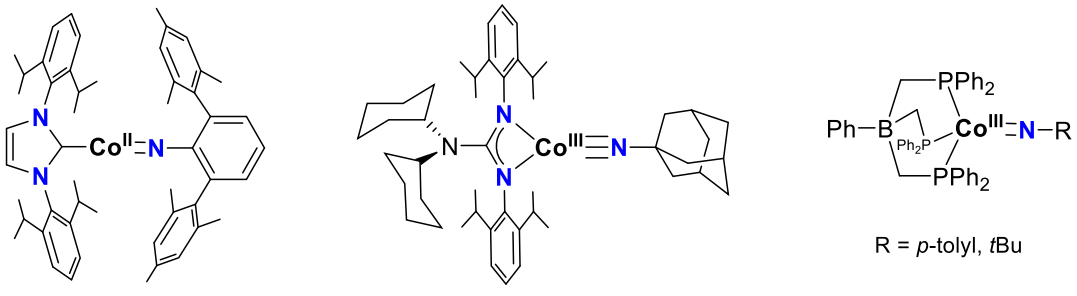

[Co^{II}(Ndmp)(IPr)] [Co^{III}(NAd)(guanidinato)] [Co^{III}(NR)($PhBP_3$)]

Figure I.19. Schematic representation of some well-characterized terminal imidocobalt complexes.

In the case of nickel, stable imidonickel complexes have only been isolated in two and three-coordinate geometries. Thus, with the increasing lateness of the transition metals, metal-ligand multiple bonds can only be stabilized for lower-coordination geometries, which presumably make more metal d orbitals available to accept the π-electron density.[146]

Hillhouse and co-workers were the first to report the synthesis of imidonickel(II) and imidonickel(III) complexes using sterically hindered diphosphines and *N*-heterocyclic carbenes as exemplified by [Ni^{II}(Ndipp)(dtbpe)] and [Ni^{II}(Ndmp)(IPr*)] (Figure I.20).[147-149] The generation of these compounds could be done following different pathways: a) by deprotonation of an amidonickel(II) precursor,[147] b) by reaction of a Ni^{0} precursor with a nitrene source (such as organic azides),[148] c) by hydrogen-atom abstraction of the amidonickel starting material with a phenoxyl radical[149] or d) by one-electron oxidation of imidonickel(II) to form imidonickel(III).[150] The group of Warren reported the formation of an imidonickel(III) with a β-diketiminate ligand [Ni^{II}(NAd)(^{Mes}Nacnac)] by reaction of nickel(I) with an organic azide (Figure I.20). In general, these compounds behave as weak oxidants capable of nitrene-group transfer to substrates such as CO, CNR, PMe_3, Cp_2Co, olefins (e.g. ethylene), benzylic C−H bonds and 1,4-cyclohexadiene.[151]

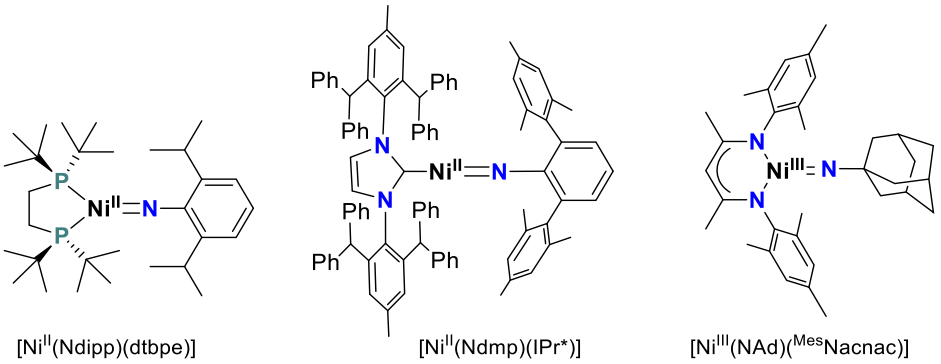

Figure I.20. Schematic representation of some well-characterized terminal imidonickel complexes.

I.3.4. High-valent imidocopper species

Over the last decades, numerous examples of aziridination and amination reactions catalyzed by copper have been reported. Most of the results showed the transfer of a nitrene group from iminoiodanes to substrates that contained an activated carbon-hydrogen bond, whereas very few examples of amination of unactivated C-H bonds have been reported to date.[152]

The earliest examples of C-H amination involved the copper-promoted functionalization of sp^3 C-H bonds and were reported over 50 years ago.[153] These pioneer works created an interest in the development of more efficient catalytic systems and understanding the mechanism behind these transformations. Kwart and Khan in 1967 performed the reaction between benzenesulfonyl azide and cyclohexene in the presence of excess copper powder to afford the corresponding aziridine and C-H amination products (Scheme I.22a). The authors suggested that this reaction occurred through the mediation of an imidocopper species "Cu=NSO_2Ph". It was not until 1991 that an

efficient and general nitrene-transfer aziridination procedure was developed by the group of Evans.[154] Simple copper(I) and copper(II) salts (e.g. $CuClO_4$, $Cu(acac)_2$, and $Cu(OTf)_2$) were found to give high yields of aziridines from a wide range of alkenes using PhI=NTs, with limited amounts of allylic insertions (Scheme I.22b). Then, the same group employed bis(oxazoline) ligands with copper to obtain the chiral aziridination of olefins,[155] and afterwards Jacobsen used chiral diimines ligands for the same reaction.[156] Taylor and co-workers also reported the use of simple copper catalysts for the efficient aziridination of alkenes and amination of activated hydrocarbons with chloramine-T as *N*-source.[157] The group of Pérez have extensively applied the copper(I) complex $[Cu^{I}(Tp^{Br3})(CH_3CN)]$ as catalyst in combination with PhI=NTs for C-H amination reactions of substrates such as benzene, and cyclohexane with high yields at room temperature (Scheme I.22c).[158] The same group used similar catalysts with different substituents on the pyrazole ring for the amination of alkyl aromatics and cyclic ethers using PhI=NTs as the nitrene source affording the corresponding amines in moderate to high yields.[159] Finally, Nicholas and co-workers have examined the selective amination of benzylic and allylic C-H bonds using copper catalysts in combination with chloramine-T.[160]

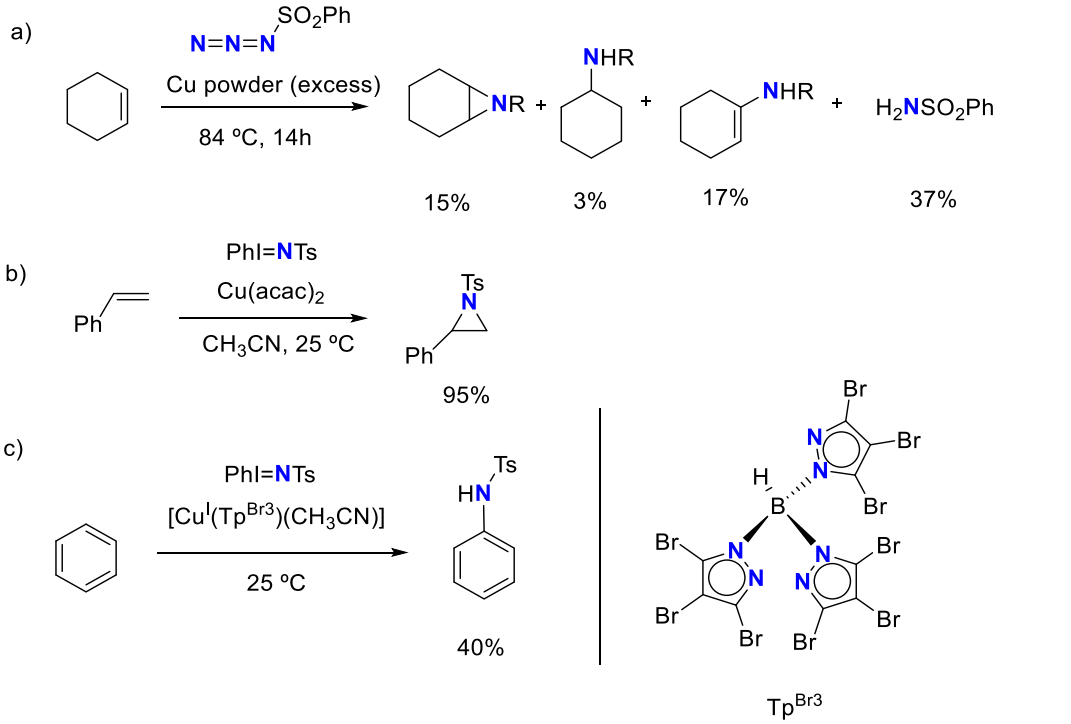

Scheme I.22. Schematic representation of catalytic C-H bond amination and aziridination reactions using copper powder (a) copper salt (b) or $[Cu^{I}(Tp^{Br3})(CH_3CN)]$ (c).

The success in aziridination and C-H amination reactions catalyzed by copper in combination with nitrene sources have created a strong interest in the chemical nature of the putative imidocopper species that enable these nitrene-transfer reactions. The electronic structure of such intermediates has been controversially discussed in the literature. These mechanistic questions and controversy have provided tremendous motivation to probe the accessibility and reactivity of high-valent imidocopper. In contrast to the array of imidometal species based on iron, cobalt, and

nickel that have been isolated (see sections I.3.2 and I.3.3), detection and characterization of the corresponding copper species has remained elusive.

An early key experiment by Jacobsen provided clear support for the formation of imidocopper species. Thus, the combination of a chiral diamine ligand with $CuPF_6$ afforded identical enantiomeric excesses in the aziridination of styrene with either PhI=NTs or tosyl azide. This suggested that the two nitrogen sources led to the same active species, the imidocopper, Cu=NTs.[161]

Later, Vedernikov and Caulton described the addition of PhI=NTs to their copper(I) catalyst to provide a purple substance formulated as an imidodicopper(II). This diamagnetic species was characterized by NMR spectroscopy as well as by mass spectrometry but unfortunately it did not perform nitrene-transfer to alkenes or alkanes.[162]

Then, Warren and co-workers published the crystal structure of an imidodicopper(II) complex $[Cu^{II}_2(NAr)(^{Mes}Nacnac)_2]$ prepared by reaction of a copper(I) β-diketiminate precursor with an arylazide in 77% yield (Scheme I.23a). [163] The XRD crystal structure revealed short Cu-$N_{nitrene}$ distances of 1.794 and 1.808 Å. The authors suggested that this compound was the precursor of a terminal imidocopper compound that performed nitrene transfer to phosphines (e.g. PMe_3) and isocyanides (e.g. CN*t*Bu) to give Me_3P=NAr and *t*BuN=C=NAr in 94% and 92% yields, respectively. Then, the same group reported an analogous imidocopper(II) compound but using a chlorine-substituted β-diketiminate ligand with the general formula $[Cu^{II}_2(NAd)(^{Cl}Nacnac)_2]$ (Scheme I.23b). According to the authors, the putative mononuclear imidocopper(II) formed in solution was responsible for nitrene transfer to C-H bonds (e.g. indane, toluene and cyclohexane) under catalytic conditions.[164]

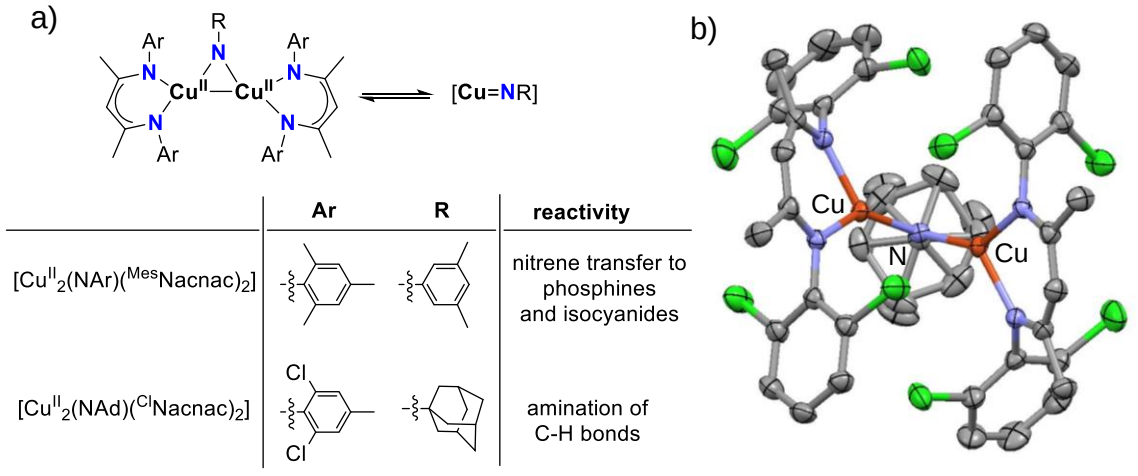

Scheme I.23. a) Schematic representation of the two imidodicopper(II) compounds $[Cu^{II}_2(NAr)(^{Mes}Nacnac)_2]$ and $[Cu^{II}_2(NAd)(^{Cl}Nacnac)_2]$ as precursors of terminal imidocopper(II) capable of performing nitrene transfer reactions. b) XRD structure of $[Cu^{II}_2(NAd)(^{Cl}Nacnac)_2]$ (ellipsoids drawn at 50% probability and hydrogen atoms omitted for clarity).

More recently, Lewis acid adducts of terminal imidocopper species supported by a tridentate amine have been reported by the group of Ray (Figure I.21).[165] Trapping of these Lewis acid adducts with the general formula {[Cu(NR)(MeHAN)]$^{+}$-Sc(OTf)$_3$} was performed at -90 ºC by reaction of a copper(I) triamine precursor with PhI=NTs (R = Ts) or mesityl azide (R = mesityl) in the presence of Sc^{3+}. Despite the fact that these species have not been crystallographically characterized, X-ray absorption spectroscopy, EPR and resonance Raman studies at low temperature together with DFT studies were used to propose a possible formulation. Electronic structure analyses described these compounds as a copper(II) center coordinated to an imidyl radical instead of imidocopper(III). Reactivity studies carried out at low temperature (-90 ºC) revealed that these species were able to perform H-atom abstraction (1,4-cyclohexadiene to benzene) and C-H amination (toluene and cyclohexane). The spectroscopic properties and reactivity of the imidylcopper(II) was found to be independent of the nature of the Lewis acid used (e.g. Sc^{3+},Y^{3+}, Eu^{3+}, Ce^{3+}, Zn^{2+} or Ca^{2+}).[166]

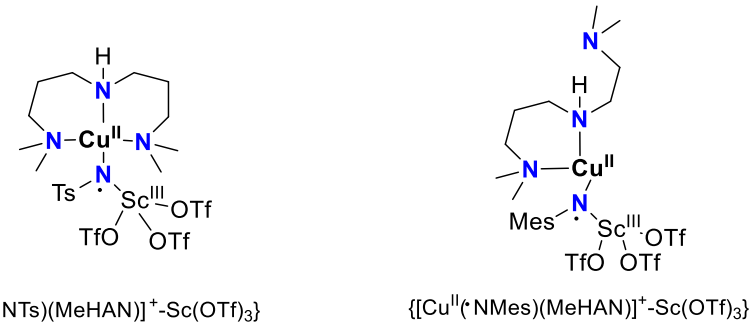

{[Cu^{II}(•NTs)(MeHAN)]$^{+}$-Sc(OTf)$_3$} {[Cu^{II}(•NMes)(MeHAN)]$^{+}$-Sc(OTf)$_3$}

Figure I.21. Schematic representation of the two imidylcopper(II) compounds adducts with Sc^{3+}.

More recently, Bertrand and co-workers isolated bisimidocopper(II) and imidodicopper(II) species by reaction of a bulky phosphinonitrene ligand with 0.5 and 2 equiv. of copper(I) triflate, respectively (Figure I.22). However, no terminal imidocopper species could be isolated in these reactions, although their formation was suggested based on ^{31}P-NMR studies.[167]

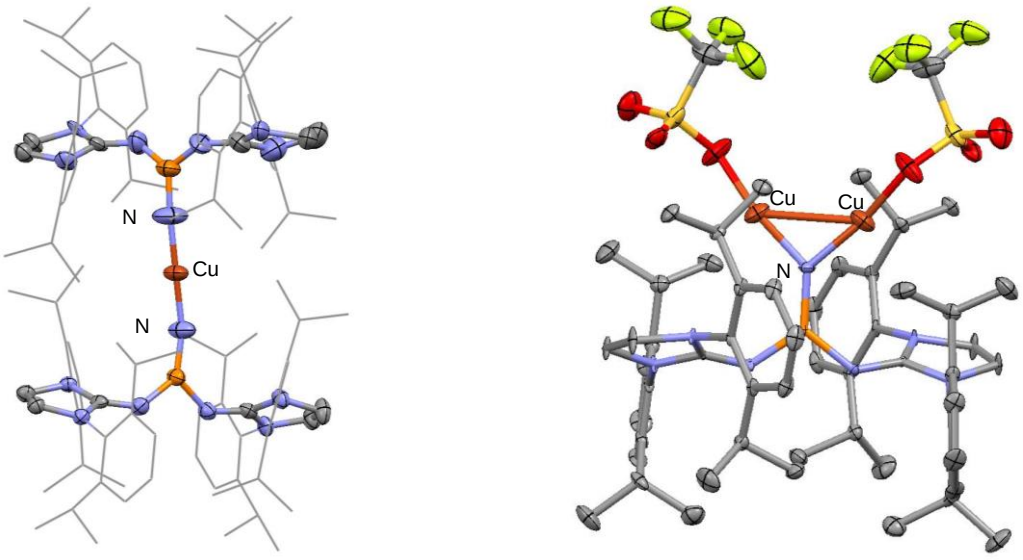

Figure I.22. XRD structures of the bisimidocopper(II) and imidodicopper(II) species using a bulky phosphinonitrene ligand (ellipsoids drawn at 50% probability and hydrogen atoms omitted for clarity).

Overall, iron, cobalt, and specially copper-based complexes have been extensively used as catalysts in C-H amination and olefin aziridination, while no nickel complexes have been reported to catalyze these transformations. These reactions occur through the mediation of imidometal species which to date have never been isolated for copper, despite being one of the most efficient metals to catalyze C-H amination reactions.

I.4. References

[1] Bergman, R. G., *Nature*, **2007**, *446*, 391.

[2] Godula, K.; Sames, D., *Science*, **2006**, *312*, 67.

[3] Newhouse, T.; Baran, P. S., *Angew. Chem. Int. Ed.,* **2011,** *50*, 3362.

[4] Anastas, P. T.; Warner, J. C., *Green chemistry: theory and practice,* Oxford: Oxford Unviersity Press, 1998.

[5] Ribas, X., *C-H and C-X Functionalization. Transition Metal Mediation*. RSC Publishing: Cambridge, UK, 2013.

[6] a) Que, L.; Tolman, W. B. *Nature,* **2008**, *455*, 333. Punniyamurthy, T.; Velusamy, S.; Iqbal, J., *Chem. Rev.,* **2005**, *105*, 2329. b) Crabtree, R. H., *Chem. Rev*., **2010**, *110*, 575.

[7] a) Gutekunst, W. R; Baran, P. S., *Chem. Soc. Rev*., **2011**, *40*, 1976. b) McMurray, L.; O'Hara, F.; Gaunt, M. J., *Chem. Soc. Rev.,* **2011**, *40*, 1885.

[8] Barton, D. H. R; Doller, D., *Acc. Chem. Res*., **1992**, *25*, 504.

[9] Godula, K; Sames, D., *Science,* **2006**, *312*, 67.

[10] Collins, J. C.; Hess, W. M.; Frank, F. J., *Tetrahedron Lett.,* **1968**, 3363.

[11] Lee, D. G.; Lamb, S. E.; Chang, V. S., *Org. Synth.,* **1981**, *60*, 11.

[12] Bäckvall, J.-E. *Modern Oxidation Methods*; Wiley-VCH Verlag, 2010.

[13] Vaska. L, *Acc. Chem. Res.*, **1976**, *9*, 175.

[14] Kraatz, H. B.; Metzler-Nolte, N., *Concepts and Models in Bioinorganic Chemistry*. Wiley-VCH: Weinheim: 2006.

[15] Que, L.; Tolman, W. B., *Nature,* **2008**, *455*, 333.

[16] Montellano, P. O., *Cytochrome P450: Structure, Mechanism, and Biochemistry*. 3rd ed.; Springler ed.: New York, 2005.

[17] Bertini, I.; Gray, H.B.; Stiefel, E. I.; Valentine, S. J., *Biological inorganic Chemistry: Structure & Reactivity*. University Science Books: Sausalito, California, 2007.

[18] Schlichting, I.; Berendzen, J.; Chu, K.; Stock, A.M.; Maves, S. A.; Benson, D. E.; Sweet, R. M.; Ringe, D.; Petsko, G. A.; Sligar, S. G., *Science*, **2000**, *287*, 1615.

[19] Company, A.; Lloret-Fillol, J.; Costas, M*., Small molecule models for nonporhyrinic iron and manganes oxygenases*. Chaper in: *Comprehensive inorganic chemistry II*, vol. 3. Oxford: Elsevier, 2013, 487.

[20] Sirajuddin, S.; Rosenzweig, A. C., *Biochemistry*, **2015**, *54*, 2283.

[21] a) Ferraro, D. J.; Gakhar, L.; Ramaswamy, S., *Biochem. Biophys. Res. Commun*., **2005**, *338*, 175. b) Neibergall, M. B.; Stubna, A.; Mekmouche, Y.; Münck, E.; Lipscomb, J. D., *Biochemistry*, **2007**, *46*, 8004.

[22] Chen, M. S.; White, M. C., *Science*, **2010**, *327*, 566.

[23] Cussó, O.; Garcia-Bosch, I.; Ribas, X.; Lloret-Fillol, J.; Costas, M., *J. Am. Chem. Soc.*, **2013**, *135*, 14871.

[24] Chow, T. W.-S.; Wong, E. L.-M.; Guo, Z.; Liu, Y.; Huang, J.-S.; Che, C.-M., *J. Am. Chem. Soc.,* **2010**, *132*, 13229.

[25] Cuff, M. E.; Miller, K. I.; Holde, K. E.; Hendrickson, W. A., *J. Mol. Biol.,* **1998**, *278*, 855.

[26] Matoba, Y.; Kumagai, T.; Yamamoto, A.; Yoshitsu, H.; Sugiyama, M., *J. Biol. Chem*., **2006**, *281*, 8981.

[27] Hatcher, L. Q.; Karlin, K. D., *J. Biol. Inorg. Chem*., **2004***, 9*, 669.

[28] Sirajuddin, S.; Rosenzweig, A. C., *Biochemistry*, **2015**, *54*, 2283.

[29] Serrano-Plana, J.; Garcia-Bosch, I.; Company, A.; Costas, M., *Acc. Chem. Res.,* **2015**, *48*, 2397.

[30] a) Lewis, E. A.; Tolman, W. B., *Chem. Rev*., **2004**, *104*, 1047. b) Mirica, L. M.; Ottenwaelder, X.; Stack, T. D. P., *Chem. Rev*., **2004**, *104*, 1013.

[31] Würtele, C.; Gaoutchenova, E.; Harms, K.; Holthausen, M. C.; Sundermeyer, J.; Schindler, S., *Angew. Chem. Int. Ed.,* **2006**, *45*, 3867.

[32] Kitajima, N.; Fujisawa, K.; Fujimoto, C.; Moro-oka, Y.; Hashimoto, S.; Kitagawa, T.; Toriumi, K.; Tatsumi, K.; Nakamura, A., *J. Am. Chem. Soc*., **1992**, *114*, 1277.

[33] Betley, T. A.; Wu, Q.; Van Voorhis, T.; Nocera, D. G., *Inorg. Chem*., **2008**, *47*, 1849.

[34] O'Halloran, K. P.; Zhao, C.; Ando, N. S.; Schultz, A. J.; Koetzle, T. F.; Piccoli, P. M. B.; Hedman, B.; Hodgson, K. O.; Bobyr, E.; Kirk, M. L.; Knottenbelt, S.; Depperman, E. C.; Stein, B.; Anderson, T. M.; Cao, R.; Geletii, Y. V.; Hardcastle, K. I.; Musaev, D. G.; Neiwert, W. A.; Fang, X.; Morokuma, K.; Wu, S.; Kogerler, P.; Hill, C. L., *Inorg. Chem*., **2012**, *51,* 7025.

[35] Hay-Motherwell, R. S.; Wilkinson,, G.; Hussain-Bates, B.; Hursthouse, M. B., *Polyhedron*, **1993**, *12*, 2009.

[36] Egan, J. W.; Haggerty, B. S.; Rheingold, A. L.; Sendlinger, S. C.; Theopold, K. H., *J. Am. Chem. Soc*., **1990**, *112*, 2445.

[37] Saffer A, Babyside NY (1958) Barker RS Preparation of aromatic polycarboxylic acids. US Patent 2,833,816.

[38] Srinivas D, Chavan SA, Ratnasamy P (2001) Process for the preparation of adipic acid. US Patent 6,521,789 B1, 2001.

[39] F.A. Chavez, J.A. Briones, M.M. Olmstead, P.K. Mascharak, *Inorg. Chem*., **1999**, *38*, 1603.

[40] Ishii, Y.; Iwahama, T.; Sakaguchi, S.; Makayama, K.; Nishiyama, Y., *J. Org. Chem*., **1996**, *61*, 4520.

[41] Ishii, Y.; Kato, S.; Iwahama, T.; Sakaguhi, S., *Tetrahedron Lett*., **1996**, *37*, 4993.

[42] Yoshino, Y.; Hayashi, Y.; Iwahama, T.; Sakaguchi S.; Ishii, Y., *J. Org. Chem*., **1997**, *62*, 6810.

[43] Pérez, P. J., Alkane C-H activation by single-site metal catalysis. Springer, 2012.

[44] Hoffman, B. M.; Petering, D. H., *Proc. Natl. Acad. Sci.*, **1970**, *67*, 637.

[45] Schaefer , W. P.; Marsh, R. E., *Acta Crystallogr.*, **1966**, *21*, 735.

[46] Jones, R. D.; Summerville, D. A.; Basolo, F., *Chem. Rev*., **1979**, *79*, 139.

[47] Egan, J. W.; Haggerty, B. S.; Rheingold, A. L.; Sendlinger, S. C.; Theopold, K. H., *J. Am. Chem. Soc.,* **1990**, *112,* 2445.

[48] Ramdhanie, B.; Telser, J.; Caneschi, A.; Zakharov, L .N; Rheingold, A. L.; Goldberg, D. P**.,** *J. Am. Chem. Soc.,* **2004**, *126*, 2515.

[49] Corcos, A. R.; Villanueva, O.; Walroth, R. C.; Sharma, S. K.; Bacsa, J.; Lancaster, K. M.; MacBeth, C. E.; Berry, J. F., *J. Am. Chem. Soc.,* **2016,** *138*, 1796.

[50] Hu, X., Castro-Rodriguez, I., Meyer, K. *J. Am. Chem. Soc.,* **2004**, *126*, 13464.

[51] Rahman, A. F. M. M.; Jackson, W. G.; Willis, A. C., *Inorg. Chem*., **2004**, *4*3, 7558.

[52] Cho, J.; Sarangi, R.; Kang, H. Y.; Lee, J. Y.; Kubo, M.; Ogura, T.; Solomon, E. I.; Nam. W., *J. Am. Chem. Soc.,* **2010**, *132*, 16977.

[53] Jo, Y.; Annaraj, J.; Seo, M. S.; Lee, Y.-M.; Kim, S. Y.; Cho, J.; Nam. W., *J. Inorg. Biochem*., **2008***, 102*, 2155.

[54] Tcho, W.; Wang, B.; Lee, Y.; Cho, K.; Shearer, J.; Nam, W., *Dalton Trans*., **2016,** *45*, 14511.

[55] Chavez, F. A.; Mascharak, P. K., *Acc. Chem. Res.,* **2000**, *33*, 539.

[56] Giannotti, C.; Fontaine, C.; Chiaroni, A.; Riche, C., *J. Organomet. Chem*., **1976**, *113*, 57.

[57] Nishinaga, A.; Tomita, H.; Nishizawa, K.; Matsuura, T.; Ooi, S.; Hirotsu, K., *J. Chem. Soc., Dalton Trans*., **1981**, 1504.

[58] Mikolaiski, W.; Baum, G.; Massa, W.; Hoffman, R. W*., J. Organomet.Chem*., **1989**, *376*, 397.

[59] Saussine L.; Brazi, E.; Robine, A.; Mimoun, H.; Fischer, J.; Weiss, R., *J. Am. Chem. Soc*., **1985**, *107,* 3534.

[60] Chavez, F. A.; Nguyen, C. V.; Olmstead, M. M.; Mascharak, P. K., *Inorg. Chem*., **1996**, *35,* 6282.

[61] Chavez, F. A.; Rowland, J. M.; Olmstead, M. M.; Mascharak, P. K., *J. Am. Chem. Soc*., **1998**, *120,* 9015.

[62] Chavez, F. A.; Briones, J. B.; Olmstead, M. M.; Mascharak, P. K., *Inorg. Chem*., **1999**, *38*, 1603.

[63] a) Reinaud, O. M.; Theopold, K. H., *J. Am. Chem. Soc.,* **1994**, *116*, 6979. b) Hikichi, S.; Komatsuzaki, H.; Akita, M.; Moro-oka, Y., *J. Am. Chem. Soc.,* **1998**, *120*, 4699. c) Chavez, F. A.; Rowland, J. M.; Olmstead, M. M.; Mascharak, P. K., *J. Am. Chem. Soc.,* **1998**, *120*, 9015. e) Chavez, F. A.; Rowland, J. M.; Olmstead, M. M.; Mascharak, P. K., *J. Am. Chem. Soc.,* **1998**, *120*, 9015. d) Chavez, F. A.; Mascharak, P. K., *Acc. Chem. Res.,* **2000**, *33*, 539. e) Nam, W.; Kim, I.; Kim, Y.; Kim, C., *Chem. Commun.,* **2001**, 1262. h) Nguyen, A. I.; Hadt, R. G.; Solomon, E. I.; Tilley, T. D., *Chem. Sci*., **2014**, *5*, 2874.

[64] Pfaff, F. F.; Kundu, S.; Risch, M.; Pandian, S.; Heims, F.; Pryjomska-Ray, I.; Haack, P; Metzinger, R.; Bill, E.; Dau, H.; Comba, P.; Ray, K., *Angew.Chem. Int. Ed.,* **2011**, *50*, 1711.

[65] Lacy, D. C.; Park, Y. J.; Ziller, J. W.; Yano, J.; Borovik, A. S., *J. Am. Chem. Soc*., **2012**, *134*, 17526.

[66] Hong, S.; Pfaff, F. F.; Kwon, E.; Wang, Y.; Seo, M.-S.; Bill, E.; Ray, K; Nam, W., *Angew. Cehm. Int. Ed.*, **2014**, *53*, 10403.

[67] Barondeau, D. P.; Kassmann, C. J.; Bruns, C. K.; Tainer, J. A.; Getzoff, E. D., *Biochemistry,* **2004**, *43*, 8038.

[68] Jeoung, J.-H.; Nianios, D.; Fetzner, S.; Dobbek, H., *Angew. Chem. Int. Ed.,* **2016**, *55*, 3281.

[69] Maroney, M. J.; Ciurli, S., *Chem. Rev.,* **2014**, *114*, 4206.

[70] Koola, J. D.; Kochi, J. K., *Inorg. Chem*., **1987**, *26*, 908.

[71] Nagataki, T.; Ishii, K.; Tachi, Y.; Itoh, S., *Dalton Trans.*, **2007**, 1120.

[72] Nagataki, T.; Tachi, Y.; Itoh, S., *Chem. Commun.,* **2006**, 4016.

[73] Morimoto, Y.; Bunno, S.; Fujieda, N.; Sugimoto, H.; Itoh, S., *J. Am. Chem. Soc.,* **2015**, *137*, 5867.

[74] Burrows, C. J.; Muller, J. G.; Poulter, G. T.; Rokita, S. E., *Acta Chem. Scand.,* **1996**, *50*, 337.

[75] Yoon, H.; Wagler, T. R.; O'Connor, K. J.; Burrows, C. J., *J. Am. Chem. Soc.,* **1990**, *112*, 4568.

[76] Grill, J. M.; Ogle, J. W.; Miller, S. A., *J. Org. Chem.,* **2006**, *71*, 9291.

[77] Kieber-Emmons, M. T.; Schenker, R.; Yap, G. P. A.; Brunold, T. C.; Riordan, C. G., *Angew. Chem. Int. Ed.,* **2004**, *43*, 6716.

[78] Adhikari, D.; Mossin, S.; Basuli, F.; Dible, B. R.; Chipara, M.; Fan, H.; Huffman, J. C.; Meyer, K.; Mindiola, D. J., *Inorg. Chem.,* **2008**, *47*, 10479.

[79] Cámpora, J.; Palma, P.; del Río, D.; Álvarez, E., *Organometallics,* **2004**, *23*, 1652.

[80] Cámpora, J.; Matas, I.; Palma, P.; Graiff, C.; Tiripicchio, A., *Organometallics,* **2005**, *24*, 2827.

[81] Powell-Jia, D.; Ziller, J. W.; Dipasquale, A. G.; Rheingold, A. L.; Borovik, S., *Dalton Trans.,* **2009**, 2986.

[82] Draksharapu, A.; Codolà, Z.; Gómez, L.; Lloret-Fillol, J.; Browne, W. R.; Costas, M., *Inorg. Chem*., **2015**, *54*, 10656.

[83] Chmielewski, P. J.; Latos-graz, L., *Inorg. Chem.,* **1997**, *1669*, 840.

[84] Huang, D.; Makhlynets, O. V.; Tan, L. L.; Lee, S. C.; Rybak-Akimova, E. V.; Holm, R. H., *Inorg. Chem.,* **2011**, *50*, 10070.

[85] Huang, D.; Holm, R. H., *J. Am. Chem. Soc.,* **2010**, *132*, 4693.

[86] Huang, D.; Makhlynets, O. V.; Tan, L. L.; Lee, S. C.; Rybak-Akimova, E. V.; Holm, R. H., *Proc. Natl. Acad. Sci. U. S. A.,* **2011**, *108*, 1222.

[87] a) Pirovano, P.; Farquhar, E. R.; Swart, M.; Fitzpatrick, A. J.; Morgan, G. G.; McDonald, A. R., *Chem. Eur. J.,* **2015**, *21*, 3785. b) Pirovano, P.; Farquhar, E. R.; Swart, M.; McDonald, A. R*., J. Am. Chem. Soc.,* **2016**, *138*, 14362.

[88] Tietze, D.; Voigt, S.; Mollenhauer, D.; Tischler, M.; Imhof, D.; Gutmann, T.; González, L.; Ohlenschläger, O.; Breitzke, H.; Görlach, M., *Angew. Chem. Int. Ed.,* **2011**, *50*, 2946.

[89] Ryan, K. C.; Guce, A. I.; Johnson, O. E.; Brunold, T. C.; Cabelli, D. E.; Garman, S. C.; Maroney, M. J., *Biochemistry,* **2015**, *54*, 1016.

[90] Fujita, K.; Schenker, R.; Gu, W.; Brunold, T. C.; Cramer, S. P.; Riordan, C. G., *Inorg. Chem..* **2004**, *43*, 3324.

[91] Mandimutsira, B. S.; Yamarik, J. L.; Brunold, T. C.; Gu, W., Cramer, S. P.; Riordan, C. G.; *J. Am. Chem. Soc.,* **2001**, *123*, 9194.

[92] Kieber-Emmons, M. T.; Annaraj, J.; Seo, M. S.; Van Heuvelen, K. M.; Tosha, T.; Kitagawa, T.; Brunold, T. C.; Nam, W.; Riordan, C. G., *J. Am. Chem. Soc.,* **2006**, *128*, 14230.

[93] Kieber-Emmons, M. T.; Schenker, R.; Yap, G. P. A.; Brunold, T. C.; Riordan, C. G.; *Angew. Chem. Int. Ed.,* **2004**, *43*, 6716.

[94] Cho, J.; Kang, Y.; Liu, L. V.; Sarangi, R.; Solomon, E. I.; Nam, W., *Chem. Sci.,* **2013**, *4*, 1502.

[95] Yao, S.; Bill, E.; Milsmann, C.; Wieghardt, K.; Driess, M., *Angew. Chem. Int. Ed.,* **2008**, *47*, 7110.

[96] Company, A.; Yao, S.; Ray, K.; Driess, M., *Chem. Eur. J.,* **2010**, *16*, 9669.

[97] Otsuka, S.; Nakamura, A.; Tatsuno, Y., *J. Am. Chem. Soc.,* **1969**, *191*, 6994.

[98] Nakamura, A.; Tatsuno, Y.; Yamamoto, M.; Otsuka, S., *J. Am. Chem. Soc.,* **1971**, *533*, 6052.

[99] Matsumoto, M.; Nakatsu, K., *Acta Cryst.,* **1975**, *B31*, 2711.

[100] Yao, S.; Xiong, Y.; Vogt, M.; Grützmacher, H.; Herwig, C.; Limberg, C.; Driess, M., *Angew. Chem. Int. Ed.,* **2009**, *48*, 8107.

[101] Rettenmeier, C. A.; Wadepohl, H.; Gade, L. H., *Angew. Chem. Int. Ed.,* **2015**, *54*, 4880.

[102] Cho, J.; Sarangi, R.; Annaraj, J.; Kim, S. Y.; Kubo, M.; Ogura, T.; Solomon, E. I.; Nam, W., *Nat. Chem.,* **2009**, *1*, 568.

[103] Hikichi, S.; Okuda, H.; Ohzu, Y.; Akita, M., *Angew. Chem. Int. Ed.,* **2009**, *48*, 188.

[104] Balamurugan, M.; Mayilmurugan, R.; Suresh, E.; Palaniandavar, M., *Dalton Trans.,* **2011**, *40*, 9413.

[105] Sankaralingam, M.; Balamurugan, M.; Palaniandavar, M.; Vadivelu, P.; Suresh, C. H., *Chem. Eur. J.,* **2014**, *20*, 11346.

[106] Hikichi, S.; Hanaue, K.; Fujimura, T.; Okuda, H.; Nakazawa, J.; Ohzu, Y.; Kobayashi, C.; Akita, M., *Dalton Trans.,* **2013**, *42*, 3346.

[107] Nakazawa, J.; Terada, S.; Yamada, M.; Hikichi, S., *J. Am. Chem. Soc.,* **2013**, *135*, 6010.

[108] Schroder, D.; Schwarz, H., *Angew. Chem. Int. Ed.,* **1995**, *34*, 1973.

[109] Shiota, Y.; Yoshizawa, K., *J. Am. Chem. Soc.,* **2000**, *122*, 12317.

[110] Pfaff, F. F.; Heims, F.; Kundu, S.; Mebs, S.; Ray, K., *Chem. Commun.,* **2012**, *48*, 3730.

[111] Trogler, W. C., *Coord. Chem. Rev.,* **1999**, *187*, 303.

[112] Chen, P.; Gorelsky, S. I.; Ghosh, S.; Solomon, E. I. *Angew. Chem. Int. Ed.* **2004**, *43,* 4132.

[113] Tolman, W. B., *Angew. Chem. Int. Ed*., **2010**, *49*, 1018.

[114] Strukul, G. *Catalytic oxidations with hydrogen peroxide as oxidant*; Kluwer Academic Publishers: The Netherlands, 1992.

[115] a) Parmon, V. N.; Panov, G. I.; Uriarte, A.; Noskov, A. S. *Catal. Today* **2005**, *100*, 115. b) Poh, S.; Hernandez, R.; Inagaki, M.; Jessop, P. G. *Org. Lett.* **1999**, *1*, 583. c) Bridson-Jones, F. S.; Buckley, G. D. *J. Chem. Soc.* **1951**, 3009. d) Bridson-Jones, F. S.; Buckley, G. D.; Cross, L. H.; Driver, A. P. *J. Chem. Soc.* **1951**, 2999.

[116] Groves, J. T.; Roman, J. S., *J. Am. Chem.Soc.,* **1995**, *117*, 5594.

[117] Yamada, T.; Hashimoto, K.; Kitaichi, Y.; Suzuki, K.; Ikeno, T., *Chem. Lett.,* **2001**, *3*, 268.

[118] Hashimoto, K.; Kitaichi, Y.; Tanaka, H.; Ikeno, T.; Yamada, T., *Chem. Lett.,* **2001**, *9*, 922.

[119] Harman, W. H.; Chang, C. J., *J. Am. Chem. Soc.,* **2007**, *129*, 15128.

[120] Yao, S.; Bill, E.; Milsmann, C.; Wieghardt, K.; Driess, M., *Angew. Chem. Int. Ed.,* **2008**, *47*, 7110.

[121] Yamamoto, A.; Kitazume, S.; Pu, L. S.; Ikeda, S., *J. Am.Chem. Soc.,* **1971**, *93*, 371.

[122] Esmieu, C.; Orio, M.; Torelli, S.; Pape, L. L.; Pecaut, J.; Lebrun, C.; Menage, S., *Chem. Sci.*, **2014,** *5*, 4774.

[123] Panov, G. I.; Kharitonov, A. S.; Soholev V. I., *Applied Catalysis A*, **1993**, *98*, 1.

[124] Fellah, M. F.; van Santen, R. A.; Onal, I., *J. Phys. Chem. C,* **2009,** *113,* 15307.

[125] Panov, G. I.; Sobolev, V. I.; Dubkov, K. A.; Parmon, V. N.; Ovanesyan, N. S.; Shilov, A. E.; Shteinman, A. A., *React. Kinet. Catal. Lett.*, **1997**, *61*, 251.

[126] Xiao, D.J.; Bloch, E. D.; Mason, J. A.; Queen, W. L.; Hudson, M. R.; Planas, N.; Borycz, J.; Dzubak, A. L.; Verma, P.; Lee, K.; Bonino, F.; Crocellà, V.; Yano, J.; Bordiga, S.; Truhlar, D. G.; Gagliardi, L.; Brown, C. M.; Long, J. R., *Nat. Chem.*, **2014***, 6*, 590.

[127] Ben-Daniel, R.; Neumann, R., *Angew. Chem. Int. Ed.,* **2003**, *42*, 92.

[128] Ettedgui, J.; Neumann, R., *J. Am. Chem. Soc.,* **2009**, *131*, 4.

[129] Ben-Daniel, R.; Weiner, L.; Neumann, R., *J. Am. Chem. Soc.* ,**2002**, *124*, 8788.

[130] Kiefer, G.; Jeanbourquin, L.; Severin, K., *Angew. Chem. Int. Ed.,* **2013**, *52*, 6302.

[131] Hili, R.; Yudin, A. K., *Nat. Chem. Biol*., **2006**, *2*, 284.

[132] a) Evano, G.; Blanchard, N.; Toumi, M., *Chem. Rev.,* **2008**, *108*, 3054. b) Hartwig, J. F., *Acc. Chem. Res.,* **2008**, *41*, 1534. c) Surry, D. S.; Buchwald, S. L. Biaryl, D., *Angew. Chem. Int. Ed.,* **2008**, *47*, 6338. d) Bariwal, J.; Van der Eycken, E., *Chem. Soc. Rev*., **2013**, *42*, 9283.

[133] a) Collet, F.; Dodd, R. H.; Dauban, P., *Chem. Commun.,* **2009**, 5061. b) Dequirez, G.; Pons, V.; Dauban, P., *Angew. Chem., Int. Ed.,* **2012**, *51*, 7384.

[134] Shin, K.; Kim, H.; Chang, S., *Acc. Chem. Res*., **2015**, *48*, 1040.

[135] Bräse, S.; Gil, C.; Knepper, K.; Zimmermann, V., *Angew. Chem. Int. Ed.,* **2005**, *44*, 5188.

[136] Suarez, A. I. O.; Lyaskovskyy, V.; Reek, J. N. H.; van der Vlugt,J. I.; de Bruin, B., *Angew. Chem. Int. Ed*., **2013**, *52*, 12510.

[137] Hohenberger, J.; Ray, K.; Meyer, K., *Nature Comm*., **2012** 3:720 | DOI: 10.1038/ncomms1718

[138] Einsle, O.;Tezcan, F. A.; Andrade, S. L. A.; Schmid, B.; Yoshida, M.; Howard, J. B.; Rees, D. C., *Science*, **2002**, *297*, 1696.

[139] Svastits, E. W., Dawson, J. H., Breslow, R. & Gellman, S. H., *J. Am. Chem. Soc.,* **1985***, 107***,** 6427.

[140] Long, Z.; Liang, D., *Chin. Sci. Bull.*, **2012**, *57*, 2352.

[141] King, E. R.; Hennessy, E. T.; Betley, T. A., *J. Am. Chem. Soc.,* **2011,** *133*, 4917.

[142] Iovan D. A.; Betley, T. A., *J. Am. Chem. Soc.* **2016**, *138*, 1983.

[143] a) Cenini, S.; Gallo, E.; Penoni, A.; Ragainia, F.; Tollari S., *Chem. Commun.*, **2000**, 2265. b) Harden, J. D; Ruppel, J. V.; Gao, G.-Y.; Zhang, X. P., *Chem. Commun*., **2007**, 4644. c) Ruppel, J. V.; Kamble, R. M.; Zhang, X. P., *Org. Lett*., **2007**, *9*, 4889. d) Caselli, A.; Gallo, E.; Fantauzzi, S.; Morlacchi, S.; Ragaini, F.; Cenini, S.; *Eur. J. Inorg. Chem.,* **2008**, 3009. e) Ruppel, J. V.;

Kamble, R. M.; Zhang, X. P., *Org. Lett.*, **2010**, *12*, 1248. f) Lu, H., Subbarayan, V.; Tao, J.; Zhang, X. P., *Organometallics,* **2010**, *29*, 389.

[144] a) Jenkins, D. M.; Betley, T. A.; Peters, J. C., *J. Am. Chem. Soc.,* **2002**, *124*, 11238. b) Thyagarajan, S.; Shay, D. T.; Incarvito, C. D.; Rheingold, A. L.; Theopold, K. H., *J. Am. Chem. Soc.,* **2003**, *125*, 4440. Shay, D. T.; Yap, G. P. A.;Zakharov, L. N.; Rheingold, A. L.; Theopold, K. H., *Angew. Chem. Int. Ed.*, **2005**, *44*, 1508. c) Cowley, R. E.; Bontchev, R. P.; Sorrell, J.; Sarracino, O.; Wang, Y. F. H.; Smith, J. M., *J. Am. Chem. Soc.,* **2007**, *129*, 2424. d) Hu, X.; Meyer, K., *J. Am. Chem. Soc.,* **2004**, *126*, 16322. e) Du, J.; Wang, L.; Xie, M.; Deng, L., *Angew. Chem. Int. Ed.*, **2015**, *54*, 12640. f) Dai, X.; Kapoor, P.; Warren, T. H., *J. Am. Chem. Soc.,* **2004**, *126*, 4798. g) Jones, C.; Schulten, C.; Rose, R. P.; Stasch, A.; Aldridge, S.; Woodul, W. D.; Murray, K. S.; Moubaraki, B.; Brynda, M.; La Macchia, G.; Gagliardi, L., *Angew.Chem. Int. Ed.,* **2009**, *48*, 7406. h) King, E. R.; Sazama, G. T.; Betley, T. A., *J. Am. Chem. Soc.,* **2012**, *134*, 17858.

[145] Du, J.; Wang, L.; Xie, M.; Deng, L., *Angew. Chem. Int. Ed.,* **2015**, *54*, 12640.

[146] Ray, K.; Heims, F.; Pfaff, F. F., *Eur. J. Inorg. Chem*., **2013**, 3784.

[147] Mindiola, D. J.; Hillhouse, G. L., *J. Am. Chem. Soc.,* **2001**, *123*, 4623.

[148] Waterman, R.; Hillhouse, G. L., *J. Am. Chem. Soc.,* **2008**, *130*, 12628.

[149] Lluc, V. M.; Hillhouse, G. L., *J. Am. Chem. Soc.,* **2010**, *132*, 15148.

[150] Lluc, V. M.; Miller, A. J. M.; Anderson, J. S.; Monreal, M. J.; Mehn, M. P.; Hillhouse, G. L., *J. Am. Chem. Soc.,* **2011**, *133*, 13055.

[151] a) Waterman, R.; Hillhouse, G. L., *J. Am. Chem. Soc.,* **2003**, *125*, 13350. b) Mindiola, D. J.; Hillhouse, G. L., *Chem. Commun*., **2002**, 1840. c) Wiese, S.; McAfee, J. L.; Pahls, D. R.; McMullin, C. L.; Cundari, T. R.; Warren, T. H., *J. Am. Chem. Soc.,* **2012**, *134*, 10114. d) Laskowski, C. A.; Miller, A. J. M.; Hilhouse, G. L.; Cundari, T. R., *J. Am. Chem. Soc*., **2011**, *133*, 771. e) Kogut, E.; Wiencko, H. L.; Zhang, L.; Cordeau, D .E.; Warren, T. H., *J. Am. Chem. Soc.,* **2005**, *127*, 11248.

[152] Gephart, R. T.; Warren, T. H., *Organometallics,* **2012**, *31*, 7728.

[153] Kwart, H.; Khan, A. A., *J. Am. Chem. Soc*., **1967***, 89*, 1951.

[154] D. A. Evans, M. M. Faul and M. T. Bilodeau, *J. Org. Chem.*, **1991**, *56*, 6744.

[155] Evans, D. A.; Faul, M. M.; Bilodeau, M. T., *J. Am. Chem. Soc*., **1994**, *116*, 2742.

[156] Li, Z.; Conser, K. R.; Jacobsen, E. N.*, J. Am. Chem. Soc*., **1993**, *115*, 5326.

[157] Albone, D. P.; Aujla, P. S.; Taylor, P. C., *J. Org. Chem.,* **1998,** *63,* 9569.

[158] Díaz-Requejo, M. M.; Belderraín, T. R.; Nicasio, M. C.; Trofimenko, S.; Pérez, P. J., *J. Am. Chem. Soc.* **2003**, *125,* 12078.

[159] Fructos, M. R.; Trofimenko, S.; Díaz-Requejo, M. M.; Pérez, P. J., *J. Am. Chem. Soc.,* **2006**, *128*, 11784.

[160] Bhuyan, R.; Nicholas, K. M., *Org. Lett.,* **2007**, *9*, 3957.

[161] Li, Z.; Quan, R. W.; Jacobsen, E. N. *J., Am. Chem. Soc*., **1995**, *117*, 5889.

[162] Vedernikov, A. N.; Caulton, K. G., *Org. Lett*., **2003**, *5*, 2591. *Chem. Commun*., **2004**, 162.

[163] a) Badiei, Y. M.; Krishnaswamy, A.; Melzer, M. M.; Warren, T. H., J*. Am. Chem. Soc*., **2006**, *128*, 15056. b) Dai, X.; Warren, T. H., *J. Am. Chem. Soc*., **2004**, *126*, 10085.

[164] Badiei, Y. M.; Dinescu, A.; Dai, X.; Palomino, R. M.; Heinemann, F. W.; Cundari, T. R.; Warren, T. H., *Angew. Chem. Int. Ed.,* **2008**, *47*, 9961.

[165] a) Kundu, S.; Miceli, E.; Farquhar, E.; Pfaff, F. F.; Kuhlmann, U.; Hildebrandt, P.; Braun, B.; Greco, C.; Ray, K., *J. Am. Chem. Soc.,* **2012**, *134*, 14710. b) Abram, S.-L.; Monte-Pérez, I.; Pfaff, F. F.; Farquhar, E. R.; Ray, K., *Chem. Commun.,* **2014**, *50*, 9852.

[166] Monte-Pérez, I.; Kundu, S.; K. Ray, K., *Z. Anorg. Allg. Chem.,* **2015**, *641*, 78.

[167] Dielmann, F.; Andrada, D. M.; Frenking, G.; Bertrand, G., *J. Am. Chem. Soc.,* **2014**, *136*, 3800.

Chapter II.

Objectives

II. OBJECTIVES

The transformation of C-H bonds into functional groups such as C-O or C-N bonds is a process of general interest in organic synthesis, but controlling the reactivity and selectivity among the multiple C-H bonds existing in most molecules is a very challenging task. Traditional methodologies usually rely on the use of unselective stoichiometric reagents that generate important amounts of waste and require relatively harsh reaction conditions. A sustainable alternative to these methods is the use of catalysts, which can carry out these transformations under milder reaction conditions, with improved selectivities and using less hazardous reagents. The use of catalysts based on first-row transition metals is specially appealing due to their lower toxicity and cost compared to second and third-row counterparts. Only by gathering a profound knowledge on the mechanisms behind these transformations, a rational design of better catalysts will be possible, affording reactions with improved efficiency and selectivity.

Activation of C-H bonds performed by terminal high-valent metal-oxygen or metal-nitrogen species is a common mechanism to achieve their functionalization into C-O or C-N bonds. In this sense, the nature and electronic properties of these active species have been widely studied for iron or manganese, which is in part due to their biological relevance. In contrast, the corresponding compounds based on late first-row transition metals are poorly understood, despite being very promising catalysts for these transformations. Thus, the general objective of this thesis is the synthesis and characterization of elusive terminal high-valent metal-oxygen or metal-nitrogen species based on late first-row transitions metals (e.g. cobalt, nickel or copper) which are relevant in C-H oxidation and amination reactions. In order to accomplish this objective we have designed very particular ligands that enable the stabilization and the study of these highly active compounds. We have used a dianionic unsymmetric tetradentate macrocyclic ligand that contains a 2,6-pyridinecarboxamidate motif as a platform for the stabilization of the prospective high-valent metal species.

Thus, in **Chapters III** and **IV** we will explore the reactivity of the corresponding nickel(II) complex towards different oxidants. The characterization of the resulting prospective high-valent nickel-oxygen species will be performed in detail using spectroscopic techniques as well as computational studies. Then, the oxidative power of such species towards different organic substrates including not only C-H bonds but also C=C bonds and sulfides will be explored. This project is specially challenging considering the limited number of previously described terminal high-valent nickel-oxygen species that are able to perform substrate oxidation and that are catalytically relevant.

In **Chapter V** we will turn our interest towards the use of green oxidants, and in particular we will focus on the activation of nitrous oxide (N_2O). This gas is thermodynamically a potent oxidant but it is kinetically very inert, which means that it needs to be activated. One strategy to achieve its activation is by reducing it using transition metals. In this chapter we will use the same ligand architecture as described above for the synthesis of first-row transition metal complexes with the adequate properties to achieve the activation of N_2O. Our aim is the use of this waste gas as an oxidant for the performance of catalytic oxidation reactions. Entrapment and characterization of the prospective high-valent metal-oxygen species formed along the reaction will also be pursued.

Finally, in **Chapter VI** we will focus on trapping imidocopper (copper-nitrene) species that have been long postulated as active species in copper catalyzed C-N bond formation reactions, including C-H amination and C=C aziridination reactions. In order to do that, we will study the reaction of a copper(I) salt with an azide-containing macrocyclic ligand that is designed to allow the stabilization and characterization of imidocopper species. The ability of this species to perform nitrene-transfer reactions to several substrates including C-H bonds will be evaluated.

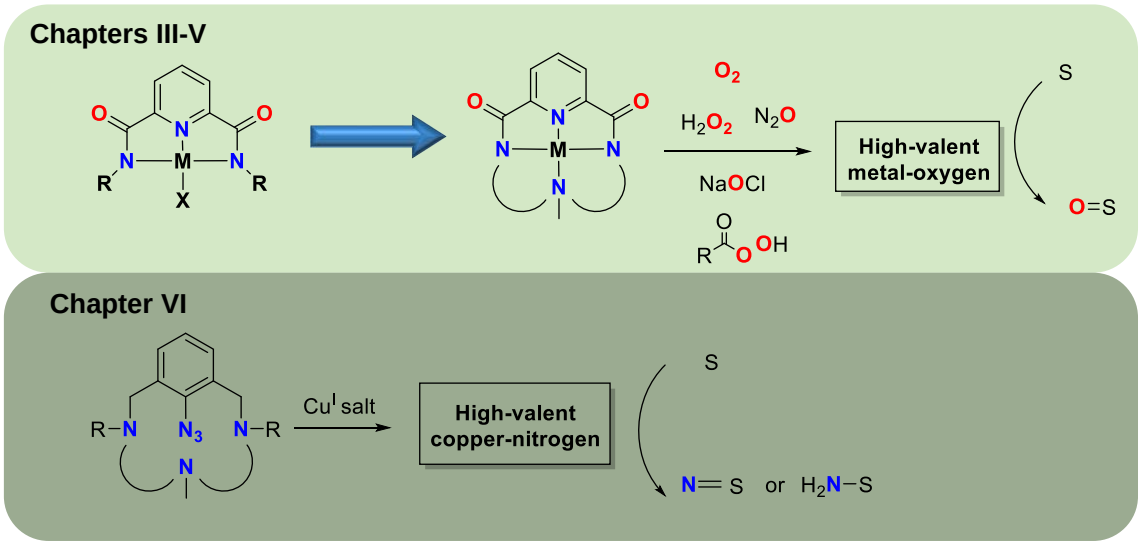

Scheme II.1. Schematic representation of the objectives of this thesis.

Chapter III.

Reactivity of a nickel(II) bis(amidate) complex with *meta*-chloroperbenzoic acid: formation of a potent oxidizing species

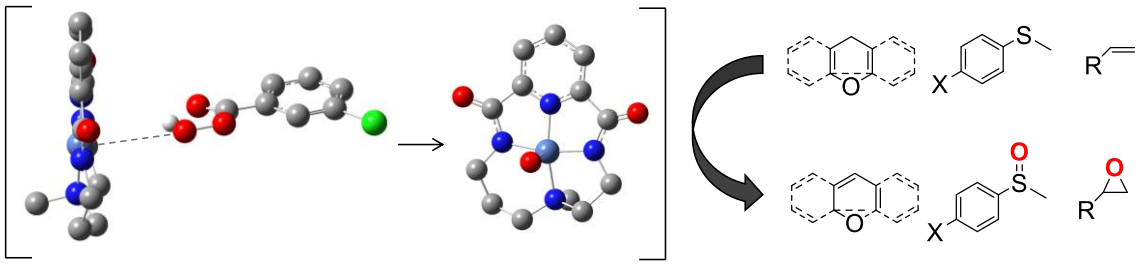

This chapter corresponds to the following publication:

Teresa Corona, Florian F. Pfaff, Ferran Acuña-Parés, Apparao Draksharapu, Christopher J. Whiteoak, Vlad Martin-Diaconescu, Julio Lloret-Fillol, Wesley R. Browne, Kallol Ray, and Anna Company*

Chem. Eur. J. **2015**, *21*, 15029–15038.

ChemPubSoc Europe

DOI: 10.1002/chem.201501841

CHEMISTRY A European Journal Full Paper

Nickel Intermediates

Reactivity of a Nickel(II) Bis(amidate) Complex with *meta*-Chloroperbenzoic Acid: Formation of a Potent Oxidizing Species

Teresa Corona,[a] Florian F. Pfaff,[b] Ferran Acuña-Parés,[a] Apparao Draksharapu,[c] Christopher J. Whiteoak,[a] Vlad Martin-Diaconescu,[a] Julio Lloret-Fillol,[a, d] Wesley R. Browne,[c] Kallol Ray,[b] and Anna Company*[a]

Abstract: Herein, we report the formation of a highly reactive nickel–oxygen species that has been trapped following reaction of a Ni^{II} precursor bearing a macrocyclic bis(amidate) ligand with *meta*-chloroperbenzoic acid (H*m*CPBA). This compound is only detectable at temperatures below 250 K and is much more reactive toward organic substrates (i.e., C–H bonds, C=C bonds, and sulfides) than previously reported well-defined nickel–oxygen species. Remarkably, this species is formed by heterolytic O–O bond cleavage of a Ni–H*m*CPBA precursor, which is concluded from experimental and computational data. On the basis of spectroscopy and DFT calculations, this reactive species is proposed to be a Ni^{III}–oxyl compound.

Introduction

The study of high-valent nickel complexes in particular and the redox chemistry of nickel species in general has attracted the attention of the bioinorganic-chemistry community, thus providing models of nickel-containing enzymes that catalyze redox processes.[1] Enzymes with redox-active nickel sites include [NiFe] hydrogenases,[2] CO dehydrogenase,[3] acetyl-coenzyme A (CoA) synthase,[4] and nickel superoxide dismutase.[5] Moreover, high-valent nickel species have been frequently postulated to be key reaction intermediates in the catalytic cycle of oxidation reactions[6,7] and in coupling reactions.[8,9]

In the field of oxidation chemistry, nickel–oxygen species are perceived to be formed upon homolytic or heterolytic O–O bond cleavage of the terminal oxidant bound to a Ni^{II} precursor. For example, alkane oxidation catalyzed by the $[Ni^{II}(tpa)(OAc)(H_2O)]^+$ ion (tpa = tris(pyridylmethyl)amine) and related systems that use the oxidant *meta*-chloroperbenzoic acid (H*m*CPBA) occurs through Ni^{III}–oxo or Ni^{II}–oxyl intermediate species.[10–12] Furthermore, experimental and theoretical studies have indicated that a $[Ni^{III}–O]^+$ species is a potent oxidant in the gas phase for the conversion of methane into methanol.[13,14] However, the evidence available for Ni^{IV}–oxygen intermediates is limited.[7]

In contrast to the large number of mononuclear Mn–oxygen and Fe–oxygen species reported over the past decade,[15] relatively few examples of such species based on late-transition metals such as nickel have been described. Recently, Ray and co-workers have shown that a Ni^{II}–acylperoxo species coordinated to tris[2-(*N*-tetramethylguanidyl)ethyl]amine (TMG_3tren) is the precursor to a Ni^{III}–oxo/hydroxo compound that can perform an oxo transfer and C–H activation with a rate-determining hydrogen-atom abstraction.[16] Moreover, Hikichi and co-workers reported the selective hydroxylation of cyclohexane catalyzed by tris(pyrazolyl)borate-based Ni^{II} complexes with H*m*CPBA.[17] For these latter systems, thermally stable Ni^{II}–acylperoxo species were spectroscopically detected and crystallographically characterized.[17] Evidence for the formation of a transient $[Ni^{IV}(OH)(cyclam)]^{2+}$ species (cyclam = 1,4,8,11-tetraazacyclotetradecane) competent to epoxidize olefins was gathered for the reaction of the corresponding Ni^{II} precursor with H_2O_2 in acidic media.[7] Most recently, McDonald and co-workers reported the characterization and reactivity of a terminal Ni^{III}–oxygen adduct, which could perform hydrogen-atom abstraction of weak C–H bonds and oxygen-atom transfer to triphenylphosphine.[18]

There are precedents that show that pincerlike tridentate 2,6-pyridinecarboxamidate ligands can support well-defined Ni^{III} or Ni^{IV} complexes[19] (including a Ni^{III}–OCOOH species[18]) and a highly reactive Cu^{III}–OH motif, as reported by Tolman

[a] T. Corona, F. Acuña-Parés, Dr. C. J. Whiteoak, Dr. V. Martin-Diaconescu, Dr. J. Lloret-Fillol, Dr. A. Company
Group de Química Bioinorgànica, Supramolecular i Catàlisi (QBIS-CAT)
Institut de Química Computacional i Catàlisi (IQCC)
Departament de Química, Universitat de Girona
Campus Montilivi, 17071 Girona (Spain)
Fax: (+34) 972-41-81-50
E-mail: anna.company@udg.edu

[b] F. F. Pfaff, Dr. K. Ray
Humboldt Universität zu Berlin, Department of Chemistry
Brook-Taylor Strasse 2, 12489 Berlin (Germany)

[c] Dr. A. Draksharapu, Prof. Dr. W. R. Browne
Stratingh Institute for Chemistry
Faculty of Mathematics and Natural Sciences, University of Groningen
Nijenborgh 4, 9747 AG Groningen (The Netherlands)

[d] Dr. J. Lloret-Fillol
Current address: Institute of Chemical Research of Catalonia (ICIQ)
Av. Països Catalans 16, 43007 Tarragona (Spain)

Supporting information for this article is available on the WWW under http://dx.doi.org/10.1002/chem.201501841.

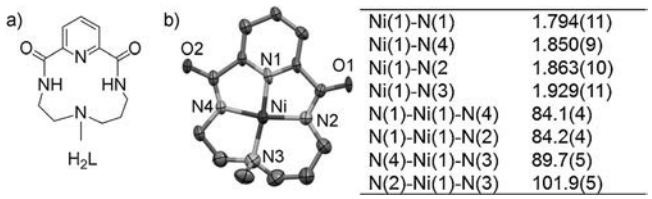

Ni(1)-N(1)	1.794(11)
Ni(1)-N(4)	1.850(9)
Ni(1)-N(2	1.863(10)
Ni(1)-N(3)	1.929(11)
N(1)-Ni(1)-N(4)	84.1(4)
N(1)-Ni(1)-N(2)	84.2(4)
N(4)-Ni(1)-N(3)	89.7(5)
N(2)-Ni(1)-N(3)	101.9(5)

Figure 1. a) Schematic representation of H_2L. b) X-ray structure and selected bond lengths [Å] and angles [°] of **1**·$NaCF_3SO_3$. Hydrogen atoms and cocrystallized $NaCF_3SO_3$ have been omitted for clarity.

and co-workers.[20] Herein, we show that the reaction of [Ni^{II}(L)] (**1**; L is a tetradentate dianionic macrocyclic ligand with two amidate, one pyridine, and one aliphatic amine groups; Figure 1 a) with H*m*CPBA forms a transient nickel–oxygen species **2**, which has been spectroscopically characterized. Compound **2** is only stable at subambient temperatures (< 250 K) and is more reactive toward organic substrates (C–H bonds, C=C bonds, and sulfides) than the previously reported well-defined nickel–oxygen species. Experimental and computational methods indicate that this species is formed by heterolytic O–O bond cleavage.

Results and Discussion

The ligand H_2L was synthesized following a four-step synthetic route (see Scheme S1 in the Supporting Information). Selective methylation of the central amine group of the commercially available *N*-(2-aminoethyl)-1,3-propanediamine required prior protection of the two terminal amine functionalities with phthalic anhydride. After methylation and amine deprotection with hydrazine, [1 + 1] cyclization with 2,6-pyridinedicarbonyl chloride yielded H_2L. This step was the most critical due to the formation of [2 + 2] macrocyclic byproducts. Thus, the reaction was carried out under high-dilution conditions to obtain the desired [1 + 1] product in at least modest yields (see the Supporting Information). The reaction of equimolar amounts of H_2L and [$Ni^{II}(CF_3SO_3)_2(CH_3CN)_3$] with two equivalents of NaH under anaerobic conditions in acetonitrile afforded complex [Ni^{II}(L)], which cocrystallizes with $NaCF_3SO_3$ in 72% yield as **1**·$NaCF_3SO_3$. The nickel center is present in a square-planar geometry with coordination to the pyridine ring, an aliphatic tertiary amine group, and two amidate units *trans* to each other (Figure 1 b). The bond lengths Ni–N_{py}, Ni–N_{CH_3}, and Ni–N_{amide} (i.e., 1.80, 1.93, and 1.85–1.87 Å, respectively) are consistent with previously reported Ni^{II} square-planar complexes with pyridine, amine, or amidate-based ligands.[21–23] The geometry renders the complex diamagnetic, thus enabling characterization by using 1D and 2D ^1H and ^{13}C NMR spectroscopy (see Figures S1–S4 in the Supporting Information). As expected, the complex does not present C_2 symmetry and the β protons of the pyridine ring appear as two well-resolved doublets at $\delta =$ 7.43 and 7.36 ppm. Analysis with high-resolution QTOF-MS showed a major peak at *m/z* 341.053, with an isotopic pattern fully consistent with {[Ni(L)] + Na}$^+$.

Monitoring the reaction of **1** with three equivalents of H*m*CPBA in acetonitrile at −30 °C by means of UV/Vis absorption spectroscopy indicated the formation of the metastable dark-yellow species **2** with an absorption band at $\lambda = 420$ nm ($\varepsilon > 7000\ M^{-1}cm^{-1}$) and a shoulder at $\lambda = 580$ nm ($\varepsilon > 800\ M^{-1}cm^{-1}$; Figure 2). The half-life of this species at −30 °C was 4.5 hours. Compound **2** was not detected when the reaction was carried out at room temperature.

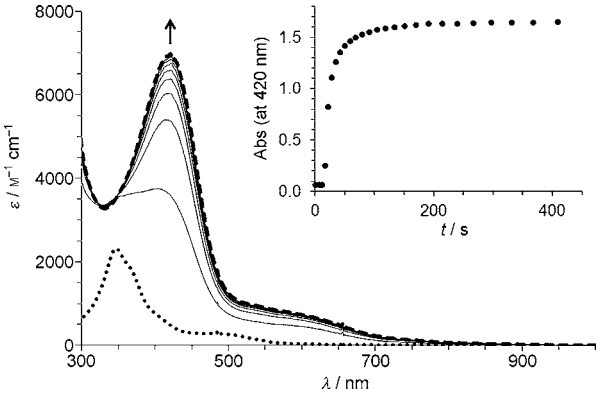

Figure 2. UV/Vis absorption spectroscopic changes observed upon the reaction of **1** (dotted line) with 3 equivalents of H*m*CPBA in CH_3CN at −30 °C to form **2** (dashed line). Inset: kinetic trace at $\lambda = 420$ nm.

Compound **2** reacts with various substrate classes. Indeed, the decay of **2** was accelerated substantially by the addition of thioanisole, which was ascertained by UV/Vis absorption spectroscopic analysis (see Figure S5 in the Supporting Information). Under conditions of excess substrate, the decay in absorbance showed pseudo-first-order behavior and could be fitted with a monoexponential function. The value of k_{obs} varied linearly with the thioanisole concentration, thus affording a second-order rate constant (k) of $0.56\ M^{-1}s^{-1}$ at −30 °C (see Figure S6 in the Supporting Information). Reaction rates were dependent on the substituent at the *para* positon to the sulfide group. The logarithm of the second-order rate constants of a series of *para*-substituted methylphenyl sulfides, namely, *para*-X-thioanisoles (k_X; X = Me, Cl, CN), showed a correlation with the Hammett parameter (σ_p) with a reaction constant (ρ) of −0.86 (Figure 3 a). The negative ρ value indicates a buildup of positive charge in the transition state; hence, **2** has an electrophilic character in these reactions. Moreover, a plot of log(k_X) against the one-electron oxidation potentials of each *para*-X-thioanisole species (E°_{ox}) afforded a linear correlation with a slope of −1.84 (see Figure S7 in the Supporting Information), thus indicating that the oxidation of sulfides by **2** occurs through direct oxygen-atom transfer rather than electron-transfer oxidation.[24]

Compound **2** also behaves as an electrophilic oxygen-atom transfer reagent toward alkenes. Thus, under pseudo-first-order reaction conditions, a second-order rate constant of $k =$ $0.18\ M^{-1}s^{-1}$ was obtained for the oxidation of cyclooctene, whereas this value decreased to $k = 0.04\ M^{-1}s^{-1}$ for 1-octene. The reaction of **2** with a series of *para*-substituted styrenes, namely, *para*-Y-styrenes (Y = OMe, Me, H, Cl, and NO_2), further evidences the electrophilic character of **2** as it affords a negative reaction constant of $\rho = -0.86$ (Figure 3 b). Analysis of the final oxidation products for the reaction of **2** with alkenes at

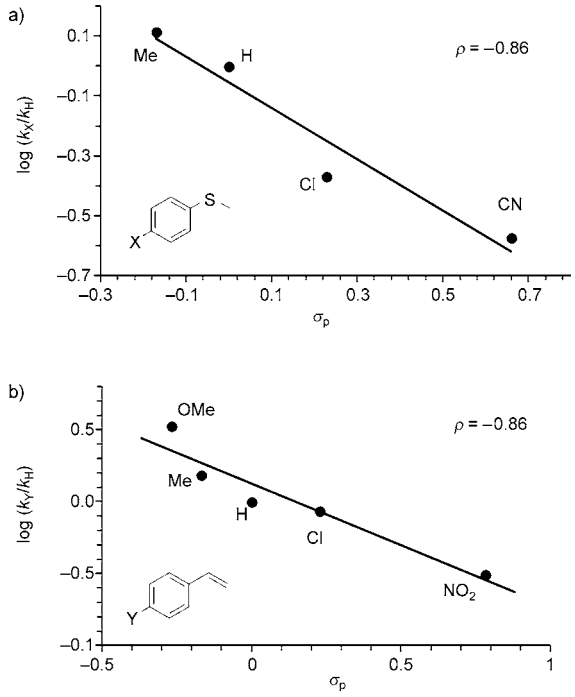

Figure 3. The Hammett plot log(k_X/k_H) versus the Hammett parameter σ_p for the reaction of **2** in acetonitrile at −30 °C with a) *para*-X-thioanisoles and b) *para*-Y-styrenes.

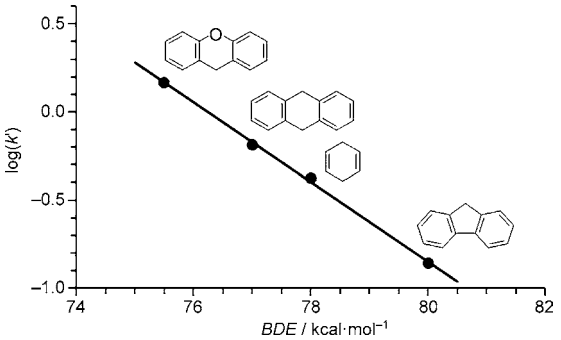

Figure 4. Plot of log(*k*′) (determined at −30 °C) against the C–H BDE for the oxidation of alkanes with activated C–H bonds by **2**.

−30 °C indicates the formation of the corresponding epoxides with yields that range from 140% for cyclooctene oxide and styrene oxide to 50% for 1,2-epoxyoctane (with respect to the nickel complex). Despite the fact that peracids are well known to be capable of directly oxidizing alkenes without the mediation of a metal complex,[25] control experiments (in the absence of a nickel complex) indicated that no epoxide was formed by direct reaction of H*m*CPBA with the alkene substrate under the current reaction conditions (i.e., the reaction mixture was quenched with excess $NaHSO_3$ after full decay of **2** at −30 °C). These results suggest that the slight excess of oxidant necessary to maximize the formation of **2** triggered a catalytic reaction as a background, which explains the yields of over 100% obtained for some of the substrates tested. Thus, the combination of **1** and H*m*CPBA might afford an efficient catalytic system for the oxidation of selected substrates (see below).

Compound **2** could perform hydrogen-atom abstraction from O–H bonds by reacting with 2,4,6-tri-*tert*-butylphenol to quantitatively form the corresponding phenoxyl radical, which manifested in the appearance of the intense absorption band at $\lambda = 626$ nm that is characteristic of this radical (see Figure S11 in the Supporting Information).[26] Remarkably, **2** was also reactive toward hydrocarbon substrates with activated methylene C–H bonds, such as fluorene, 1,4-cyclohexadiene, 9,10-dihydroanthracene, and xanthene, again obeying pseudo-first-order kinetics under conditions with excess substrate and k_{obs} values linearly dependent on substrate concentration (see Figure S13 in the Supporting Information). The obtained second-order rate constants were adjusted for the reaction stoichiometry to yield the corrected rate constants (*k*′). As expected, the rate constants decreased with an increase of C–H bond-dissociation energy (BDE). More interestingly, log(*k*′) values correlated linearly with BDE with a slope of −0.23 (Figure 4). Such a linear relationship between the reaction rates and BDE provides strong evidence for hydrogen-atom abstraction as the rate-determining step for the oxidation. Parallel reactions with deuterated 9,10-dihydroanthracene ([D_4]DHA) yielded a kinetic-isotope effect (KIE) of 4 (see Figure S14 in the Supporting Information), which is a value consistent with C–H bond cleavage as the rate-determining step.[27,28]

The reaction of **2** with substrates bearing stronger C–H bonds was also examined. The addition of alkanes, such as toluene, ethylbenzene, or cyclohexane (300 equiv), to a solution of **2** in CH_3CN at −30 °C caused the decay of its characteristic band at $\lambda = 420$ nm with significantly higher rates than in the absence of these substrates (see Figure S15 in the Supporting Information). However, the decay of **2** did not follow simple single-exponential functions, most probably because the background catalytic reaction significantly interferes with the kinetic trace. Analysis of the final organic products showed the formation of oxidized products (i.e., benzaldehyde, acetophenone, or cyclohexanone, respectively) in yields from 21 to 47% with respect to **1**.

The oxidizing power of **2** was compared with the previously spectroscopically characterized Ni^{II}–acylperoxo complex [$Ni^{II}(Tp^{CF_3Me})$(*m*CPBA)] (Tp^{CF_3Me} = hydrotris(3-trifluoromethyl-5-methylpyrazolyl)borate)[29] and Ni^{III}–hydroxo(oxo) compound $[Ni^{III}\{O(H)\}(TMG_3tren)]^{n+}$[16] obtained by the reaction of the Ni^{II} precursors with H*m*CPBA (Table 1). Interestingly, **2** reacts more than 200 times faster with C–H bonds than $[Ni^{III}\{O(H)\}(TMG_3tren)]^{n+}$ at the same temperature (−30 °C). The same reaction is up to three orders of magnitude faster relative to [$Ni^{II}(Tp^{CF_3Me})$(*m*CPBA)], whereas the reaction toward the *para*-Y-styrenes proceeds about 50 times faster. However, the much higher temperature (+70 °C) used for the reactivity studies with the Tp-based system indicates that differences with respect to **2** are indeed much greater. Overall, compound **2** is significantly more active than previously reported well-defined nickel–oxygen species. A comparison with the reactivity of the Ni^{III}–oxygen adduct recently reported by McDonald and coworkers[18] was hampered because studies with this last compound are limited to substrates containing weaker O–H and

Table 1. Second-order rate constants (k, $M^{-1}s^{-1}$) for the oxidation of different substrates by **2**, $[Ni^{III}\{O(H)\}(TMG_3tren)]^{n+}$, and $[Ni^{II}(Tp^{CF_3Me})(mCPBA)]$.

	2 (−30 °C)	$[Ni^{III}\{O(H)\}(TMG_3tren)]^{n+}$ (−30 °C)[16]	$[Ni^{III}(Tp^{CF_3Me})(mCPBA)]$ (+70 °C)[29]
xanthene	2.93	0.0131	0.0018
9,10-dihydroanthracene	2.62	0.0125	0.00051
1,4-cyclohexadiene	1.69	0.0073	0.019
fluorene	0.28	–	0.0010
styrene	0.45	–	0.0088
4-methylstyrene	0.69	–	0.017
4-methoxystyrene	1.51	–	0.022

C–H bonds (i.e., 2,6-di-*tert*-butylphenol and 1-benzyl-1,4-dihydronicotinamide, respectively; BDE = 64 kcal mol^{-1}) or triphenylphosphine.

Given the high reactivity of compound **2** toward several substrate classes, including alkanes bearing strong C–H bonds, we tested the ability of **1** to act as a catalyst in the oxidation of cyclohexane with H*m*CPBA as oxidant. The slow addition of H*m*CPBA (150 equiv) to a solution containing **1** and cyclohexane (15 000 equiv) afforded a mixture of cyclohexanol (A) and cyclohexanone (K) with a total turnover number of 100 and a product ratio of A/K ≈ 1:1, with an overall 67% yield based on the oxidant. Blank experiments in the absence of the nickel catalyst showed the formation of only trace amounts of oxidized products (< 0.5% yield).

Further insight into the nature of the oxidizing species was gained through the oxidation of *cis*-1,2-dimethylcyclohexane and adamantane. The oxidation of this substrate (150 equiv) by **1** (1 equiv) with H*m*CPBA (150 equiv) as an oxidant afforded the corresponding tertiary alcohol product with 84% retention of configuration (RC) of the tertiary carbon atoms. Under similar experimental conditions, adamantane was oxidized with a high preference for the tertiary carbon atom with a tertiary/secondary ratio of 18:1 (corrected according to the number of equivalent secondary and tertiary C–H bonds). Much lower RC values and tertiary/secondary ratios would be obtained if freely diffusing radicals (i.e., hydroxyl or alkoxyl) were involved.[30] This data indicates that a metal-based oxidant, most likely the spectroscopically detected species **2** (see below), is mainly responsible for the observed oxidation reactions.

The characterization of **2** with cryospray ionization mass spectrometry (CSI-MS) at −30 °C revealed a clean spectrum with a major peak at *m/z* 318.0605, with an isotopic pattern fully consistent with the $[Ni^{III}(L)]^+$ ion. Interestingly, monitoring the reaction of **2** with 1-octene by means of CSI-MS showed the progressive formation of the Ni^{II} species (*m/z* 355.0319). However, no Ni^{II} species was formed during the reaction with 9,10-dihydroanthracene, and only a Ni^{III} species was observed (*m/z* 318.0605; see Figures S20–S21 in the Supporting Information). In any case, the mass spectra of the reaction mixture obtained upon warming to room temperature, either in the presence or absence of the substrate, only exhibited signals that corresponded to Ni^{II} species with an oxidized/dehydrogenated ligand (*m/z* 355.0319).

The EPR spectrum of a sample frozen to 77 K after mixing **1** and H*m*CPBA at −30 °C shows signals of two rhombic $S = 1/2$ species: a major species (95%) with $g_1 = 2.03$, $g_2 = 2.22$, and $g_3 = 2.24$ and a minor species (5%) with $g_1 = 2.02$, $g_2 = 2.19$,and $g_3 = 2.31$ (Figure 5). These EPR properties, that is, $g_{av} = 2.16$ and 2.18 for the major and minor species, respectively, and $g^{\|} > g^{\perp}$ are indicative of a Ni^{III} species with distorted-square-planar, trigonal-bipyramidal, or compressed-octahedral coordination and the unpaired electron in the d_{xy} or $d_{x^2-y^2}$ orbitals.[31–34] The maximum concentration of the Ni^{III} species, however, amounts to only 16%. Moreover, the time dependence of the change in the intensity of the EPR signal did not directly correlate with that of the UV/Vis absorbance at $\lambda =$ 420 nm (or its shoulder at $\lambda = 580$ nm) assigned to **2**. The concentration of the Ni^{III} species steadily increased over time, even after the disappearance of the chromophore (see Figure S22 in the Supporting Information). These data indicate that the signal of the Ni^{III} species corresponds to a decayed species of **2** that is not responsible for the observed oxidation chemistry.

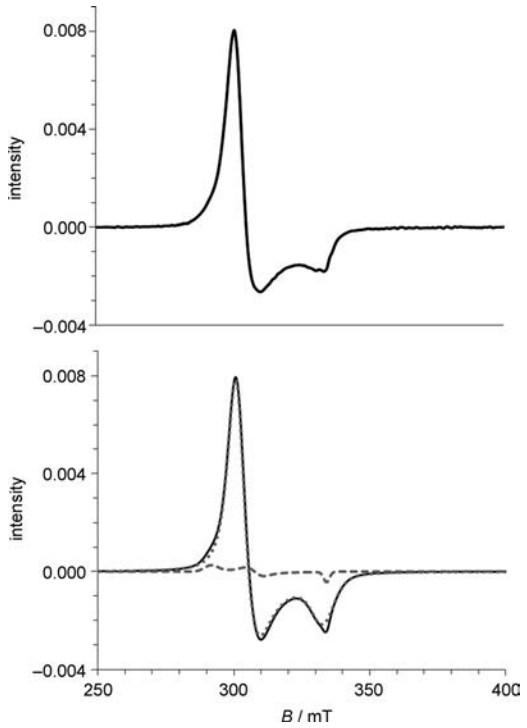

Figure 5. Top: EPR spectrum of the reaction of **1** (1.9 mM) with 3 equivalents of H*m*CPBA in acetonitrile at −30 °C after 60 seconds under argon. Bottom: Simulated EPR spectrum (black line), which accounts for a major species (95%, dotted line) $g_1 = 2.03$, $g_2 = 2.22$, and $g_3 = 2.24$ (anisotropic broadening: $H_1 = 200$, $H_2 = 235$, and $H_3 = 100$ MHz) and a minor species (5%, dashed line) with $g_1 = 2.02$, $g_2 = 2.19$, and $g_3 = 2.32$ (anisotropic broadening $H_1 = 50$, $H_2 = 180$, and $H_3 = 180$ MHz).

Indeed, the addition of **1** to preformed **2** causes the immediate decay of the latter species, as followed by using UV/Vis absorption spectroscopy (see Figure S19 in the Supporting Information). The EPR spectrum of the resultant solution shows the formation of the Ni^{III} species in a much higher yield of 35% (relative to the total nickel concentration after adding 2.75 equivalents of the Ni^{II} complex to the preformed solution of **2**; note that the maximum possible yield is 53%; see Figure S23 and Scheme S2 in the Supporting Information). Analysis of the reaction mixture by means of ESI-MS also shows the presence of a Ni^{III} species, thus further suggesting that comproportionation occurred between **2** (possibly a formal Ni^{IV} species; see below) and **1** (a Ni^{II} species) to give the $[Ni^{III}(L)]^+$ ion (*m/z* 318.0617; see Figure S18 in the Supporting Information).

To help further characterize the Ni center of **2**, XAS was applied at the metal K-edge. The pre-edge of **2**, associated with 1s→3d transitions, occurs at approximately 8333.5 eV and has a normalized area of 0.16, thus indicating the presence of a high-valence Ni species (see Figure S24 in the Supporting Information). Generally for Ni^{II} complexes, the 1s→3d transitions occur at around 8332 eV and are 2–3-fold less intense.[35] A higher oxidation state for **2** is further emphasized by a higher rising-edge energy determined by using the half-height method. This energy in **2** is at approximately 8343.4 eV, which is between 1.5 and 2 eV higher in energy than reported for a Ni^{II} species[35] and is consistent with a Ni^{III} species.[36–38] Previous studies on Ni–oxido and Ni–cyclam derivatives show a shift of 1.5–2 eV on going from Ni^{II} to Ni^{III} species, whereas a shift of approximately 4 eV would be expected for a Ni^{IV} species.[36–38] Relative to Ni foil, this translates to a shift of approximately 4 eV for a Ni^{III} center, whereas a Ni^{IV} species would be expected to have a shift of approximately 6 eV to higher energy (see Figure S24 in the Supporting Information).[37] Therefore, the X-ray absorption near-edge structure (XANES) spectra of **2** is most consistent with a Ni^{III} oxidation of the metal center. The Fourier-transformed EXAFS spectra of **2** is shown in Figure 6. Three scattering shells are implied by the features at 1.4, 1.8, and 2.2 Å. Single-scatter fits are consistent with the first two peaks that correspond to two N/O scattering shells (see Table S4 in the Supporting Information). On the other hand, the feature at 2.2 Å is consistent with contributions from multiple scattering of the pyridine ring. Several multiple scattering models were attempted (see Table S5 in the Supporting Information), and the EXAFS analysis converged on a model with two longer metal–N/O bonds of approximately 2.12 Å, and three shorter N–O bonds of approximately 1.88 Å, including the pyridine ligand (Table 2).

DFT calculations were carried out to explore the possible nature of **2**. Previous reports on related systems indicate four distinct mechanistic scenarios for the reaction of **1** with H*m*CPBA (reactions A-D; Scheme 1). Pathway A involves the formation of the Ni^{II}–acylperoxy $[(L)Ni^{II}$-*m*CPBA$]^-$ species. However, this process was considered to be kinetically and thermodynamically unfeasible due to the high free-energy difference of the $[(L)Ni^{II}$-*m*CPBA$]^-$ ion relative to the starting reactants ($\Delta G^{\circ} = +47.7$ kcal mol^{-1}). This difference may be rationalized by the acidity of H*m*CPBA ($pK_a = 31$), which was computed to be much lower than that of **1**–$\mathbf{H}^+$ ($pK_a = 7$) in acetonitrile, so that proton transfer from H*m*CPBA to **1** is unfavorable. An al-

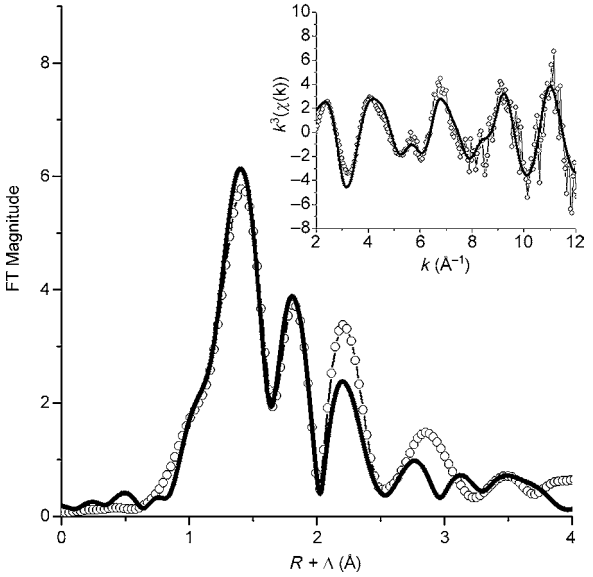

Figure 6. Fourier-transformed EXAFS spectra of **2** (no phase correction, FT window = 2–12 Å^{-1}): dotted line = data, black line = best fit. Inset: k^3-weighted unfiltered EXAFS spectra: dotted line = data, black line = best fit.

Table 2. EXAFS multiple-scattering model showing Ni–ligand bond lengths and the coordination number for complex **2**.[a]

Model	Path	Δr [Å]	σ^2 [×10^3 Å^2]	R [%]	χ^2_v
N_2N_3(Pyr)	2 $N^{2.0}$	0.12(1)	1.9(6)		
	3 $N^{1.8}$	0.08(1)	1.9(6)	8.7	7.2
	1 Pyr[b]	0.08(1)	6(2)		

[a] $E_0 = 8344.2$ eV and $S_0 = 0.9$. [b] The pyridine scattering paths do not include the primary N–Ni single-scatter path.

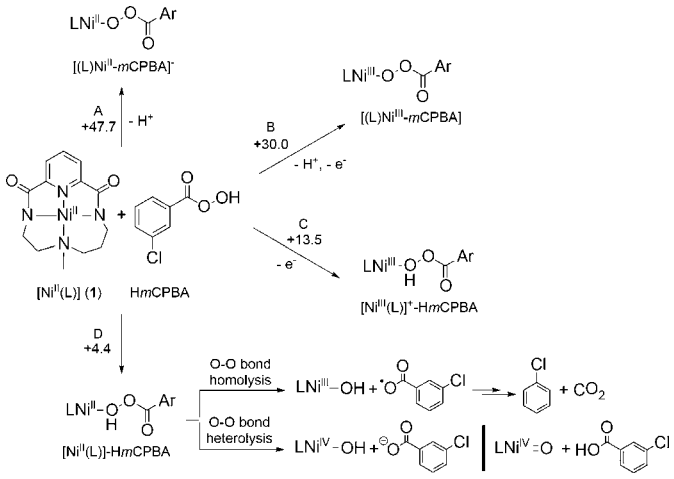

Scheme 1. Possible pathways (A–D) studied by DFT that correspond to the reaction of **1** with H*m*CPBA in acetonitrile. Free energies are given in kcal mol^{-1} at −30 °C.

ternative mechanism involves the formal oxidation of Ni^{II} to Ni^{III} (accompanied by the $1e^-$ reduction of H*m*CPBA to give the radical anion), and the subsequent coordination of another H*m*CPBA or *m*CPBA molecule to the +3 metal center. However, DFT calculations suggest the thermodynamic unviability of these two processes (pathway B: $\Delta G^{\circ} = +30.0$ kcal mol^{-1}; pathway C: $\Delta G^{\circ} = +13.5$ kcal mol^{-1}). This result is in agreement with the EPR data, which indicated that the Ni^{III} species is not related to chromophore **2**.

Instead, the complexation of **1** with H*m*CPBA is thermodynamically reasonable with a ΔG° value of +4.4 kcal mol^{-1} (pathway D, Scheme 1). Complex [Ni^{II}(L)]–H*m*CPBA may evolve through two different reaction pathways as previously postulated for other nickel systems (Scheme 1): 1) homolytic O–O bond cleavage to form a Ni^{III}–hydroxo species and a carboxyl radical, which decomposes to give chlorobenzene and carbon dioxide or 2) heterolytic O–O bond cleavage to form a Ni^{IV}–oxo/hydroxo intermediate and the corresponding benzoic acid (H*m*CBA). Computational studies indicate that the homolytic pathway is kinetically unfavorable by +30.0 kcal mol^{-1} (Scheme 2). Instead, the O–O heterolysis shows a lower barrier of only +9.0 kcal mol^{-1} to afford a nickel–oxygen species. Interestingly, chromatographic analysis of the reaction mixture after the self-decay of **2** did not show the presence of chlorobenzene or CO_2, but the formation of quantitative amounts of H*m*CBA was ascertained instead by using NMR spectroscopy and GC-MS, thus indicating that an O–O heterolysis pathway is followed under the experimental conditions (see Figure S17 in the Supporting Information). Thus, both experimental and theoretical data point toward an O–O heterolytic pathway as the most plausible mechanism. According to DFT calculations, the terminal oxygen atom of the Ni product **2** formed after O–O heterolysis bears an interaction with the acidic proton of the acid byproduct (i.e., H*m*CBA). This compound would carry out the oxidation of the substrate.

Analysis of the Hirshfeld spin density on the nickel center (ρ(Ni) = 0.66) and the oxo moiety (ρ(O) = 1.29) suggests that **2** is best described as a Ni^{III}–$O^{\cdot}$ species (see Tables S6 and S7 and Figure S26 in the Supporting Information). Interestingly, inspection of the spin natural orbitals (SNOs) of complex **2** shows two single occupied orbitals: 1) $\sigma^*(d_z^2/p_z)$ distributed between the Ni and O centers and 2) p_y orbital centered on the terminal oxygen atom (see Figure S27 in the Supporting Information). This electron distribution may be responsible for the weakening of the Ni–O bond (1.95 Å) and the significant oxyl character of the oxygen group. Moreover, the Mayer index for the Ni–O bond is about 0.6, which is in agreement with the half broken σ bond and the lack of π bonding showed in the SNOs. Finally, an atoms-in-molecules (AIM) analysis was performed on **2** to better understand the nature of the Ni–O bond. We found negative but close to zero values of $\nabla^2\rho(r)$ and $H(r)$, which suggests a very weak Ni–O interaction with almost no

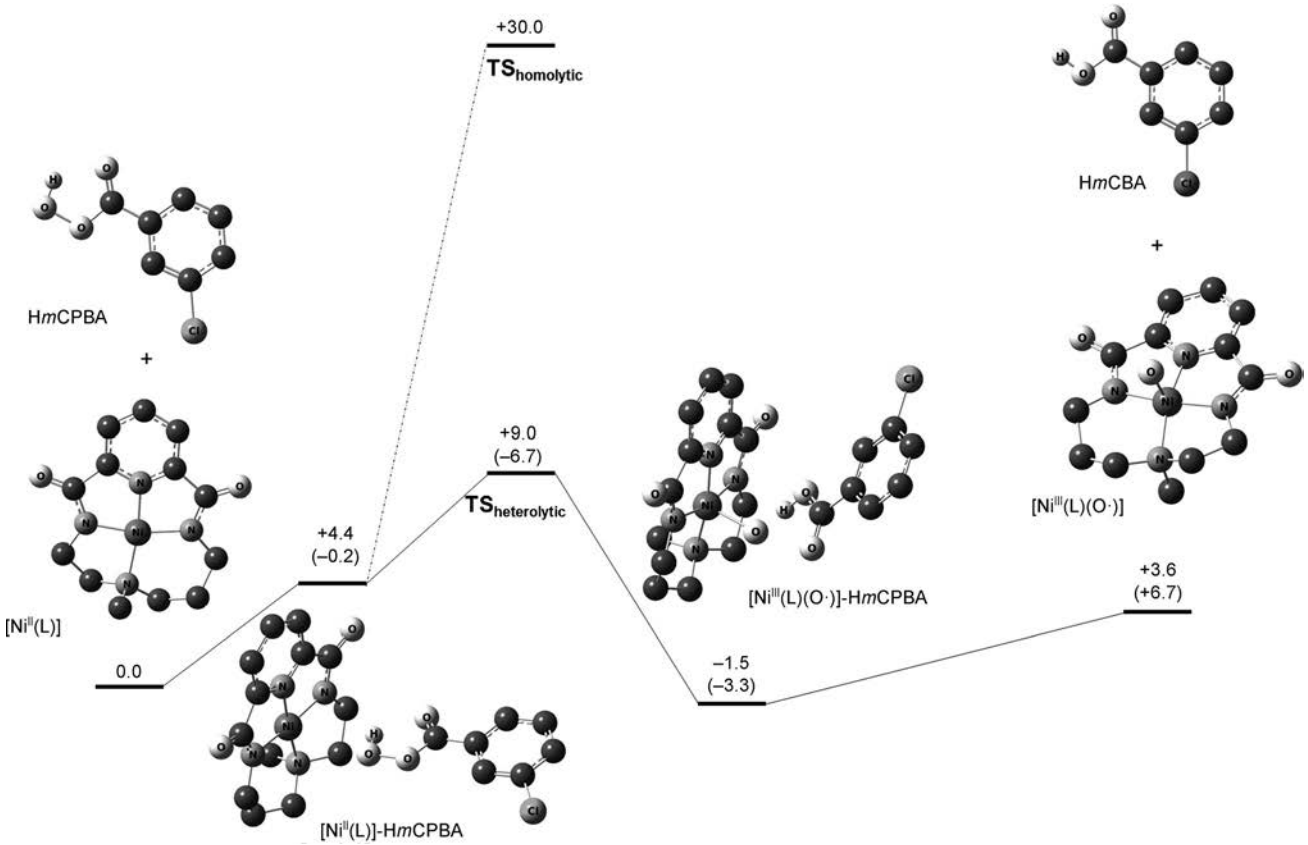

Scheme 2. Energetic profile of pathway D for the reaction of **1** with H*m*CPBA in CH_3CN (homolytic and heterolytic O–O bond cleavage). Free energies are given in kcal mol^{-1} at −30 °C. ΔE_{ZPE} values in kcal mol^{-1} are shown in parentheses (ZPE = zero-point energy).

covalent character (see Figure S28 in the Supporting Information). Therefore, the DFT analysis of the electronic structure of [Ni^{III}(L)(O·)] reveals that the Ni and O atoms are weakly connected, thus making the terminal oxygen atom highly reactive.

The experimental extended X-ray absorption fine structure (EXAFS) distances of **2** are consistent with the Ni^{III}–oxyl radical theoretical model, with three shorter and two longer N–O bonds. The Ni^{III}–oxyl radical model predicts a pyridine–Ni bond of 1.85 Å, with the two proximal Ni–N bonds of 1.86 and 1.90 Å, which is consistent with the N/O scattering shell of 1.88 Å. The Ni^{III}–oxyl radical model also predicts two longer bonds for Ni–O and Ni–N (1.95 and 1.96 Å, respectively), thus corresponding to the two longer N–O distances of 2.12 Å derived from EXAFS analysis. This finding is well within the resolution of the EXAFS single-scatter fits (ca. 0.14 Å) for the long Ni–N/O distances.

Resonance Raman spectroscopic analysis of **2** in frozen acetonitrile (77 K) showed enhancement of two sets of bands at $\tilde{\nu}=450$ and 477 cm^{-1} and $\tilde{\nu}=736$ and 879 cm^{-1}, which appear concomitantly with the absorbance of **2** (Figure 7). Simulation

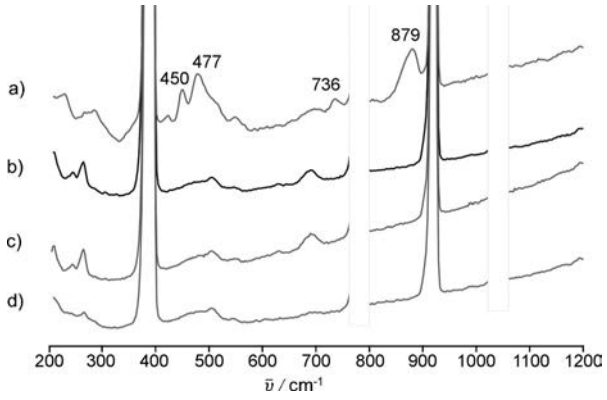

Figure 7. Resonance Raman spectra ($\lambda_{ex}=457$ nm) in frozen acetonitrile (77 K) of a) **2** formed after the reaction of **1** (0.24 mM) with 3 equivalents of H*m*CPBA at −30 °C, b) H*m*CPBA (0.72 mM), c) **1** (0.25 mM), and d) decomposed **2**.

of the Raman spectra of [Ni^{III}(L)(O·)]–H*m*CBA by using DFT methods predicted a Ni–O vibration at $\tilde{\nu}=433$ cm^{-1} and a ligand-based stretching vibration at $\tilde{\nu}=443$ cm^{-1} (see Figure S29 in the Supporting Information). Thus, within error, the experimental and theoretical results are in agreement for the first set of bands at $\tilde{\nu}=450$ and 477 cm^{-1}. The bands at $\tilde{\nu}=$ 736 and 879 cm^{-1} are tentatively assigned to O–O stretching modes from a byproduct, most likely a Ni^{III}–peroxy species.

The formulation of **2** as a Ni^{III}–oxyl species is consistent with the DFT calculations and with the fact that a heterolytic O–O bond cleavage is experimentally observed (i.e., the formation of H*m*CBA as a reaction byproduct). This formulation would also be in agreement with the EPR and NMR silence of **2** and with the EXAFS data. Analysis by CSI-MS that showed the lack of signals with intensity–time profiles similar to those observed by UV/Vis absorption spectroscopic analysis agrees with the neutral character of **2**. Finally, the reaction of **2** with 1-octene (100 equiv) in CH_3CN and in the presence of ^{18}O-labeled water at −30 °C affords 7% of the corresponding ^{18}O-labeled epoxide product. This data indicates that water exchange can occur prior to reaction with substrates, as previously observed for other metal–oxo species.[39]

The formulation of **2** as a Ni^{III}–oxyl species is controversial. To date, metal–oxyl species have been postulated several times, but have been scarcely directly detected.[40,41] A possible alternative to this mechanism would be the formulation of **2** as the [Ni^{II}(L)]–H*m*CPBA adduct, a precursor to the high-valent nickel species (Scheme 3). However, this possibility would not

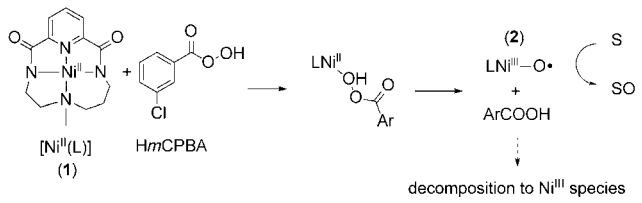

Scheme 3. Schematic representation of the nickel species formed upon the reaction of **1** with H*m*CPBA.

agree with the data from X-ray absorption spectroscopy (XAS), which supports a metal center with a higher valence. Moreover, the reaction of **1** with an aliphatic peracid, such as pernonanoic acid, under the same conditions as those used for the generation of **2** (3 equivalents of peracid, CH_3CN, −30 °C) affords a UV/Vis absorption spectrum almost identical to **2**, with a characteristic absorption band centred at $\lambda=416$ nm (see Figure S25 in the Supporting Information). Given the different nature of the two peracids (i.e., pernonanoic acid and H*m*CPBA), markedly different UV/Vis absorption spectra would be expected for both systems if the peracid unit was coordinated to the nickel center in **2**, which is not the case. Moreover, the formation of a Ni^{III}–oxyl species by heterolytic O–O bond cleavage is in agreement with the much higher reactivity of the present system relative to the previously reported and well-defined Ni–*m*CPBA species.[16,29]

Conclusion

The Ni^{II} complex of the bis(amidate) macrocyclic ligand (L) has been shown to react with H*m*CPBA at low temperatures to form compound **2**, which has been spectroscopically trapped. This species is kinetically competent enough to carry out the oxidation of different substrates, such as olefins, sulfides, and C–H bonds. Remarkably, the activity of **2** is much higher than that previously established for well-defined nickel–oxygen systems, which may indicate that an alternative mechanism occurs in the present system. A combination of experimental and theoretical results have suggested that a heterolytic O–O bond cleavage in a Ni–H*m*CPBA adduct occurs, thus giving rise to the formation of a high-valent nickel–oxygen species that is best formulated as a Ni^{III}–oxyl complex. This work suggests that the use of a dianionic ligand may lead to alternative reaction pathways relative to previous systems, thus favoring the

formation of high-valent nickel species that behave as strong oxidants. In this line of research, work in our group is aimed at ligand tuning and the use of alternative oxidants to increase the reactivity of the nickel species further.

Experimental Section

Materials and methods

The reagents and solvents used are commercially available and were purchased from Panreac, Scharlau, and Aldrich. The preparation and handling of air-sensitive materials were carried out in a N_2 drybox (MBraun ULK 1000) with O_2 and H_2O concentrations of <1 ppm. Commercially available 70% *meta*-chloroperbenzoic acid was purified prior to use by following a reported procedure.[42] The deuterated substrate [D_4]-9,10-dihydroanthracene was prepared from 9,10-dihydroanthracene by following previously reported procedures.[43]

Elemental analyses of C, H, and N were performed on a PerkinElmer EA2400 series II elemental analyzer. Mass spectrometric analysis was performed by electrospray ionization (ESI) on a high-resolution Bruker micrOTOF QII (Q-TOF) mass spectrometer with a quadrupole analyzer and positive and negative ionization modes. ^{1}H NMR, ^{13}C NMR, COSY, and HSQC spectra were performed on Bruker Ultrashield Avance III400 and Ultrashield DPX300 spectrometers. UV/Vis absorption spectra were performed on a diode-array Agilent Cary 60 spectrophotometer and low-temperature control was maintained with a cryostat from Unisoku Scientific Instruments. X-ray analyses were carried out on Bruker Smart Apex CCD diffractometer with graphite-monochromated MoKα radiation ($\lambda=0.71073$ Å) from an X-ray tube. GC analyses were carried out on an Agilent 7820A gas chromatograph (HP5 column, 30 m) with a flame-ionization detector. GC-MS was performed on an Agilent 7890A gas chromatograph interfaced with an Agilent 5975c mass spectrometer with a triple-axis detector. The identification of CO_2 was carried out on an Agilent 7820A GC system equipped with three columns, washed molecular sieves (5 Å; outside diameter (OD)= 2 m×1/8 inch, mesh 60/80 SS; Porapak Q, OD=4 m×1/8 inch, mesh 80/100 SS), and a thermal-conductivity detector. Raman spectra were recorded in NMR tubes (diameter=5 mm) at 77 K in a liquid-nitrogen-filled quartz dewar. Spectra were collected in the back-scattering mode (135°) with excitation at $\lambda=457$ nm (Cobolt Lasers, 50 mW) and planoconvex lens (diameter=25 mm) to collect and collimate the Raman scattering, which was passed through the long pass cutoff filter (Semrock). The scattering was focused at the entrance slits of a Shamrock 303i spectrograph with a grating of 1200 L mm^{-1} blazed at $\lambda=500$ nm and a iDUS-420-BRDD CCD detector (Andor Technology). Spectral calibration was carried out in acetonitrile and toluene (1:1 v/v). The spectra were processed on Andor Solis and Spectrum 10 (PerkinElmer). Cyclic voltammetry (CV) was performed by using a potentiostat from CHInstruments with a three-electrode cell. The working electrode was a glassy carbon disk from BAS (0.07 cm^2), the reference electrode was a saturated KCl calomel electrode, and the auxiliary electrode was a platinum wire. CV was carried out with nBu$_4$NPF$_6$ (TBAP) as a supporting electrolyte (0.1 M). The EPR spectra were recorded on an ESP 300 X-Band EPR spectrometer from Bruker with a TE011 superhigh Q microwave resonator. The samples were cooled to 77 K in a liquid-nitrogen Dewar. Spin quantifications were calculated on the basis of double integrals of the recorded spectra relative to a measured standard of Cu^{II} ions of a given concentration. Sample tubes were filled higher than the cavity dimension to guarantee an equally filled cavity for all the measured samples. Spin quantifications were additionally corrected for volume errors, thus resulting in slight differences in tube diameter. EPR simulation was performed by using EASYSPIN.[44]

A sample of **2** (4 mM; prepared by reaction of **1** with 3 equivalents of H*m*CPBA in CH_3CN at -30°C) was loaded into a holder (2 mm) with Kapton tape windows and stored at liquid-nitrogen temperatures until run. Data was collected at the SOLEIL synchrotron SAMBA beamline equipped with a Si(220) double-crystal monochromator and a liquid-helium cryostat (20 K). X-ray absorption (XAS) was detected in fluorescence mode by using a Canberra 35-element Ge detector and a Z-1 filter. An internal-energy calibration was performed by using the first inflection point of the XANES spectrum of nickel foil ($E_{cal}=8331.6$ eV). Data reduction and normalization was performed by using the Athena software package with the AUTOBK algorithm. To extract intensities and energy positions, the XANES pre-edge and edge were fit with pseudo-Voigt functions and the edge jump was modeled by using a cumulative Gaussian–Lorentzian sum function. EXAFS were extracted by using a R_{bkg} value of 1.05 Å and a spline between $k=1$ and 13.7 Å^{-1}. The Artemis software program with an IFEFFIT engine and FEFF6 code was used for EXAFS analysis.[45–47] The k^3-weighted data was fit in r space over a range of $k=2$–12 Å^{-1}, with $S_0=0.9$ and a Kaiser–Bessel window (dk 2). The spectra were not phase corrected and a global ΔE_0 value was employed, with the initial E_0 value set to the inflection point of the rising edge at 8344.2 eV. Single-scatter paths for Ni–N with initial r_{eff} values of 1.8 and 2.0 Å and multiple scattering from pyridine (initial $r_{eff}=1.8$ Å) were fit in terms of Δr_{eff} and σ^2, as previously described.[48–50] To assess the goodness of fit from different models, the R_{factor} (%R) and the reduced χ^2 (χ^2_v) were minimized. Although the R_{factor} is generally expected to decrease with the number of adjustable parameters, χ^2_v may eventually increase, thus indicating that the model is overfitting the data.[51]

Synthesis of [Ni^{II}(CF$_3$SO$_3$)$_2$(CH$_3$CN)$_3$]

$NiCl_2$ (2.36 g, 0.018 mmol) was suspended in dry acetonitrile (50 mL) in a Schlenk flask (100 mL). Me_3SiOTf (7.1 mL, 0.039 mmol) was added to the solution in an N_2 atmosphere. The skin-colored suspension was stirred vigorously at room temperature for 3 weeks while the color darkened to deep blue. The mixture was then filtered to remove the starting material, the solvent was evaporated under reduced pressure, and a purple precipitate was formed. The solid was collected, dissolved in acetonitrile (5 mL), and slow diffusion of diethyl ether at room temperature over the resulting solution afforded a purple solid, which was dried under vacuum to yield [Ni^{II}(CF$_3$SO$_3$)$_2$(CH$_3$CN)$_3$] as a pale-purple solid (5.43 g, 0.011 mmol, 63%). Elemental analysis (%) calcd for $C_8H_9F_6N_3NiO_6S_2$: C 20.02, H 1.89, N 8.75; found: C 19.76, H 1.97, N 8.63.

Synthesis of [Ni^{II}(L)] (1)

A solution of [Ni^{II}(CF$_3$SO$_3$)$_2$(CH$_3$CN)$_3$] (32.09 mg, 0.057 mmol) in anhydrous acetonitrile (0.5 mL) in a glove box was added dropwise to a vigorously stirred suspension of H_2L (15.10 mg, 0.057 mmol) in anhydrous acetonitrile (0.5 mL). After a few seconds, the solution became colorless. The addition of NaH (2.71 mg, 0.11 mmol, 2 equiv) caused a further color change to orange. The reaction mixture was stirred for 3 h, the solvent was removed, and the resulting residue dissolved in methanol, filtered through celite, and concentrated. Slow diffusion of diethyl ether over the resulting solution afforded **1** in a few days as orange crystals (20.07 mg, 0.041 mmol, 72%). ESI-MS: m/z (%): 341.05 [M+Na]$^+$ (100), 659.12 [2M+Na]$^+$ (40); ^{1}H NMR (CD_3CN, 400 MHz, 298 K): $\delta=7.95$ (t, $J=7.6$ Hz, 1H; H_a), 7.43 (dd, $J=7.6$ Hz, 1H; H_b), 7.36 (dd, $J=7.6$ Hz,

1H; H_c), 3.43–3.35 (m, 1H; H_d), 3.33–3.20 (m, 3H; $H_{e/f/g}$), 2.94–2.87 (m, 1H; H_h), 2.82–2.74 (m, 1H; H_i), 2.73–2.71 (m, 1H; H_j), 2.69 (s, 3H; CH_3), 2.50–2.45 (m, 1H; H_k), 1.81–1.73 ppm (m, 2H; $H_{l/m}$); ^{13}C NMR (CD_3CN, 100 MHz, 298 K): $\delta = 169.39$ (C_{12} or C_{13}), 166.14 (C_{12} or C_{13}), 153.54 (C_{10} or C_{11}), 152.53 (C_{10} or C_{11}), 141.27 (C_1), 121.72 (C_2), 121.60 (C_3), 65.38 (C_4), 58.28 (C_5), 41.54 (C_6), 41.23 (C_7), 40.90 (C_8), 26.21 ppm (C_9); elemental analysis (%) calcd for $C_{13}H_{16}N_4NiO_2{\cdot}NaCF_3SO_3$: C 34.24, H 3.28, N 11.61; found: C 33.98, H 3.08, N 11.23; CV (CH_3CN vs. SCE): $E_{1/2} = 0.96$ V.

Generation of 2

In a typical experiment, a solution of **1** in acetonitrile (2.5 mL, 0.24 mM) was placed in a cuvette (pathlength = 1 cm; [**1**] = 0.6 μmol). The quartz cell was placed in the Unisoku cryostat of a UV/Vis absorption spectrophotometer and cooled to 243 K. After reaching thermal equilibrium, an UV/Vis absorption spectrum of the starting complex was recorded. Then, a solution of H*m*CPBA (3 equiv) in acetonitrile (105 μL, 17 mM) was added. The formation of a band at $\lambda_{max} = 420$ nm ($\varepsilon > 7000\ M^{-1}cm^{-1}$) and a shoulder at $\lambda_{max} = 580$ nm ($\varepsilon > 800\ M^{-1}cm^{-1}$) was observed. Compound **2** was fully formed within 100 s.

Analysis of the reaction of 2 with substrates

Once **2** was fully formed, an aliquot of a solution in acetonitrile (150 μL) containing the corresponding equivalents of the desired substrate was added to the cuvette. The decay of the band at $\lambda =$ 420 nm was monitored, and the reaction was quenched after complete decay by adding an excess of $NaHSO_3$ (0.1 mL of a commercially available 40% aqueous solution). Biphenyl was added as an internal standard, and the nickel complex was removed by passing the solution through a short plug of silica. The products were eluted with ethyl acetate and analyzed by using a gas chromatography flame-ionization detector (GC-FID). The organic products were identified by comparison with authentic compounds.

Catalytic experiments at room temperature with H*m*CPBA

In a typical reaction, a solution of H*m*CPBA (0.58 M, 0.5 mL, 290 μmol) in acetonitrile was delivered by syringe pump over 30 min at 25 °C to a vigorously stirred a solution of the nickel catalyst (2.0 μmol) and the substrate (1900 μmol) in acetonitrile (2.5 mL). The final concentrations of the reagents were 0.7 mM nickel catalyst, 97 mM H*m*CPBA, and 0.62 M substrate. After syringe-pump addition, the resulting solution was stirred for another 30 min. For the oxidation of cyclohexane, biphenyl was added as an internal standard and the nickel complex was removed by passing the solution through a short path of silica gel. The products were eluted with ethyl acetate and analyzed by using a GC-FID. The organic products were identified by comparison with authentic compounds.

Computational details

All DFT calculations were carried out by using the Gaussian09 set of programs.[52] The X-ray diffraction structure of [Ni^{II}(L)] (**1**) was chosen as a starting point for geometry optimizations by using the B3LYP exchange-correlation functional[53,54] and the TZVP basis set.[55] Nickel species were considered in all possible spin states without symmetry constraints. The CH_3CN solvation and effects were included in the geometry optimizations through the solvent model D (SMD) polarizable continuum model.[56] Dispersion effects were introduced through single-point calculations with the Grimme D_3 correction with Becke–Johnson damping.[57] The connection between the transition states and minimum values was verified by using intrinsic reaction coordinate (IRC) calculations.

The Hirshfeld spin densities and charges, Mayer bond-order index,[58,59] and spin natural orbitals (SNO) were computed to rationalize the electronic structure of intermediate **2**. A Bader AIM analysis[60–62] was also conducted on **2** to elucidate the nature of the Ni–O bond.

Analytical frequency calculations were performed to evaluate the thermal corrections and entropic effects at 243.15 K and to characterize the located stationary points in the condensed phase. Raman spectra intensities of intermediate **2** were simulated at 77 K and with laser excitation at $\lambda = 457$ nm by using the GaussSum 3.0 software.[63]

Final Gibbs energies (G) were evaluated by using the following equation:

$$G = E_{TZVP}(SMD + D_3) + G_{corr} \quad (1)$$

where $E_{TZVP}(SMD + D_3)$ was obtained by using single-point calculations with the TZVP basis set on equilibrium geometries, including solvation and dispersion effects, and G_{corr} is the thermal correction obtained from a thermostatistical analysis at the B3LYP/SMD level. The pK_a values were computed according to:

$$pk_a = \frac{\Delta G^{\circ}}{RT\ln(10)} \quad (2)$$

where R is the universal gas constant and T is the temperature.[64] The standard dissociation free-energy change (ΔG°) between an acid (AH) and its conjugate base (A^-) in the solvent phase may be calculated by using the following equations:

$$\Delta G^{\circ} = G(A^-_{sol}) + G(H^+_{sol}) - G(AH_{sol}) + \Delta G^* \quad (3)$$

$$G(H^+_{aq}) = G(H^+_{gas}) + \Delta G^{H+}_{solv} \quad (4)$$

where $G(AH_{sol})$ and $G(A^-_{sol})$ are the standard free energies of the acid and its conjugate base, respectively. The $G(H^+_{sol})$ is the free energy of the proton in acetonitrile, obtained from the solvation free energy of a proton in acetonitrile ($\Delta G^{H+}_{solv} = -260.2$ kcal mol^{-1})[56] and its gas-phase free energy ($G(H^+_{gas}) = -6.3$ kcal mol^{-1}).[57] ΔG^* is the standard-state thermodynamic correction associated with the conversion from a standard state of 1 M in the aqueous phase and 1 atm in the gas phase into 1 M in both phases, with a value of 1.54 kcal mol^{-1} at 243.15 K.

Acknowledgements

Financial support for this work was provided by the European Commission (FP7-PEOPLE-2011-CIG-303522 to A.C.) and the COST Action CM1305 (ECOSTBio) including a STSM grant (COST-STSM-CM1305-21541) to T.C. The Spanish Ministry of Science is acknowledged for a Ramón y Cajal contract to A.C. Also F.A.-P. thanks the Universitat de Girona for a predoctoral grant. K.R. thanks the Cluster of Excellence "Unifying Concepts in Catalysis" (EXC 314/2), Berlin and the Heisenberg Programme of the Deutsche Forschungsgemeinschaft for financial support. J.L.-F. thanks the Cellex Foundation for financial support from the starting-career program. W.R.B. acknowledges

the European Research Council (ERC-2011-StG-279549) and the Ministry of Education, Culture and Science (Gravity program 024.001.035 to A.D. and W.R.B.).

Keywords: high-valent metal species · nickel · oxidation · reactive intermediates · redox chemistry

[1] S. B. Mulrooney, R. P. Hausinger, *FEMS Microbiol. Rev.* **2003**, *27*, 239 – 261.
[2] H. Ogata, W. Lubitz, Y. Higuchi, *Dalton Trans.* **2009**, 7577 – 7587.
[3] H. Dobbek, V. Svetlitchnyi, L. Gremer, R. Huber, O. Meyer, *Science* **2001**, *293*, 1281 – 1285.
[4] T. I. Doukov, T. M. Iverson, J. Seravalli, S. W. Ragsdale, C. L. Drennan, *Science* **2002**, *298*, 567 – 572.
[5] H.-D. Youn, E.-J. Kim, J.-H. Roe, Y. C. Hah, S.-O. Kang, *Biochem. J.* **1996**, *318*, 889 – 896.
[6] M. Sankaralingam, M. Balamuruguan, M. Palaniandavar, V. P, C. H. Suresh, *Chem. Eur. J.* **2014**, *20*, 11346 – 11361.
[7] X. Solans-Monfort, J. L. G. Fierro, L. Hermosilla, C. Sieiro, M. Sodupe, R. Mas-Ballesté, *Dalton Trans.* **2011**, *40*, 6868 – 6876.
[8] S. Z. Tasker, E. A. Standley, T. F. Jamison, *Nature* **2014**, *509*, 299 – 309.
[9] Y. Aihara, N. Chatani, *J. Am. Chem. Soc.* **2014**, *136*, 898 – 901.
[10] T. Nagataki, K. Ishii, Y. Tachi, S. Itoh, *Dalton Trans.* **2007**, 1120 – 1128.
[11] T. Nagataki, Y. Tachi, S. Itoh, *Chem. Commun.* **2006**, 4016 – 4018.
[12] M. Balamurugan, R. Mayimurugan, E. Suresh, M. Palaniandavar, *Dalton Trans.* **2011**, *40*, 9413 – 9424.
[13] D. Schröder, H. Schwarz, *Angew. Chem. Int. Ed. Engl.* **1995**, *34*, 1973 – 1995; *Angew. Chem.* **1995**, *107*, 2126 – 2150.
[14] Y. Shiota, K. Yoshizawa, *J. Am. Chem. Soc.* **2000**, *122*, 12317 – 12326.
[15] A. Company, J. Lloret-Fillol, M. Costas, in *Comprehensive Inorganic Chemistry II*, (Eds.: J. Reedijk, K. Poeppelmeier), Elsevier, Oxford, **2013**, Vol. 3.
[16] F. F. Pfaff, F. Heims, S. Kundu, S. Mebs, K. Ray, *Chem. Commun.* **2012**, *48*, 3730 – 3732.
[17] S. Hikichi, K. Hanaue, T. Fujimura, H. Okuda, J. Nakazawa, Y. Ohzu, C. Kobayashi, M. Akita, *Dalton Trans.* **2013**, *42*, 3346 – 3356.
[18] P. Pirovano, E. R. Farquhar, M. Swart, A. J. Fitzpatrick, G. G. Morgan, A. R. McDonald, *Chem. Eur. J.* **2015**, *21*, 3785 – 3790.
[19] A. K. Patra, R. Mukherjee, *Inorg. Chem.* **1999**, *38*, 1388 – 1393.
[20] P. J. Donoghue, J. Tehranchi, C. J. Cramer, R. Sarangi, E. I. Solomon, W. B. Tolman, *J. Am. Chem. Soc.* **2011**, *133*, 17602 – 17605.
[21] D. Huang, R. H. Holm, *J. Am. Chem. Soc.* **2010**, *132*, 4693 – 4701.
[22] S. K. Sharma, S. Upreti, R. Gupta, *Eur. J. Inorg. Chem.* **2007**, 3247 – 3259.
[23] D. H. Lee, J. Y. Lee, J. Y. Ryu, Y. Kim, C. Kim, I.-M. Lee, *Bull. Korean Chem. Soc.* **2006**, *27*, 1031 – 1037.
[24] Y. Goto, T. Matsui, S. Ozaki, Y. Watanabe, S. Fukuzumi, *J. Am. Chem. Soc.* **1999**, *121*, 9497 – 9502.
[25] F. A. Carey, R. Giuliano, *Orgnaic Chemistry*, McGraw-Hill, **2013**, 9th ed..
[26] V. W. Manner, T. F. Markle, J. H. Freudenthal, J. P. Roth, J. M. Mayer, *Chem. Commun.* **2008**, 256 – 258.
[27] C. V. Sastri, J. Lee, K. Oh, Y. J. Lee, J. Lee, T. A. Jackson, K. Ray, H. Hirao, W. Shin, J. A. Halfen, J. Kim, L. Que, S. Shaik, W. Nam, *Proc. Natl. Acad. Sci. USA* **2007**, *104*, 19181 – 19186.
[28] J. M. Mayer, *Acc. Chem. Res.* **1998**, *31*, 441 – 450.
[29] J. Nakazawa, S. Terada, M. Yamada, S. Hikichi, *J. Am. Chem. Soc.* **2013**, *135*, 6010 – 6013.
[30] M. Costas, K. Chen, L. Que, *Coord. Chem. Rev.* **2000**, *200*, 517 – 544.
[31] Y. H. Huang, J. B. Park, M. W. W. Adams, M. K. Johnson, *Inorg. Chem.* **1993**, *32*, 375 – 376.
[32] C.-M. Lee, C.-H. Chen, F.-X. Liao, C.-H. Hu, G.-H. Lee, *J. Am. Chem. Soc.* **2010**, *132*, 9256 – 9258.
[33] N. Yang, M. Reiher, M. Wang, J. Harmer, E. C. Duin, *J. Am. Chem. Soc.* **2007**, *129*, 11028 – 11029.
[34] M. Dey, J. Telser, R. C. Kunz, N. S. Lees, S. W. Ragsdale, B. M. Hoffman, *J. Am. Chem. Soc.* **2007**, *129*, 11030 – 11032.
[35] G. J. Colpas, M. J. Maroney, C. Bagyinka, M. Kumar, W. S. Willis, S. L. Suib, N. Baidya, P. K. Mascharak, *Inorg. Chem.* **1991**, *30*, 920 – 928.
[36] L. R. Furenlid, M. W. Renner, E. Fujita, *Physica B* **1995**, *208*, 739 – 742.
[37] W. E. O'Grady, K. I. Pandya, K. E. Swider, D. A. Corrigan, *J. Electrochem. Soc.* **1996**, *143*, 1613 – 1616.
[38] M. Risch, K. Klingan, J. Heidkamp, D. Ehrenberg, P. Chernev, I. Zaharieva, H. Dau, *Chem. Commun.* **2011**, *47*, 11912 – 11914.
[39] J. Bernadou, B. Meunier, *Chem. Commun.* **1998**, 2167 – 2173.
[40] D. Moonshiram, I. Alperovich, J. J. Concepcion, T. J. Meyer, Y. Pushkar, *Proc. Natl. Acad. Sci. USA* **2013**, *110*, 3765 – 3770.
[41] B. Lassalle-Kaiser, C. Hureau, D. A. Pantazis, Y. Pushkar, R. Guillot, V. K. Yachandra, J. Yano, F. Neese, E. Anxolabéhère-Mallart, *Energy Environ. Sci.* **2010**, *3*, 924 – 938.
[42] V. K. Aggarwal, Z. Gültekin, R. S. Grainger, H. Adams, P. L. Spargo, *J. Chem. Soc. Perkin Trans. 1* **1998**, 27714 – 22782.
[43] C. R. Goldsmith, R. T. Jonas, T. D. P. Stack, *J. Am. Chem. Soc.* **2002**, *124*, 83 – 96.
[44] S. Stoll, A. Schweiger, *J. Magn. Reson.* **2006**, *178*, 42 – 55.
[45] M. Newville, *J. Synchrotron Radiat.* **2001**, *8*, 96 – 100.
[46] B. Ravel, M. Newville, *J. Synchrotron Radiat.* **2005**, *12*, 537 – 541.
[47] J. J. Rehr, R. C. Albers, *Rev. Mod. Phys.* **2000**, *72*, 621 – 654.
[48] K. Banaszak, V. Martin-Diaconescu, M. Bellucci, B. Zambelli, W. Rypniewski, M. J. Maroney, S. Ciurli, *Biochem. J.* **2012**, *441*, 1017 – 1026.
[49] V. Martin-Diaconescu, M. Bellucci, F. Musiani, S. Ciurli, M. J. Maroney, *J. Biol. Inorg. Chem.* **2012**, *17*, 353 – 361.
[50] B. Zambelli, A. Berardi, V. Martin-Diaconescu, L. Mazzei, F. Musiani, M. J. Maroney, S. Ciurli, *J. Biol. Inorg. Chem.* **2014**, *19*, 319 – 334.
[51] R. W. Herbst, I. Perovic, V. Martin-Diaconescu, K. O'Brien, P. T. Chivers, S. S. Pochapsky, T. C. Pochapsky, M. J. Maroney, *J. Am. Chem. Soc.* **2010**, *132*, 10338 – 10351.
[52] Gaussian 09, Revision D. 01, M. J. Frisch, G. W. Trucks, H. B. Schlegel, G. E. Scuseria, M. A. Robb, J. R. Cheeseman, G. Scalmani, V. Barone, B. Mennucci, G. A. Petersson, H. Nakatsuji, M. Caricato, X. Li, H. P. Hratchian, A. F. Izmaylov, J. Bloino, G. Zheng, J. L. Sonnenberg, M. Hada, M. Ehara, K. Toyota, R. Fukuda, J. Hasegawa, M. Ishida, T. Nakajima, Y. Honda, O. Kitao, H. Nakai, T. Vreven, J. A. Montgomery, Jr., J. E. Peralta, F. Ogliaro, M. Bearpark, J. J. Heyd, E. Brothers, K. N. Kudin, V. N. Staroverov, R. Kobayashi, J. Normand, K. Raghavachari, A. Rendell, J. C. Burant, S. S. Iyengar, J. Tomasi, M. Cossi, N. Rega, M. J. Millam, M. Klene, J. E. Knox, J. B. Cross, V. Bakken, C. Adamo, J. Jaramillo, R. Gomperts, R. E. Stratmann, O. Yazyev, A. J. Austin, R. Cammi, C. Pomelli, J. W. Ochterski, R. L. Martin, K. Morokuma, V. G. Zakrzewski, G. A. Voth, P. Salvador, J. J. Dannenberg, S. Dapprich, A. D. Daniels, Ö. Farkas, J. B. Foresman, J. V. Ortiz, J. Cioslowski, D. J. Fox, Gaussian, Inc., Wallingford CT, **2009**.
[53] A. D. Becke, *J. Chem. Phys.* **1993**, *98*, 1372 – 1377.
[54] A. D. Becke, *J. Chem. Phys.* **1993**, *98*, 5648 – 5652.
[55] A. Schaefer, C. Huber, R. Ahlrichs, *J. Chem. Phys.* **1994**, *100*, 5829 – 5835.
[56] A. V. Marenich, C. J. Cramer, D. G. Truhlar, *J. Phys. Chem. B* **2009**, *113*, 6378 – 6396.
[57] S. Grimme, S. Ehrlich, L. Goerigk, *J. Comput. Chem.* **2011**, *32*, 1456 – 1465.
[58] I. Mayer, *Chem. Phys. Lett.* **1983**, *97*, 270 – 274.
[59] I. Mayer, *Int. J. Quantum Chem.* **1984**, *26*, 151 – 154.
[60] R. F. W. Bader, *J. Phys. Chem. A* **1998**, *102*, 7314 – 7323.
[61] R. F. W. Bader, *Atoms in Molecules: A Quantum Theory*, Oxford University Press, Oxford, **1990**.
[62] F. Bieger-Kim, AIM Version 1.0. University of Applied Science Bielefeld, Germany, **2000**.
[63] N. M. O'Boyle, A. L. Tenderholt, K. M. Langner, *J. Comput. Chem.* **2008**, *29*, 839 – 845.
[64] C. P. Kelly, C. J. Cramer, D. G. Truhlar, *J. Phys. Chem. B* **2006**, *110*, 2493 – 2499.

Received: May 11, 2015
Published online on August 25, 2015

Chapter IV.

Rapid hydrogen and oxygen atom transfer by a high-valent nickel-oxygen species

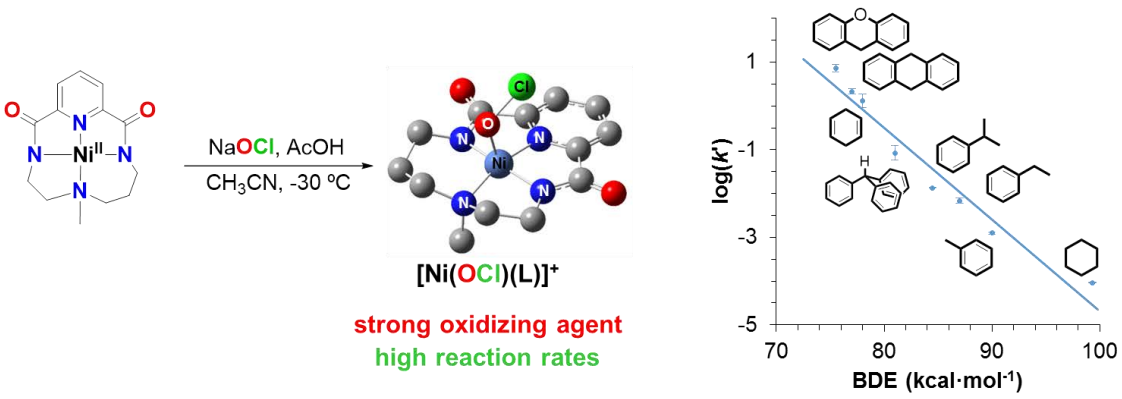

This chapter corresponds to the following publication:

Teresa Corona, Apparao Draksharapu, Sandeep K. Padamati, Ilaria Gamba, Vlad Martin-Diaconescu, Ferran Acuña-Parés, Wesley R. Browne, and Anna Company*

J. Am. Chem. Soc. **2016**, *138*, 12987−12996.

Teresa Corona, Apparao Draksharapu, Sandeep K. Padamati, Ilaria Gamba, Vlad Martin-Diaconescu, Ferran Acuña-Parés, Wesley R. Browne, and Anna Company . “Rapid hydrogen and oxygen atom transfer by a high-valent nickel-oxygen species”. *Journal of the American Chemical Society*. Vol. 138, Issue 39 (2016) : 12987−12996

http://dx.doi.org/10.1021/jacs.6b07544

JACS
JOURNAL OF THE AMERICAN CHEMICAL SOCIETY
Article
pubs.acs.org/JACS

Rapid Hydrogen and Oxygen Atom Transfer by a High-Valent Nickel–Oxygen Species

Teresa Corona,[†] Apparao Draksharapu,[‡] Sandeep K. Padamati,[‡] Ilaria Gamba,[†] Vlad Martin-Diaconescu,[†] Ferran Acuña-Parés,[†] Wesley R. Browne,[‡] and Anna Company*[,†]

[†]Grup de Química Bioinspirada, Supramolecular i Catàlisi (QBIS-CAT), Institut de Química Computacional i Catàlisi (IQCC), Departament de Química, Facultat de Ciències, Universitat de Girona, C/ Maria Aurèlia Capmany 69, E17003 Girona, Catalonia, Spain

[‡]Molecular Inorganic Chemistry, Stratingh Institute for Chemistry, Faculty of Mathematics and Natural Sciences, University of Groningen, Nijenborgh 4, 9747 AG Groningen, The Netherlands

Supporting Information

ABSTRACT: Terminal high-valent metal–oxygen species are key reaction intermediates in the catalytic cycle of both enzymes (e.g., oxygenases) and synthetic oxidation catalysts. While tremendous efforts have been directed toward the characterization of the biologically relevant terminal manganese–oxygen and iron–oxygen species, the corresponding analogues based on late-transition metals such as cobalt, nickel or copper are relatively scarce. This scarcity is in part related to the "Oxo Wall" concept, which predicts that late transition metals cannot support a terminal oxido ligand in a tetragonal environment. Here, the nickel(II) complex (**1**) of the tetradentate macrocyclic ligand bearing a 2,6-pyridinedicarboxamidate unit is shown to be an effective catalyst in the chlorination and oxidation of C–H bonds with sodium hypochlorite as terminal oxidant in the presence of acetic acid (AcOH). Insight into the active species responsible for the observed reactivity was gained through the study of the reaction of **1** with ClO^- at low temperature by UV–vis absorption, resonance Raman, EPR, ESI-MS, and XAS analyses. DFT calculations aided the assignment of the trapped chromophoric species (**3**) as a nickel-hypochlorite species. Despite the fact that the formal oxidation state of the nickel in **3** is +4, experimental and computational analysis indicate that **3** is best formulated as a Ni^{III} complex with one unpaired electron delocalized in the ligands surrounding the metal center. Most remarkably, **3** reacts rapidly with a range of substrates including those with strong aliphatic C–H bonds, indicating the direct involvement of **3** in the oxidation/chlorination reactions observed in the **1**/ClO^-/AcOH catalytic system.

INTRODUCTION

Terminal high-valent metal–oxygen species are key reaction intermediates in the catalytic cycles of both enzymes (e.g., oxygenases) and synthetic oxidation catalysts.[1−5] Many examples of natural and synthetic terminal high-valent Fe-oxygen, and Mn-oxygen species have been reported in the past decade.[6,7] In sharp contrast, and despite some efforts, detection of terminal high-valent metal–oxygen species involved in the mode of action of highly efficient oxidation catalysts based on late-transition metals such as cobalt, nickel or copper are scarce. This is in part related to the "Oxo Wall" concept, which predicts that late transition elements cannot support a terminal oxido ligand in a tetragonal environment.[8,9] Elucidating the mechanisms by which reactions catalyzed by late transition metal complexes proceed is essential for the rational development of selective catalytic reagents based on these metals, and requires a comprehensive understanding of the structure and properties of the key reactive species. It is only in recent years that the structural, spectroscopic and reactivity of well-defined oxido-cobalt(IV),[10,11] hydroxido-cobalt(III),[12] hydroxido-copper(III),[13] oxido/hydroxido-nickel(III)[14] and bicarbonate-nickel(III)[15] have been reported. Indeed, we reported earlier the formation of a metastable oxyl-nickel(III) species.[16] In all of these examples, highly basic ligand structures are necessary to stabilize the uncommonly high oxidation states of the metal center: either neutral guanidine-based ligands or the inclusion of a 2,6-pyridinedicarboxamidate unit in the ligand architecture were necessary. In particular, carboxamidate groups have proven to be a highly successful structural motif to support well-defined high-valent metal species including metal–oxygen compounds.[17−21]

Selected nickel complexes have been proven to be efficient catalysts in the challenging oxidation of alkanes and alkenes. For example, $[Ni^{II}(OAc)(tpa)(H_2O)]^+$ (tpa = tris(pyridylmethyl)amine) and related systems[22−24] catalyze the oxidation of alkanes with *m*CPBA or H_2O_2 as oxidant, while Ni-salen complexes[25,26] and Ni^{II} salts[27] have been successfully applied as catalysts in alkene epoxidation in combination with NaOCl. For hypochlorite-based nickel-mediated oxidations,

Received: July 21, 2016
Published: September 6, 2016

DOI: 10.1021/jacs.6b07544
J. Am. Chem. Soc. 2016, 138, 12987−12996

relatively little insight into the nature of the active species involved is available. Only recently, the complex $[Ni^{II}(CF_3SO_3)_2(Pytacn)]$ (Pytacn = 1-(2-pyridylmethyl)-4,7-dimethyl-1,4,7-triazacyclononane) was reported to catalyze alkane chlorination with NaOCl. Although several higher valent Ni^{III} species were observed, the role of the catalyst was concluded to be primarily to accelerate the formation of chlorine radicals through O−Cl bond cleavage via a spectroscopically characterized Ni^{II}−OCl species.[28]

Recently, we reported the formation of a metastable oxylnickel(III) species, $[Ni^{III}(O\bullet)(L)]$, by reaction of a nickel(II) precursor (**1**) with peracids at low temperature,[16] in which a macrocyclic tetradentate ligand (L) based on a 2,6-pyridinedicarboxamidate unit supported the metal center (Scheme 1). The $[Ni^{III}(O\bullet)(L)]$ was only sufficiently stable

Scheme 1. Previously Reported Reaction of 1 with *m*CPBA to Form $[Ni^{III}(O\bullet)(L)]$[16] along with the Reaction Studied in This Work

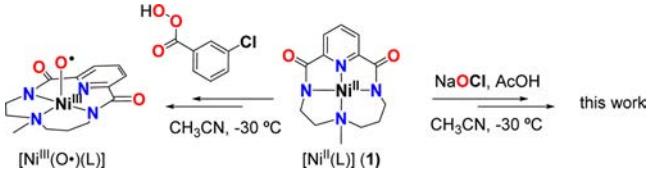

to be observed at subambient temperatures (<250 K) and reacted readily with organic substrates (C−H bonds, C−C double bonds and sulfides). Here, we show that reaction of **1** with NaOCl affords a new high valent Ni-OCl intermediate, which is characterized spectroscopically and by theoretical methods. The kinetic competence of this species in hydrogen-atom abstraction and oxygen-atom transfer reactions is demonstrated by unprecedentedly high reaction rates with a range of substrates.

RESULTS AND DISCUSSION

Catalytic Oxidation/Chlorination of Alkanes by 1 and NaOCl. Compound **1** was found to be a particularly efficient catalyst in the oxidation/chlorination of alkanes bearing strong C−H bonds (Table 1). Thus, addition of 100 equiv NaOCl into an MeCN solution containing 1 equiv **1** (1 mol % with respect to the oxidant), 100 equiv of AcOH and excess cyclohexane (300 equiv) afforded after stirring for 2 h under N_2 34 ± 4 TON (turnover number) of chlorocyclohexane and 7 ± 1 TON of cyclohexanone (entry 1). Interestingly, the yield significantly increased when the temperature was lowered down to −30 °C affording 44 ± 3 TON chlorocyclohexane and 9 ± 2 TON cyclohexanone, indicating that unproductive reaction pathways were occurring at higher temperatures (entry 3). Importantly, experiments in the absence of compound **1** or acetic acid afforded significantly lower yields (entries 4−6), indicating that all the reagents were necessary to efficiently catalyze this transformation. In order to evaluate the synthetic usefulness of this protocol, we carried out an experiment in which full conversion of the substrate could be achieved. The use of stoichiometric amounts of oxidant and cyclohexane caused a decrease in turnover numbers to 17 and 83% of substrate was not converted into products. Finally, *n*-hexane was also used as a substrate and 2-chlorohexane and 3-chlorohexane were obtained as the main products in a roughly 1:1 ratio. Remarkably, turnover numbers obtained for the present system are higher than those previously reported for alkane chlorination/oxidation reactions catalyzed by $[Ni^{II}(Pytacn)(CF_3SO_3)_2]$ or Mn(porphyrin) systems using NaOCl.[28,29] Insight into the nature of the active species involved in the oxidation/chlorination was gained through monitoring the reaction of **1** with NaOCl and AcOH in MeCN by UV−vis absorption spectroscopy at −30 °C, which unraveled the formation of two transient species, namely **2** and **3** (see below).

UV−vis Spectroscopic Detection of 2 and 3. Addition of 5 equiv AcOH to a solution of **1** (0.2 mM) did not alter its UV−vis absorption spectrum. Subsequent addition of 3 equiv ClO^- (either NaOCl or $Ca(OCl)_2$) induced an immediate decay of the absorption bands associated with **1** and the formation of a new species (**2**) with weak absorption bands at 550 and 650 nm ($\varepsilon \sim 500\ M^{-1}\ cm^{-1}$). Further addition of ClO^- up to 5 equiv. led to the appearance of an intensely colored species (**3**) with λ_{max} at 475 nm ($\varepsilon = 8000\ M^{-1}\ cm^{-1}$) and a decay half-life ($t_{1/2}$) of 4.2 h. Five equivalents of ClO^- and AcOH were found to be the optimal amounts to achieve maximum formation of **3** (Figure 1). In the absence of either ClO^- or AcOH species **2** and **3** were not formed, and, in

Table 1. Catalytic Chlorination and Oxidation of Cyclohexane and *n*-Hexane by 1 Using NaOCl/AcOH in MeCN[a]

entry	catalyst **1** (equiv)	AcOH (equiv)	substrate/equiv	*T* (°C)	$TON_{chlorination}$[b]	$TON_{oxidation}$[c]	TON_{total}[d]
1	1	100	cyclohexane/300	+25	34 ± 4	7 ± 1	41
2	0	100	cyclohexane/300	+25	14 ± 1	0	14
3	1	100	cyclohexane/300	−30	44 ± 3	9 ± 2	53
4	0	100	cyclohexane/300	−30	12 ± 2	0	12
5[e]	1	0	cyclohexane/300	−30	11 ± 2	6 ± 1	17
6[e]	0	0	cyclohexane/300	−30	4 ± 1	0	4
7	1	100	cyclohexane/100	−30	15 ± 2	2 ± 1	17
8	0	100	cyclohexane/100	−30	7 ± 2	0	7
9	1	100	*n*-hexane/300	−30	21 ± 3	8 ± 2	29
10	0	100	*n*-hexane/300	−30	4 ± 2	4 ± 2	8

[a]Reaction conditions: in typical reaction, 0.1 mL of a 0.5 M solution of AcOH (50 μmol) in MeCN and 32 μL of commercially available NaOCl 10 wt % (50 μmol) were added to a vigorously stirred MeCN solution (2.5 mL) containing compound **1** (0.5 μmol) and the substrate (50 or 150 μmol) under N_2. The mixture was stirred for 2 h. All reactions were run in duplicate. For more details, see the Experimental Section. [b]$TON_{chlorination}$ = turnover number of chlorinated products. Chlorocyclohexane for the oxidation of cyclohexane and a 1:1 mixture of 2-chlorohexane and 3-chlorohexane for *n*-hexane. [c]$TON_{oxidation}$ = turnover number of ketone products. Cyclohexanone for the oxidation of cyclohexane and a 1:1 mixture of 2-hexanone and 3-hexanone for *n*-hexane. [d]$TON_{total} = TON_{chlorination} + TON_{oxidation}$. [e]No acetic acid used.

DOI: 10.1021/jacs.6b07544
J. Am. Chem. Soc. 2016, 138, 12987−12996

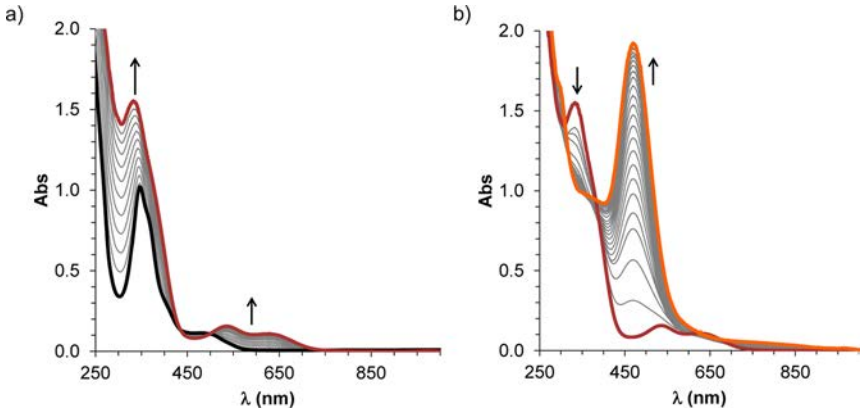

Figure 1. UV−vis absorption spectrum of **1** over time with a two-step addition of $Ca(OCl)_2$ at −30 °C in MeCN:H_2O 95:5 (v:v). (a) Step 1: 3 equiv ClO^- added to **1** (0.2 mM, black line) in MeCN in the presence of 5 equiv AcOH resulted in the formation of species **2** (red line). (b) Step 2: addition of a further 2 equiv ClO^- to **2** (red line) resulted in the formation of **3** (orange line). Equivalent results were obtained with the use of NaOCl.

addition, it was noted that with excess of AcOH the rate of formation of **3** was increased significantly.

The involvement of **2** and **3** in oxidation/chlorination of organic substrates was explored. Addition of organic substrates to a solution containing **2** had no effect on its UV−vis absorption spectrum; its characteristic absorption bands were not changed. In contrast, compound **3** reacted rapidly with alkanes, alkenes and sulfides. The spectroscopic characterization of these two species as well as the reactivity of **3** toward organic substrates will be discussed in the following sections.

Spectroscopic Characterization of 2. UV−vis absorption spectroelectrochemistry was used to gain information about the possible formulation of compound **2**. Thus, the spectroelectrochemical oxidation of **1** confirmed that the quasi-reversible redox wave ($I_{pa}/I_{pc} \sim 1$, $\Delta E \sim 70$ mV at a scan rate of 100 mV·s^{-1}) at $E_{1/2}$ 0.90 V vs Ag/AgCl (Figure S1), assigned to the Ni^{III}/Ni^{II} redox couple, was also fully reversible chemically. Electrochemical oxidation of **1** at 0.96 V in MeCN resulted in a change in its UV−vis absorption spectrum (λ_{max} 343 nm, ε = 4000 M^{-1} cm^{-1}) to that of a new species with an absorption band at λ_{max} 850 nm corresponding to $[Ni^{III}(L)]^+$ (**1**$^+$). The original absorption spectrum was fully recovered by subsequent reduction at 0.85 V (Figure S2). A similar result was obtained when water (50 equiv) and acetic acid (5 equiv) were present in the reaction medium. Remarkably, when the same experiment was performed in the presence of not only water and acetic acid but also NaCl (5 equiv), the resulting UV−vis spectrum matched well the UV−vis absorption features measured for **2** with weak absorption bands at λ_{max} ~550 and ~650 nm (Figure S3). This process could be reversed and the spectrochemical reduction of the formed species led to the recovery of the UV−vis spectrum of **1**. These data strongly support the assignment of **2** as $[Ni^{III}(L)(Cl)]$.

EPR analysis further supported this assignment. Thus, the EPR spectrum obtained from a flash frozen (77 K) solution, obtained by mixing **1** with 5 equiv AcOH and 3 equiv NaOCl in MeCN:H_2O 95:5 at −30 °C to form **2**, exhibited a signal characteristic of an axial $S = 1/2$ Ni^{III} species with $g_\perp = 2.23$ and $g_\parallel = 2.01$ which accounted for 65% of the nickel content (Figure S4).[30,31] The formulation of **2** as $[Ni^{III}(L)(Cl)]$ also fully agreed with the results obtained by cryospray ionization mass spectrometry (CSI-MS) at −30 °C. MS analysis of **2** revealed a simple spectrum with a major signal at m/z 318.0588, with a m/z value and isotopic pattern fully consistent with $[Ni^{III}(L)]^+$ in agreement with the +3 oxidation state of the nickel center determined by EPR spectroscopy (Figure S5). Finally, XAS analysis of **2** further supported the presence of a mononuclear nickel center coordinated to an apical chloride ligand (see XAS analyis below).

Kinetic Analysis of the Reaction of 3 with Organic Substrates. In contrast to species **2**, compound **3** reacted rapidly with different substrate types including alkanes, alkenes and sulfides. Under conditions of excess substrate, the decay of the absorption band of **3** (λ_{max} = 475 nm) was pseudo-first-order and fitted a monoexponential function from which observed rate constants (k_{obs}) were extracted (Figure S6, S8). Reaction rates were found to be the same within error under N_2 or air. The linear variation of k_{obs} with substrate concentration enabled calculation of second-order rate constants (k, Figure S7, S9, S10, and Table S1). Interestingly, **3** was kinetically competent in the reactions with alkanes bearing C−H bonds as strong as those of cyclohexane (bond dissociation energy, BDE, of 99.3 kcal·mol^{-1}), and a k = 0.0011 M^{-1} s^{-1} was determined for this substrate. Second order rate constants corrected by the number of C−H bonds in the substrate (k') for the reaction of **3** with various alkanes bearing C−H bonds with BDEs ranging from 75.5 to 99 kcal·mol^{-1} were determined. Log(k') values correlated linearly with the BDE values of the substrates, giving a slope of approximately −0.3 (Figure 2a). This correlation together with a KIE of 1.5 determined for the oxidation of 9,10-dihydroanthracne (Figure S11) indicates that **3** reacts with

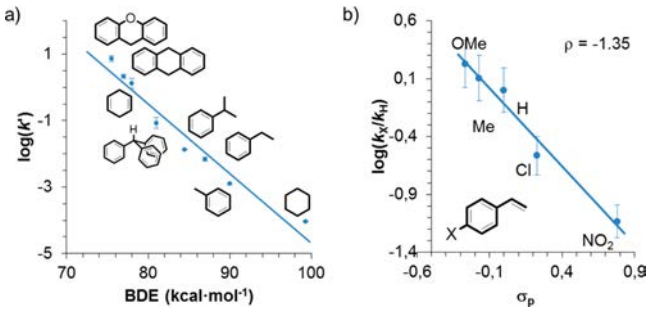

Figure 2. (a) Plot of log(k') against the C−H BDE for the reaction of **3** toward several alkanes in MeCN:H_2O 95:5 (v:v) at −30 °C. (b) Hammett plot for the reaction of **3** against *para*-substituted styrenes in MeCN:H_2O 95:5 (v:v) at −30 °C.

DOI: 10.1021/jacs.6b07544
J. Am. Chem. Soc. 2016, 138, 12987−12996

alkanes in a rate-determining hydrogen-atom abstraction step. Such behavior is consistent with that observed for the $[Ni^{III}(O•)(L)]$ species previously reported by us,[16] albeit the reactivity of **3** is substantially greater (Table 2). Analysis of the

Table 2. Second-Order Rate Constants (k) for the Oxidation of Alkanes, Alkenes and Thioethers by 3 or $[Ni^{III}(O•)(L)]$ in MeCN:H_2O 95:5 (v:v) at −30 °C

	k, M^{-1} s^{-1}	
	3	$[Ni^{III}(O•)(L)]$[16]
xanthene	14	2.93
9,10-dihydroantrhacene	8.5	2.62
1,4-cyclohexadiene	5.5	1.69
fluorene	–	0.28
styrene	4.1	0.45
cyclooctene	73	0.18
thioanisole	>100	0.56
1-octene	0.45	0.044

final oxidation products for the reaction of **3** with triphenylmethane indicated the formation of 1.4 TON of products consisting mainly of triphenylchloromethane together with small amounts of triphenylmethanol. Most of these products originated from a nickel-mediated process as ascertained by a blank experiment in the absence of nickel, which exclusively afforded 0.5 TON of chlorinated product (Table S2).

Compound **3** could also engage in oxygen-atom transfer (OAT) reactions. The rate of the reaction of **3** with 1-octene was 0.45 M^{-1} s^{-1}, which is an order of magnitude greater than that determined at the same temperature for $[Ni^{III}(O•)(L)]$. Similarly, reaction of **3** with other olefins, such as styrene or cyclooctene, were between 100 and 500 times faster than for $[Ni^{III}(O•)(L)]$ (Table 2). The electrophilic character of **3** was evidenced by the dependence of the reaction rates on the nature of the *para*-substitutent in a series of styrenes. A Hammett analysis of these reactions rates afforded a negative reaction constant (ρ) of −1.35 (Figure 2b), which indicates the electrophilic character of **3** in OAT reactions.[32] Remarkably, the reaction of **3** with thioanisole was too rapid to extract accurate kinetic data at −30 °C using our conventional UV−vis absorption spectrophotometer. Overall, the data indicate that **3** is a highly active oxidizing species with much greater reactivity than previously reported nickel systems[14,15,33] including the $[Ni^{III}(O•)(L)]$ species that bears the same ligand as **3**.[16] Similarly to the reaction with alkanes, analysis of the oxidized products after reaction of **3** with alkenes and sulfides proved that, indeed, this species mediated an oxygen-atom transfer reaction (Table S2). Thus, 1,2-epoxyoctane was formed in the reaction of 1-octene with **3** in 20% yield (with respect to nickel), while no epoxide product was detected in a blank experiment in the absence of nickel. In the case of thioanisole, the exclusive formation of 1.3 TON sulfoxide product was determined in the reaction with **3**, but only 0.3 TON were obtained in the corresponding blank experiment.

Spectroscopic Characterization of 3. Spectroscopic analysis provided insight into the chemical nature of **3**. Analysis of frozen solutions of **3** in MeCN (77 K) by Raman spectroscopy at 473 nm showed resonance enhancement of two bands, which tracked the appearance and disappearance of the visible absorption of **3** (λ_{max} 475 nm), at 703 and 443 cm^{-1} (Figure 3 and S12). ^{18}O-labeling using $Na^{18}OCl$ resulted in a downshift to 679 and 435 cm^{-1}. By comparison to previously

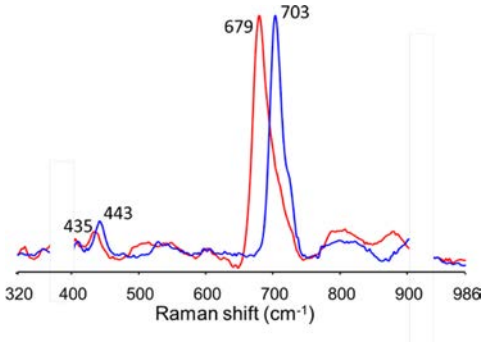

Figure 3. Resonance Raman spectra (λ_{exc} 473 nm) in frozen MeCN:H_2O 95:5 (v:v) (77 K) of **3** formed after reaction of **1** (0.48 mM) in MeCN:H_2O 95:5 (v:v) at −30 °C with 5 equiv AcOH and 5 equiv NaOCl (blue line) or 5 equiv $Na^{18}OCl$ (red line). Artifacts due to imperfect solvent subtraction were masked with white boxes.

reported Fe-OCl systems[34] these bands are assigned tentatively to O−Cl and Ni−O stretching modes, respectively. The observed shift of 24 cm^{-1} for the 703 cm^{-1} band is in good agreement with the calculated shift ($\Delta[^{18}O] = -29$ cm^{-1}) using the two-atom approximation for an O−Cl stretching mode, while the shift of 8 cm^{-1} for the 443 cm^{-1} indicates that this vibration is associated not only to the oxygen atom but also to ligand modes (expected shift for a Ni−O bond is $\Delta[^{18}O] = -20$ cm^{-1}). Importantly, both the resonantly enhanced bands at 703 and 443 cm^{-1} and the absorption band at 475 nm disappeared upon addition of 50 equiv 1-octene (Figure S13).

EPR analysis of a solution of **3** showed an EPR signal with g values $g_\perp$ = 2.23 and $g_\parallel$ = 2.01 assigned to compound **2**. However, this signal accounted for less than 30% of the overall nickel content, which indicated that compound **3** is EPR silent. CSI-MS analysis of **3** at −30 °C revealed a clean spectrum dominated by a peak at m/z 334.0585, which corresponds to $[Ni(O)(L)]^+$ (Figure 4). When compound **3** was generated using $Na^{18}OCl$, a shift of two mass units of the latter signal to m/z 336.0592 was observed (Figure 4 and S14). Collision induced dissociation (CID) experiments conducted over these signals at a collision energy of 20−25 eV afforded in both cases a new signal at m/z 317.05 indicative of the loss of an $OH/^{18}OH$ radical (Figure S14 and S16). The fact that the signal at m/z 334.06 disappeared upon addition of substrate (1-octene) and that the oxygen atom is lost in CID experiments suggests that it does not originate from incorporation of oxygen into the ligand architecture, e.g., hydroxylation of methylenic C−H bonds in ligand L.

X-ray absorption spectroscopy (XAS) at the metal K-edge was applied to probe the electronic and geometric structure of the nickel center in **3**.[35−40] For comparison purposes, XAS on compound **2**, assigned as $[Ni^{III}(L)(Cl)]$ (see above), was also performed. Figure 5 (left) shows an overlay of the XANES region of compounds **2** and **3** and the previously reported oxyl-Ni^{III} radical analog $[Ni^{III}(O•)(L)]$.[16]

The spectra of compounds **2** and **3** have similar rising edge profiles when compared to that of $[Ni^{III}(O•)(L)]$, indicating a similar square bipyramidal coordination geometry at the metal center.[39,40] However, for **2** the rising edge is 0.4 eV lower in energy than $[Ni^{III}(O•)(L)]$, with a half-height edge energy of 8343.0 eV, indicating a more electron rich metal center with a lower effective charge. On the other hand a shift to higher energy is observed for compound **3** with a rising edge at ∼8344.0 eV (Figure S17). A similar trend is also observed in

DOI: 10.1021/jacs.6b07544
J. Am. Chem. Soc. 2016, 138, 12987−12996

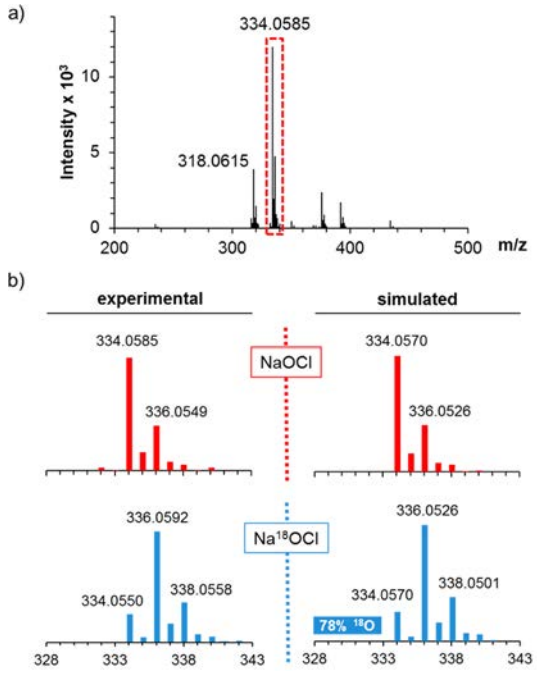

Figure 4. (a) CSI-MS of **3** at −30 °C formed by reaction of **1** with 5 equiv NaOCl in the presence of 5 equiv AcOH in MeCN:H_2O 95:5 (v/v) at −30 °C (equivalent spectra were obtained using 30 equiv NaOCl and 20 equiv AcOH). The spectrum shows major peaks at m/z 318.0615 and m/z 334.0585 corresponding to $[Ni(L)]^+$ and $[Ni(O)(L)]^+$, respectively. (b) Experimental and simulated pattern for the peak at m/z 334.06 formed with NaOCl (top) or partially ^{18}O-labeled NaOCl (bottom).

the pre-edges of **2** and **3**, associated with 1s → 3d transitions, where the pre-edge of **2** at 8333.15 eV indicates a more "effectively" reduced metal center and a weaker ligand field than in **3**, which has a pre-edge at 8333.54 similar in energy to that reported for $[Ni^{III}(O\bullet)(L)]$ at 8333.65 eV. The energies derived from the pre-edge analysis for the series are consistent with the presence of Ni^{III} centers, having pre-edges ∼1 eV higher in energy than those reported for Ni^{II}.[16,39,41] Additionally, a lower rising edge for **2** is consistent with the presence of the more electron donating Cl^- ligand in the coordination sphere of **2** versus oxygen-derived ligands in **3** and $[Ni^{III}(O\bullet)(L)]$. This is supported by EXAFS analysis of **2**, which confirms the presence of chloride in the coordination sphere of the Ni center (Figure 5 center, Table 3 and Table S3). In addition to the chloride, 4 N/O ligands are present as well as single and

Table 3. Comparison of EXAFS Determined and Density Functional Theory Derived Bond Metrics for Compounds 2 and 3[a]

	EXAFS					DFT
model	path[b]	r (Å)	σ^2 (×10³ Å²)	%R	χ^2_v	r (Å)
compound **2**	3 N/O	1.86(1)	2(1)	6.3	9.4	1.86
	1 N/O	2.07(3)	2(1)			1.93
	1 Cl	2.50(4)	7(5)			2.40
	8 C	2.72(1)	8(4)			2.76
compound **3**	5 N/O	1.89(1)	3(1)	7.5	3.9	1.93
	8 C	2.76(2)	5(2)			2.77

[a]Full scattering paths outlined in Tables S3–S4. [b]Chemical intuition was used to differentiate between N/C/O paths.

multiple scattering paths consistent with the presence of the macrocyclic ligand. Compound **3** was also characterized structurally using EXAFS analysis and shows a Ni center surrounded by a first coordination shell of 5 N/O ligands at 1.89 Å, accompanied by single and multiple scattering C/N paths at 2.77 and 2.96 Å (Figure 5 right, Table 3 and Table S4). This is consistent with a metal center surrounded by the macrocyclic ring of the ligand and coordinated by the 4 nitrogen atoms of the macrocycle in the equatorial plane with an additional axial N/O ligand. The EXAFS determined structures and bond distances for **2** and **3** are in agreement with the computational models proposed below (Table 3).

The possibility of dimerization to form Ni–X–Ni complexes was also explored using existing procedures including phase comparison and curve fitting.[37,42] Phase comparison revealed that the region of 3.4 to 3.8 Å in r-space, where Ni–Ni scattering paths should occur, is similar for all three complexes, while curve fitting of both **2** and **3** shows that inclusion of a Ni–Ni scattering path does not significantly improve the goodness of the fit, contributes to "overfitting" based on the χ^2_v parameter and results in unreasonable values for the disorder parameters (Figure S18). Therefore, EXAFS analysis does not support formation of Ni–X–Ni dimers. Lastly, previous reports have shown that in a series of Ni complexes with similar coordination environments a change of 0.7 eV in the rising edge is consistent with a +1 change in formal oxidation state.[39,43] Therefore, a change of ∼0.5 eV in the rising edge of **3** versus $[Ni^{III}(O\bullet)(L)]$ might indicate partial oxidation of the metal center and/or participation of the ligand sphere in the redox process.[44]

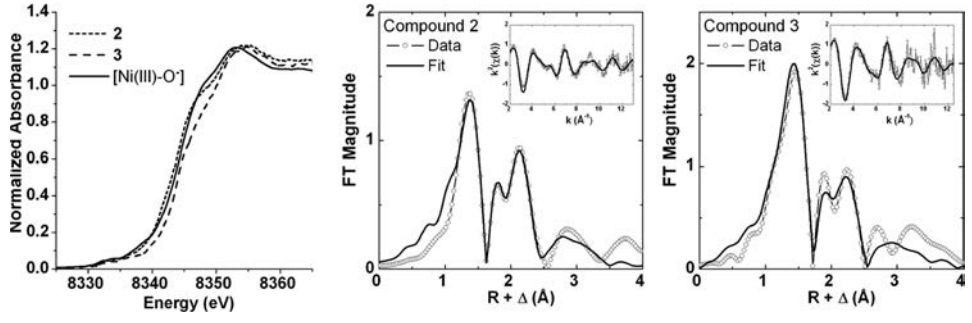

Figure 5. (Left) Comparison of the Ni K-edge XANES region for compounds **2**, **3** and $[Ni^{III}(O\bullet)(L)]$; (center) Fourier-transformed EXAFS spectra of **2** (no phase correction, FT, window = 2–13 $Å^{-1}$); (right) Fourier-transformed EXAFS spectra of **3** (no phase correction, FT, window = 2–12.5 $Å^{-1}$); Insets: k^2-weighted unfiltered EXAFS spectra.

DOI: 10.1021/jacs.6b07544
J. Am. Chem. Soc. 2016, 138, 12987–12996

Theoretical Models for Compound 3 and Correlation with Experiments. The nature of compound **3** was also explored by theoretical models and correlations were made to experimental data. The following evidences were taken into account: (i) resonance Raman indicates the presence of a Ni-OCl species in solution; (ii) CSI-MS experiments confirm the presence of a $[Ni(O)L]^+$ core; (iii) EPR spectroscopic data indicate that a $S = 1/2$ Ni^{III} species (**2**) is converted to compound **3**; (iv) XAS analysis is consistent with a monomeric high-valent Ni center surrounded by 5 N/O ligands in what is best described as a square pyramidal environment; (v) XANES analysis of the rising edge indicates a more oxidized metal center in **3** than in previously reported $[Ni^{III}(O\bullet)(L)]$,[16] albeit by only ~0.5 eV rather than 0.7 eV which would be expected for a formal +1 change in oxidation.

With all this information in hand, geometry optimizations of the nickel-OCl compound $[Ni(OCl)(L)]^+$ (**A**) in several possible spin states (S = 0, 1 or 2) were performed. The triplet multiplicity (^{3}**A**) was found to be the ground spin state, being 7 kcal·mol^{-1} more stable than the singlet (^{0}**A**). The model consists of a nickel center in a distorted square pyramidal geometry with the OCl ligand bound at the apical

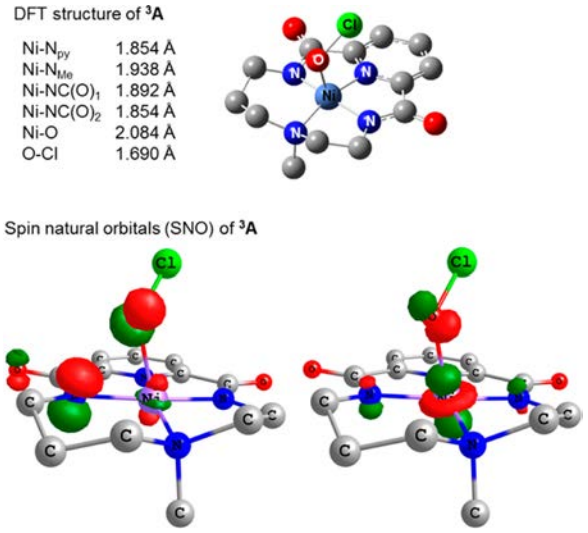

Figure 6. Top: DFT computed structure of ^{3}**A**. Bottom: Spin-natural orbitals (SNO) of ^{3}**A** (isovalue = 0.144).

position (Figure 6). Calculation of the free energy difference of ^{3}**A** relative to the starting reagents indicated that its formation is exergonic (ΔG = −12.8 kcal·mol^{-1}) (Figure 7).[45] We also considered the involvement of the corresponding 1e$^-$ reduced compound $[Ni(OCl)(L)]$ (**B**). However, formation of the most stable spin state of this species (^{2}**B**) from **1** was endergonic (ΔG = +5.3 kcal·mol^{-1}), and thus, the 1e$^-$ oxidized ^{3}**A** species is preferred on the basis of theoretical results (Figure 7, see Supporting Information for further details).

The free energy cost to cleave the O−Cl bond in ^{3}**A** was also determined. Heterolytic O−Cl cleavage to liberate Cl^- would lead to $[Ni(O)(L)]^{2+}$ in which the nickel center would be found in a formal +6 oxidation state, which is highly unlikely and thus, it was discarded. Instead, homolytic O−Cl cleavage would afford $[Ni(O)(L)]^+$ (**C**). However, the computed free energy for the conversion of ^{3}**A** to the most stable quadruplet **C** species (^{4}**C**) revealed a highly endergonic process (ΔG = +43.1

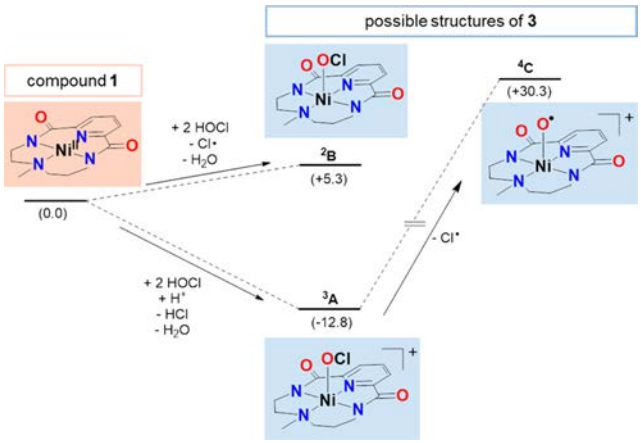

Figure 7. Possible formulations of compound **3** (**A**, **B** or **C**) derived from the reaction of **1** with NaOCl in the presence of AcOH. Free energies are given in parentheses in kcal·mol^{-1} at −30 °C in MeCN.

kcal·mol^{-1}) (Figure 7). Thus, O−Cl cleavage to form a nickel-oxido/oxyl species is disfavored on a thermodynamic basis, thus reinforcing the assignment of compound **3** as $[Ni(OCl)(L)]^+$ (^{3}**A**).

The proposed coordination geometry and bond distances of the ^{3}**A** theoretical model (Figure 6) are consistent with the experimentally derived geometry and bond metrics from XAS analysis (Table 3). Similarly, compound **2**, which is assigned as $[Ni^{III}(L)(Cl)]^+$ on the basis of several spectroscopic techniques (see above), was also modeled. A similar square pyramidal geometry to **3**, but having the ClO^- apical ligand replaced by Cl^-, and a $S = 1/2$ spin state was found to be the most stable configuration for **2** (Figure S21). This geometry was found to be almost isoenergetic with the starting complex **1**. Again, calculated bond distances for **2** agree, within error, with the experimentally derived bond distances (Table 3).

Additionally, TD-DFT calculated pre-edge XAS energies follow the observed experimental trends with **2** having the lowest energy calculated pre-edge, followed by **3** (~0.4 eV higher) and $[Ni^{III}(O\bullet)(L)]$ (~0.7 eV higher) (Figure S19a). The calculated pre-edge intensities are also consistent with experiment, with **2** and **3** having lower intensities than $[Ni^{III}(O\bullet)(L)]$ (Figure S19b). In all cases the pre-edges are predicted to have three metal based transitions (Figure S20). Difference density maps[46,47] of the pre-edge transitions highlight a core excitation to a singly occupied dz^2 orbital, which dominates the pre-edge intensities, followed by two transitions to the empty dx^2-y^2 orbital. The placement of the unpaired electron in the dz^2 orbital for **2** is also consistent with the EPR profile which suggests that the dz^2 orbital is the main contributor to the ground state.[15,48]

Furthermore, simulation of the Raman spectrum of ^{3}**A** (λ_{exc} at 473 cm^{-1}) predicts an intense O−Cl bond stretching at 701 cm^{-1} and a weaker Ni−O vibration at 406 cm^{-1} (Figure S22). This theoretically computed spectrum is in full agreement with the experimental data and the resonance enhanced bands at 703 and 443 cm^{-1}, for which ^{18}O-shifts to 679 and 435 cm^{-1} were observed. The small shift of the latter upon labeling ($\Delta[^{18}O]$ = −8 cm^{-1}) is due to the mixing of the Ni−O mode with ligand-based modes, as observed theoretically.

To better understand the effective oxidation state of the metal center and the electronic structure of ^{3}**A**, the spin populations around the metal center were investigated. Figure 6

DOI: 10.1021/jacs.6b07544
J. Am. Chem. Soc. 2016, 138, 12987−12996

shows the spin natural orbitals (SNO) for the two unpaired electrons in **3**. The figure illustrates a large extent of delocalization of spin between a proximal nitrogen (N_{ligand}), the Ni center and the OCl moiety. In fact the first SNO is composed primarily of N_{ligand} (~43%) and OCl π^* (~23%) character with only a minimal contribution from Ni (~8%) suggesting a ligand centered unpaired electron. The second SNO is composed mainly of Ni d_{z2} (62%) with 26% OCl π^* character. Mulliken spin population analysis further supports the location of the unpaired electrons (ρ(Ni) = 0.75, ρ(OCl) = 0.42 and $\rho(N_{ligand})$ = 0.55), which would suggest a Ni^{III} oxidation state at the metal center. This model is consistent with the XAS data, which shows a slightly more oxidized metal center in **3** than in the previously reported $[Ni^{III}(O\bullet)(L)]$ but not by a full formal oxidation unit. Moreover, the presence of an unpaired electron in an orbital with OCl π^* character might serve to activate the O−Cl bond and increase the reactivity of the complex. This would be consistent with the cleavage of the O−Cl bond in **3** under the MS conditions, which leads to the exclusive detection of $[Ni(O)(L)]^+$, in which the O−Cl bond of ^{3}**A** is homolytically broken, under the experimental conditions. Lastly, ligand radical character in the 2,6-pyridinedicarboxamidate ligand backbone (L) is not unexpected as pyridinecarboxamidate units may have noninnocent behavior in the presence of high valent metal centers.[49−51]

Overall, the computed structure for $[Ni(OCl)(L)]^+$ (^{3}**A**) is in agreement with the spectroscopic data obtained for **3** by EPR, rRaman, MS and XAS techniques. Despite the fact that the formal oxidation state of the nickel center in this compound is +4, our analyses indicate that its effective oxidation state is +3, with $1e^-$ oxidation distributed over the ligands.

■ CONCLUSIONS

In summary, the bis(amidate) macrocyclic ligand (L) acts as an excellent platform to support a high-valent nickel-hypochlorite species that has been trapped by reaction of the nickel(II) precursor with sodium (or calcium) hypochlorite in the presence of acetic acid at low temperatures. This compound has been characterized by UV−vis absorption and rRaman spectroscopy, XAS and cryospray mass analyses. DFT calculations indicate that this trapped species is best formulated as a formal nickel(IV) species with the formula $[Ni(OCl)(L)]^+$. Most interestingly, this species behaves as a strong oxidizing agent both toward alkanes and alkenes with reaction rates that surpass those previously reported for related nickel−oxygen species. Oxidation of C−H bonds as strong as those of cyclohexane has been achieved and the catalytic cyclohexane chlorination/oxidation has also been successfully performed. Overall, the involvement of high-valent nickel-OCl species in the catalytic cycle of nickel-catalyzed oxidation/chlorination reactions of alkanes and alkenes seems to be highly plausible. Current efforts in our group are devoted to study the influence of the electronic properties of the ligand on the high-valent nickel center and the use of ligand L in combination with other metals relevant to oxidation catalysis.

■ EXPERIMENTAL SECTION

Materials and Methods. Reagents and solvents used were commercially available and purchased from Panreac, Scharlau and Aldrich. Preparation and handling of air-sensitive materials were carried out in a N_2 drybox (MBraun ULK 1000) with O_2 and H_2O concentrations <1 ppm. $[Ni^{II}(L)]$ (**1**) was synthesized as previously reported.[16]

Mass spectra were performed by electrospray ionization in a high-resolution mass spectrometer Bruker micrOTOF QII (Q-TOF) with a quadrupole analyzer with positive and negative ionization modes. UV−vis absorption spectra were performed by a diode array spectrophotometer Agilent Cary 60 and low temperature control was maintained with a cryostat from Unisoku Scientific Instruments. GC analyses were carried out on an Agilent 7820A gas chromatograph (HP5 column, 30m) with a flame ionization detector. Raman spectra were recorded in 5 mm diameter NMR tubes at 77 K in a liquid nitrogen filled quartz Dewar. Spectra were collected in 180° backscattering mode with excitation at 473 nm (Cobolt Lasers, 50 mW) with a dichroic mirror (Semrock) at 45° to the optical collection axis and a 25 mm diameter (75 mm focal length) planoconvex lens to focus the excitation beam and collect and collimate Raman scattering, which was passed through the dichroic and a long pass cut off filter (Semrock) before being focused at the entrance slits of a Shamrock 303i spectrograph with a 1200 l/mm grating blazed at 500 nm and a iDUS-420-BUEX2-DD CCD detector (Andor Technology). Spectral calibration was carried out using a 1:1 v/v mixture of MeCN and toluene. Spectra were processed using Andor Solis and Spectrum 10 (PerkinElmer). EPR spectra were recorded with an EMX nano spectrometer (bruker instruments). Reactions were monitored by UV−vis spectroscopy and 300 μL aliquots were frozen at 77 K. All measurements were performed at 110 K. Spectra were recorded at 9.63 GHz, with a microwave power of 0.31 mW and power attenuation 25.00 dB or microwave power of 3.1 mW and power attenuation 15.00 dB. Modulation amplitude was 4.00 gauss and modulation frequency 100 kHz. Each spectrum was collected as an average of three scans. Sample tubes were filled higher than the cavity dimension to guarantee an equally filled cavity for all measured samples. Simulations of EPR spectra was carried out using EasySpin software.[52] Cyclic voltammetry was performed using a model CHI760C Electrochemical Workstation (CH Instruments) in MeCN (0.1 M $TBAPF_6$) with a 3 mm diameter Teflon-shrouded glassy carbon working electrode (CH Instruments), a Pt wire auxiliary electrode, and an Ag/AgCl reference electrode. Potentials are reported ±10 mV. Spectroelectrochemistry was performed using an OTTLE cell[53] (a liquid IR cell modified with Infrasil windows and a platinum mesh working and counter electrode and a Ag wire reference electrode) mounted in a Specord600 UV−vis absorption spectrometer. Bulk electrolysis was carried out in a divided cell (ceramic frit separation) with a 5 mM soluction of **1** in MeCN containing 500 mM water, 25 mM acetic acid and 25 mM NaCl, with a carbon mesh working electrode, platinum mesh counter electrode and Ag/AgCl working electrode. Electrolysis was carried out at 0.9 V and conversion to Ni^{III} monitored by ex situ UV−vis absorption and EPR spectroscopy.

A 1 mM sample of **3** (prepared by reaction of **1** with 5 equiv of AcOH and 5 equiv of NaOCl in CH_3CN at −30 °C) was loaded into a 1 mm holder with Kapton tape windows and stored at liquid nitrogen temperatures until run. Data collection was carried out in fluorescence mode at the ESRF synchrotron beamline Spline-BM25A equipped with a Si(111) double crystal monochromator, an Optistat CF cryostat from Oxford Instruments and a 13 channel element detector. Samples were run at 90 K under anaerobic conditions using a Z-1 filter to reduce backscattering. A 2 mM sample of **2** (prepared by reaction of **1** with 5 equiv of AcOH and 3 equiv of NaOCl in CH_3CN at −30 °C) was similarly loaded into a 1 mm holder with Kapton tape windows and stored at liquid nitrogen temperatures until run at the SAMBA beamline from SOLEIL equipped with a Si(220) double crystal monochromator, a liquid helium cryostat (25 K) and a 36 channel element detector. Energy calibration was performed using the first inflection point of the X-ray absorption near edge structure (XANES) spectrum of nickel foil (E_{cal} of 8331.6 eV). Data reduction and normalization was carried out with the Athena software package using the AUTOBK algorithm. A R_{bkg} of 1.1 Å and a spline between a k of 1 and 13.5 $Å^{-1}$ was used for EXAFS extraction. The follow up EXAFS analysis was carried out with the Artemis software program using the IFEFFIT engine and FEFF6 code.[54−56] The k^2-weighted data was fit in r-space between 1.0 and 4.0 Å without phase correction having a k-range of 2.0−12.5 $Å^{-1}$ for **3** and a k-range of 2.0−13 $Å^{-1}$ for **2**, as well

DOI: 10.1021/jacs.6b07544
J. Am. Chem. Soc. 2016, 138, 12987−12996

as using a Hanning window (dk 2). Scattering paths were fit in terms of Δr_{eff} and σ^2, having a global ΔE_0 and a S_0 value set to 0.9 for all paths. Coordination number was explored using single scattering shells with fixed degeneracies which were then varied in integral steps.[57−59] To assess the goodness of fit from different models both the R_{factor} (% R) and the reduced χ^2 (χ^2_v) were minimized. While the R_{factor} is generally expected to decrease with the number of adjustable parameters, χ^2_v may eventually increase, indicating the model is overfitting the data.[60] Lastly, in order to extract intensities and energy positions the XANES spectra was fit using pseudo-Voigt functions while the edge jump was modeled via a cumulative Gaussian−Lorentzian sum function.

*Catalytic Experiments at −30 °C Using **1** as Catalyst and AcOH/NaOCl as Oxidant.* In a typical reaction, 0.1 mL of a 0.5 M solution of AcOH (50 μmol) in MeCN and 32 μL of commercially available NaOCl 10% (50 μmol) were added at −30 °C to a vigorously stirred MeCN solution (2.5 mL) containing the nickel catalyst (0.5 μmol) and the substrate (50 or 150 μmol) for 2 h under N_2. The final concentrations of reagents were 0.2 mM nickel catalyst, 20 mM AcOH, 20 mM NaOCl, and 20 or 60 mM substrate. $Na_2S_2O_3$ (500 μmols) dissolved in MeCN:H_2O 1:1 was added at this point to destroy unreacted NaOCl and biphenyl was added as internal standard. Nickel complex and the small quantities of water were removed by passing the solution through a short path of silica and $MgSO_4$. The products were then eluted with ethyl acetate (2 mL) and the resulting mixture was analyzed by GC-FID. The organic products were identified by comparison with authentic compounds and quantified using a calibration curve.

*Generation of **2**.* In a typical experiment, 2.5 mL of a 0.2 mM solution of **1** in MeCN were placed in a 1 cm path-length cuvette (0.5 μmol of **1**). The quartz cell was placed in the Unisoku cryostat of the UV−vis absorption spectrophotometer and cooled down to −30 °C. After reaching thermal equilibrium an UV−vis absorption spectrum of the starting complex was recorded. Then, 25 μL of a 0.1 M solution of AcOH in MeCN were added (5 equiv) followed by 30 μL of a 0.05 M solution of NaOCl in MeCN:water (4:1) (3 equiv). The formation of two equally intense bands at λ_{max} = 550 and 650 nm ($\varepsilon \sim 500$ M^{-1} cm^{-1}) was observed. **2** reached its maximum within 200 s.

*Generation of **3**.* In a typical experiment, 2.5 mL of a 0.2 mM solution of **1** in MeCN were placed in a 1 cm path-length cuvette (0.5 μmol of **1**). The quartz cell was placed in the Unisoku cryostat of the UV−vis absorption spectrophotometer and cooled down to −30 °C. After reaching thermal equilibrium an UV−vis absorption spectrum of the starting complex was recorded. Then, 25 μL of a 0.1 M solution of AcOH in MeCN were added (5 equiv) followed by 50 μL of a 0.05 M solution of NaOCl in MeCN:water (4:1) (5 equiv). The formation of a band at λ_{max} = 475 nm (ε = 8000 M^{-1} cm^{-1}) was observed. The formation of **3** reached its maximum within 400 s.

*Kinetic Analyses of the Reaction of **3** with Organic Substrates.* Once **3** was fully formed (see above) the appropriate amount of substrate dissolved in 100 μL MeCN was directly injected into the UV−vis cuvette. Substrate concentration was always in pseudo-first order excess with respect to **3** and reaction kinetics were monitored by following the decay of its absorption band at 475 nm. In all cases, a satisfactory fit was obtained for the disappearance of **3** using a single exponential, from which observed rate constants (k_{obs}) were extracted. The linear variation of k_{obs} with substrate concentration enabled the calculation of the second-order rate constants (k). In the particular case of toluene and cyclohexane reactions were extremely slow and k values were determined from two replicates at a single substrate concentration (0.36 M). The kinetic isotope effect (KIE) was obtained by dividing the reaction rates obtained for the reaction of **3** with 9,10-dihydroantrhacene and 9,10-dihydroanthracene-d_4.

*Preparation of ^{18}O-Labeled **3**.* ^{18}O-labeled **3** was prepared following a similar procedure to that described above for **3** but using $Na^{18}OCl$ instead of $Na^{16}OCl$. In turn, $Na^{18}OCl$ was obtained by stirring 10 μL of NaOCl in 30 μL $H_2{}^{18}O$ for 2 h at room temperature, following a reported synthetic procedure.[28]

Product Analyses. Once the formation of **3** reached its maximum, 150 μL of a MeCN solution containing the required amount of the desired substrate were added in the UV−vis cuvette. The decay of the band at 475 nm was monitored. After complete disappearance of the chromophore, reactions were quenched by the addition of 10 equiv $Na_2S_2O_3$ dissolved in MeCN:H_2O 1:1 with respect to initial NaOCl and biphenyl was added as internal standard. Nickel complex and the small quantities of water were removed by passing the solution through a short path of silica and $MgSO_4$. The products were then eluted with ethyl acetate (2 mL) and the resulting mixture was analyzed by GC-FID. The organic products were identified by comparison with authentic compounds and quantified using a calibration curve.

Computational Details. Density functional theory (DFT) calculations were performed with the Gaussian09 program package.[61] X-ray diffraction structure of [Ni^{II}(L)] (**1**) has been chosen as starting point for geometry optimizations with the B3LYP exchange-correlation functional[62,63] and the TZVP basis set.[64] Nickel species were considered in all possible spin states without symmetry constraints. The MeCN solvation effects were included in geometry optimizations through the SMD polarizable continuum model.[65] Dispersion effects were included in geometry optimizations with the Grimme's D_3 correction with Becke-Johnson damping function.[66]

Analytical Hessian calculations were performed at the same level of theory to (i) evaluate enthalpy and entropy corrections at 243.15 K and (ii) establish the nature of stationary points in solvent-phase, where minima have no imaginary frequencies. Nonresonant Raman spectral intensities of intermediate **3** were simulated at 77 K and with a laser excitation of 473 nm employing the GaussSum 3.0.[67] The shift in the O−Cl bond stretching frequency upon ^{18}O-labeling was determined modeling the Raman spectrum with an ^{18}O−Cl bond.

Mulliken spin densities and spin natural orbitals (SNO) were computed to rationalize the electronic structure of all nickel based intermediates. The atomic orbital contribution to the SNOs was evaluated with the Multiwfn 3.3.6 software.[68]

Gibbs energies (G) were evaluated with the following equation:

$$G = E_{TZVP}(SMD + D_3) + G_{corr} \quad (1)$$

where $E_{TZVP}(SMD + D_3)$ is obtained through single point calculations with the TZVP basis set on equilibrium geometries, including the solvation and dispersion effects, and G_{corr} is the thermal correction obtained from a thermo-statistical analysis at the B3LYP/SMD level.

The dissociation free energy change ($\Delta G°$) between an acid (AH) and its conjugate base (A^-) in solvent phase was calculated using the following equations:

$$\Delta G = G(A_s^-) + G(H_s^+) - G(AH_s) + \Delta G^* \quad (2)$$

$$G(H_s^+) = G(H_{gas}^+) + \Delta G_{solv}^{H+} \quad (3)$$

where $G(AH_s)$ and $G(A_s^-)$ are the standard free energies of the acid and its conjugate base, respectively. In MeCN solution, the free energy of the proton $G(H_s^+)$ is obtained from the solvation free energy of a proton in MeCN (ΔG_{solv}^{H+} = −260.2 kcal·mol^{-1})[65] and its gas-phase free energy ($G(H_{gas}^+)$ = −6.3 kcal·mol^{-1}).[66] In the free energy balance the standard state thermodynamic correction associated with the conversion from a standard-state of 1 M in the solvent phase and 1 atm in gas phase to 1 M in both phases was considered. Its value is 1.54 kcal·mol^{-1} at 243.15 K.

The ORCA software package 3.0.1[69] was used to calculate XAS pre-edges using previously reported procedures.[46,70,71] Spin unrestricted, time-dependent calculations for XAS spectra were carried out using the Tamm−Dancoff[72,73] approximation and up to 13 nonrelativistic roots were calculated to ensure saturation of transitions spanning the pre-edge and near edge region of Ni XAS K-edge spectra. The B3LYP functional was employed along with a TZVP[74] basis set and a conductor like screening model (COSMO[75]) using acetonitrile as solvent.

DOI: 10.1021/jacs.6b07544
J. Am. Chem. Soc. 2016, 138, 12987−12996

■ ASSOCIATED CONTENT

Supporting Information

The Supporting Information is available free of charge on the ACS Publications website at DOI: 10.1021/jacs.6b07544.

Cyclic voltammetry and spectroelectrochemistry of **1**, EPR spectroscopy of **2**, CSI-MS analysis of **2** and **3**, resonance Raman, XAS analysis of **2** and **3**, kinetic analysis of the reaction of **3** with substrates, and DFT calculations including Raman simulations, thermodynamic data, spin density analysis and Cartesian coordinates of optimized geometries. (PDF)

■ AUTHOR INFORMATION

Corresponding Author

*anna.company@udg.edu

Notes

The authors declare no competing financial interest.

■ ACKNOWLEDGMENTS

Financial support for this work was provided by the European Commission (FP7-PEOPLE-2011-CIG-303522 to A.C.). The MINECO of Spain is acknowledged for a Ramón y Cajal contract to A.C. and for CTQ2013-43012-P to A.C. F. A.-P. thanks Universitat de Girona for a predoctoral grant. W.R.B. acknowledges the European Research Council (ERC-2011-StG-279549) and the Ministry of Education, Culture and Science (Gravity program 024.001.035). X-ray absorption data was collected on beamline BM25-Spline at the European Synchrotron Radiation Facility (ESRF), Grenoble, France. We are grateful to the Local Contact at ESRF, Dr. Eduardo Salas Colera, for providing assistance in using the beamline. XAS data was also collected at the SOLEIL French National Synchrotron Facility, Saint-Aubin, France, where we would like to thank Dr. Landrot Gautier for his assistance. This work was performed (partially) in the framework of COST action CM1305 "Explicit Control Over Spin-states in Technology and Biochemistry (ECOSTBio)" (STSM reference: ECOST-STSM-CM1305-32120). The authors thank Dr. Carole Duboc for fruitful discussions on analysis and interpretation of EPR data.

■ REFERENCES

(1) Costas, M.; Mehn, M. P.; Jensen, M. P.; Que, L. *Chem. Rev.* **2004**, *104*, 939−986.
(2) Denisov, I. G.; Makris, T. M.; Sligar, S. G.; Schlichting, I. *Chem. Rev.* **2005**, *105*, 2253−2278.
(3) Yano, J.; Yachandra, V. *Chem. Rev.* **2014**, *114*, 4175−4205.
(4) Bertini, I.; Gray, H. B.; Stiefel, E. I.; Valentine, J. S. *Biological Inorganic Chemistry. Structure & Reactivity*; University Science Books: Sausalito, CA, 2007.
(5) Oloo, W. N.; Que, L. *Acc. Chem. Res.* **2015**, *48*, 2612−2621.
(6) Kleespies, S. T.; Oloo, W. N.; Mukherjee, A.; Que, L. *Inorg. Chem.* **2015**, *54*, 5053−5064.
(7) Chen, Z.; Yin, G. *Chem. Soc. Rev.* **2015**, *44*, 1083−1100.
(8) Gray, H. B.; Hare, C. R. *Inorg. Chem.* **1962**, *1*, 363−368.
(9) O'Halloran, K. P.; Zhao, C.; Ando, N. S.; Schultz, A. J.; Koetzle, T. F.; Piccoli, P. M. B.; Hedman, B.; Hodgson, K. O.; Bobyr, E.; Kirk, M. L.; Knottenbelt, S.; Depperman, E. C.; Stein, B.; Anderson, T. M.; Cao, R.; Geletii, Y. V.; Hardcastle, K. I.; Musaev, D. G.; Neiwert, W. A.; Fang, X.; Morokuma, K.; Wu, S.; Kögerler, P.; Hill, C. L. *Inorg. Chem.* **2012**, *51*, 7025−7031.
(10) Hong, S.; Pfaff, F. F.; Kwon, E.; Wang, Y.; Seo, M.-S.; Bill, E.; Ray, K.; Nam, W. *Angew. Chem., Int. Ed.* **2014**, *53*, 10403−10407.
(11) Pfaff, F. F.; Kundu, S.; Risch, M.; Pandian, S.; Heims, F.; Pryjomska-Ray, I.; Haack, P.; Metzinger, R.; Bill, E.; Dau, H.; Comba, P.; Ray, K. *Angew. Chem., Int. Ed.* **2011**, *50*, 1711−1715.
(12) Lacy, D. C.; Park, Y. J.; Ziller, J. W.; Yano, J.; Borovik, A. S. *J. Am. Chem. Soc.* **2012**, *134*, 17526−17535.
(13) Donoghue, P. J.; Tehranchi, J.; Cramer, C. J.; Sarangi, R.; Solomon, E. I.; Tolman, W. B. *J. Am. Chem. Soc.* **2011**, *133*, 17602−17605.
(14) Pfaff, F. F.; Heims, F.; Kundu, S.; Mebs, S.; Ray, K. *Chem. Commun.* **2012**, *48*, 3730−3732.
(15) Pirovano, P.; Farquhar, E. R.; Swart, M.; Fitzpatrick, A. J.; Morgan, G. G.; McDonald, A. R. *Chem. - Eur. J.* **2015**, *21*, 3785−3790.
(16) Corona, T.; Pfaff, F. F.; Acuña-Parés, F.; Draksharapu, A.; Whiteoak, C. J.; Martin-Diaconescu, V.; Lloret-Fillol, J.; Browne, W. R.; Ray, K.; Company, A. *Chem. - Eur. J.* **2015**, *21*, 15029−15038.
(17) Patra, A. K.; Mukherjee, R. *Inorg. Chem.* **1999**, *38*, 1388−1393.
(18) de Oliveira, F. T.; Chanda, A.; Banerjee, D.; Shan, X.; Mondal, S.; Que, L.; Bominaar, E. L.; Münck, E.; Collins, T. J. *Science* **2007**, *315*, 835−838.
(19) Ghosh, M.; Singh, K. K.; Panda, C.; Weitz, A.; Hendrich, M. P.; Collins, T. J.; Dhar, B. B.; Sen Gupta, S. *J. Am. Chem. Soc.* **2014**, *136*, 9524−9527.
(20) Taguchi, T.; Gupta, R.; Lassalle-Kaiser, B.; Boyce, D. W.; Yachandra, V. K.; Tolman, W. B.; Yano, J.; Hendrich, M. P.; Borovik, A. S. *J. Am. Chem. Soc.* **2012**, *134*, 1996−1999.
(21) Lacy, D. C.; Gupta, R.; Stone, K. L.; Greaves, J.; Ziller, J. W.; Hendrich, M. P.; Borovik, A. S. *J. Am. Chem. Soc.* **2010**, *132*, 12188−12190.
(22) Nagataki, T.; Ishii, K.; Tachi, Y.; Itoh, S. *Dalton Trans.* **2007**, 1120−1128.
(23) Nagataki, T.; Tachi, Y.; Itoh, S. *Chem. Commun.* **2006**, 4016−4018.
(24) Morimoto, Y.; Bunno, S.; Fujieda, N.; Sugimoto, H.; Itoh, S. *J. Am. Chem. Soc.* **2015**, *137*, 5867−5870.
(25) Yoon, H.; Wagler, T. R.; O'Connor, K. J.; Burrows, C. J. *J. Am. Chem. Soc.* **1990**, *112*, 4568−4570.
(26) Burrows, C. J.; Muller, J. G.; Poulter, G. T.; Rokita, S. E. *Acta Chem. Scand.* **1996**, *50*, 337−344.
(27) Grill, J. M.; Ogle, J. W.; Miller, S. A. *J. Org. Chem.* **2006**, *71*, 9291−9296.
(28) Draksharapu, A.; Codolà, Z.; Gómez, L.; Lloret-Fillol, J.; Browne, W. R.; Costas, M. *Inorg. Chem.* **2015**, *54*, 10656−10666.
(29) Liu, W.; Groves, J. T. *J. Am. Chem. Soc.* **2010**, *132*, 12847−12849.
(30) Yang, N.; Reiher, M.; Wang, M.; Harmer, J.; Duin, E. C. *J. Am. Chem. Soc.* **2007**, *129*, 11028−11029.
(31) Huang, Y. H.; Park, J. B.; Adams, M. W. W.; Johnson, M. K. *Inorg. Chem.* **1993**, *32*, 375−376.
(32) Sastri, C. V.; Seo, M. S.; Park, M. J.; Kim, K. M.; Nam, W. *Chem. Commun.* **2005**, 1405−1407.
(33) Nakazawa, J.; Terada, S.; Yamada, M.; Hikichi, S. *J. Am. Chem. Soc.* **2013**, *135*, 6010−6013.
(34) Cong, Z.; Yanagisawa, S.; Kurahashi, T.; Ogura, T.; Nakashima, S.; Fujii, H. *J. Am. Chem. Soc.* **2012**, *134*, 20617−20620.
(35) Sarangi, R. *Coord. Chem. Rev.* **2013**, *257*, 459−472.
(36) Penner-Hahn, J. E. *Coord. Chem. Rev.* **2005**, *249*, 161−177.
(37) Yano, J.; Yachandra, V. K. *Photosynth. Res.* **2009**, *102*, 241−254.
(38) Westre, T. E.; Kennepohl, P.; DeWitt, J. G.; Hedman, B.; Hodgson, K. O.; Solomon, E. I. *J. Am. Chem. Soc.* **1997**, *119*, 6297−6314.
(39) Colpas, G. J.; Maroney, M. J.; Bagyinka, C.; Kumar, M.; Willis, W. S.; Suib, S. L.; Baidya, N.; Mascharak, P. K. *Inorg. Chem.* **1991**, *30*, 920−928.
(40) Kau, L. S.; Spira-Solomon, D. J.; Penner-Hahn, J. E.; Hodgson, K. O.; Solomon, E. I. *J. Am. Chem. Soc.* **1987**, *109*, 6433−6442.
(41) Blusch, L. K.; Mitevski, O.; Martin-Diaconescu, V.; Pröpper, K.; DeBeer, S.; Dechert, S.; Meyer, F. *Inorg. Chem.* **2014**, *53*, 7876−7885.
(42) Scott, R. A.; Eidsness, M. K. *Comments Inorg. Chem.* **1988**, *7*, 235−267.

DOI: 10.1021/jacs.6b07544
J. Am. Chem. Soc. 2016, 138, 12987−12996

(43) Gu, W.; Wang, H.; Wang, K. *Dalton Trans.* **2014**, *43*, 6406−6413.
(44) Ray, K.; DeBeer George, S.; Solomon, E. I.; Wieghardt, K.; Neese, F. *Chem. - Eur. J.* **2007**, *13*, 2783−2797.
(45) In the presence of acetic acid, NaOCl becomes HOCl (the energy balance for NaOCl + AcOH → NaOAc + HOCl is −11 kcal·mol^{-1}), the latter being the oxidant used to calculate the thermodynamics.
(46) Martin-Diaconescu, V.; Gennari, M.; Gerey, B.; Tsui, E.; Kanady, J.; Tran, R.; Pécaut, J.; Maganas, D.; Krewald, V.; Gouré, E.; Duboc, C.; Yano, J.; Agapie, T.; Collomb, M.-N.; DeBeer, S. *Inorg. Chem.* **2015**, *54*, 1283−1292.
(47) Krewald, V.; Lassalle-Kaiser, B.; Boron, T. T.; Pollock, C. J.; Kern, J.; Beckwith, M. A.; Yachandra, V. K.; Pecoraro, V. L.; Yano, J.; Neese, F.; DeBeer, S. *Inorg. Chem.* **2013**, *52*, 12904−12914.
(48) Garribba, E.; Micera, G. *J. Chem. Educ.* **2006**, *83*, 1229.
(49) Hazra, S.; Naskar, S.; Mishra, D.; Gorelsky, S. I.; Figgie, H. M.; Sheldrick, W. S.; Chattopadhyay, S. K. *Dalton Trans.* **2007**, 4143−4148.
(50) Singh, A. K.; Balamurugan, V.; Mukherjee, R. *Inorg. Chem.* **2003**, *42*, 6497−6502.
(51) Rajput, A.; Mukherjee, R. *Coord. Chem. Rev.* **2013**, *257*, 350−368.
(52) Stoll, S.; Schweiger, A. *J. Magn. Reson.* **2006**, *178*, 42−55.
(53) Krejčik, M.; Daněk, M.; Hartl, F. *J. Electroanal. Chem. Interfacial Electrochem.* **1991**, *317*, 179−186.
(54) Newville, M. *J. Synchrotron Radiat.* **2001**, *8*, 96−100.
(55) Ravel, B.; Newville, M. *J. Synchrotron Radiat.* **2005**, *12*, 537−541.
(56) Rehr, J. J.; Albers, R. C. *Rev. Mod. Phys.* **2000**, *72*, 621−654.
(57) Banaszak, K.; Martin-Diaconescu, V.; Bellucci, M.; Zambelli, B.; Rypniewski, W.; Maroney, M. J.; Ciurli, S. *Biochem. J.* **2012**, *441*, 1017−1026.
(58) Martin-Diaconescu, V.; Bellucci, M.; Musiani, F.; Ciurli, S.; Maroney, M. J. *JBIC, J. Biol. Inorg. Chem.* **2012**, *17*, 353−361.
(59) Zambelli, B.; Berardi, A.; Martin-Diaconescu, V.; Mazzei, L.; Musiani, F.; Maroney, M. J.; Ciurli, S. *JBIC, J. Biol. Inorg. Chem.* **2014**, *19*, 319−334.
(60) Herbst, R. W.; Perovic, I.; Martin-Diaconescu, V.; O'Brien, K.; Chivers, P. T.; Pochapsky, S. S.; Pochapsky, T. C.; Maroney, M. J. *J. Am. Chem. Soc.* **2010**, *132*, 10338−10351.
(61) *Gaussian 09, Revision D.01*; Frisch, M. J.; Trucks, G. W.; Schlegel, H. B.; Scuseria, G. E.; Robb, M. A.; Cheeseman, J. R.; Scalmani, G.; Barone, V.; Mennucci, B.; Petersson, G. A.; Nakatsuji, H.; Caricato, M.; Li, X.; Hratchian, H. P.; Izmaylov, A. F.; Bloino, J.; Zheng, G.; Sonnenberg, J. L.; Hada, M.; Ehara, M.; Toyota, K.; Fukuda, R.; Hasegawa, J.; Ishida, M.; Nakajima, T.; Honda, Y.; Kitao, O.; Nakai, H.; Vreven, T.; Montgomery, J. A., Jr.; Peralta, J. E.; Ogliaro, F.; Bearpark, M.; Heyd, J. J.; Brothers, E.; Kudin, K. N.; Staroverov, V. N.; Kobayashi, R.; Normand, J.; Raghavachari, K.; Rendell, A.; Burant, J. C.; Iyengar, S. S.; Tomasi, J.; Cossi, M.; Rega, N.; Millam, M. J.; Klene, M.; Knox, J. E.; Cross, J. B.; Bakken, V.; Adamo, C.; Jaramillo, J.; Gomperts, R.; Stratmann, R. E.; Yazyev, O.; Austin, A. J.; Cammi, R.; Pomelli, C.; Ochterski, J. W.; Martin, R. L.; Morokuma, K.; Zakrzewski, V. G.; Voth, G. A.; Salvador, P.; Dannenberg, J. J.; Dapprich, S.; Daniels, A. D.; Farkas, Ö.; Foresman, J. B.; Ortiz, J. V.; Cioslowski, J.; Fox, D. J. Gaussian, Inc.: Wallingford, CT, 2009.
(62) Becke, A. D. *J. Chem. Phys.* **1993**, *98*, 1372−1377.
(63) Becke, A. D. *J. Chem. Phys.* **1993**, *98*, 5648−5652.
(64) Schaefer, A.; Huber, C.; Ahlrichs, R. *J. Chem. Phys.* **1994**, *100*, 5829−5835.
(65) Marenich, A. V.; Cramer, C. J.; Truhlar, D. G. *J. Phys. Chem. B* **2009**, *113*, 6378−6396.
(66) Grimme, S.; Ehrlich, S.; Goerigk, L. *J. Comput. Chem.* **2011**, *32*, 1456−1465.
(67) O'Boyle, N. M.; Tenderholt, A. L.; Langner, K. M. *J. Comput. Chem.* **2008**, *29*, 839−845.
(68) Lu, T.; Chen, F. *J. Comput. Chem.* **2012**, *33*, 580−592.
(69) Neese, F. *Wiley Interdisciplinary Reviews: Computational Molecular Science* **2012**, *2*, 73−78.
(70) DeBeer George, S.; Petrenko, T.; Neese, F. *Inorg. Chim. Acta* **2008**, *361*, 965−972.
(71) Roemelt, M.; Beckwith, M. A.; Duboc, C.; Collomb, M.-N.; Neese, F.; DeBeer, S. *Inorg. Chem.* **2012**, *51*, 680−687.
(72) Hirata, S.; Head-Gordon, M. *Chem. Phys. Lett.* **1999**, *314*, 291−299.
(73) Neese, F.; Olbrich, G. *Chem. Phys. Lett.* **2002**, *362*, 170−178.
(74) Schäfer, A.; Horn, H.; Ahlrichs, R. *J. Chem. Phys.* **1992**, *97*, 2571−2577.
(75) Klamt, A.; Schuurmann, G. *J. Chem. Soc., Perkin Trans. 2* **1993**, 799−805.

DOI: 10.1021/jacs.6b07544
J. Am. Chem. Soc. 2016, 138, 12987−12996

Chapter V.

Nitrous oxide activation by a cobalt(II) complex for aldehyde oxidation under mild conditions

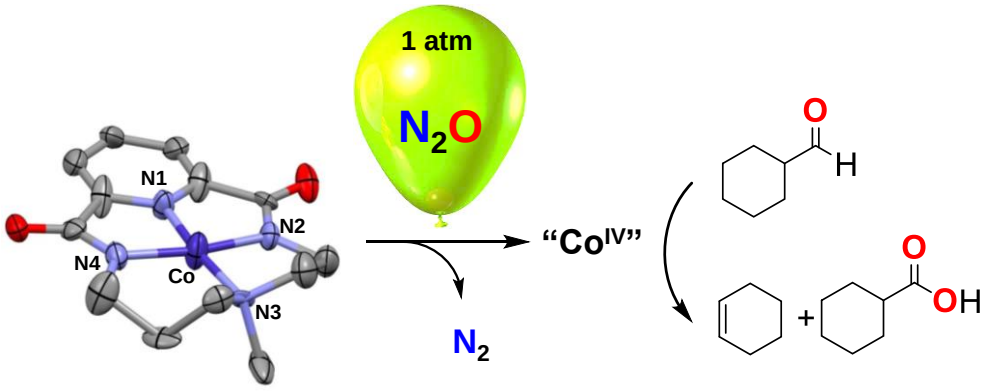

This chapter corresponds to the following publication:

Teresa Corona and Anna Company*

Dalton Trans. **2016**, *45*, 14530-14533.

Teresa Corona and Anna Company. “Nitrous oxide activation by a cobalt(II) complex for aldehyde oxidation under mild conditions”. *Dalton Transactions*. Vol. 45 (2016) : 14530−14533

http://dx.doi.org/10.1039/C6DT01704E

Dalton Transactions

COMMUNICATION

View Article Online
View Journal | View Issue

Cite this: *Dalton Trans.*, 2016, **45**, 14530

Received 30th April 2016,
Accepted 15th July 2016

DOI: 10.1039/c6dt01704e

www.rsc.org/dalton

Nitrous oxide activation by a cobalt(II) complex for aldehyde oxidation under mild conditions†

Teresa Corona and Anna Company*

Nitrous oxide (N_2O) is a waste gas produced in many industrial processes with an important environmental impact. Thus, its application as an oxidant is highly desirable because it produces innocuous N_2 as a by-product. In this work we report a new cobalt(II) complex that reacts with N_2O under mild conditions and the catalytic application of this system to carry out the oxidation of aldehydes.

Traditional stoichiometric oxidants used in industrial processes (chromate or permanganate) require high temperatures and extended reaction times. Moreover, they exhibit low efficiencies and selectivities and they produce large amounts of inorganic salts as waste. Due to environmental and economic costs, these methodologies are being discarded in favour of less toxic oxidants such as air, O_2 and peroxides in combination with transition metal complexes as catalysts.[1] Along these lines, the use of nitrous oxide (N_2O) as an oxidizing reagent in chemical processes would be especially interesting because it only produces N_2 as an innocuous by-product.

Despite the fact that N_2O is a natural component of the earth's atmosphere it has been identified as an environmental problem because it is 300 times more potent than carbon dioxide as a greenhouse gas[2,3] and it is implicated in the destruction of the ozone layer.[4] Indeed, the N_2O concentration is increasing every year in large part owing to anthropogenic sources, including manufacturing, fossil fuel use and agricultural activities. For example, it is produced as a by-product at multimillion kg per year in nylon manufacture worldwide.[5]

The use of N_2O as an oxidant has proven to be highly challenging[6] because, despite being thermodynamically a potent oxidant, it is kinetically recalcitrant. In biological systems these kinetic barriers are overcome by binding and activation to metal ions. That is, decomposition of N_2O into innocuous N_2 and H_2O is carried out by the copper-based metalloenzyme nitrous oxide reductase.[7,8] Thus, inspired by biological systems, an interesting strategy to apply N_2O as an oxidant is its activation mediated through metal ions.[6,9–12] A pioneering work by Groves *et al.* in 1995 demonstrated the synthesis of a porphyrin dioxo-ruthenium(IV) by efficient oxidation of the Ru^{II} precursor with N_2O,[13] which could be used as a catalyst in alkene epoxidation using N_2O as the oxygen source.[14] Two-electron reductive activation of this gas accompanied by N–O bond scission was proposed. A benchmark in the field was established by Chang *et al.* who reported a non-heme iron pyrrole platform and its ability to activate N_2O for intra- and intermolecular oxidation reactions, through the formation of a putative oxoiron(IV) species.[15] An analogous process was proposed to explain the reactivity of a nickel(I) complex towards N_2O.[16]

Interestingly, in all these systems a highly electron rich metal is required, so that it is able to transfer electrons to N_2O. In order to attain this peculiarity, metal complexes have either metal centers in a low oxidation state or they possess high donor (anionic) ligand scaffolds.

In this work, we report the activation of N_2O with a cobalt(II) complex under mild conditions (1 atm N_2O and 273 K). The designed cobalt(II) complex bears a tetradentate dianionic ligand (H_2L, Fig. 1a) which combines two amides, an aliphatic amine and a pyridine group as donor atoms. This ligand was previously used in our group to successfully stabilize high-valent nickel–oxygen species.[17] Furthermore, we show that the prepared cobalt(II) complex can be successfully applied as a catalyst in the oxidation of aldehydes using N_2O as the terminal oxidant.

The reaction of equimolar amounts of H_2L and $[Co^{II}(CF_3SO_3)_2(CH_3CN)_2]$ with 2 equiv. $K[N(SiMe_3)_2]$ in anhydrous CH_3CN at room temperature under N_2 resulted in a deep red solution. Slow diethyl ether diffusion over the solution afforded compound $[Co^{II}(L)]$ (**1**) as a dark red microcrystalline

Grup de Química Bioinspirada, Supramolecular i Catàlisi (QBIS-CAT), Institut de Química Computacional i Catàlisi (IQCC), Departament de Química, Universitat de Girona, Campus Montilivi, E17071 Girona, Catalonia, Spain.
E-mail: anna.company@udg.edu

†Electronic supplementary information (ESI) available: Materials and methods, synthesis and characterization of **1** and **2**, EPR spectra, complementary material on the kinetic analysis and qualitative identification of CO_2 by GC-TCD. CCDC 1477417 and 1477418. For ESI and crystallographic data in CIF or other electronic format see DOI: 10.1039/c6dt01704e

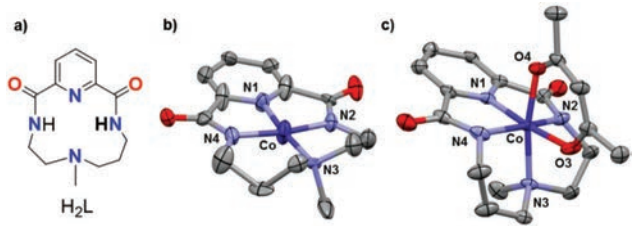

Fig. 1 Schematic representation of ligand H_2L (a) and crystal structures of **1**·$NaBF_4$ (b) and **2** (c). Hydrogen atoms and co-crystallized $NaBF_4$ in **1** have been omitted for clarity. Thermal ellipsoids are set at 50% probability. Selected distances [Å] and angles [°]: (b) Co–N1 1.802(9), Co–N2 1.852(7), Co–N3 1.918(16), Co–N4 1.858(8), N1–Co–N2 84.0(4), N1–Co–N4 84.4(4), N2–Co–N3 87.8(8), N4–Co–N3 103.8(8). (c) Co–N1 1.861(5), Co–N2 1.924(6), Co–N3 1.992(10), Co–N4 1.932(6), Co–O3 1.914(5), Co–O4 1.919(5), N1–Co–O4 81.4(2), O3–Co–O4 93.4(2), N1–Co–N2 82.1(2), N1–Co–N4 82.0(2), N1–Co–N3 104.6(3), N2–Co–N3 78.1(4), N4–Co–N3 96.6(4).

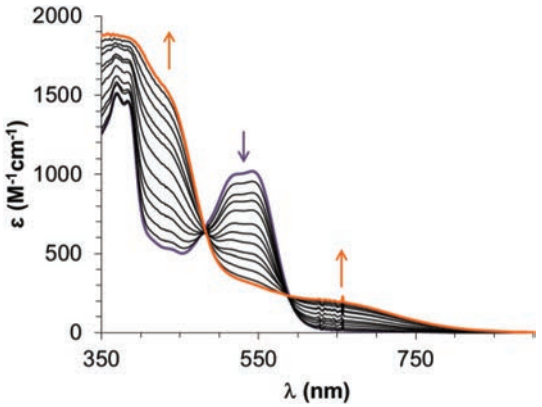

Fig. 2 UV-vis spectral changes of a solution of **1** upon reaction with N_2O (1 atm) in CH_3CN at 273 K.

powder in 58% yield which co-crystallized with KCF_3SO_3. Compound **1** rapidly decomposed upon exposure to O_2 as evidenced by a colour change from red to brown. Crystals suitable for X-ray diffraction were obtained by addition of equimolar amounts of $NaBF_4$, which co-crystallized with the complex to afford **1**·$NaBF_4$ (Fig. 1b). Compound **1** exhibits a square planar geometry with the cobalt coordinating to the pyridine, an aliphatic tertiary amine and two amidate groups *trans* to each other (Fig. 1b). The measured bond lengths Co–N_{py} (1.80 Å), Co–N_{CH_3} (1.92 Å) and Co–$N_{amidate}$ (1.85–1.86 Å) are consistent with those previously reported for Co^{II} square planar complexes.[18] The ^{1}H-NMR spectrum of **1** in CD_3CN at 298 K showed broad bands that span from 70 to −30 ppm (Fig. S1†). The measured magnetic moment of 1.69μ_B determined by the Evans' method revealed a low spin cobalt(II) center (d^7) with a single unpaired electron. High-resolution mass spectrometry showed peaks at *m*/*z* 342.0476 and 358.0238 with mass values and isotopic patterns fully consistent with $\{[Co^{II}(L)] + Na\}^+$ and $\{[Co^{II}(L)] + K\}^+$ but the major peak at *m*/*z* 319.0590 corresponded to the 1e$^-$ oxidized species $[Co^{III}(L)]^+$, due to the unavoidable presence of O_2 in our mass spectrometer. Finally, a redox potential of $E_{1/2}$ = −0.13 V *vs.* Ag/Ag^+ (0.17 V *vs.* SCE) was determined for **1** in CH_3CN under N_2 (Fig. S2†).

For comparison purposes the corresponding cobalt(III) complex was synthesized following a similar methodology but using $[Co^{III}(acac)_3]$ as the metal source. X-ray analysis shows that the resulting $[Co^{III}(L)(acac)]$ complex (**2**) presents a metal center with an octahedral geometry in which the ligand L is bent and the acetylacetonate anion occupies two coordination positions in a relative *cis* configuration (Fig. 1c). In contrast to **1**, compound **2** exhibited a diamagnetic ^{1}H-NMR spectrum in CD_3CN with well resolved signals, indicative of a low-spin Co^{III} center (d^6) which could be fully assigned (Fig. S3 and S4†).

The reaction of **1** towards N_2O was qualitatively evaluated by UV-vis spectroscopy. Compound **1** was extremely reactive and its absorption spectrum immediately changed upon reaction with N_2O (Fig. 2). The characteristic absorption band of complex **1** at 535 nm readily disappeared and a new species with features at 430 nm and 650 nm appeared within 1 min of reaction at 273 K. The presence of isosbestic points (482 and 589 nm) indicated that a clean transformation from reactants to products took place without detection of any reaction intermediate.

Despite the fact that the purity of N_2O was checked to be >99% by GC-TCD analysis, further confirmation that the observed reaction with **1** was not due to the presence of trace amounts of O_2 in the commercial N_2O gas was considered necessary. The reaction of **1** with O_2 or N_2O was carried out using controlled amounts of these two gases. The equivalents of gas added into the solution were adjusted by direct injection of the appropriate volume of the pure gas (or a dilution of it in N_2) into the solution of **1** in CH_3CN. As shown in Fig. S5† the reaction of **1** with 5 equiv. O_2 or N_2O was faster than with 1 equiv. More importantly, reaction rates with N_2O were comparable to those obtained with O_2, indicating that traces of O_2 present in commercial nitrous oxide cannot be responsible for the observed chemistry. If this was the case, reaction with a controlled amount of N_2O would be much slower. A blank experiment carried out by direct injection of a controlled amount of N_2 into the solution of **1** demonstrated that no air contamination occurred during the injection because **1** remained unreacted in this case (Fig. S5†).

Kinetic analysis of the reaction between **1** and N_2O could be performed by UV-vis spectroscopy by monitoring the decay of the band at 535 nm characteristic of **1** at 273 K in CH_3CN. Under conditions of excess N_2O (5–100 equiv. with respect to cobalt) reactions showed pseudo-first-order behaviour so that the observed reaction rates (k_{obs}) were linearly dependent on the amount of N_2O (Fig. 3). Using the initial rate method, the reaction was established to be first order with respect to **1**. This was determined by measuring the slope of the trend line obtained by plotting the ln(initial rates) *versus* ln[**1**] (slope = 1.2, Fig. S8†). Overall, a second order rate constant (k) of 1.2 M^{-1} s^{-1} was estimated from these experiments. Thus, the reaction was first order with respect to N_2O and **1**. Finally, GC-TCD analysis of the headspace gas was carried out to quantify the

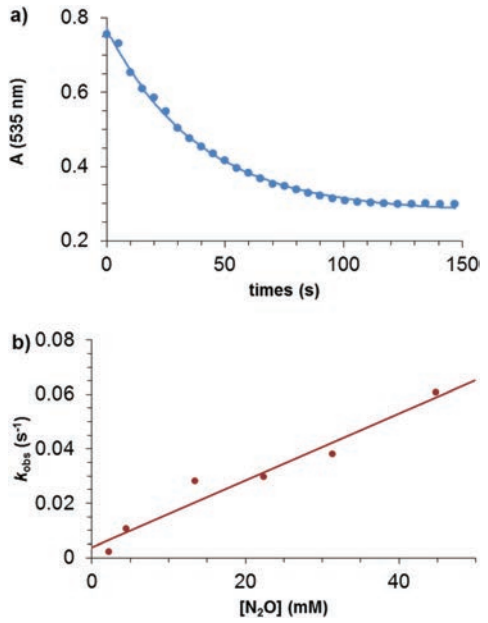

Fig. 3 (a) Time trace at 535 nm for the reaction of **1** with 35 equiv. N_2O in CH_3CN at 273 K monitored by UV-vis spectroscopy. The decay could be fitted to a single exponential function. (b) Plot of k_{obs} as a function of the amount of N_2O for the reaction of **1** with N_2O in CH_3CN at 273 K. A second-order rate constant (k) of 1.2 M^{-1} s^{-1} was extracted from this analysis.

amount of N_2 released during the reaction of **1** with N_2O at 273 K. Compound **1** was dissolved in anhydrous CH_3CN under Ar and excess N_2O was added using a syringe. Once the reaction was complete, the amount of liberated N_2 was determined by GC-TCD by interpolation in a calibration curve. The production of 1.0 ± 0.2 equiv. of N_2 with respect to **1** further confirmed that the stoichiometry of the reaction between **1** and N_2O was 1 : 1 (see the ESI for details, Fig. S9 and S10†). As full reduction of N_2O to N_2 requires 2 electrons, we hypothesized that nitrous oxide reduction occurs through the mediation of a Co^{IV} species, likely a cobalt–oxygen compound, which is not visible under our reaction conditions (attempts to lower the temperature to trap a reaction intermediate were unsuccessful).

$$[Co^{II}(L)]\ (\mathbf{1}) + N_2O \rightarrow \text{“}Co^{IV}\text{”} + N_2 \qquad v = k[\mathbf{1}][N_2O] \qquad (1)$$

No clear information on the nature of the intermediate species was unraveled by ^{1}H-NMR, UV-vis or MS analyses, while EPR analysis indicated the presence of an EPR active species with a signal at $g \sim 2.03$ (Fig. S6†). However, remarkable changes were observed in the cyclic voltammetry of **1** when this molecule was exposed to N_2O. The initial reversible redox wave corresponding to the Co^{III}/Co^{II} redox pair of **1** disappeared and a new wave at $E_{1/2}$ = 0.80 (*vs.* SCE) took shape (Fig. 4). This might correspond to the Co^{IV}/Co^{III} redox pair of the putatively formed “Co^{IV}” species, as it falls in the range of redox potentials determined for the oxidation of other Co^{III} complexes bearing N-based anionic ligands.[19–22]

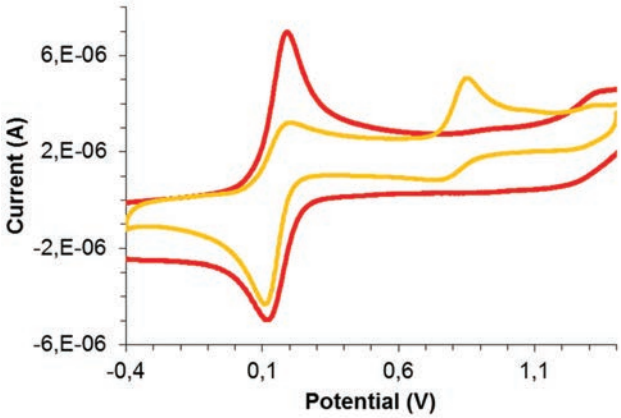

Fig. 4 Cyclic voltammetry corresponding to **1** (red line) and to the reaction of **1** with N_2O (yellow line) in CH_3CN at 273 K. Potential measured *vs.* SCE.

Overall, the reaction of **1** with N_2O occurs in a 1 : 1 stoichiometry to liberate N_2, so that formation of a cobalt(IV) species is proposed. However, this species is not stable and it evolves towards the formation of cobalt(III) as evidenced by NMR analysis of the reaction mixture over time, in which peaks analogous to those of **2** appeared (Fig. S11†).

The ability of **1** in combination with N_2O to oxidize different substrates was evaluated. Analysis of the final products by GC-FID, GC-MS or NMR allowed us to determine if substrate oxidation had occurred. Firstly, as we envisioned that cobalt–oxygen species could have been formed along the $2e^-$ reduction of N_2O, we studied oxygen-atom transfer (OAT) and hydrogen-atom transfer (HAT) of selected substrates, which are typical processes for electrophilic metal–oxygen oxidants.[23–25] Triphenylphosphine and 4-methoxy-thioanisole were the substrates of choice for OAT, while HAT was evaluated using 9,10-dihydroanthracene (weak C–H bonds) and cyclohexanol (oxidizable O–H bond). However, no oxidized products were detected in any case.

Given the lack of reactivity in OAT and HAT reactions, substrates susceptible to undergo a nucleophilic attack were selected. In particular, we studied the oxidation and deformylation of cyclohexanecarboxaldehyde. In a typical experiment, a solution of **1** and cyclohexanecarboxaldehyde (50 equiv.) was stirred at room temperature in a N_2O atmosphere (1 atm). Gas chromatographic analysis revealed the formation of cyclohexanecarboxylic acid and cyclohexene over the course of the reaction (Scheme 1 and Fig. S12†). The deformylation reaction was

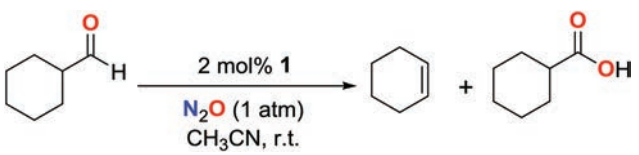

Scheme 1 Reaction of **1** with cyclohexanecarboxaldehyde using N_2O as an oxidant.

further confirmed by chromatographic analysis of the headspace by GC-TCD, which clearly showed the release of CO_2 in the reaction of **1** with cyclohexanecarboxaldehyde in the presence of N_2O (Fig. S13†). Deformylation reactions have been previously observed in the nucleophilic oxidation of aldehydes by metal–oxygen species.[26–28] In particular, 2.1 ± 0.1 TN of cyclohexene and 25 ± 5 TN of carboxylic acid were obtained after 24 h of reaction under a N_2O atmosphere. Importantly, blank experiments in the absence of **1** showed minimal amounts of both products. Thus, the combination of **1** and N_2O affords a catalytic system for aldehyde oxidation.

Conclusions

Overall, in this manuscript we have reported the fast activation of N_2O by a cobalt(II) complex under mild reaction conditions. Moreover, the system has been applied for the catalytic oxidation of aldehydes. Despite the fact that the nature of the cobalt species resulting from N_2O activation and responsible for substrate oxidation is not known, kinetic studies indicate a 1 : 1 stoichiometry that would be in agreement with the involvement of a cobalt(IV) compound. The work reported herein is specially remarkable considering that the activation of this waste gas under mild conditions is highly challenging due to its chemical inertness.

Acknowledgements

Financial support for this work was provided by the European Commission (2011-CIG-303522 to A. C.) and the MINECO of Spain ("Ramón y Cajal" contract and CTQ2013-43012-P to A. C.). The authors acknowledge the help of Prof. Guillem Aromí for providing access to EPR spectroscopy.

References

1 J.-E. Bäckvall, *Modern Oxidation Methods*, Wiley-VCH, Weinheim, 2004.
2 W. C. Trogler, *Coord. Chem. Rev.*, 1999, **187**, 303–327.
3 W. B. Tolman, *Angew. Chem., Int. Ed.*, 2010, **49**, 1018–1024.
4 A. R. Ravishankara, J. S. Daniel and R. W. Portmann, *Science*, 2009, **326**, 123–125.
5 2016 U.S. Greenhouse Gas Inventory Report: 1990–2014, United States Environmental Protection Agency (http://tinyurl.com/emissionsreport).
6 K. Severin, *Chem. Soc. Rev.*, 2015, **44**, 6375–6386.
7 K. Paraskevopoulos, S. V. Antonyuk, R. G. Sawers, R. R. Eady and S. S. Hasnain, *J. Mol. Biol.*, 2006, **362**, 55–65.
8 K. Brown, M. Tegoni, M. Prudencio, A. S. Pereira, S. Besson, J. J. Moura, I. Moura and C. Cambillau, *Nat. Struct. Mol. Biol.*, 2000, **7**, 191–195.
9 C. Esmieu, M. Orio, S. Torelli, L. Le Pape, J. Pecaut, C. Lebrun and S. Menage, *Chem. Sci.*, 2014, **5**, 4774–4784.
10 D. J. Xiao, E. D. Bloch, J. A. Mason, W. L. Queen, M. R. Hudson, N. Planas, J. Borycz, A. L. Dzubak, P. Verma, K. Lee, F. Bonino, V. Crocellà, J. Yano, S. Bordiga, D. G. Truhlar, L. Gagliardi, C. M. Brown and J. R. Long, *Nat. Chem.*, 2014, **6**, 590–595.
11 G. Kiefer, L. Jeanbourquin and K. Severin, *Angew. Chem., Int. Ed.*, 2013, **52**, 6302–6305.
12 S. Saito, H. Ohtake, N. Umezawa, Y. Kobayashi, N. Kato, M. Hirobe and T. Higuchi, *Chem. Commun.*, 2013, **49**, 8979–8981.
13 J. T. Groves and J. S. Roman, *J. Am. Chem. Soc.*, 1995, **117**, 5594–5595.
14 T. Yamada, K. Hashimoto, Y. Kitaichi, K. Suzuki and T. Ikeno, *Chem. Lett.*, 2001, **30**, 268–269.
15 W. H. Harman and C. J. Chang, *J. Am. Chem. Soc.*, 2007, **129**, 15128–15129.
16 S. Yao, E. Bill, C. Milsmann, K. Wieghardt and M. Driess, *Angew. Chem., Int. Ed.*, 2008, **47**, 7110–7113.
17 T. Corona, F. F. Pfaff, F. Acuña-Parés, A. Draksharapu, C. J. Whiteoak, V. Martin-Diaconescu, J. Lloret-Fillol, W. R. Browne, K. Ray and A. Company, *Chem. – Eur. J.*, 2015, **21**, 15029–15038.
18 M. Cibian, S. Derossi and G. S. Hanan, *Dalton Trans.*, 2011, **40**, 1038–1040.
19 J. Halpern, M. S. Chan, J. Hanson, T. S. Roche and J. A. Topich, *J. Am. Chem. Soc.*, 1975, **97**, 1606–1608.
20 S. Will, J. Lex, E. Vogel, V. A. Adamian, E. Van Caemelbecke and K. M. Kadish, *Inorg. Chem.*, 1996, **35**, 5577–5583.
21 S. Hong, F. F. Pfaff, E. Kwon, Y. Wang, M.-S. Seo, E. Bill, K. Ray and W. Nam, *Angew. Chem., Int. Ed.*, 2014, **53**, 10403–10407.
22 I. Levitin, A. I. Sigan and M. E. Vol'pin, *J. Chem. Soc., Chem. Commun.*, 1975, 469–470.
23 J. E. M. N. Klein and L. Que, in *Encyclopedia of Inorganic and Bioinorganic Chemistry*, John Wiley & Sons, Ltd, 2011.
24 J. Chen, Y.-M. Lee, K. M. Davis, X. Wu, M. S. Seo, K.-B. Cho, H. Yoon, Y. J. Park, S. Fukuzumi, Y. N. Pushkar and W. Nam, *J. Am. Chem. Soc.*, 2013, **135**, 6388–6391.
25 S. Hong, H. So, H. Yoon, K.-B. Cho, Y.-M. Lee, S. Fukuzumi and W. Nam, *Dalton Trans.*, 2013, **42**, 7842–7845.
26 J. Annaraj, Y. Suh, M. S. Seo, S. O. Kim and W. Nam, *Chem. Commun.*, 2005, 4529–4531.
27 R. A. Geiger, S. Chattopadhyay, V. W. Day and T. A. Jackson, *Dalton Trans.*, 2011, **40**, 1707–1715.
28 Y. Jo, J. Annaraj, M. S. Seo, Y.-M. Lee, S. Y. Kim, J. Cho and W. Nam, *J. Inorg. Biochem.*, 2008, **102**, 2155–2159.

Chapter VI.

Characterization and reactivity studies of a terminal copper-nitrene species

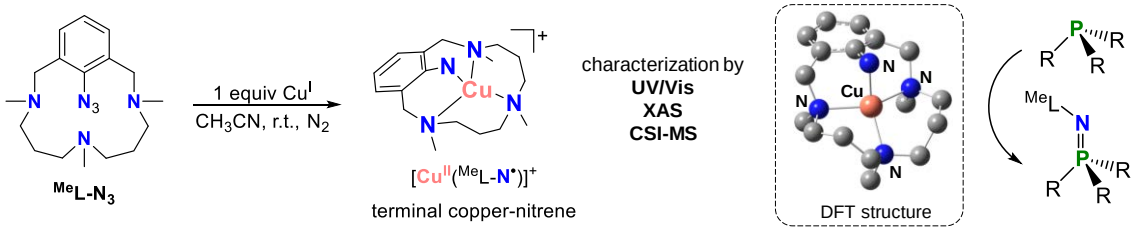

This chapter corresponds to the following publication:

Teresa Corona, Lídia Ribas, Mireia Rovira, Erik Farquhar, Xavi Ribas*, Kallol Ray*, and Anna Company*

Angew. Chem. Int. Ed. **2016**, *55*, 14005-14008.

Teresa Corona, Lídia Ribas, Mireia Rovira, Erik Farquhar, Xavi Ribas, Kallol Ray, and Anna Company. "Characterization and reactivity studies of a terminal copper-nitrene species". Angewandte Chemie International Edition. Vol. 55 (2016) : 14005−14008

http://dx.doi.org/10.1002/anie.201607238

Copper Complexes Hot Paper

International Edition: DOI: 10.1002/anie.201607238
German Edition: DOI: 10.1002/ange.201607238

Characterization and Reactivity Studies of a Terminal Copper–Nitrene Species

Teresa Corona, Lídia Ribas, Mireia Rovira, Erik R. Farquhar, Xavi Ribas, Kallol Ray,* and Anna Company**

Abstract: *High-valent terminal copper–nitrene species have been postulated as key intermediates in copper-catalyzed aziridination and amination reactions. The high reactivity of these intermediates has prevented their characterization for decades, thereby making the mechanisms ambiguous. Very recently, the Lewis acid adduct of a copper–nitrene intermediate was trapped at −90 °C and shown to be active in various oxidation reactions. Herein, we describe for the first time the synthesis and spectroscopic characterization of a terminal copper(II)–nitrene radical species that is stable at room temperature in the absence of any Lewis acid. The azide derivative of a triazamacrocyclic ligand that had previously been utilized in the stabilization of aryl–Cu^{III} intermediates was employed as an ancillary ligand in the study. The terminal copper(II)–nitrene radical species is able to transfer a nitrene moiety to phosphines and abstract a hydrogen atom from weak C–H bonds, leading to the formation of oxidized products in modest yields.*

Terminal high-valent copper–nitrene intermediates have long been proposed as key intermediates in aziridination and amination reactions.[1–3] Obtaining mechanistic insight into these transformations and developing selective catalytic reagents and processes are only possible if the structure and properties of these key species are fully understood. Whereas metal–nitrene species based on iron, cobalt, and nickel have been isolated,[4–9] terminal copper–nitrene intermediates have eluded detection for decades. Warren and co-workers indirectly proposed the involvement of terminal copper–nitrene intermediates derived from dicopper–nitrene species by NMR exchange experiments and kinetic measurements of C–H functionalization reactions.[2,10] More recently, the involvement of such species in copper-mediated oxidation reactions was corroborated by the spectroscopic trapping of Lewis acid adducts of a copper–nitrene intermediate at −90 °C.[11,12] Furthermore, Bertrand and co-workers recently reported isolated examples of copper(II)–bis(nitrene) and dicopper(II)–nitrene species that were obtained by reacting a bulky phosphinonitrene ligand with 0.5 and 2 equiv of copper(I) triflate, respectively. However, terminal copper–nitrene intermediates could not be isolated in these reactions although their formation was suggested based on ^{31}P NMR studies.[13] Herein, we report the unprecedented spectroscopic and theoretical characterization of terminal copper–nitrene species (**1** and **3**) in the absence of any Lewis acid by employing azide derivatives of triazamacrocyclic ligands (^{H}L-N_3 and ^{Me}L-N_3). Such ligand architectures have previously been utilized in the successful stabilization of aryl–Cu^{III} intermediates by enforcing a square-planar geometry at the copper center.[14,15] Moreover, copper–nitrene species **3**, which is stable at room temperature, participates in a number of nitrene transfer and C–H activation reactions, thus providing a key precedent for the possible involvement of such species in oxidation catalysis.

While some of us studied the relevance of aryl–Cu^{III} species in model copper-catalyzed C_{aryl}–C_{sp^3},[16] C_{aryl}–C_{sp},[17] and C_{aryl}–heteroatom[14,15,18,19] bond-formation reactions, we envisaged that compound ^{H}L-N_3 (Scheme 1) could be a good candidate as a starting material for the preparation of elusive copper–nitrene complexes (see the Supporting Information

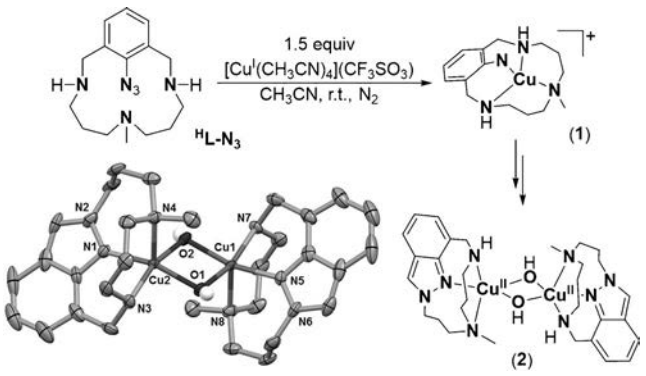

Scheme 1. Schematic representations of **1** and **2**. X-ray structure of **2**. Thermal ellipsoids set at 50% probability. Hydrogen atoms (except for those belonging to the OH groups) and triflate anions omitted for clarity.

[*] T. Corona, L. Ribas, M. Rovira, Dr. X. Ribas, Dr. A. Company
Grup de Química Bioinspirada, Supramolecular i Catàlisi (QBIS-CAT)
Institut de Química Computacional i Catàlisi (IQCC)
Departament de Química, Universitat de Girona
Campus Montilivi, E17003 Girona, Catalonia (Spain)
E-mail: xavi.ribas@udg.edu
anna.company@udg.edu
Dr. E. R. Farquhar
Case Western Reserve University Center for Synchrotron Biosciences and Center for Proteomics and Bioinformatics
National Synchrotron Light Source II
Brookhaven National Laboratory, Upton, New York 11973 (USA)
Prof. Dr. K. Ray
Department of Chemistry
Humboldt Universität zu Berlin
Brook-Taylor Strasse 2, 12489 Berlin (Germany)
E-mail: kallol.ray@chemie.hu-berlin.de
Supporting information and the ORCID identification number(s) for the author(s) of this article can be found under: http://dx.doi.org/10.1002/anie.201607238.

for its synthesis). Accordingly, the reaction of ^{H}L-N$_3$ with 1.5 equiv [Cu^{I}(CH$_3$CN)$_4$](CF$_3$SO$_3$) in acetonitrile at room temperature under argon atmosphere was monitored by UV/Vis spectroscopy (see the Supporting Information, Figure S3). The formation of a green transient species (**1**, $\lambda_{max} = 380$ and 790 nm) was observed during the first stages of the reaction. However, this compound quickly evolved into a purple species (**2**, $\lambda_{max} = 550$ nm, $\varepsilon = 1000\,M^{-1}cm^{-1}$), which proved to be stable for several hours at room temperature. Violet crystals (isolated in 56% yield) were obtained by slow diethyl ether diffusion into an acetonitrile solution of **2** at −30 °C.

The X-ray structure of **2** reveals a dimeric core with significant modification of the initial ^{H}L-N$_3$ structure (Scheme 1). Loss of a N$_2$ molecule from the azide unit is accompanied by N−N bond formation, giving rise to the formation of an indazole ring. Each Cu center adopts a distorted square-pyramidal geometry ($\tau = 0.1$)[20] and binds to the N−CH$_3$, NH, and N$_{aryl}$ groups of the resulting indazole-based ligand (L^{in}) as well as to two additional hydroxo ligands, thereby forming a bis(μ-hydroxo)dicopper(II) core in **2** (Scheme 1). The hydroxo groups in **2** presumably originate from adventitious water present in the anhydrous solvents used in the glovebox;[21] they also enforce a strong antiferromagnetic coupling between the two copper centers, which results in an $S = 0$ ground state.[22] The integrity of this dimeric structure in solution was confirmed by ^{1}H NMR studies, which showed a diamagnetic spectrum in which the indazole protons could be clearly observed at 8.2, 7.7, 7.2, and 7.1 ppm (Figure S4). Although unknown in copper chemistry, the N−N bond-formation reaction associated with the formation of **2** is typically exhibited by high-valent terminal metal–imido or –nitrido complexes.[5,23–25] A similar terminal copper–nitrene intermediate could also play a key role during the copper-mediated N−N bond-formation reaction that leads to the formation of **2**.

Whereas UV/Vis studies clearly confirmed the presence of a transient intermediate (**1**) along the reaction of ^{H}L-N$_3$ with Cu^{I} at 25 °C to form **2**, spectroscopic assignment of the electronic structure of **1** proved to be difficult because of its instability at 25 °C. However, the stability of **1** could be significantly increased by generating it in acetone at −50 °C (λ_{max} [ε, $M^{-1}cm^{-1}$] = 380 [> 1300], 650 [> 150], and 790 nm [> 200]; Figure S7). Notably, cold spray ionization mass spectrometry (CSI-MS) of **1** (Figure S8) gave rise to a major peak centered at m/z 323.1284 with a mass and isotope distribution pattern consistent with a terminal copper–nitrene species [Cu(^{H}L-N)]$^+$, where ^{H}L-N is the ligand formed after N$_2$ release from ^{H}L-N$_3$. The low temperatures required to prevent the decomposition of **1** into **2**, however, prevented us from investigating the oxidizing capability of **1**.

To increase the thermal stability of the putative copper–nitrene intermediate, efforts were made to block the facile decomposition of **1** into **2** by introducing methyl groups in the secondary amine units of the ^{H}L-N$_3$ ligand (see the Supporting Information for synthetic procedures). UV/Vis monitoring of the stoichiometric reaction between the methylated version of the azide-derived ligand (^{Me}L-N$_3$, Scheme 2) and [Cu^{I}(CH$_3$CN)$_4$](CF$_3$SO$_3$) in acetonitrile at 25 °C showed the formation of a stable green species (**3**; $t_{1/2} \approx 45$ h) with

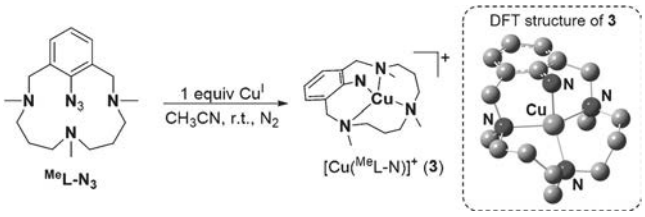

Scheme 2. Schematic representation of **3** together with its DFT optimized structure.

a distinct absorption spectrum (λ_{max} [ε, $M^{-1}cm^{-1}$] = 360 [> 1200], 710 nm [> 200], and 980 nm [> 150]; Figure 1a) relative to **1**.[26] CSI-MS analysis revealed a dominant peak at m/z 351.1597 with a mass and isotope pattern fully consistent with [Cu(^{Me}L-N)]$^+$, which was partially shifted to m/z 352.1601 when 50% ^{15}N-labeled **3**[27] was used (Figure 1b). Moreover, the EPR spectrum of **3** only exhibited a small signal of Cu^{II}, which accounted for less than 5% of the sample; the majority of the species present in solution were not detectable by X-band EPR spectroscopy. Importantly, FTIR analysis of a concentrated solution of **3** did not exhibit any azide vibration at about 2200 cm^{-1}, further confirming N$_2$ release in line with the MS experiments. Furthermore, a low-intensity band at 426 cm^{-1} could be observed in the IR spectrum, which was attributed to a Cu–N vibration based on

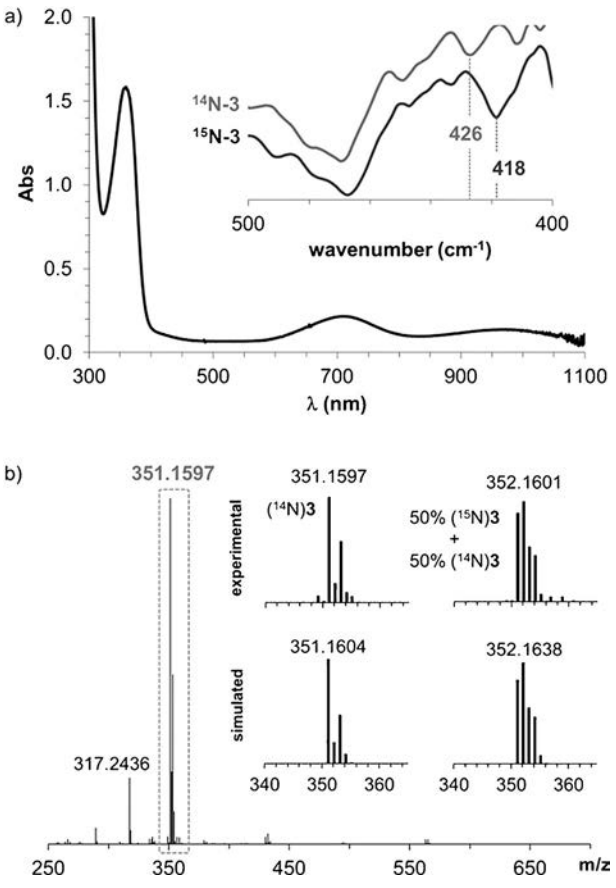

Figure 1. a) UV/Vis spectrum of **3** in acetonitrile at 25 °C. Inset: FTIR spectrum of **3** (gray) and its 50% ^{15}N-labeled analogue (black). b) ESI-MS spectrum of **3** in acetonitrile at 25 °C under N$_2$ atmosphere.

the $^{15}N/^{14}N$ downshift of 8 cm^{-1} upon ^{15}N labeling (Figure 1a, inset). Finally, an effective magnetic moment (μ_{eff}) of 2.14 μ_B, as determined by the Evans' method,[28,29] confirmed the $S=1$ ground state of **3**. Note that the μ_{eff} of **3** is significantly lower than expected for the spin-only value of a typical $S=1$ system ($\mu_{eff}=2.83\ \mu_B$); this can be attributed to the presence of unreacted copper(I) or copper(II) impurities in solutions of **3**.

We then turned to X-ray absorption spectroscopy (XAS) to directly probe the oxidation state of copper in **3**. Notably, **3** exhibited X-ray absorption near-edge structure (XANES) features nearly identical to those of the dinuclear Cu^{II} complex **2**. This finding strongly suggests that **3** also contains a Cu^{II} center (Figure S9); together with the experimentally determined μ_{eff} value of 2.14 μ_B, this may indicate an $[Cu^{II}(^{Me}L\text{-}N^{\bullet-})]^+$ electronic structure for **3**. Extended X-ray absorption fine structure (EXAFS) analysis revealed further structural details. For **3**, the first coordination sphere could be satisfactorily fitted by four nitrogen scatterers at a distance of 2.04 Å (Table S3, Figure S10). The outer-shell features could be accounted for by single scattering paths arising from two carbon atoms at 2.44 Å and twelve carbon atoms at 3.23 Å. EXAFS analysis of **2** was also performed to determine whether the solid-state dimeric structure is retained in a frozen acetonitrile solution. The best fit (Table S4) of the Cu EXAFS data of **2** consists of two subshells of four short N/O scatterers at 1.99 Å and one long N/O scatterer at 2.13 Å, supporting a five-coordinate Cu center in **2**, which is in agreement with the XRD studies (see above). Fits to a single shell of 5–6 nitrogen scatterers produced a significant decrease in fit quality. Cu EXAFS analysis of **2** also showed a shell at 2.93 Å corresponding to the Cu scatterer, which is in reasonable agreement with the Cu–Cu distance of 3.03 Å determined by XRD.

DFT calculations at the B3LYP/TZVP level of theory in acetonitrile at 298 K predicted a triplet ($S=1$; $J=+3.2\ cm^{-1}$) ground state for **3**. The excited open- and closed-shell singlet electronic states were determined to be 3 and 18 kcal mol^{-1} higher in energy, respectively. The copper center in the calculated structure of **3** (Scheme 2) adopts a strongly distorted tetrahedral geometry involving coordination of the four nitrogen atoms of ^{Me}L-N. Notably, the calculated metrical parameters are in reasonable agreement with the experimentally determined values (Table S3). Furthermore, the theoretically predicted Cu–N_{aryl} vibration at 427 cm^{-1} with a −6 cm^{-1} shift upon ^{15}N labeling is fully congruent with the experimental IR spectrum (see above). Interestingly, a spin density of 1.20 was obtained for the N_{aryl} atom, indicating that the excess unpaired electron density on nitrogen is larger than expected for a classical metal–nitrene radical system (Figures S18 and S19). Such a non-classical electronic structure has been reported previously for a cobalt–oxo species[30] and may be understood by considering the contribution of the Cu^{I}–nitrene biradical resonance form, where two electrons from the N_{aryl} atom moiety are transferred to the Cu center. The calculated spin density of 0.4 on the copper atom, which is significantly lower than the expected value of 1 for a Cu^{II} center, further confirms the contribution of both $[Cu^{II}(^{Me}L\text{-}N^{\bullet-})]^+$ and $[Cu^{I}(^{Me}L\text{-}N^{\bullet\bullet})]^+$ resonance forms to the electronic structure of **3**.

The reactivity of **3** in various oxidation reactions was also investigated. For example, transfer of the ^{Me}L-N unit of the copper–nitrene species **3** to phosphines was evaluated. The green color of a solution of **3** in acetonitrile disappeared upon addition of triphenylphosphine (PPh_3). ESI-MS analysis of the final reaction mixture gave rise to a peak at m/z 551.35, which is consistent with nitrogen insertion to the phosphorus atom to form ^{Me}L-N=PPh_3; this peak was shifted by one mass unit when 50% ^{15}N-labeled **3** (Figure S13) was used in the reaction. ^{31}P NMR analysis showed the presence of a resonance at 25.6 ppm, which falls in the region typical for N=P bonds,[31] that accounted for a yield of 41% with respect to **3** (NMR quantification using $OPPh_3$ as an internal standard). Interestingly, ^{31}P NMR analysis of a sample prepared by reacting 50% ^{15}N-labeled **3** with PPh_3 afforded the peak at 25.6 ppm together with a doublet at 25.3 ppm, corresponding to ^{Me}L-^{15}N=PPh_3, where coupling of ^{31}P with ^{15}N ($S=1/2$) occurs (Figure S14). The measured coupling constant of $J_{N,P}=38.2$ Hz is in accordance with those typically measured for N–P bonds, further supporting the formation of the nitrene transfer product.[32] UV/Vis monitoring of this reaction using excess substrate showed that the decay of the bands at 710 and 980 nm, which are associated with **3**, followed a pseudo-first-order behavior, so that the kinetic traces could be fitted with single exponentials (Figure S12). The observed reaction rate (k_{obs}) was in turn found to be linearly dependent on the substrate concentration, affording a second order constant (k_2) of 7.5 $M^{-1}s^{-1}$ for the reaction with PPh_3. Interestingly, the k_2 values were highly dependent on the substituents at the phosphorus atom. Thus the reaction of **3** with sterically bulkier tri(*o*-tolyl)phosphine was two orders of magnitude slower (0.052 $M^{-1}s^{-1}$) than that with PPh_3 whereas the reaction with tri(*n*-butyl)phosphine was too fast, and the reaction rate could not be determined. Finally, the reaction rates were found to be dependent on the substituent at the *para* position of the aryl groups attached to the phosphine. The logarithm of the second-order rate constants of a series of *para*-X-triarylphosphine (X = Me, H, and Cl) derivatives gave a negative correlation with the Hammett parameter (σ_p) with a reaction constant (ρ) of −1.9, which is indicative of the electrophilic character of **3** (Figure S15).

Reactions of **3** with hydrocarbons bearing C–H bonds with low dissociation energies (BDEs) were also evaluated, and xanthene was used as a model substrate. Strikingly, the k_2 value measured for this reaction ($k_2=0.009\ M^{-1}s^{-1}$, BDE = 75.5 kcal mol^{-1}) was lower than that determined for the reaction with 1,4-cyclohexadiene ($k_2=0.020\ M^{-1}s^{-1}$, BDE = 78 kcal mol^{-1}), which does not correlate with the C–H bond strength. Again, steric hindrance could be a reason for this result so that the smaller 1,4-cyclohexadiene substrate reacts faster despite its increased C–H bond strength (Table S5). Furthermore, a kinetic isotope effect of 5.2 was measured when $[D_2]$xanthene was used as the substrate at 25 °C (Figure S16).

In summary, we have reported the synthesis and spectroscopic characterization of a terminal copper–nitrene species (**3**) without the need of using redox-innocent cations such as Sc^{3+}. The apparently simple methylation of the secondary amines in ^{H}L-N_3 was crucial to slow down the N–N bond-

formation event, thus retarding the main decomposition pathway for the copper–nitrene species in this system. Interestingly, this species could be trapped at room temperature, and it can undergo nitrogen-transfer reactions to organic substrates such as phosphines and abstract hydrogen atoms from weak C–H bonds.

Acknowledgements

This work was supported by the European Commission (2011-CIG-303522 to A.C.), the MINECO of Spain ("Ramón y Cajal" contract to A.C. and CTQ2013-43012-P to A.C. and X.R.), the Clara Immerwahr award of UniCat (to A.C.), the European Research Council (Starting Grant ERC-2011-StG-277801 to X.R.), and the Generalitat de Catalunya (2014 SGR 862). K.R. thanks the DFG for a Heisenberg Professorship. X.R. also acknowledges an ICREA Acadèmia award. The XAS measurements at SSRL BL 2-2 were made possible by the US Department of Energy, Office of Science (DE-AC02-76SF00515 and DE-SC0012704 to SSRL and NSLS-II, respectively) and the US National Institutes of Health (P30-EB-009998 to the CWRU Center for Synchrotron Biosciences).

Keywords: copper–nitrene species · density functional calculations · hydrogen atom abstraction · mass spectrometry · nitrene transfer

How to cite: *Angew. Chem. Int. Ed.* **2016**, *55*, 14005–14008
Angew. Chem. **2016**, *128*, 14211–14214

[1] R. T. Gephart, T. H. Warren, *Organometallics* **2012**, *31*, 7728–7752.
[2] Y. M. Badiei, A. Krishnaswamy, M. M. Melzer, T. H. Warren, *J. Am. Chem. Soc.* **2006**, *128*, 15056–15057.
[3] Y. M. Badiei, A. Dinescu, X. Dai, R. M. Palomino, F. W. Heinemann, T. R. Cundari, T. H. Warren, *Angew. Chem. Int. Ed.* **2008**, *47*, 9961–9964; *Angew. Chem.* **2008**, *120*, 10109–10112.
[4] K. Ray, F. Heims, F. F. Pfaff, *Eur. J. Inorg. Chem.* **2013**, 3784–3807.
[5] J. Hohenberger, K. Ray, K. Meyer, *Nat.Commun.* **2012**, *3*, 720.
[6] X. Hu, K. Meyer, *J. Am. Chem. Soc.* **2004**, *126*, 16322–16323.
[7] D. A. Iovan, T. A. Betley, *J. Am. Chem. Soc.* **2016**, *138*, 1983–1993.
[8] C. A. Laskowski, A. J. M. Miller, G. L. Hillhouse, T. R. Cundari, *J. Am. Chem. Soc.* **2011**, *133*, 771–773.
[9] L. Zhang, Y. Liu, L. Deng, *J. Am. Chem. Soc.* **2014**, *136*, 15525–15528.
[10] M. J. B. Aguila, Y. M. Badiei, T. H. Warren, *J. Am. Chem. Soc.* **2013**, *135*, 9399–9406.
[11] S. Kundu, E. Miceli, E. Farquhar, F. F. Pfaff, U. Kuhlmann, P. Hildebrandt, B. Braun, C. Greco, K. Ray, *J. Am. Chem. Soc.* **2012**, *134*, 14710–14713.
[12] I. Monte-Pérez, S. Kundu, K. Ray, *Z. Anorg. Allg. Chem.* **2015**, *641*, 78–82.
[13] F. Dielmann, D. M. Andrada, G. Frenking, G. Bertrand, *J. Am. Chem. Soc.* **2014**, *136*, 3800–3802.
[14] A. Casitas, M. Canta, M. Solà, M. Costas, X. Ribas, *J. Am. Chem. Soc.* **2011**, *133*, 19386–19392.
[15] A. Casitas, A. E. King, T. Parella, M. Costas, S. S. Stahl, X. Ribas, *Chem. Sci.* **2010**, *1*, 326–330.
[16] M. Rovira, M. Font, X. Ribas, *ChemCatChem* **2013**, *5*, 687–691.
[17] M. Rovira, M. Font, F. Acuña-Parés, T. Parella, J. M. Luis, J. Lloret-Fillol, X. Ribas, *Chem. Eur. J.* **2014**, *20*, 10005–10010.
[18] L. M. Huffman, A. Casitas, M. Font, M. Canta, M. Costas, X. Ribas, S. S. Stahl, *Chem. Eur. J.* **2011**, *17*, 10643–10650.
[19] M. Font, T. Parella, M. Costas, X. Ribas, *Organometallics* **2012**, *31*, 7976–7982.
[20] D. S. Marlin, M. M. Olmstead, P. K. Mascharak, *Inorg. Chem.* **2001**, *40*, 7003–7008.
[21] The hydroxo ligands in the structure of **2** were found to undergo exchange with $H_2{}^{18}O$, as determined by ESI-MS (see Figure S6).
[22] M. Costas, X. Ribas, A. Poater, J. M. López Valbuena, R. Xifra, A. Company, M. Duran, M. Solà, A. Llobet, M. Corbella, M. A. Usón, J. Mahía, X. Solans, X. Shan, J. Benet-Buchholz, *Inorg. Chem.* **2006**, *45*, 3569–3581.
[23] T. A. Betley, J. C. Peters, *J. Am. Chem. Soc.* **2004**, *126*, 6252–6254.
[24] K. C. MacLeod, D. J. Vinyard, P. L. Holland, *J. Am. Chem. Soc.* **2014**, *136*, 10226–10229.
[25] N. D. Harrold, R. Waterman, G. L. Hillhouse, T. R. Cundari, *J. Am. Chem. Soc.* **2009**, *131*, 12872–12873.
[26] Analogously to **1**, self-decomposition of **3** occurred by N_2 release and N–N bond formation to form an indazole ring (70% yield) along with methane release (see the Supporting Information).
[27] 50% ^{15}N-labeled **3** was formed by reaction of $[Cu^{I}(CH_3CN)_4](CF_3SO_3)$ with singly ^{15}N-labeled ^{Me}L-N_3 (synthesized by reaction of ^{Me}L-Br with singly terminal-labeled sodium azide).
[28] D. F. Evans, *J. Chem. Soc.* **1959**, 2003–2005.
[29] M. L. Naklicki, C. A. White, L. L. Plante, C. E. B. Evans, R. J. Crutchley, *Inorg. Chem.* **1998**, *37*, 1880–1885.
[30] D. W. Crandell, S. Ghosh, C. P. Berlinguette, M.-H. Baik, *ChemSusChem* **2015**, *8*, 844–852.
[31] S. Kundu, PhD Thesis, Department of Chemistry, Humboldt Universität zu Berlin (Germany), **2013**.
[32] W. Gombler, R. W. Kinas, W. J. Stec, *Z. Naturforsch* **1983**, *38*, 815–818.

Received: July 26, 2016
Published online: October 10, 2016

Chapter VII.

Results and Discussion

VII. RESULTS AND DISCUSSION

This thesis is presented using the “compendium of publications” format following the rules of the School of Doctoral Studies from University of Girona. According to these rules, the publications must be accompanied by a “Results and Discussion” chapter which consists of a discussion of the publications (Chapters III to VI).

This “Results and Discussion” chapter is divided in different parts. Section VII.1 depicts our progress in trapping two highly reactive high-valent nickel-oxygen species by the reaction of a novel Ni^{II} complex bearing an unsymmetric macrocyclic bis(carboxamidate) ligand with *meta*-chloroperbenzoic acid (*m*CPBA) or NaOCl as oxidants. Both compounds are much more reactive towards organic substrates (e.g. C-H bonds, C=C bonds, and sulfides) than previously reported well-defined nickel–oxygen species. In section VII.2, we will turn out attention to the activation of nitrous oxide (N_2O) with first-row transition metals. We present a novel cobalt(II) complex using the same ligand that in the previous work that proved to be highly reactive with N_2O under mild conditions (T= 0 ºC and P= 1 atm). Despite the fact that the formed cobalt species could not be trapped, some mechanistic studies were performed suggesting the involvement of a cobalt(IV) species. This species is able to deformylate aldehydes under catalytic conditions. Finally, in section VII.3 we will turn our interest in trapping imidocopper species that have been long considered the active species in copper catalyzed C-N bond formation reactions, but have eluded detection for decades. The present work reports the spectroscopic trapping of an elusive Cu^{II}-N• species (characterized by FT-IR, EPR, XAS as well as MS and DFT) and detailed investigation of its reactivity (nitrene-transfer to weak C-H bonds and phosphines).

VII.1. Spectroscopy and reactivity of two high-valent nickel-oxygen oxidizing species

This section corresponds to the contents of the manuscript by Corona *et al. Chem. Eur. J.* **2015**, *21*, 15029-15038, which can be found in **Chapter III** of this thesis and the manuscript by Corona *et al. J. Am. Chem. Soc.* **2016**, *138*, 12987-12996, which can be found in **Chapter IV** of this thesis. In **Chapter III** and **Chapter IV** Teresa Corona (T.C.) synthesized and fully characterized the ligand and the corresponding nickel(II) complex, and she also performed the reactivity studies. T.C. also performed the computational studies under the supervision of Ferran Acuña-Parés and Julio Lloret-Fillol. EPR studies were performed in collaboration with Ray's group at Humboldt Universität zu Berlin (Florian F. Pfaff and Kallol Ray) through a short research stay of T.C. (1 week). Resonance Raman studies were done in collaboration with Browne's group at University of Groningen (Apparao Draksharapu, Sandeep K. Padamati and Wesley R. Browne) through a short visit of T.C. (1 week). Besides, T.C. carried out the reactivity studies towards substrates and was involved in the generation of XAS samples that were run by Christopher J. Whiteoak, Ilaria Gamba and Vlad Martin-Diaconescu at SOLEIL synchrotron (France) and European synchrotron radiation facility in Genoble (France). Vlad Martin-Diaconescu carried out the analysis of the XAS data. These works were supervised and coordinated by Anna Company.

Terminal high-valent metal-oxygen species are key reaction intermediates in the catalytic cycle of both enzymes (e.g. oxygenases) and synthetic oxidation catalysts. While tremendous efforts have been directed towards the characterization of the biologically relevant terminal manganese-oxygen and iron-oxygen species, the corresponding analogues based on late-transition metals such as cobalt, nickel or copper are relatively scarce. This scarcity is in part related to the "Oxo-wall" concept, which predicts that late transition metals cannot support a terminal oxido ligand in a tetragonal environment (see I.2.3). Elucidating the mechanisms by which reactions catalyzed by late transition metal complexes proceed is essential for the rational development of selective catalytic reagents based on these metals, and requires a comprehensive understanding of the structure and properties of the active species. In **Chapters III** and **IV** of this thesis we report the detection of high-valent nickel-oxygen species which are relevant in nickel-mediated oxidation catalysis.

VII.1.1. Ligand design and synthesis

We have chosen a very particular ligand in order to stabilize high-valent oxometal species. The ligand is a tetradentate macrocycle ligand which combines carboxamide, aliphatic amines and pyridine groups as donor atoms (H_2L1, Scheme VII.1). Deprotonation of the two carboxamide functional groups enables the preparation of the dianionic ligand L1. Due to the highly donor character of the deprotonated ligand, the metal that coordinates becomes particularly electron rich and it is eager to transfer electrons to oxidants achieving their reductive activation. Indeed,

carboxamidate groups have proved to be highly successful structural motifs to support well-defined high-valent species including metal-oxygen compounds.[1] The availability of free coordination sites around the metal center for interaction with the oxidants is also a prerequisite to achieve the formation of the desired metal-oxygen species. The dianionic ligand L1 does not only increase the electron-richness of the metal center, but it also may be suitable for the stabilization of high-valent metal species generated upon reaction with oxidants.

The synthetic strategy to prepare H_2L1 consisted of four reaction steps (Scheme VII.1). Selective methylation of the central amine of the commercially available *N*-(2-aminoethyl)-1,3-propanediamine was necessary.[2] In order to do so, firstly the two primary amines of the triamine were selectively protected by reaction with phthalic anhydride to give a phthaloyl group (**a**). Methylation and amine deprotection with hydrazine afforded the desired monomethylated triamine (**c**). Cyclization with 2,6-pyridinedicarbonyl dichloride gave H_2L1 in 21% isolated yield as a white solid after purification by column chromatography. In this final step high dilution conditions and slow addition of the triamine over 2,6-pyridinedicarbonyl dichloride were necessary in order to obtain the desired 1+1 product and to minimize the formation of 2+2 and 3+3 products as well as higher molecular weight oligomers as reaction by-products. Compound H_2L1 was fully characterized by elemental analysis, high resolution ESI-MS, NMR spectroscopy (^{1}H-NMR, ^{13}C-NMR, COSY and HSQC) and X-ray diffraction (Scheme VII.1). A detailed description of the synthesis and characterization of H_2L1 is included in the annex (p.145-149).

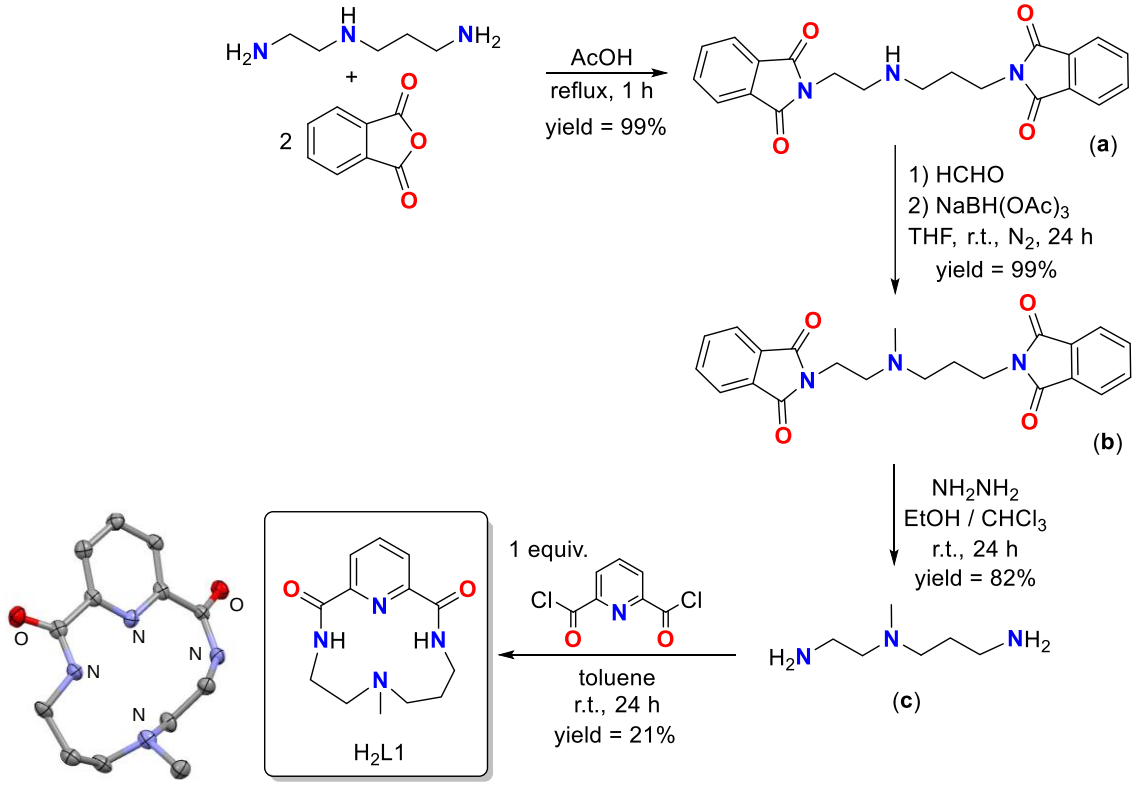

Scheme VII.1. Synthetic route for the preparation of H_2L1 and XRD structure of ligand H_2L1 (ellipsoids drawn at 50% probability and hydrogen atoms omitted for clarity).

VII.1.2. Synthesis of the nickel(II) complex (**1**)

Reaction of H_2L1 in anhydrous CH_3CN with 1 equiv. $[Ni^{II}(CF_3SO_3)_2(CH_3CN)_3]$ followed by addition of 2 equiv. NaH under an inert atmosphere at room temperature afforded after crystallization the corresponding nickel(II) complex $[Ni^{II}(L1)]$ (**1**) as an orange crystalline solid, which co-crystallized with $NaCF_3SO_3$ (72% yield). The XRD structure of **1** (Figure VII.1) shows a nickel(II) center in a square planar geometry with coordination to the four N-donor atoms of the macrocyclic ligand. The Ni-nitrogen bond lengths (Ni-N_{py} 1.80 Å; Ni-N_{CH3} 1.93 Å; Ni-$N_{carboxamidate}$ 1.85-1.87 Å) fit well with those previously reported for nickel(II) square planar complexes with pyridine, amine or carboxamidate-based ligands.[3,4] The complex is diamagnetic (Figure VII.2), as expected for a d^8 metal with a square planar geometry, so that complete ^{1}H-NMR and ^{13}C-NMR characterization by 1-D and 2-D NMR techniques could be carried out. Due to the asymmetric nature of H_2L1, the complex does not present C_2 symmetry and the β protons of the pyridine appear as two separate doublets at 7.43 and 7.36 ppm. High resolution ESI-MS exhibited a major peak at *m/z* 341.0530 with a mass value and an isotopic pattern fully consistent with $\{[Ni(L1)]+Na\}^+$.

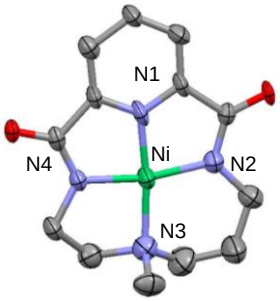

$[Ni^{II}(L1)]$ (compound **1**)	
Ni(1)-N(1)	1.794(11)
Ni(1)-N(4)	1.850(9)
Ni(1)-N(2	1.863(10)
Ni(1)-N(3)	1.929(11)
N(1)-Ni(1)-N(4)	84.1(4)
N(1)-Ni(1)-N(2)	84.2(4)
N(4)-Ni(1)-N(3)	89.7(5)
N(2)-Ni(1)-N(3)	101.9(5)

Figure VII.1. XRD structure and selected bond lengths (Å) and angles (°) for $[Ni^{II}(L1)]$ (**1**) (ellipsoids drawn at 50% probability; hydrogen atoms and co-crystallized $NaCF_3SO_3$ omitted for clarity).

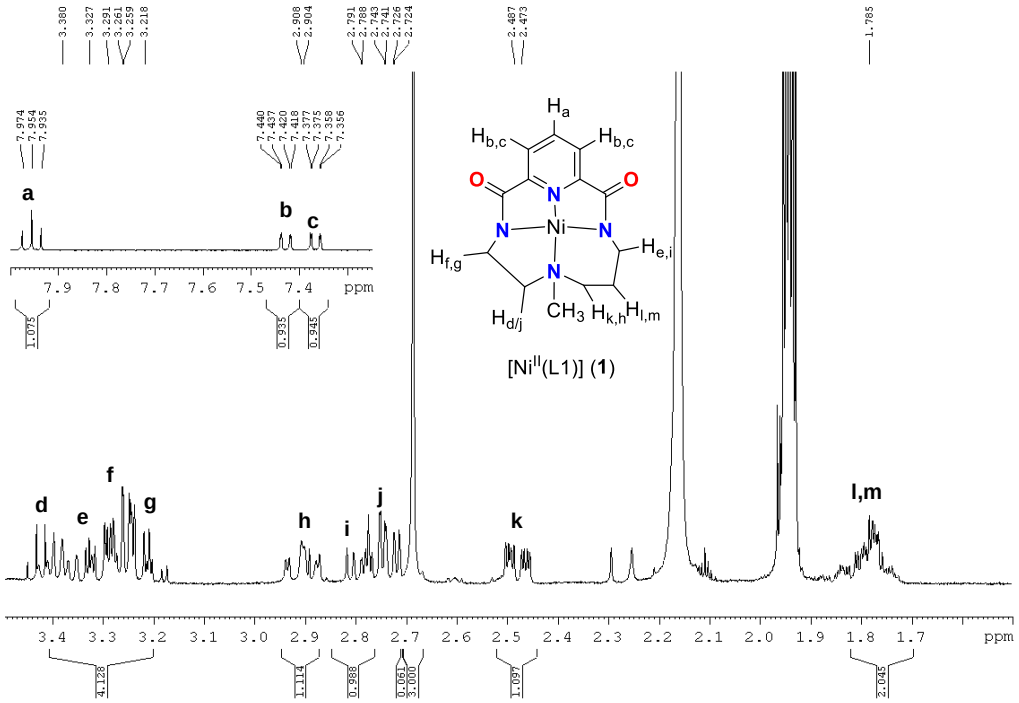

Figure VII.2. ^{1}H-NMR spectrum of $[Ni^{II}(L1)]$ (**1**) in CD_3CN at 25 ºC (400 MHz).

*VII.1.3. Catalytic oxidation/chlorination of alkanes by **1** and mCPBA or NaOCl*

The performance of compound **1** as catalyst in oxidation reactions under mild reaction conditions using cyclohexane as a model substrate was tested. Firstly, environmentally friendly oxidants such as O_2, H_2O_2, N_2O or ROOH were used but unfortunately only traces of oxidized products were detected. Instead, the use of *meta*-chloroperbenzoic acid (*m*CPBA) and NaOCl as oxidants afforded very promising results.

The combination of compound **1** (1 equiv.) with *m*CPBA (150 equiv.) in CH_3CN at room temperature afforded the oxidation of cyclohexane (15000 equiv.) to form equal amounts of cyclohexanol and cyclohexanone with a total of 100 ± 3 turnovers after stirring for 1 hour (67% yield based on the oxidant). Importantly, blank experiments without nickel afforded only trace amounts of the oxidized products (<0.5% yield based on the oxidant).

Catalytic oxidation of C-H bonds was also achieved when NaOCl was used as oxidant. Treatment of **1** (1 equiv.) with NaOCl (100 equiv.) in the presence of acetic acid (AcOH) (100 equiv.) and cyclohexane (300 equiv.) in CH_3CN at -30 ºC for 2 hours under N_2 afforded 34 ± 4 turnovers of chlorocyclohexane and 7 ± 1 turnovers of cyclohexanone. Surprisingly, lower turnover numbers were obtained when the same reaction was carried out at room temperature, indicating that at higher temperatures other parallel unproductive reactivity is taking place. Interestingly, blank experiments in the absence of compound **1** or AcOH showed lower yields, indicating that all the reagents were necessary to obtain efficient oxidation/chlorination. Remarkably, these yields and turnover numbers are higher than those previously reported for alkane chlorination/oxidation reactions catalyzed by $[Ni^{II}(Pytacn)(CH_3CN)_2](CF_3SO_3)_2$ (Pytacn = 1-(2-pyridylmethyl)-4,7-dimethyl-1,4,7-triazacyclononane)[5], or [Mn(TPP)Cl] (TPP = tetraphenylporphyrin) using NaOCl as oxidant.[6]

Given the catalytic reactivity of **1** with *m*CPBA and NaOCl towards cyclohexane, at this point, insight into the nature of the oxidizing species involved in both systems was gained through spectroscopic techniques. Therefore, in the following sections we will summarize the results obtained for the **1**/*m*CPBA and **1**/NaOCl systems.

*VII.1.4. Spectroscopic characterization of the active species in the **1**/mCPBA system*

Reaction of **1** towards *m*CPBA was qualitatively evaluated. Generally, metal-oxygen species are colored species due to ligand-to-metal or metal-to-ligand charge transfer bands and thus they can be readily detected by UV-vis spectroscopy. Moreover, this technique enables the monitoring of reactions using minimum amounts of metal complexes and at very low temperature. This may be necessary to detect highly reactive and elusive molecules, which is commonly the case for high-valent metal-oxygen species.

UV-vis monitoring of the reaction of **1** with 3 equiv. *m*CPBA in CH_3CN at -30 ºC evidenced the formation of a metastable orange species (**2**) with a visible absorption band at 420 nm ($\varepsilon > 7000$ $M^{-1}cm^{-1}$) and a shoulder at 580 nm ($\varepsilon > 800$ $M^{-1}cm^{-1}$) (Figure VII.3). Compound **2** was not observed when the reaction was run at room temperature and its half-life time at -30 ºC was 4.5 hours.

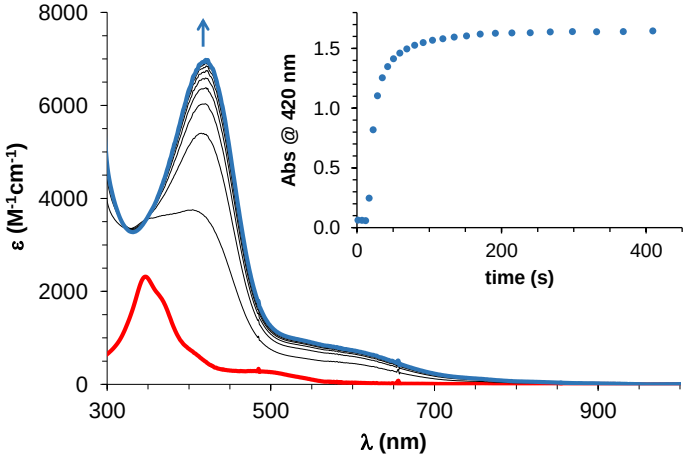

Figure VII.3. UV-vis absorption spectral changes observed upon reaction of **1** (red line) with 3 equiv. *m*CPBA in CH_3CN at -30 ºC to form **2** (blue line). Inset: kinetic trace at 420 nm.

At this point, we tested the stoichiometric reactivity of compound **2** in the presence of different substrates. Thus, addition of several substrates to fully formed **2** caused the immediate decay of this species indicating that this compound interacted with the substrate. Analysis of the final product after the reaction of **2** with alkanes (cyclohexane, toluene or ethylbenzene) showed the formation of the corresponding ketone as the major product. Similarly, reaction of **2** with alkenes afforded the epoxide product (Table VII.1). Due to the fact that peracids are strong oxidants which under certain conditions can oxidize substrates without the need of a metal catalyst, blank experiments using *m*CPBA without nickel complex (**1**) were carried out. In all cases, under our experimental conditions, only small traces of oxidized products were obtained.

Table VII.1. Turnover numbers of oxidation products (with respect to the nickel complex **1**) obtained in the reaction of **2** with different substrates in CH_3CN at -30 ºC.[a]

Substrate	Oxidation products	Turnovers (blank[b])
cyclohexane	cyclohexanol / cyclohexanone	0.08 (0) / 0.5 (0)
toluene	benzyl alcohol / benzaldehyde	0.01 (0) / 0.2 (0)
ethylbenzene	1-phenylethanol / acetophenone	0.02 (0) / 0.3 (0)
cyclooctene	cyclooctene oxide	1.4 (0.01)
1-octene	1,2-epoxyoctane	0.5 (0)
4-methylstyrene	4-methylstyrene oxide	1.4 (0.1)
cis-2-octene	*cis*-2,3-epoxyoctane	2.0 (1.1)

[a] Compound **2** (formed by reaction of **1** with 3 equiv. *m*CPBA in CH_3CN at -30 ºC) was reacted with a known amount of substrate and the reaction monitored by UV-vis spectroscopy. Once compound **2** had completely decayed, the reaction was quenched by the addition of excess $NaHSO_3$ and an internal standard (biphenyl) was added. The reaction mixture was analyzed by GC-FID. [b] Blank experiments performed in the absence of **1**.

Given the high reactivity of compound **2** towards several substrates, including alkanes bearing strong C-H bonds, further insight into the nature of compound **2** was pursued by using several spectroscopic techniques. First of all, we attempted the characterization of **2** by cryospray

ionization mass spectrometry (CSI-MS) at -30 ºC, which showed a clean spectrum with a major peak at *m/z* 318.0605, with a mass value and an isotopic pattern fully consistent with $\{[Ni(L1)]\}^+$, corresponding to a nickel(III) complex containing ligand L1. Importantly, the mass spectrum obtained after the self-decay of **2** only exhibited signals corresponding to nickel(II) species with oxidized/dehydrogenated ligand (*m/z* = 355.0319 and 369.0105).

In order to establish the oxidation state of compound **2**, electron paramagnetic resonance (EPR) experiments were carried out. EPR spectra of **2** at 77 K showed the presence of 16% of two rhombic *S* = 1/2 species; a major species (95%) with g_1= 2.03, g_2= 2.22, and g_3= 2.24 and a minor component (5%) with g_1= 2.02, g_2= 2.19,and g_3= 2.31 (Figure VII.4). The *g* values suggested the presence of nickel(III) in a distorted square planar, trigonal bipyramidal, or compressed octahedral geometries with the unpaired electron in d_{xy} or d_{x2-y2} orbital.[7] In order to confirm if the chromophoric species **2** corresponded to the nickel(III) observed by EPR, several EPR samples were taken over the course of the formation and decay of **2** (Figure VII.5). However, the time-dependence of the EPR signal intensity did not correlate with the behaviour of the UV-vis band at 420 nm (or its shoulder at 580 nm) assigned to **2**. The concentration of nickel(III) increased when compound **2** disappeared. Presumably, nickel(III) corresponds to a decomposition species of **2** which is not responsible for the oxidation chemistry. Moreover, in the presence of substrate the intensity of the EPR signal remained more or less constant along the decomposition of **2**, supporting the idea that compound **2** is not correlated with the EPR signal attributed to a nickel(III) species.

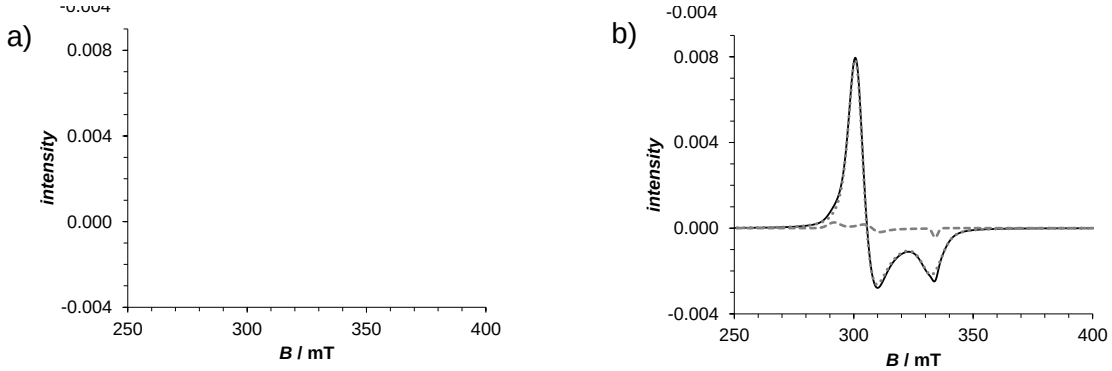

Figure VII.4. a) EPR spectrum of the reaction of **1** (1.9 mM) with 3 equiv. *m*CPBA in CH_3CN at -30 ºC after 60 seconds under argon. b) Simulated EPR spectrum (black line), which accounts for a major species (95%, dotted line) and a minor species (5%, dashed line).

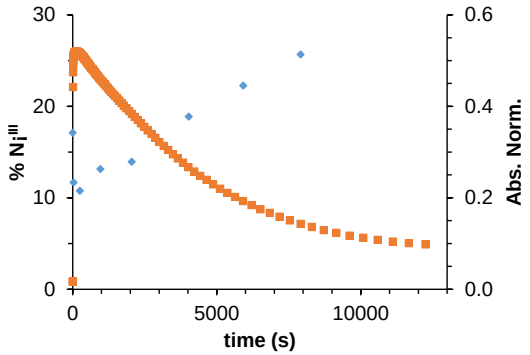

Figure VII.5. Orange dots: time-course of the self-decay of **2** generated by adding 3 equiv. *m*CPBA to **1** (0.5 mM) in CH_3CN at -25 ºC followed by UV-vis absorption spectroscopy (λ = 580 nm). Blue dots: Total intensity of the nickel(III) EPR signals.

Interestingly, the addition of 2.75 equiv. of **1** to fully formed **2** showed an immediate decay of the characteristic band at 420 nm by UV-vis spectroscopy (the addition of 1 equiv. of **1** over **2** resulted in a very slow reaction, and for this reason higher amounts of **1** were used). Moreover, EPR analysis of the resulting solution indicated the presence of 35% nickel(III) species (maximum possible yield is 53%, Scheme VII.2). Furthermore, the high-resolution ESI-MS of the resulting solution presented a clean spectrum with a major peak at *m/z* 318.0617, corresponding to nickel(III) complex at room temperature (Figure VII.6). All this data suggested that most likely compound **2** could be formulated as a formal nickel(IV) species that comproportionates with the nickel(II) species (**1**) to form the corresponding nickel(III) complex as detected by EPR.

$$\text{Ni(II)} + m\text{CPBA} \longrightarrow \text{Ni(IV)=O} + \text{H}^+$$
$$\text{Ni(IV)=O} + 2.75\ \text{Ni(II)} + 2\text{H}^+ \longrightarrow 2\text{Ni(III)-OH} + 1.75\ \text{Ni(II)}$$
$$\text{Total reaction: } 3.75\ \text{Ni(II)} + m\text{CPBA} + \text{H}^+ \longrightarrow 2\text{Ni(III)-OH} + 1.75\ \text{Ni(II)}$$

Maximum possible yield of Ni(III) = (2/3.75) * 100 **= 53 %**

Scheme VII.2. Balanced equation for the reaction of **2** with 2.75 equiv. of **1**.

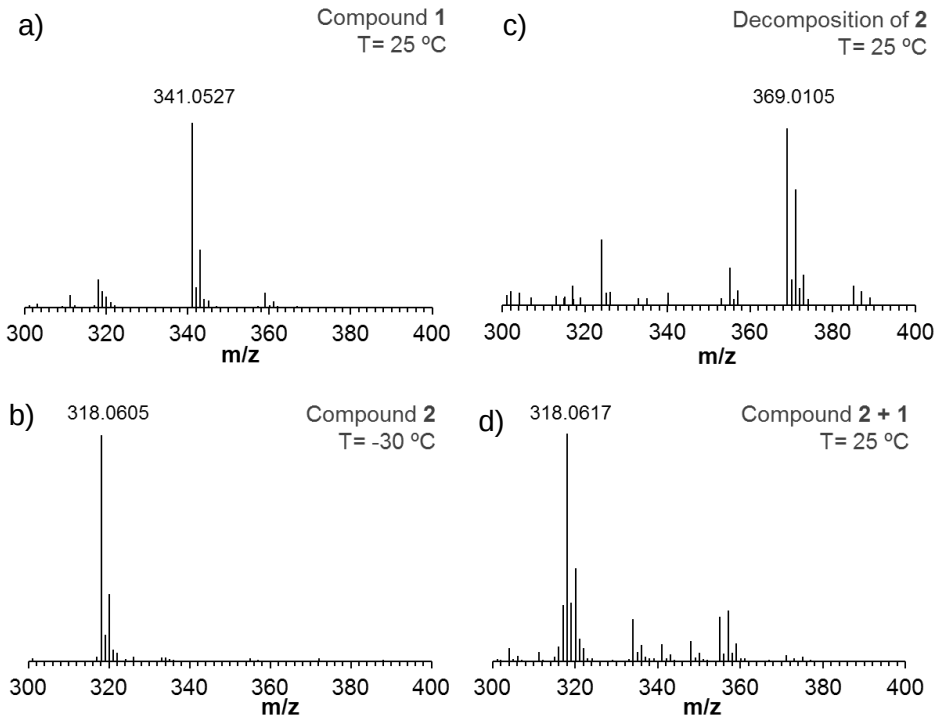

Figure VII.6. MS spectra in CH_3CN of: (a) compound **1**; (b) compound **2** obtained by reaction of **1** with 3 equiv. *m*CPBA at -30 ºC; (c) the final reaction mixture after decomposition of **2** at room temperature; (d) the reaction mixture obtained after reaction of compound **2** with 2 equiv. of **1** at room temperature.

Further insight into the nature of the oxidizing species **2** was gained through X-ray absorption spectroscopy (XAS) experiments at the metal K-edge. The pre-edge of **2**, associated to the 1s → 3d transition, showed the presence of high-valent nickel species because it occurred at ~8333.5

eV with a normalized area of 0.16. Normally, the 1s $\rightarrow$ 3d transition for nickel(II) complexes appear at ~8332 eV and are 2 to 3 fold less intense. The presence of a 1.5–2 eV higher rising edge energy (~8343.4 eV) compared to previously reported nickel(II) complexes is consistent with a nickel(III) species.[8,9] Overall, X-ray absorption near edge structure (XANES) analysis of compound **2** suggested a +3 oxidation state of the nickel center (Figure VII.7a). On the other hand, extended X-ray absorption fine structure (EXAFS) studies showed two longer Ni-N/O bonds at ~2.12 Å and three shorter N/O bonds at ~1.88 Å for compound **2** (Figure VII.7b).

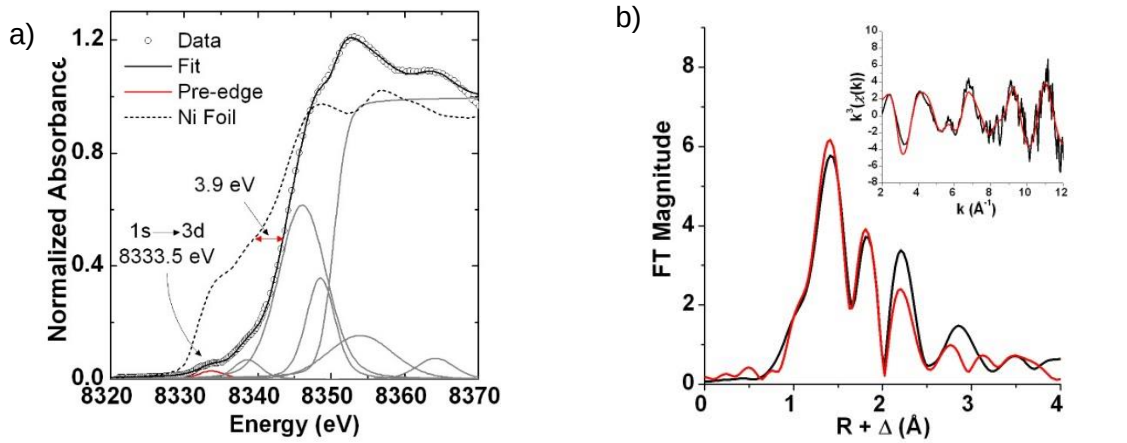

Figure VII.7. a) Ni K-edge XANES region for Ni foil and compound **2**. b) Fourier-transformed EXAFS spectra of **2** (no phase correction, FT window 2-12 $Å^{-1}$): *black line* data, *red line* best fit. Inset: k^3-weighted unfiltered EXAFS spectra: *black line* data, *red line* best fit.

At this point, density functional theory (DFT) calculations (uB3LYP/TZVP) were carried out to support the experimental data. Given the precedents in the literature, four different mechanistic pathways were considered for the reaction of **1** with *m*CPBA (pathways A-D, Scheme VII.3). Pathway A generates an acylperoxonickel(II) species. Nonetheless, this pathway was found to be kinetically and thermodynamically unfavourable because it required a high free energy (ΔG^o = +47.7 kcal·mol^{-1}). This could be due to the pK_a of *m*CPBA (pK_a = 31), which was computed to be much higher than for **1** (pK_a = 7) in CH_3CN, so the proton transfer from *m*CPBA to **1** is not likely to occur. Pathways B and C would involve the formal oxidation of nickel(II) to nickel(III) and then coordination of *m*CPBA or its deprotonated form. However, DFT calculations suggested that these two pathways were thermodynamically unfeasible (pathway B: ΔG^o = +30.0 kcal·mol^{-1}; pathway C: ΔG^o = +13.5 kcal·mol^{-1}). This agrees well with experimental results suggesting that species **2** is not EPR active and it is not a simple nickel(III) species.

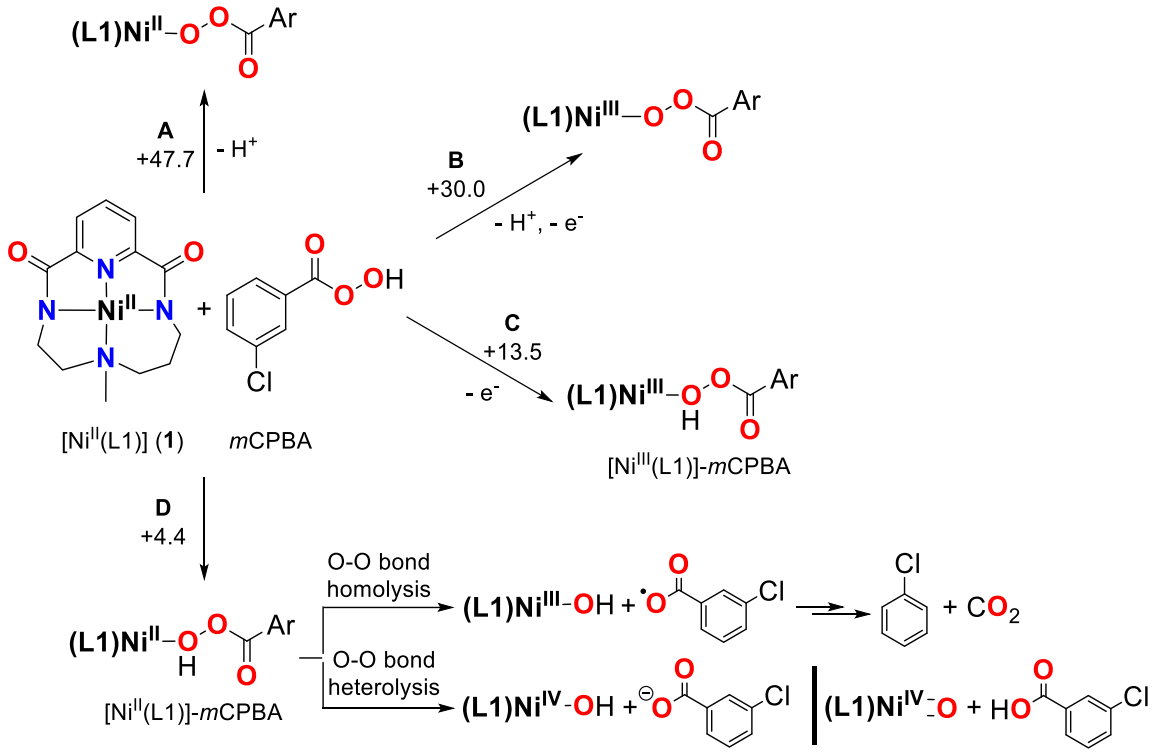

Scheme VII.3. Possible pathways (A-D) corresponding to the reaction of **1** with *m*CPBA in CH_3CN studied by DFT. Gibbs free energies are in kcal·mol^{-1} at -30 ºC.

In contrast, we found that the formation of an adduct between **1** and *m*CPBA, [Ni^{II}(L1)]-*m*CPBA was thermodynamically plausible with a ΔG^{o} value of +4.4 kcal·mol^{-1} (pathway D, Scheme VII.3). [Ni^{II}(L1)]-*m*CPBA may evolve through two different pathways:

a) *Homolytic O-O bond cleavage* to form a hydroxonickel(III) species together with the carboxyl radical, which decomposes to generate chlorobenzene and carbon dioxide.

b) *Heterolytic O-O bond cleavage* to form an oxo/hydroxonickel(IV) intermediate together with the corresponding benzoate or benzoic acid.

DFT studies showed that the homolytic O-O bond cleavage was kinetically forbidden by +30.0 kcal·mol^{-1} (Scheme VII.4). In contrast, the heterolytic O-O bond cleavage presented a smaller kinetic barrier of only +9.0 kcal·mol^{-1} to form [Ni(L1)(O)]. Indeed, gas chromatographic analysis (GC-FID and GC-TCD) of the reaction mixture after self-decay of **2** did not show the presence of chlorobenzene or CO_2 but instead *meta*-chlorobenzoic acid (*m*CBA) was detected both by NMR and GC-MS. Overall, computation and experimental data supported the idea of heterolytic O-O bond cleavage in a [Ni^{II}(L1)]-*m*CPBA adduct to form compound **2**.

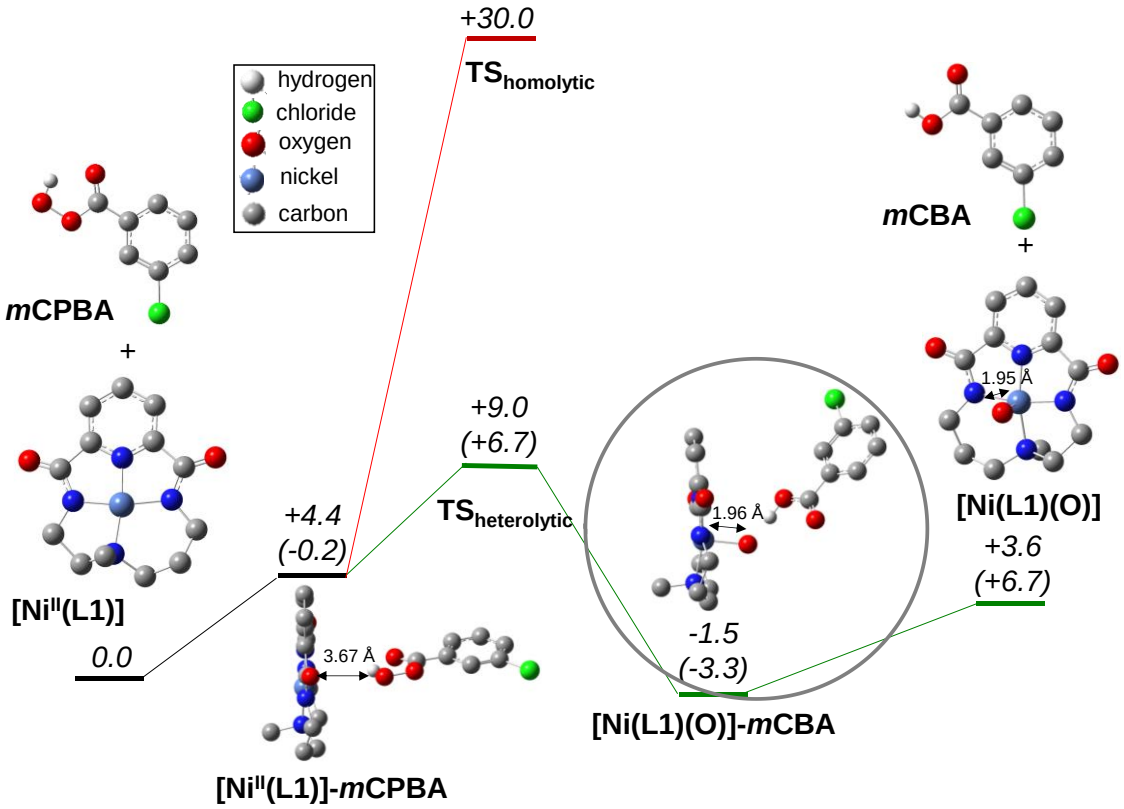

Scheme VII.4. Energetic profile of pathway D for the reaction of **1** with *m*CPBA in CH_3CN (homolytic and heterolytic O-O bond cleavage). Gibbs free energies are in kcal·mol^{-1} at -30 ºC. ΔE_{ZPE} in kcal·mol^{-1} are shown in parentheses.

Thus, a mononuclear terminal nickel-oxygen species with the general formula [Ni(L1)(O)] in a triplet ground state (S = 1) was predicted as the most plausible structure for **2**, in which the nickel center presents a distorted square pyramidal geometry with the oxygen atom occupying the apical position. Interestingly, the lowest energy structure entailed a weak interaction between the terminal oxygen atom bound to nickel and the benzoic acid by-product (*m*CBA), giving [Ni(L1)(O)]-*m*CBA. Spin density analysis of the computed structure of compound **2** indicated that this compound is best formulated as an oxylnickel(III) species [Ni^{III}(L1)(O•)] rather than an oxonickel(IV) species [Ni^{IV}(L1)(O)] (Figure VII.8a). Thus, the nickel center has significant spin density (ρ(Ni) = 0.66) but most of it is located on the oxygen moiety (ρ(O) = 1.29). Furthermore, analysis of the spin natural orbitals (SNOs) of **2** showed two single occupied orbitals (Figure VII.8b). The first one is distributed between the nickel and oxygen atoms, and the second one mainly involves the oxygen ligand. This formulation is reasonable if the “Oxo-wall” concept is taken into account (see Introduction section I.2.3) for which oxometal species are only possible for metals with a +4 minimum oxidation state and no more than 4 d electrons in tetragonal environments.

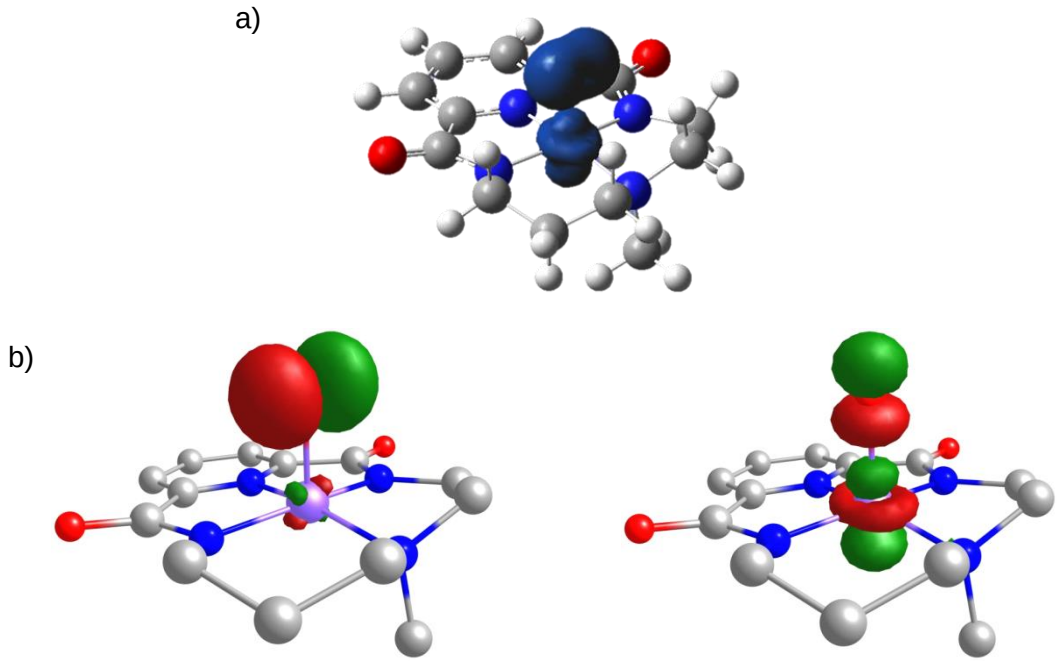

Figure VII.8. a) Isodensity surface (isovalue = 0.01) of the spin density for [Ni(L1)(O)]. b) Spin natural orbitals (SNOs) for [Ni(L1)(O)].

Finally, resonance Raman (rRaman) spectroscopy of **2** was attempted using a frozen CH_3CN sample (77 K) and laser excitation at 457 nm. At maximum accumulation of compound **2** the enhancement of two sets of bands at 450 and 477 cm^{-1} and 736 and 879 cm^{-1} was observed and these bands disappeared concomitantly with the decay of **2**. A Ni-O vibration at 433 cm^{-1} and a ligand stretching vibration at 443 cm^{-1} were predicted for the computed structure of compound **2**, $[Ni^{III}(L1)(O\bullet)]$-*m*CBA. Thus, the experimentally detected first set of bands at 450 and 477 cm^{-1} bands may correspond to the Ni-O and ligand stretching frequencies computationally predicted. Instead, the other set of bands at around 800 cm^{-1} are tentatively assigned to O-O stretching modes from a by-product, which may correspond to the coordination of excess peracid with oxidized nickel(III) species.

The proposed theoretical structure for compound **2** was also in agreement with the experimental data (Table VII.2). Thus, EXAFS of compound **2** suggested three short Ni-N/O bonds at 1.88 Å and two long Ni-N/O bonds 2.12 Å, which is in accordance with the bond distances in the computed structure of $[Ni^{III}(L1)(O\bullet)]$ (Ni- N_{py}, 1.85 Å; Ni-$N_{carboxamidate}$, 1.86 and 1.90 Å; Ni-O 1.95 Å; Ni-N_{CH3} 1.96 Å). The +3 oxidation state of the nickel center predicted for **2** by XANES also agrees with the theoretical model. This formulation is also in accordance with the lack of EPR signals related to **2** observed in the X-band EPR analysis, for which compounds with an even number of unpaired electrons, as in the case of $[Ni^{III}(L1)(O\bullet)]$, are rarely detected. Finally, the lack of mass peaks with intensity time-profiles similar to the UV-vis chromophoric species **2** would agree with the fact that the computed structure, $[Ni^{III}(L1)(O\bullet)]$, is neutral.

In summary, both computational and experimental data supported that **2** is formed by heterolytic O-O bond cleavage in a nickel(II)-peracid adduct affording an oxylnickel(III) species [Ni^{III}(L1)(O•)] that weakly interacts with the acidic proton of *meta*-chlorobenzoic acid affording [Ni^{III}(L1)(O•)]-*m*CBA.

Table VII.2. Summary of the experimental characterization of **2** and comparison with the theoretically predicted model [Ni^{III}(L1)(O•)]-*m*CBA.

techniques	**experimental data for compound 2**	**theoretical model [Ni^{III}(L1)(O•)]-*m*CBA**
rRaman	450 cm^{-1} / 477 cm^{-1}	υ(Ni-O) 433 cm^{-1} / υ(ligand) 443 cm^{-1}
CSI-MS	no molecular mass peak detected	neutral molecule
X-band EPR	no signal related to **2** detected	S = 1 (even number of unpaired electrons)
XANES	the oxidation state of nickel fits with +3	the oxidation state of nickel is +3
EXAFS	5-coordinate Ni center (3 Ni-N/O 1.88 Å, 2 Ni-N/O 2.12 Å)	5-coordinate Ni center (Ni-N_{py} 1.85 Å, Ni-$N_{carboxamidate}$ 1.86-1.90 Å, Ni-N_{CH3} 1.96 Å, Ni-O 1.95 Å)

*VII.1.5. Spectroscopic characterization of the active species in the **1**/NaOCl system*

Reaction of **1** towards NaOCl in the presence of acetic acid (AcOH) was qualitatively evaluated by UV-vis spectroscopy. UV-vis monitoring of the reaction of **1** in the presence of 5 equiv. AcOH and subsequent addition of 3 equiv. hypochlorite (either NaOCl or $Ca(OCl)_2$) in CH_3CN at -30 ºC evidenced the formation of a metastable red species (**3**) with two weak visible absorption bands at 550 nm (ε > 500 $M^{-1}cm^{-1}$) and 650 nm (ε > 500 $M^{-1}cm^{-1}$) (Figure VII.9). Interestingly, the subsequent addition of 2 extra equivalents of ClO^- (in total 5 equiv. ClO^-) showed the formation of another metastable dark orange compound (**4**) with an intense absorption band at 475 nm (ε > 8000 $M^{-1}cm^{-1}$). Compound **4** was not observed when the reaction was run at room temperature and its half-life time at -30 ºC was 4.2 hours. Importantly, both AcOH and ClO^- were necessary to observe the above-described spectral changes.

At this point, reactivity studies of compounds **3** and **4** in the presence of organic substrates were done. On the one hand, compound **3** did not react with any of the substrates tested (9,10-dihydroanthracene and cyclooctene). In contrast, the decay of **4** became significantly accelerated by the addition of alkanes, alkenes and sulfides as ascertained by UV-vis monitoring. Analysis of the final products showed that the reaction of compound **4** with alkanes afforded the chloroalkane as the major product and the alcohol as the minor product. For alkenes and sulfides the corresponding epoxide and sulfoxide products were obtained, respectively. Due to the fact that NaOCl is a relatively potent oxidant that can oxidize or chlorinate some substrates in the absence of a metal catalyst, blank experiments without the nickel complex **1** were carried out. Only low amounts of oxidized products were detected in all cases.

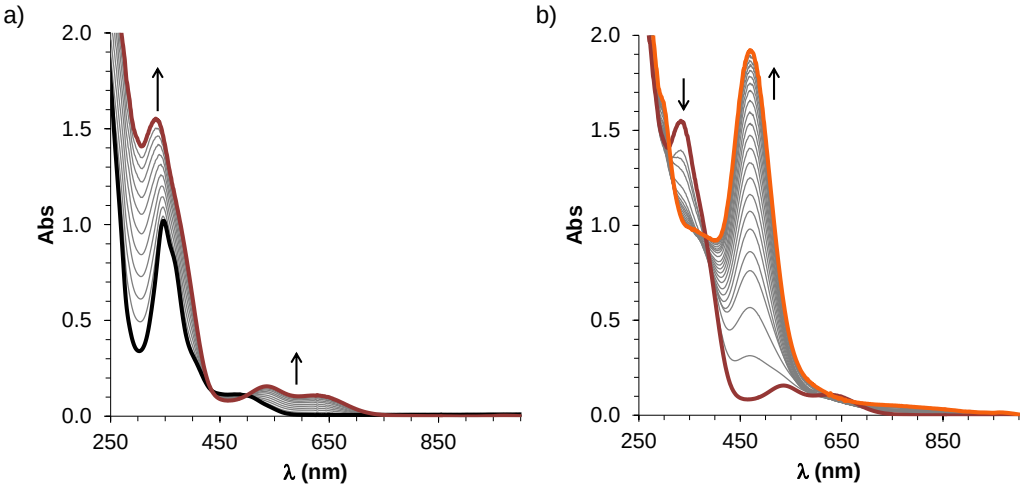

Figure VII.9. UV-vis absorption spectral changes of **1** over time with a two-step addition of $Ca(OCl)_2$ at -30 ºC in CH_3CN:H_2O 95:5 (v:v). a) Step 1: 3 equiv. ClO^- added to **1** (0.2 mM, black line) in CH_3CN in the presence of 5 equiv. AcOH resulted in the formation of species **3** (red line). b) Step 2: addition of a further 2 equiv. ClO^- to **3** (red line) resulted in the formation of **4** (orange line). Equivalent results were obtained with the use of NaOCl.

In order to get insight into the nature of compound **3**, CSI-MS studies were performed. The mass spectrum of **3** at -30 ºC was dominated by a major peak at *m/z* 318.0588, with a mass value and an isotopic pattern fully consistent with $\{[Ni(L1)]\}^+$, which corresponds to the $1e^-$ oxidation of **1** to form the corresponding nickel(III) complex. Spectroelectrochemistry provided interesting information about the possible formulation of **3**. Thus, electrochemical oxidation of **1** (quasi-reversible redox wave at $E_{1/2}$ = 0.90 V vs Ag/Ag^+ assigned to the Ni^{III}/Ni^{II} redox couple) at 0.96 V showed the formation of a new band at 850 nm in the UV-vis spectrum corresponding to the $1e^-$ oxidized species. Interestingly, the characteristic UV-vis band of **1** at 343 nm was fully recovered by subsequent reduction at 0.85 V (Figure VII.10a). Equivalent results were obtained in presence of water (50 equiv.) and AcOH (5 equiv.). Instead, when the spectroelectrochemical oxidation of **1** was carried out in the presence of NaCl (5 equiv.), in addition to AcOH (5 equiv.) and water (50 equiv.), a UV-vis spectrum analogous to that of **3** was obtained (Figure VII.10b), thus suggesting that **3** may correspond to the mononuclear nickel(III)-chloride species $[Ni^{III}(L1)(Cl)]$. The proposed formulation of **3** as a nickel(III)-chloride was also supported by XAS studies on this species. On one hand, XANES analysis suggested a +3 oxidation state of the nickel center. On the other hand, EXAFS was in accordance with the presence of a Ni-Cl bond of around 2.50 Å, which fitted with the computed structure of $[Ni^{III}(L1)(Cl)]$ (Ni-Cl distance of 2.40 Å). EPR analysis of **3** at 77 K showed the presence of a S = 1/2 species with g values at $g_{\perp}$= 2.23 and $g_{//}$= 2.01 characteristic of nickel(III) that accounted for 65% of the nickel content.[7] Overall, compound **3** corresponded to the nickel(III)-chloride species $[Ni^{III}(L1)(Cl)]$ which, as expected for this formulation, was inactive towards the oxidation of organic substrates.

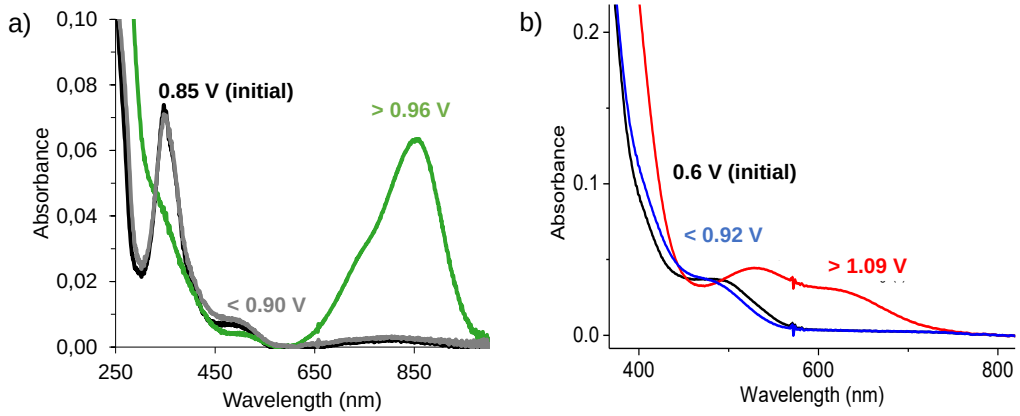

Figure VII.10. a) UV-vis spectroelectrochemistry of **1** (1 mM) in CH_3CN with 0.1 M $TBAPF_6$. b) UV-vis spectroelectrochemistry of **1** (5 mM) with 5 equiv. AcOH and 50 equiv. water and 5 equiv. NaCl in CH_3CN with 0.1 M $TBAPF_6$.

Characterization of compound **4**, which exhibited marked reactivity against organic substrates, by rRaman spectroscopy was attempted. At maximum accumulation of compound **4** in CH_3CN:H_2O 95:5 at -30 ºC the sample was frozen (77 K) and analyzed by rRaman with laser excitation at 473 nm (Figure VII.11). Enhancement of two bands at 703 and 443 cm^{-1} was observed, which appeared and decayed concomitantly with the chromophore at 475 nm associated to **4** and they both disappeared upon addition of substrate (50 equiv. 1-octene). A well-defined Fe-OCl system had been previously reported[10] and it exhibited resonance enhanced bands at 780 and 459 nm that were assigned to O-Cl and Fe-O stretching frequencies, respectively. By comparison, an analogous assignment was done for the bands at 703 and 443 cm^{-1} observed for **4**. Moreover, isotope labelling experiments using ^{18}O-labeled **4** (formed by reaction of **1** with $Na^{18}OCl$ in the presence of AcOH) resulted in a shift of these two bands down to 679 and 435 cm^{-1} (Figure VII.11). The observed shift of 24 cm^{-1} for the 703 cm^{-1} band is in agreement with the calculated shift using the two-atom approximation for a O-Cl vibration ($\Delta[^{18}O]$ = - 29 cm^{-1}), while the shift of 8 cm^{-1} for the 443 cm^{-1} indicates that this vibration is associated not only to the oxygen unit but also to ligand vibrations (expected shift for a Ni-O bond upon ^{18}O-labeling is $\Delta[^{18}O]$ = - 20 cm^{-1}).

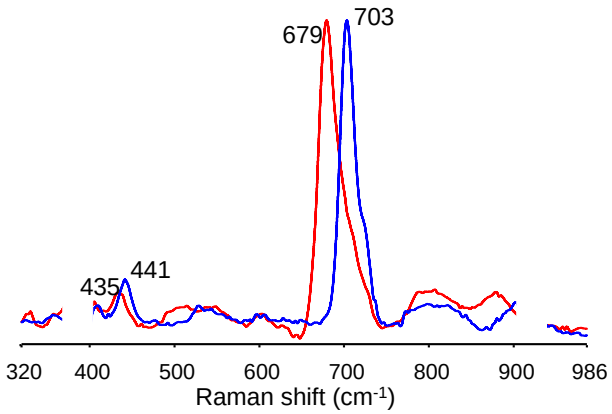

Figure VII.11. rRaman spectra (λ_{exc} 473 nm) in frozen CH_3CN:H_2O 95:5 (v:v) (77 K) of **4** formed after reaction of **1** (0.48 mM) in CH_3CN:H_2O 95:5 (v:v) at -30 ºC with 5 equiv. AcOH and 5 equiv. NaOCl (blue line) or 5 equiv. $Na^{18}OCl$ (red line). Artifacts due to imperfect solvent subtraction were masked with white boxes.

CSI-MS of **4** carried out at -30 ºC showed a clean spectrum with a major peak at *m/z* 334.0585, with a mass value and an isotopic pattern fully consistent with {[Ni(L1)(O)]}$^{+}$, and a minor peak at 318.0615 corresponding to {[Ni(L1)]}$^{+}$ (Figure VII.12). Interestingly, analysis of ^{18}O-labeled **4** showed a shift of two mass units of the major peak which appeared at *m/z* 336.0592, further supporting the presence of an oxygen atom coming from the oxidant into the structure of **4**. Furthermore, collision induced dissociation (CID) experiments conducted at 20-25 eV over the *m/z* 334.0585 (for compound **4**) and 336.0592 (for ^{18}O-**4**) showed in both cases a new peak at *m/z* 317.05 indicative of the loss of an OH and ^{18}OH radical, respectively. Remarkably, the peak at *m/z* 334.0585 disappeared upon substrate addition (1-octene). Importantly, the mass spectrum obtained after the self-decay of **4** only exhibited signals corresponding to nickel(II) species with oxidized/dehydrogenated ligand (*m/z* = 355.0319 and 369.0105).

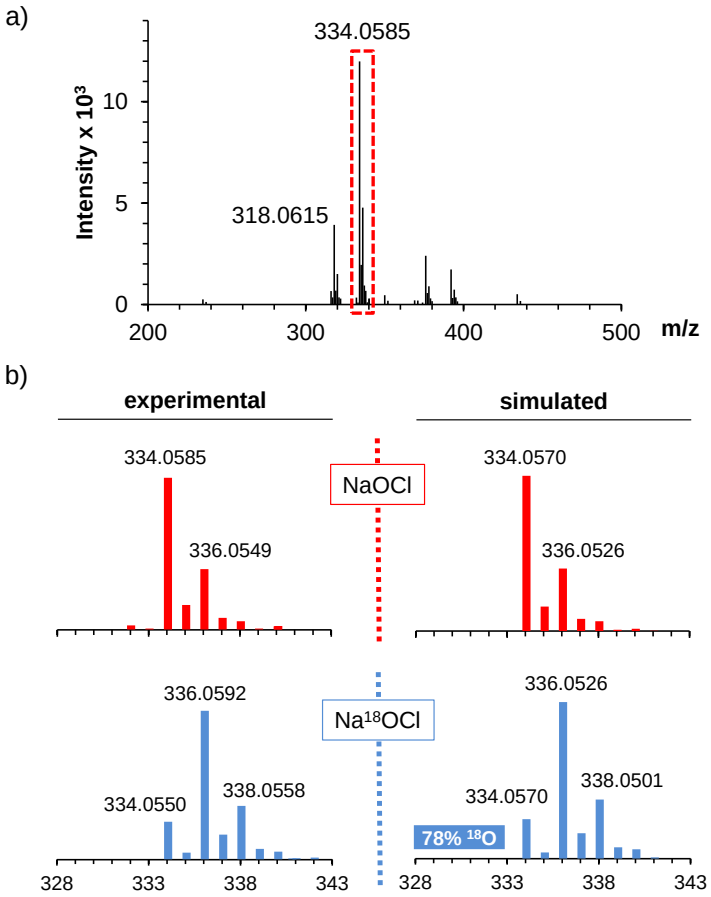

Figure VII.12. a) CSI-MS of **4** formed by reaction of **1** with 5 equiv. NaOCl in the presence of 5 equiv. AcOH in CH_3CN:H_2O 95:5 (v/v) at -30 ºC. b) Experimental and simulated pattern for the peak at m/z 334.06 formed with NaOCl (top) or partially ^{18}O-labeled NaOCl (bottom).

EPR analysis of a sample upon maximum accumulation of **4** showed the presence of *S* = 1/2 rhombic species with *g* values at $g_{\perp}$= 2.23 and $g_{//}$= 2.01 analogous to those exhibited for **3**. However, this signal only accounted for 30% of the nickel content, which suggested that it originated from the presence of significant amounts of **3** in the sample. Indeed, the EPR spectrum measured after the addition of a substrate (1-octene) showed a similar concentration of nickel(III)

in the sample indicating that this EPR active species is not responsible for the observed oxidation chemistry and it is not related to the chromophoric species **4**.

Further insight into the nature of **4** was gained through XAS experiments at the metal K-edge.[11] XANES of compound **4** compared to **2** showed similar results but the rising edge of **4** suggested a more oxidized metal center than **2** (Figure VII.13a). The comparison between compound **4** and **2** was performed by the half-height method, which showed a shift of ~1.7 eV in the maximum of the white-line at 8354.8 eV and a ~0.5 eV increase in the rising edge energy. The determination of oxidation states of metal centers using this methodology can be difficult. However, it is known that a shift of 0.7 eV in the rising edge is consistent with a +1 change in the formal oxidation state.[12] Thus, the observed shift of ~0.5 eV could be attributed to a partial oxidation of the metal center, which could involve the ligand in this oxidation.[13] On the other hand, EXAFS studies showed 5 N/O atoms coordinated in the first shell of the nickel center in **4** at a distance around 1.89 Å, accompanied by single and multiple scattering C/N paths at 2.77 and 2.96 Å (Figure VII.13b). This structure is also supported by the broad shoulder in the rising edge of **4**, that it is typical for square pyramidal geometry. The possible formulation of **4** as a dimeric Ni-X-Ni species was also explored using existing procedures including phase comparison and curve fitting. However, in either case this analysis did not support the formation of Ni-X-Ni dimers.[14]

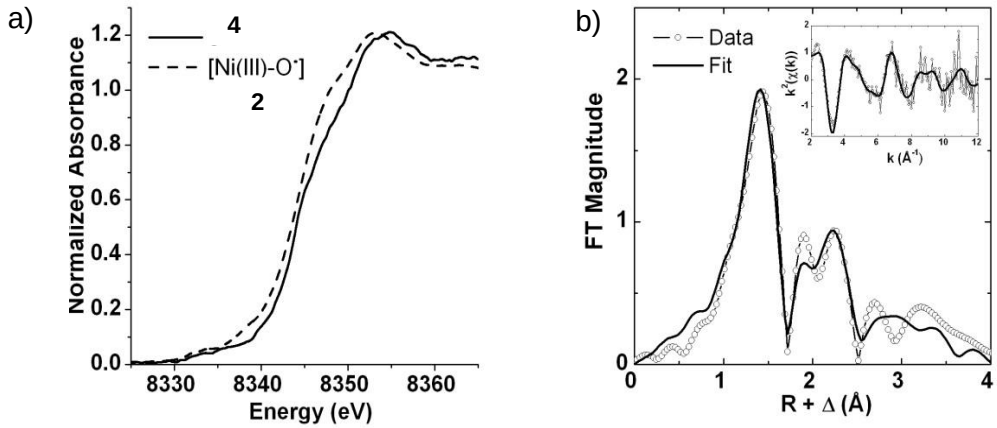

Figure VII.13. a) Comparison of the Ni K-edge XANES region for complex **4** and **2**. b) Fourier-transformed EXAFS spectrum of **4** (no phase correction, FT, window**=** 2–12 $Å^{-1}$); Inset: k^2-weighted unfiltered EXAFS spectra.

Density functional theory (uB3LYP/TZVP) was employed to support the experimental data of **4** taking into account the solvent (acetonitrile), optimized with dispersion and the temperature (243 K) (Scheme VII.5). According to the above described experimental results, several formulations were postulated for this species (Scheme VII.5). We firstly optimized the structure of $[Ni(L1)(OCl)]^+$ (**A**) in all possible spin states (**A**: *S* = 0, 1 or 2) and the triplet multiplicity (^{3}**A**) was found to be more stable than the singlet by 7 kcal·mol^{-1}. The model consisted of a nickel center in a distorted square pyramidal geometry with the OCl ligand bound at the apical position (Figure VII.14a). When the free energy difference of ^{3}**A** relative to the starting reactants was calculated, formation of compound ^{3}**A** was found to be a thermodynamically favoured process (ΔG^o = -12.8

kcal·mol^{-1}). Other possible structures, for instance, [Ni(L1)(OCl)] (**^{2}B**) and [Ni(L1)(O)]$^{+}$ (**^{4}C**) were also computed but in both cases their formation from **1** was thermodynamically unfavored by +5.3 and +30.3 kcal·mol^{-1}, respectively. Overall, theoretical calculations indicated that compound **4** was best formulated as a [Ni(L1)(OCl)]$^{+}$ (**^{3}A**).

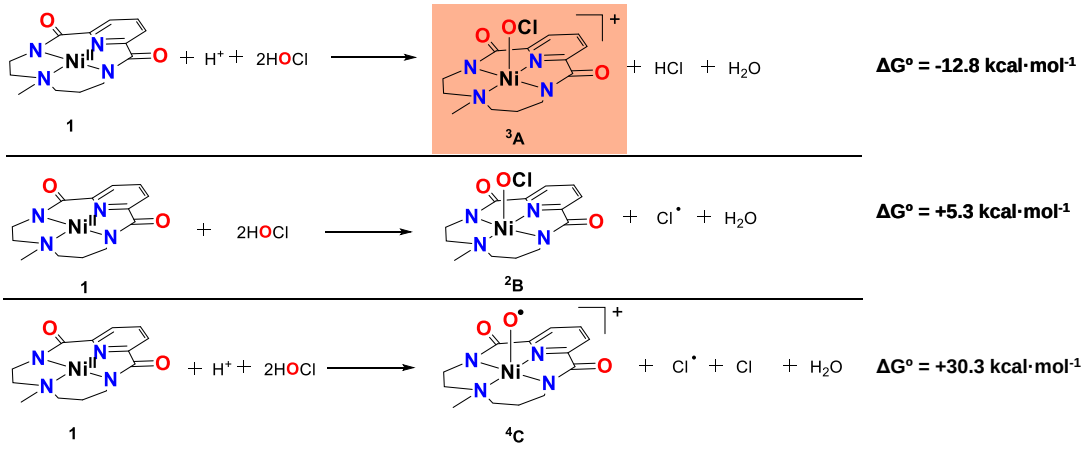

Scheme VII.5. Possible formulations of compound **4** (**A**, **B** or **C**) derived from the reaction of **1** with NaOCl in the presence of AcOH. Free energies are given in parentheses in kcal·mol^{-1} at -30 ºC in CH_3CN.

Analysis of the spin natural orbitals of [Ni(L1)(OCl)]$^{+}$ (**^{3}A**) indicated that this structure corresponds to a nickel(III) species with a delocalized radical over the OCl and L1 ligand (Figure VII.15). The analysis of the SNOs of **^{3}A** showed two single occupied orbitals: the first one was distributed between $N_{carboxamidate}$ (~43%) and OCl (~23%) ligands and a minimal contribution from Ni (~8%), and the second one had a main contribution from nickel (d_{z2}, 62%) with 26% contribution from OCl. Furthermore, the Mulliken spin density demonstrated the radical character of the ligands because the nickel center only had part of the spin density (ρ(Ni) = 0.75), and the rest was distributed between ligand ($\rho(N_{ligand})$ = 0.55) and ρ(OCl) = 0.42) (Figure VII.14b). Thus, both results showed a spin delocalization between a proximal nitrogen atom ($N_{carboxamidate}$), the metal center and the OCl moiety. Thus, despite the fact that compound **4** is formulated formally as the nickel(IV) species [Ni(L1)(OCl)]$^{+}$ (**^{3}A**), an in-depth analysis of its electronic structure indicates that it is best described as a nickel(III) center with a radical distributed in the ligands surrounding the metal center.[15]

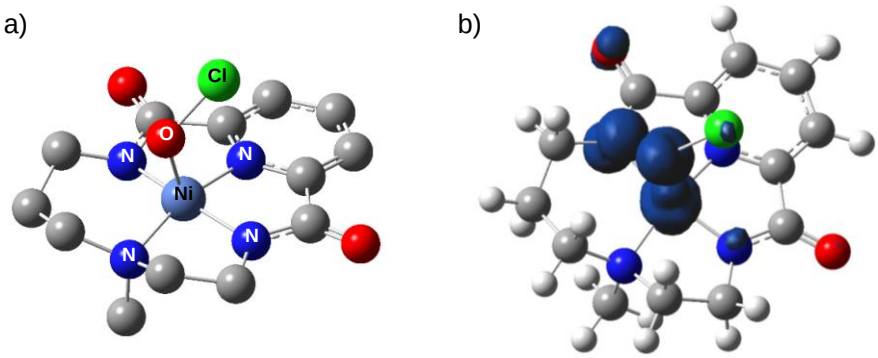

Figure VII.14. a) DFT computed structure of [Ni(L1)(OCl)]$^{+}$ (**^{3}A**). b) Isodensity surface (isovalue = 0.01) of the spin density for [Ni(L1)(OCl)]$^{+}$ (**^{3}A**).

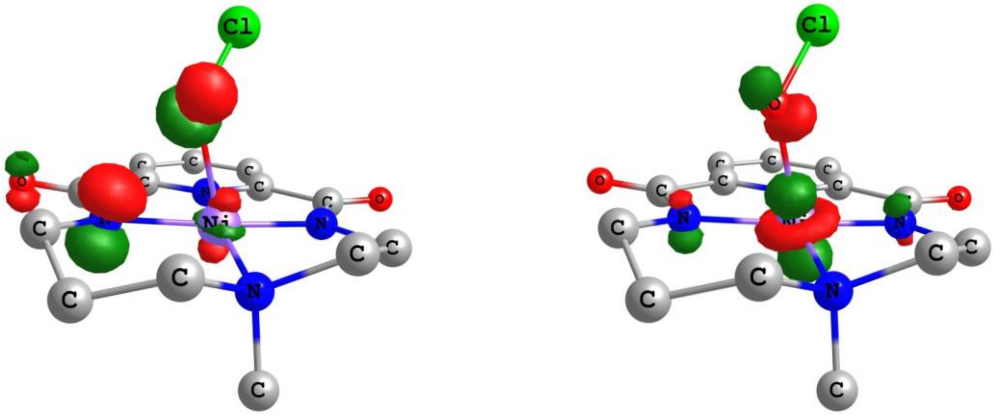

Figure VII.15. Spin-natural orbitals of $[Ni(L1)(OCl)]^+$ (^{3}**A**) (isovalue = 0.144).

Very interestingly, the Raman spectrum predicted for $[Ni(L1)(OCl)]^+$ (^{3}**A**) showed an intense O-Cl vibration at 701 cm^{-1} and a weaker Ni-O vibration at 406 cm^{-1} that downshifted to 676 and 397 cm^{-1} upon labeling with ^{18}O, respectively. These results fitted well with the experimentally determined O-Cl and Ni-O vibrations for **4** (703 and 443 cm^{-1} that shifted to 679 and 435 cm^{-1} for ^{18}O-**4**) and further supported the theoretical model proposed for **4**. Furthermore, XANES and EXAFS analysis of **4** was fully congruent with the theoretical model. Thus, the computed structure of ^{3}**A** contains a nickel(III) center as experimentally determined by XANES, and within the resolution of the EXAFS data the bond metrics obtained from EXAFS analysis of **4** correlated with those of ^{3}**A**. Finally, CSI-MS analysis of **4** showing the presence of a major peak corresponding to $\{[Ni(L1)(O)]\}^+$ suggested cleavage of the O-Cl bond of $[Ni(L1)(OCl)]^+$ under the MS conditions due to the weakened O-Cl bond as indicated by the theoretically predicted structure ^{3}**A**. Overall, the computed structure for $[Ni(L1)(OCl)]^+$ (^{3}**A**) is fully congruent with the above-described EPR, rRaman, CSI-MS and XAS analyses carried out on **4** (Table VII.3).

Table VII.3. Summary of the experimental characterization of **4** and comparison with the theoretical model.

techniques	**experimental data for compound 4**	**theoretical model $[Ni(L1)(OCl)]^+$**
rRaman	703 cm^{-1} ($\Delta[^{18}O]$ = -24 cm^{-1}) 443 cm^{-1}($\Delta[^{18}O]$ = -8 cm^{-1})	υ(O-Cl) 701 cm^{-1} ($\Delta[^{18}O]$ = -25 cm^{-1}) υ(Ni-O) 406 cm^{-1} ($\Delta[^{18}O]$ = -9 cm^{-1})
CSI-MS	major peak assigned to $\{[Ni(L1)(O)]\}^+$	cleavage of the weakened O-Cl bond under the MS conditions
X-band EPR	no signal related to **4** detected	*S* = 1 (even number of unpaired electrons)
XANES	the oxidation state of nickel fits with +3	the oxidation state of nickel is +3
EXAFS	5-coordinate Ni center (5 Ni-N/O 1.89 Å)	5-coordinate Ni center (Ni-N_{py} 1.85 Å, Ni-$N_{carboxamidate}$ 1.85-1.89 Å, Ni-N_{CH3} 1.94 Å, Ni-O 2.08 Å)

VII.1.6. Kinetic analysis of the reaction of **2** and **4** with organic substrates

As explained above species **2** and **4** were very reactive towards different substrates because the decay of **2** or **4** (monitored by UV-vis spectroscopy) became significantly accelerated by the addition of alkanes, alkenes and sulfides. Indeed, under conditions of excess substrate kinetic traces showed pseudo-first order behaviour and could be fitted to single exponential functions (Figure VII.16). The corresponding k_{obs} values were found to be linearly dependent on substrate concentration, affording a second order rate constant (k) (Figure VII.17).

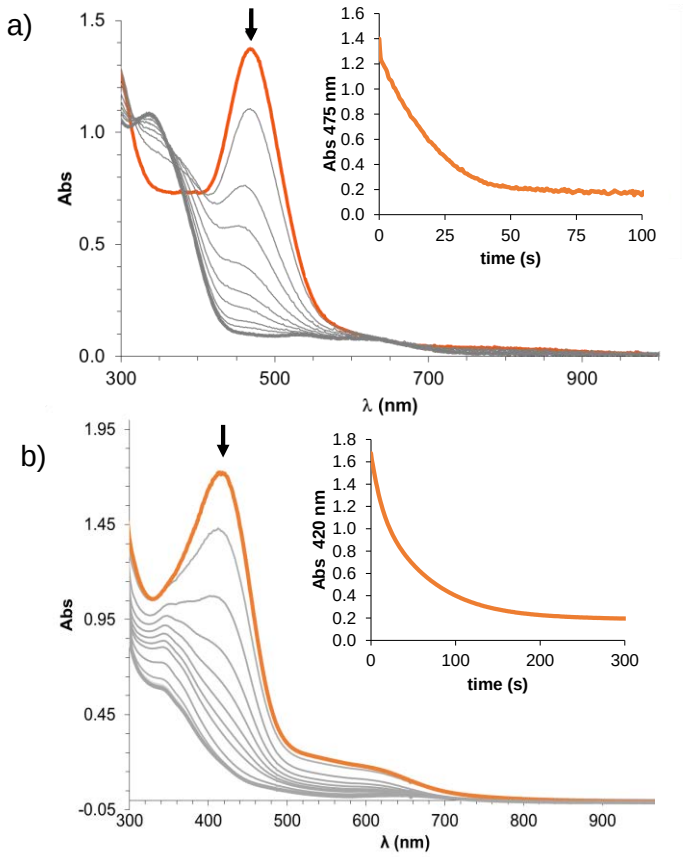

Figure VII.16. UV-vis spectral changes of a solution of **2** (0.24 mM **1**) (a) or **4** (0.2 mM **1**) (b) upon addition of 50 equiv. styrene in CH_3CN at -30 ºC. Inset: kinetic trace at 420 nm (a) and 475 nm (b) which fits to a monoexponential decay.

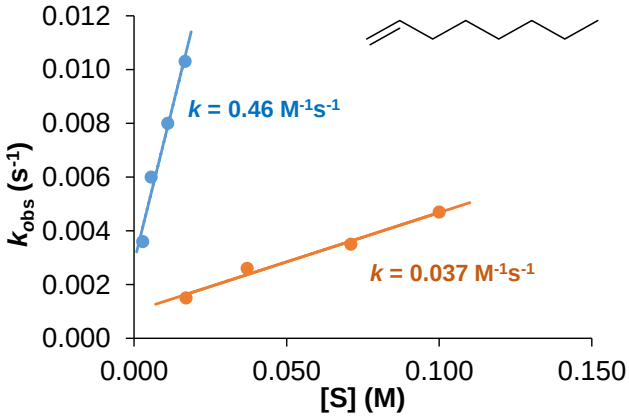

Figure VII.17. Plot of k_{obs} against substrate concentration for the reaction of **2** (orange) and **4** (blue) with 1-octene in CH_3CN at -30 ºC.

More information about the mechanism operating in the oxidation of substrates by **2** and **4** was gained through the initial observation that reaction rates were highly dependent on the *para* substituent present in the aromatic ring of styrene derivatives. Thus, the second order rate constants corresponding to the reaction of **2** or **4** with a series of *para*-substituted styrenes (*para*-substituent = OMe, Me, H, Cl and NO_2) were measured. Plotting of $\log(k_X/k_H)$ for the different substrates against the corresponding Hammett parameter (σ_p) afforded a good correlation and a Hammett value with negative slope was obtained in both cases (-0.86 for **2** and -1.35 for **4**, Figure VII.18). The negative Hammett value indicated that **2** and **4** behaved as electrophilic oxidants.[16] In the case of **2** similar results were obtained for the reaction with a series of *para*-substituted methyl phenyl sulfides, *p*-X-thioanisoles (k_X, X = Me, Cl, CN), while this experiment could not be done with **4** because reactions with thioanisole derivatives were too fast to obtain proper kinetic data using our conventional UV-vis spectrophotometer.

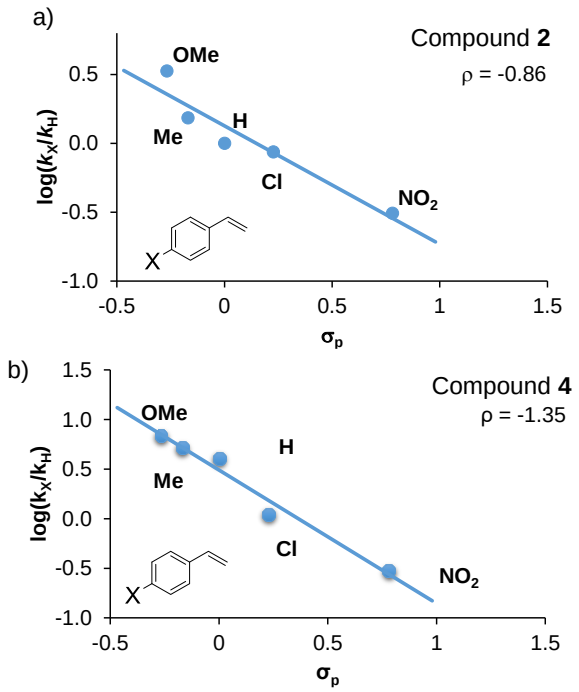

Figure VII.18. Hammett plot, $\log(k_X/k_H)$ vs the Hammett parameter (σ_p), for the reaction of **2** (a) or **4** (b) against *para*-substituted-styrenes in CH_3CN at -30 ºC.

Moreover, compounds **2** and **4** were able to perform hydrogen-atom abstraction from O-H bonds and they reacted with 2,4,6-tri-*tert*-butylphenol to form the corresponding phenoxyl radical. This was evidenced by UV-vis spectroscopy which showed the appearance of an intense band at 626 nm characteristic of the corresponding phenoxyl radical species in both cases.[17] Remarkably, compounds **2** and **4** were kinetically competent to oxidize hydrocarbon substrates. Interestingly, compound **4** was much more reactive than compound **2** and it was even able to react with strong C-H bonds such as those of cyclohexane (bond dissociation energy of 99.3 kcal·mol^{-1}). In contrast, compound **2** was only kinetically well-behaved towards substrates with much weaker C-H bonds and reactions with substrates bearing stronger C-H bonds were extremely slow and they did not follow simple single-exponential decays. In any case, the representation of the logarithm of the second order rate constant corrected by the number of C-H bonds in the substrates (*k'*) in

front of the bond dissociation energy (BDE) for different alkanes gave a linear correlation (Figure VII.19). As expected, the rate constant decreased with the increase of C-H BDE. Moreover, the analysis of kinetic isotope effect (KIE) using deuterated 9,10-dihydroanthracene (d_4-DHA) was 4 and 1.5, respectively for **2** and **4** compounds. The linear correlation of log (*k'*) *vs* BDE and the observed KIE value gave a strong evidence of hydrogen-atom abstraction as the rate-determining step in the reaction of **2** or **4** towards C-H bonds.[18]

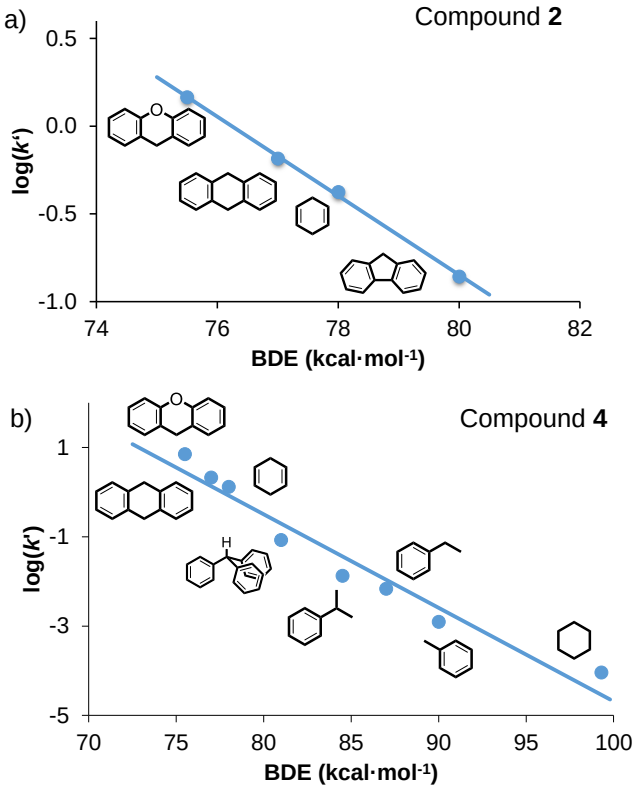

Figure VII.19. Plot of log(*k'*) against the C-H BDE for the reaction of **2** (a) or **4** (b) towards several alkanes in CH_3CN at -30 ºC.

Comparison of the reactivity of compounds **2** and **4** with that reported for well-defined mononuclear nickel-oxygen systems (Figure VII.20) indicated that these two compounds were much more reactive (Table VII.4). Thus, **2** and **4** reacted between 200 and 1000 times faster with C-H bonds than $[Ni^{III}(O(H))(TMG_3tren)]^{n+}$ at the same temperature (-30 ºC).[19] The same reaction was up to 3-4 orders of magnitude faster compared to $[Ni^{II}(m\text{CPBA})(Tp^{CF3Me})]$ but at much higher reaction temperatures (+70 ºC).[20] Furthermore, for the oxidation of styrene our systems (**2** and **4**) reacted between 50 and 500 times faster than $[Ni^{II}(m\text{CPBA})(Tp^{CF3Me})]$ (+70 ºC). On the other hand, the system $[Ni^{III}(py{N_2}^{Me2})(HCO_3)]$ could only perform hydrogen-atom abstraction of O-H and very weak C-H bonds (e.g. 1-benzyl-1,4-dihydronicotinamide) and oxygen-atom transfer to triphenylphosphine.[21] Very recently, $[Ni^{III}(py{N_2}^{Me2})(OAc)]$ was reported to carry out hydrogen-atom abstraction of O-H and weak C-H bonds (e.g. 1-benzyl-1,4-dihydronicotinamide and 10-methyl-9,19-dihydroacridine) at -40 ºC.[22] Importantly, only at room temperature this compound was capable to oxidize xanthene, 9,10-dihydroanthracene (DHA), fluorene, benzyl alcohol,

ethylbenzene and toluene but the comparison of reaction rates with **2** and **4** is hampered due to the different temperatures used.

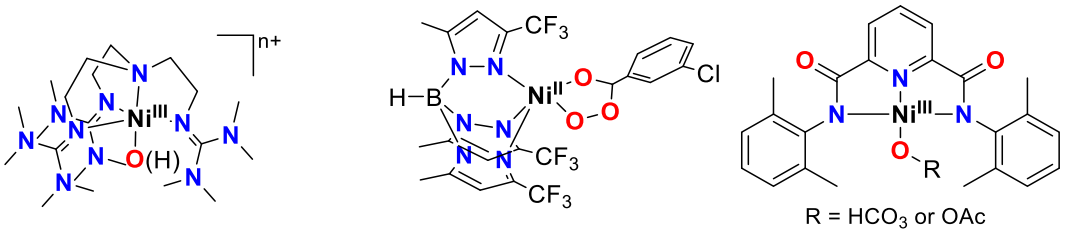

$[Ni^{III}(O(H))(TMG_3tren)]^{n+}$ $[Ni^{II}(mCPBA)(Tp^{CF3Me})]$ $[Ni^{III}(pyN_2^{Me2})(OR)]$

Figure VII.20. Well-defined nickel-oxygen that perform C-H bond or C=C bond oxidation.

Table VII.4. Second-order rate constants (*k,* $M^{-1}s^{-1}$) for the reaction of **2**, **4** and previously reported nickel-oxygen species with alkanes and alkenes.

Substrate	**4**[a] **(-30 ºC)**	**2 (-30 ºC)**	**$[Ni^{III}(O(H))(TMG_3tren)]^{n+}$ (-30 ºC)**	**$[Ni^{II}(mCPBA)(Tp^{CF3Me})]$ (+70 ºC)**	**$[Ni^{III}(pyN_2^{Me2})(OAc)]$ (+25 ºC)**
xanthene	14	2.9	0.01	0.002	35.1
DHA	8.5	2.6	1	0.0005	8.1
1,4-cyclohexadiene	5.3	1.7	0.007	0.02	-
fluorene	-	0.3	-	0.001	3.9
ethylbenzene	0.01	-	-	-	0.2
toluene	0.004[b]	-	-	-	0.008
styrene	4.1	0.5	-	0.009	-

[a] In the case of compound **4**, reaction rates were found to be the same under N_2 or air.
[b] Due to extremely slow reaction, rate constants for the reaction of **4** with toluene was determined from two replicates at a given substrate concentration (0.36 M).

In summary, the bis(carboxamidate) macrocyclic ligand H_2L1 acts as an excellent platform to support high-valent nickel-oxygen species at low temperatures that could be well-characterized by spectroscopic and computational studies. Most interestingly, these species (**2** and **4**) behaved as strong oxidizing agents both towards C-H and C=C bonds with reaction rates that surpass those reported for related nickel-oxygen species.

VII.2. Nitrous oxide activation by a cobalt(II) complex for aldehyde oxidation under mild conditions

This section corresponds to the contents of the manuscript by T. Corona and A. Company *Dalton Trans.* **2016**, *45*, 14530-14533, which can be found in **Chapter V** of this thesis. In **Chapter V** Teresa Corona (T.C.) synthesized and fully characterized the ligand and the corresponding cobalt(II) complex, and she also performed the reactivity studies towards O_2 and N_2O. Besides, T.C. did the reactivity studies towards substrates and was involved in the generation and analysis of EPR samples. All work was supervised and coordinated by Anna Company.

Traditional stoichiometric oxidants used in industrial processes are obsolete because they are very toxic, require harsh conditions and extended reaction times. In addition, these reactions are rather inefficient, barely selective and produce large amounts of, often toxic, inorganic salts as waste. On the basis of economic and environmental costs, such methodologies are being discarded in favor of less toxic oxidants. In this line, there is an increasing interest in the use of nitrous oxide (N_2O) as an oxidizing reagent. This reagent would constitute a clean alternative to the polluting oxidation processes used in industry as it only generates N_2 as waste.

Despite the fact that N_2O is a natural component of the Earth's atmosphere, its concentration is increasing every year due to anthropogenic sources. Thus, N_2O is an important environmental problem because it is 300 times more potent than carbon dioxide as a greenhouse gas and it is involved in the destruction of the ozone layer. For this reason, the use of N_2O as oxidizing agent in useful chemical synthesis would be interesting. Indeed, N_2O is a very powerful oxidant from the thermodynamic point of view but its reactivity is largely limited by its kinetic stability against decomposition or reduction. However, these kinetic barriers can be overcome through coordination and activation by metal ions that react with nitrous oxide under mild conditions. In this project, we targeted the activation of nitrous oxide using first-row transition metals under mild conditions.

VII.2.1. Ligand design and synthesis of the complex

In this case, ligand H_2L1 was considered to be the perfect platform to achieve this objective because it forms metal complexes with highly electronrich metal centers, which *a priori* would be eager to transfer electrons to N_2O and achieve its activation. Several first-row transition metals such as copper(II), iron(II) and nickel(II) were tested[23] but clean N_2O activation was only achieved in the case of cobalt(II).

The reaction of H_2L1 in anhydrous CH_3CN with 1 equiv. $[Co^{II}(CF_3SO_3)_2(CH_3CN)_2]$ followed by addition of 2 equiv. $K[N(SiMe_3)_2]$ under an inert atmosphere at room temperature afforded the corresponding cobalt(II) complex, $[Co^{II}(L1)]$ (**5**), which co-crystallized with KCF_3SO_3 (58% yield). Single crystals of **5** suitable for XRD analysis were obtained after exchange of the KCF_3SO_3 salt

by $NaBF_4$ (Figure VII.21a). The cobalt(II) complex presented a square planar geometry with coordination to the pyridine, an aliphatic tertiary amine and two carboxamidate units *trans* one to each other. The bond lengths were Co-N_{py} (1.80 Å), Co-N_{CH3} (1.92 Å) and Co-$N_{carboxamide}$ (1.85-1.86 Å), and they were in the range of those previously reported for cobalt(II) square planar complexes.[24] As expected for a cobalt(II) complex, **5** was paramagnetic and it exhibited broad signals between 70 and -30 ppm in its ^{1}H-NMR. An effective magnetic moment (μ_{eff}) of 1.69 μ_B was determined by the Evans' method, which agrees with a low-spin cobalt(II) center (d^7) with a single unpaired electron. High resolution ESI-MS of **5** showed peaks corresponding to cobalt(II) and cobalt(III) species, due to the extreme air sensitivity of **5**. The mass spectrum was dominated by a peak at *m/z* 319.0590 with a mass value and an isotopic pattern fully consistent with the cobalt(III) complex, $\{[Co(L1)]\}^+$ and two small peaks at *m/z* 342.0476 and 358.0238 corresponding to $\{[Co(L1)]+Na\}^+$ and $\{[Co(L1)]+K\}^+$, respectively. Cyclic voltammetry of **5** was obtained under nitrogen (inside the glovebox) and a quasi-reversible redox wave at $E_{1/2}$ = +0.17 V (vs SCE) was determined for the Co^{III}/Co^{II} redox pair.

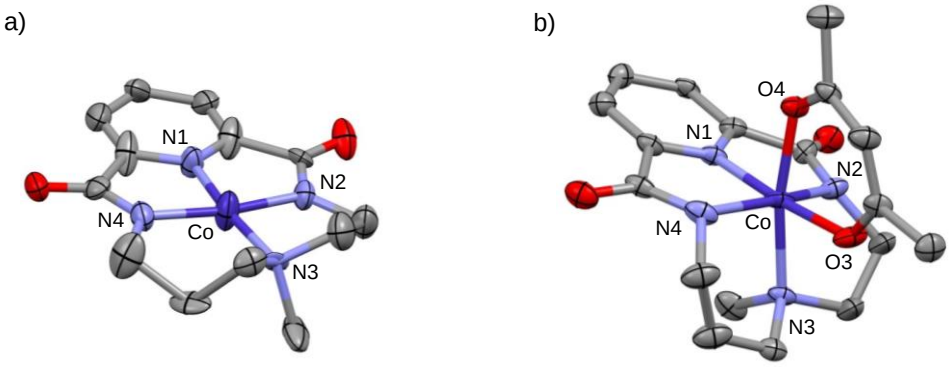

Figure VII.21. Crystal structures of **5**·$NaBF_4$ (a) and **6** (b). Hydrogen atoms and co-crystallized $NaBF_4$ in **5** have been omitted for clarity. Thermal ellipsoids are set at 50% probability.

For comparison purposes, the corresponding cobalt(III) complex was also prepared by reaction of H_2L1 with $[Co^{III}(acac)_3]$ in the presence of 2 equiv. $K[N(SiMe_3)_2]$. The XRD structure of $[Co^{III}(L1)(acac)]$ (6) exhibited a cobalt center in an octahedral geometry (Figure VII.21b). The tetradentate ligand L1 coordinated in a tripodal fashion and the other two coordination positions were occupied by the acetylacetonate anion. The Co-N bond lengths in **6** (Co-N_{py} 1.86 Å; Co-N_{CH3} 2.00 Å; Co-$N_{carboxamide}$ 1.92-1.93 Å) are higher than in **5**. Noteworthy, complex **6** presented a diamagnetic ^{1}H-NMR spectrum as expected for low-spin cobalt(III) complex (d^6).

*VII.2.2. Reactivity of cobalt(II) complex (**5**) towards nitrous oxide*

Very remarkably, compound **5** was especially reactive with N_2O. UV-vis monitoring of the reaction of **5** with N_2O (1 atm) in CH_3CN at 0 ºC evidenced the progressive decay of the characteristic absorption band of **5** at 535 nm to form a new species (**7**) with UV-vis bands centered at 430 nm and 650 nm (Figure VII.22). Two isosbestic points (482 and 589 nm) were observed along this transformation which was complete in less than 1 minute. Unfortunately, no reaction intermediate

was detected along the transformation of **5** into **7**, even when the reaction was monitored at lower temperature (193 K).

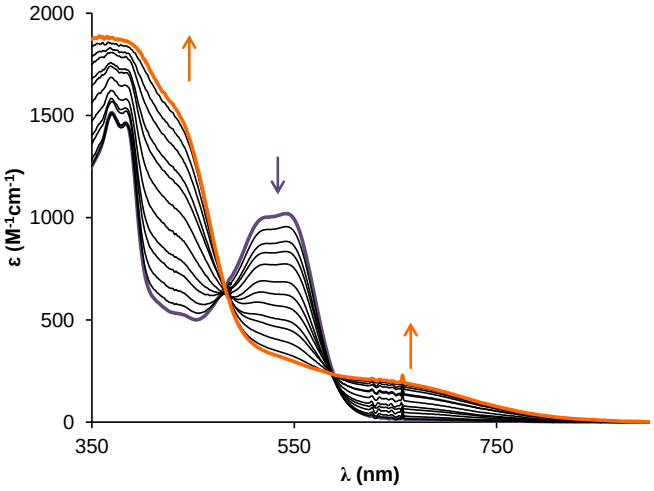

Figure VII.22. UV-vis absorption spectral changes observed upon reaction of **5** (purple line) with N_2O (1 atm) in CH_3CN at 0 ºC to form **7** (orange line).

In order to make sure that the observed reaction of **5** towards N_2O was not a result of the interaction of **5** with possible trace amounts of O_2 present in this gas, its purity was analyzed by GC-TCD and it was found that the commercial N_2O was >99% pure. Moreover, the reaction rate of **5** with known amounts of N_2O increased when higher amounts of this gas were used and reaction rates were comparable to those measured with O_2 (to control the equivalents of N_2O or O_2 added into the reaction mixture, a dilution of the pure N_2O or O_2 in N_2 was done in a vial capped with a septum). If the observed reaction was due to the interaction of **5** with trace amounts of O_2 present in N_2O, the use of controlled amounts of N_2O would result in much slower rates than using controlled amounts of pure O_2. These results together with a blank experiment to discard O_2 leakage into the solution during N_2O injection proved that reaction of **5** occurs with N_2O and not with traces of O_2 present in this gas or originating from atmospheric contamination.

In order to get some information about the mechanism, a kinetic analysis of the reaction of **5** with N_2O was performed by monitoring the decay of the band at 535 nm characteristic for **5** in CH_3CN at 0 ºC. The reaction of **5** with excess N_2O showed pseudo-first order behavior and the measured k_{obs} values were linearly dependent on the concentration of N_2O (Figure VII.23a), thus the reaction was first order with respect to N_2O. On the other hand, the reaction was found to be first order with respect to **5** using the initial rate method. Thus, at a fixed amount of N_2O (134 equiv. N_2O) representation of ln(intial rates) in front of ln[**5**] showed a linear correlation (Figure VII.23b). Furthermore, GC-TCD analysis of the headspace was used to determine the amount of N_2 released. Analysis of the headspace after addition of a known amount of N_2O into a solution of **5** in a CH_3CN under Ar revealed that 1.0 ± 0.2 equiv. N_2 with respect to **5** had been released. Due to the fact that the reduction of N_2O to N_2 needs 2 electrons, presumably this reaction took place through a cobalt(IV) species, which could not be detected either by UV-vis spectroscopy or CSI-MS.

$$a\ [Co^{II}(L1)] + b\ N_2O \rightarrow\ Prod\ +\ N_2$$

$$v = k[Co(L1)]^a[N_2O]^b \quad \rightarrow \quad a = b = 1 \quad \rightarrow \quad v = k[Co(L1)]^a[N_2O]^b$$

$$[Co^{II}(L1)]\ (\mathbf{5}) + N_2O \rightarrow \text{“}[Co^{IV}(L1)]\text{”}\ (\mathbf{7}) + N_2$$

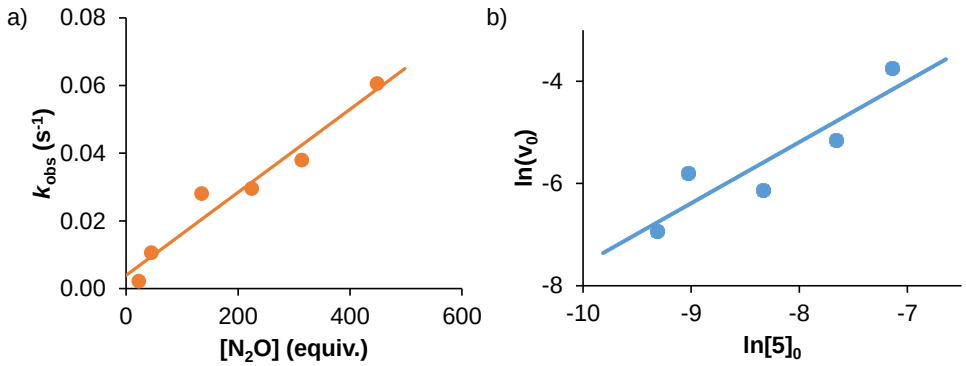

Figure VII.23. a) Plot of k_{obs} as a function of the amount of N_2O for the reaction of **5** with N_2O in CH_3CN at 0 ºC. b) Plot of ln(initial rates) in front of ln[**5**]$_0$ corresponding to the reaction of **5** with N_2O (134 equiv. N_2O) in CH_3CN at 0 ºC ([**5**]$_0$ = initial concentration of **5**).

Getting more insight into the mechanism of the reaction was attempted using electrochemical studies. Compound **5** presented a quasi-reversible Co^{III}/Co^{II} redox wave ($E_{1/2}$ = +0.17 vs SCE), but after the addition of N_2O this band diminished and a new wave at ~0.8 V (vs SCE) appeared, which was correlated with a Co^{IV}/Co^{III} redox couple (Figure VII.24a). This experiment suggested the formation of a Co^{IV} species along the reaction. The observed redox potential for the Co^{IV}/Co^{III} couple fell in the range observed for other systems with anionic *N*-based ligands.[25]

Furthermore, EPR analysis on a solution of complex **5** after reaction with N_2O was carried out (Figure VII.24b). The spectrum was characterized by an isotropic signal at *g* ~2.03, a value which might also point towards the presence of cobalt(IV) species in solution.[26] This EPR signal could also be attributed to the a cobalt(II) metal center, but this highly unlikely in this case because no paramagnetic ^{1}H-NMR signals characteristic of cobalt(II) were observed after the reaction of **5** with excess N_2O.

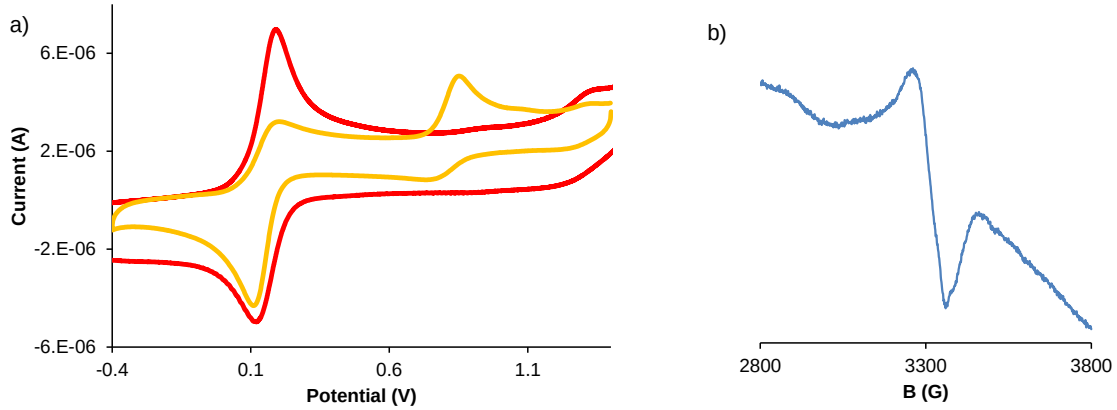

Figure VII.24. a) Cyclic voltammetry corresponding to **5** (red line) and to the reaction of **5** with N_2O (yellow line) in CH_3CN under Ar at 0 ºC. Potential measured vs. SCE. b) EPR spectrum of the reaction mixture obtained after the decay of compound **5** (2 mM) upon reaction with excess N_2O in CH_3CN at 0 ºC.

VII.2.3. Analysis of the reaction of **5** with N_2O towards organic substrates

Given the reactivity of **5** towards N_2O which generates N_2 through the mediation of a putative high-valent cobalt species, the reaction in the presence of oxidizable substrates was attempted. Substrates for which hydrogen-atom transfer (HAT) or oxygen-atom transfer (OAT) were likely to occur were firstly used.[27] Triphenylphosphine and 4-methoxy-thioanisole were the substrates of choice for oxygen-atom transfer reactions, for which formation of triphenylphosphine oxide and sulfoxide were envisioned. For hydrogen-atom abstraction processes 9,10-dihydroanthracene, which has a weak C-H bond, and cyclohexanol with an oxidizable O-H bond were selected. However, no oxidation products could be detected in any case as readily established by GC-FID, GC-MS or NMR.

Given the lack of reactivity with nucleophilic substrates, electrophilic substrates such as aldehydes were tested. The reaction of **5** in the presence of cyclohexanecarboxaldehyde with N_2O (1 atm) in CH_3CN at room temperature afforded the catalytic formation of the corresponding deformylated[28] and oxidized products, cyclohexene (2.1 ± 0.1 turnovers in 24 h) and benzoic acid (25 ± 5 turnovers in 24 h) respectively (Scheme VII.6). Blank experiments in the absence of **5** showed the presence of only trace amounts of both products, indicating that both the complex (**5**) and N_2O were necessary to achieve oxidation. The release of some CO_2 along the reaction, as determined by GC-TCD analysis of the reaction headspace, confirmed that cyclohexene was formed through a deformylation reaction. The mechanism of this transformation has not been explored. As previously postulated by other research groups, most likely it occurs by an attack of the oxygen moiety coordinated to the cobalt over the carbonyl group.[28] The resulting species may evolve through the formation of the corresponding acid or the decarboxylated product concomitant with CO_2 release. Such reactions are commonly observed for nucleophilic peroxo-type of species.

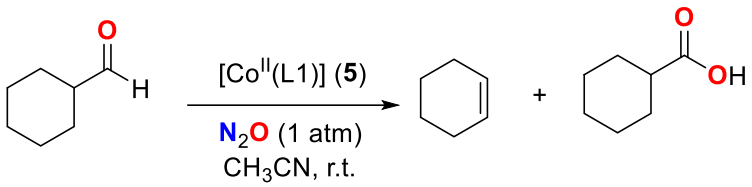

Scheme VII.6. Reaction of **5** with N_2O (1 atm) in CH_3CN at 25 ºC with excess cyclohexanecarboxaldehyde.

Overall, a novel cobalt(II) complex was prepared and characterized using the dianionic ligand L1. Moreover, this complex proved to be highly reactive and its oxidation with N_2O (1 atm) occurred within 1 min at 0 ºC. This work demonstrates that N_2O can be used as oxidant in chemical transformations (e.g. oxidation of aldehydes) through the mediation of particular metal complexes. This study establishes the bases for further development in this direction.

VII.3. Characterization and reactivity studies of a terminal copper-nitrene species

This section corresponds to the contents of the manuscript by Corona *et al. Angew. Chem. Int. Ed.* **2016**, *55*, 14005-14008, which can be found in **Chapter VI** of this thesis. In **Chapter VI** Teresa Corona (T.C.) synthesized and fully characterized the ligand following a procedure previously optimized by Lídia Ribas, Mireia Rovira and Xavi Ribas. T.C. prepared and characterized the corresponding imidylcopper(II) complex. T.C. also performed the computations under the supervision of Kallol Ray. Besides, T.C. performed the reactivity studies towards substrates and was involved in the generation of XAS samples that then were measured by Erik Farquhar at CWRU Center forSynchrotron Biosciences, New York (USA). Kallol Ray analyzed the XAS data. Part of this work was carried out at the Humboldt Universität zu Berlin (Germany) in the group of Kallol Ray through a scientific stay of T.C. (4 months). These work was supervised and coordinated by Kallol Ray and Anna Company.

High-valent terminal imidocopper (copper-nitrene) species have been postulated as active species in copper-catalyzed aziridination and amination reactions.[29] Obtaining mechanistic insight into these transformations and developing selective catalytic reagents and processes is only possible if the structure and properties of these key species are fully understood. Whereas imidometal species based on iron, cobalt, and nickel have been isolated, no terminal imidocopper species has been isolated yet, and only recently the Lewis acid adduct of an imidocopper could be trapped.[30] The high reactivity of these species has prevented their characterization for decades, thereby making the mechanisms ambiguous.

VII.3.1. Ligand design and synthesis

Recently, a family of well-defined aryl-Cu^{III}-halide species have been reported by our research group[31] using a well-defined macrocyclic ligand scaffold (^{H}L2) thanks to the enforcement of a square planar geometry which fits well with the d^8 copper(III) ion. Thus, we envisioned that these characteristics would make this ligand the perfect candidate to support high-valent imidocopper species using the corresponding azide derivative (^{H}L2-N_3, Scheme VII.7). ^{H}L2-N_3 was prepared in 95% isolated yield by reaction of ^{H}L2-Br (1 equiv.)[32] with NaN_3 (15 equiv.) in the presence of $[Cu^{I}(CH_3CN)_4](CF_3SO_3)$ (1 mol%) for 2 h at room temperature under a N_2 atmosphere. By analogy to previously reported C_{aryl}-heteroatom bond formation reactions using ^{H}L2-Br, formation of ^{H}L2-N_3 occurs through a $2e^-$ Cu^{I}/Cu^{III} catalytic cycle involving oxidative addition, ligand-exchange and reductive elimination steps (Scheme VII.7). ^{H}L2-N_3 was fully characterized by NMR, FT-IR and high-resolution ESI-MS and proved to be stable for several weeks in solution. Importantly, reaction time was found to be critical to afford high yields of ^{H}L2-N_3. Reaction times longer than 2 h caused its progressive decomposition into a new species derived from the loss of a N_2 molecule

as verified by ESI-MS. Most probably once the starting ^{H}L2-Br substrate is consumed the catalytic amounts of copper present in the crude reaction mixture interact with newly formed ^{H}L2-N$_3$ leading to its decomposition.

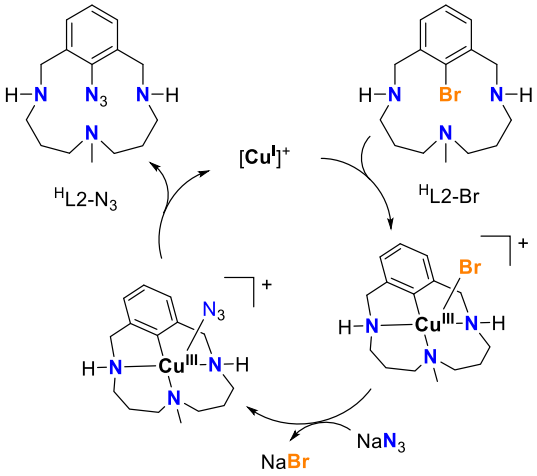

Scheme VII.7. Cu^{I}/Cu^{III} catalytic cycle for the synthesis of ^{H}L2-N$_3$ from ^{H}L2-Br.

VII.3.2. Reaction of ^{H}L2-N$_3$ with copper(I): spectroscopic characterization of copper products

In order to unravel if an imidocopper species was involved during this decomposition pathway, the stoichiometric reaction between ^{H}L2-N$_3$ and copper(I) was studied in detail. Reaction of ^{H}L2-N$_3$ with copper(I) salt was qualitatively evaluated (Scheme VII.8). Due to the fact that previously reported imidometal are colourful, the reaction was monitored by UV-vis spectroscopy. UV-vis monitoring of the reaction of ^{H}L2-N$_3$ with 1.5 equiv. [Cu^{I}(CH$_3$CN)$_4$](CF$_3$SO$_3$) in anhydrous CH$_3$CN under Ar atmosphere at room temperature evidenced the formation of an unstable green-colored transient species (**8**) with visible absorption bands at 380 and 790 nm. Compound **8** rapidly decomposed into a metastable purple species (**9**) with a visible absorption band at 550 nm (ε = 1000 M^{-1}cm^{-1}). The structure of **9** could be unequivocally established by XRD analysis as crystals of this compound appeared upon slow diffusion of diethyl ether into the crude CH$_3$CN solution at -30 ºC under an inert atmosphere. Compound **9** corresponded to a bis(μ-hydroxo)dicopper(II) species, in which each copper center was coordinated to two hydroxo units and three N atoms of the nitrogenated ligand in a distorted square pyramidal geometry (τ = 0.1) (Scheme VII.8).[33] Interestingly, the initial ^{H}L2-N$_3$ structure was significantly modified in **9**. Loss of a N$_2$ molecule of the azide unit was accompanied by abstraction of the hydrogen atom of one of the secondary amines forming a new N-N bond, which gave rise to an indazole ring. The copper(II) center was coordinated to the N-CH$_3$, NH, and N$_{aryl}$ groups of the resulting indazole-based ligand (^{H}L2^{in}). Due to the antiferromagnetic coupling between the two copper(II) centers, compound **9** was diamagnetic and could be analyzed by ^{1}H-NMR.[34] Analysis of the aromatic protons confirmed the formation of an indazole ring with protons at 8.2 (singlet), 7.7 (doublet) 7.2 (doublet) and 7.1 (triplet) ppm. High-resolution ESI-MS exhibited a major peak at *m/z* 321.1167 with an isotopic

pattern fully consistent with the monomeric $\{[Cu(^{H}L2^{in})]\}^{+}$ ion derived from the fragmentation of **9** under MS conditions accompanied with a minor peak at *m/z* 825.2118 consistent with $\{[Cu_2(OH)_2(^{H}L2^{in})_2](CF_3SO_3)]\}^{+}$. The two hydroxo groups in compound **9** could originate from adventitious water in the solvent. In this line, reaction of $^{H}L2\text{-}N_3$ and copper(I) in the presence of trace amounts of $H_2{}^{18}O$ afforded **9** with incorporation of ^{18}O as evidenced by a mass peak at *m/z* 829.1866.

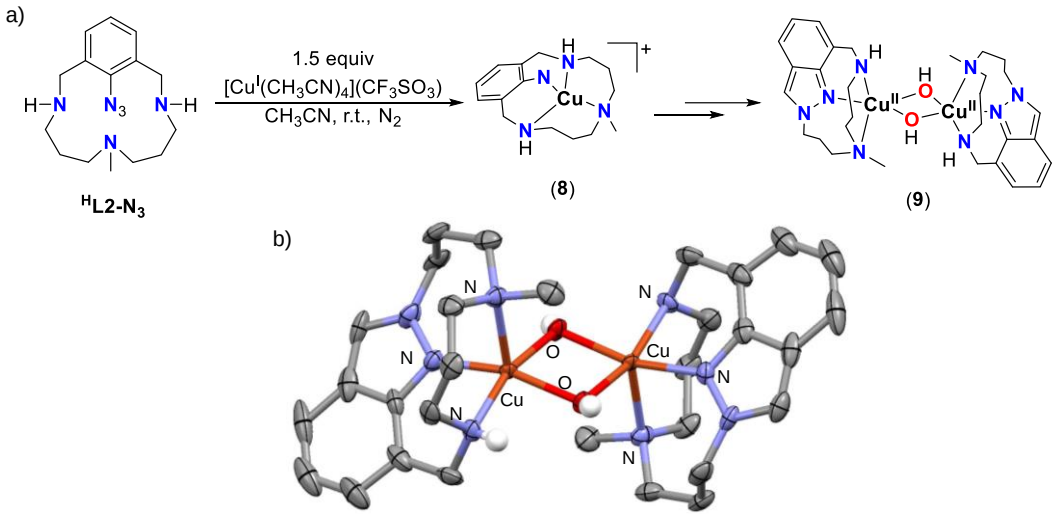

Scheme VII.8. a) Schematic representation of compounds **8** and **9** formed by reaction of $^{H}L2\text{-}N_3$ with 1.5 equiv. $[Cu^{I}(CH_3CN)_4](CF_3SO_3)$ in CH_3CN at 25 ºC under N_2. b) Thermal ellipsoid plot (50% probability) of **9**. Hydrogen atoms (except for those belonging to the OH groups) and triflate anions have been omitted for clarity.

Characterization of compound **8** proved to be much more difficult because of its unstability at room temperature. Attempts to trap this transient species were pursued by running the reaction between $^{H}L2\text{-}N_3$ and copper(I) at low temperature. Actually, **8** was stable in acetone at -50 ºC (λ_{max} [ε, $M^{-1}cm^{-1}$] =380 [>1300], 650 [>150] and 790 nm [>200]). Interestingly, CSI-MS of **8** exhibited a major peak at m/z 323.1284 consistent with the imidocopper species $\{[Cu(^{H}L2\text{-}N)]\}^{+}$ where $^{H}L2\text{-}N$ is the dianionic ligand formed after $2e^{-}$ reduction of $^{H}L2\text{-}N_3$ and N_2 release. As expected, CSI-MS of 50% ^{15}N-labeled* **8** showed a shift of 1 mass unit in ~50% of the sample, indicating that one of the nitrogen atoms in $^{H}L2\text{-}N$ originated from a terminal nitrogen atom of the azide. Nonetheless, **8** reacted very slowly towards organic substrates, most probably due to the low temperatures necessary to prevent its decomposition into **9**.

VII.3.3. Reaction of $^{Me}L2\text{-}N_3$ with copper(I): spectroscopic characterization of copper products

In order to block the decomposition of the putative imidocopper species (**8**), methyl groups were introduced in the secondary amines of the structure of the starting azide-derived ligand. Thus,

*Commercially available azide corresponds to the singly terminal labelled azide, $^{15}N\text{-}^{14}N\text{-}^{14}N$, for this reason 50% ^{15}N-labeled **8** was obtained.

after formic acid-formaldehyde methylation of the secondary amines in ^{H}L2-Br, the copper-catalyzed replacement of the Br group by N_3 afforded the methylated version of the azide-derived ligand (^{Me}L2-N_3, Figure VII.25). Interestingly, UV-vis monitoring of the reaction of ^{Me}L2-N_3 with 1 equiv. [$Cu^{I}(CH_3CN)_4$](CF_3SO_3) in anhydrous CH_3CN under Ar atmosphere at room temperature evidenced the instant formation of a metastable green species (**10**) ($t_{1/2}$ ~45 h) with visible absorption bands at λ_{max} [ε, $M^{-1}cm^{-1}$] = 360 nm [>1200], 710 nm [>200] and 980 nm [>150] (Figure VII.25). Getting insight into the nature of compound **10** was pursued by using several spectroscopic techniques. First of all, we attempted the characterization of **10** by high resolution ESI-MS (Figure VII.26), which showed a clean spectrum with a major peak at *m/z* 351.1597, with a mass value and isotopic pattern fully consistent with {[Cu(^{Me}L2-N)]}$^{+}$, corresponding to the imidocopper(III) species. As expected, the mass spectrum obtained by the reaction of copper(I) with ^{15}N-labeled ^{Me}L2-N_3 exhibited a shift of one mass unit up to *m/z* 352.1601. In order to establish the oxidation state of compound **10**, EPR experiments were carried out. The signal obtained by X-band EPR of a sample of **10** at 77 K accounted for less than 5% of the copper content. Vibrational spectroscopy was undertaken to get further information on the structure of compound **10**. Thus, vibrations derived from the CF_3SO_3 anion dominated the corresponding FT-IR spectrum and no azide vibration around 2200 cm^{-1} was observed, indicating that N_2 had been released. Moreover, a low-intensity band at 426 cm^{-1} shifted to 418 cm^{-1} when ^{15}N-labeled **10** was used, which was attributed to a Cu-N vibration. Finally, the effective magnetic moment (μ_{eff}) of a sample of **10** was determined to be 2.14 μ_B by the Evans' method.[35] This value is between that expected for one (1.73 μ_B) and two (2.83 μ_B) unpaired electrons, which may be indicative of the presence of some unreacted copper(I) or some copper(II) decomposition species along with the imidocopper(III) species in solution which, according to this analysis, would have 2 unpaired electrons.

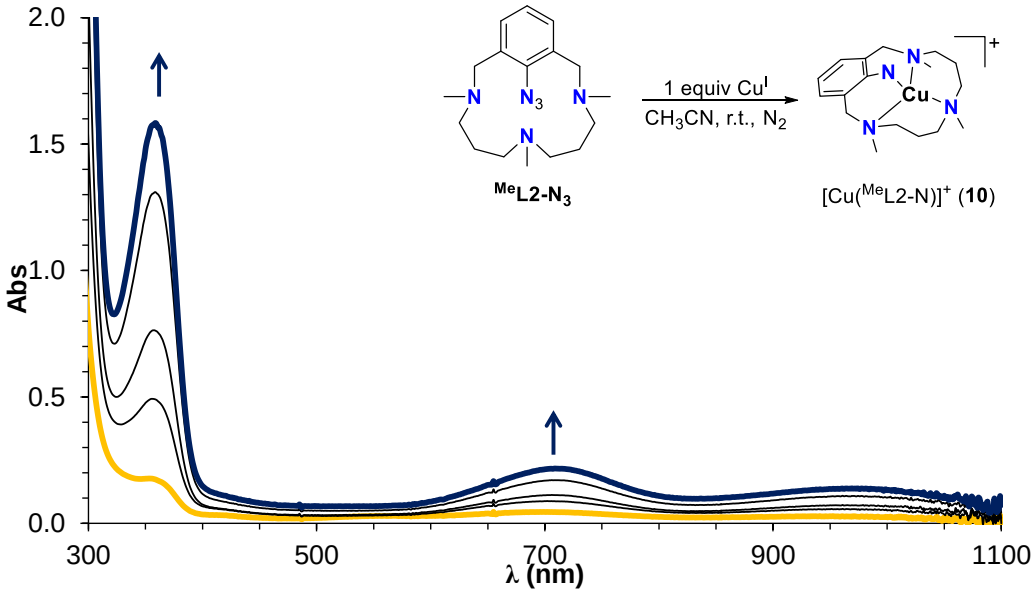

Figure VII.25. UV-vis formation of **10** in CH_3CN at 25 ºC under Ar (blue line). The sample was irradiated every 1 s to obtain the immediate formation of **10**. Inset: Reaction of ^{Me}L2-N_3 with Cu^{I} to form **10**.

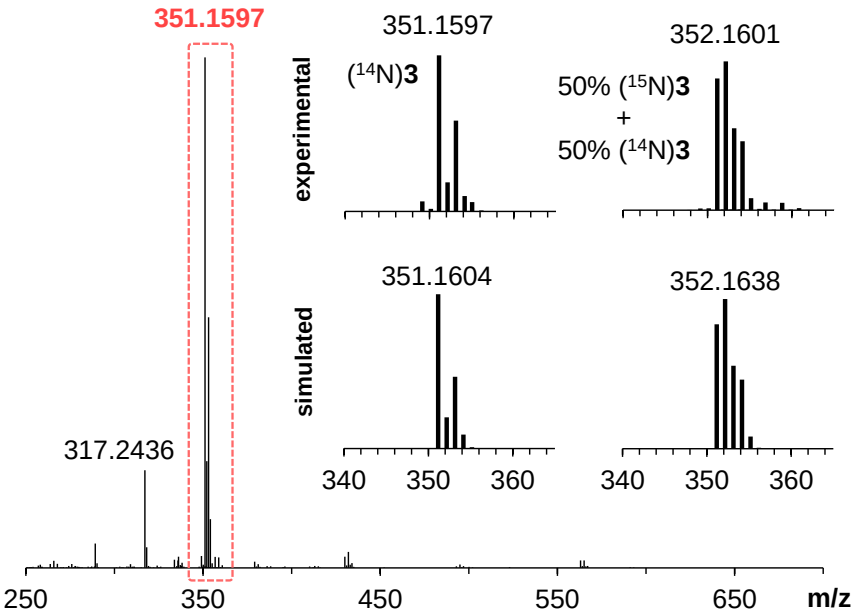

Figure VII.26. High resolution ESI-MS spectrum of **10** in CH_3CN at 25 ºC under N_2 showing a main peak at *m/z* 351.1597. Inset: simulated and experimental molecular peak of **10** and its 50% ^{15}N-labeled analogue.

Further insight into the nature of **10** was gained through XAS experiments. Compound **10** presented XANES features very similar to those of **9**, which corresponds to a dinuclear copper(II) complex (Figure VII.27a). This result indicated that **10** contained a copper(II) center, suggesting an imidylcopper(II) electronic structure $[Cu^{II}(^{Me}L2\text{-}N\bullet)]^+$ for **10**. On the other hand, EXAFS analyses suggested that in compound **10** copper was coordinated to 4 nitrogen atoms located at a ~2.04 Å (Figure VII.27b). For comparison purposes EXAFS analysis of compound **9** was also performed. In this case the data could be fitted to two subshells of four short Cu-N/O bonds at 1.99 Å, one long Cu-N/O bond at 2.13 Å and a Cu-Cu bond at 2.93 Å, which is fully consistent with the XRD structure of **9** corresponding to a dimeric species with two five-coordinate copper centers.

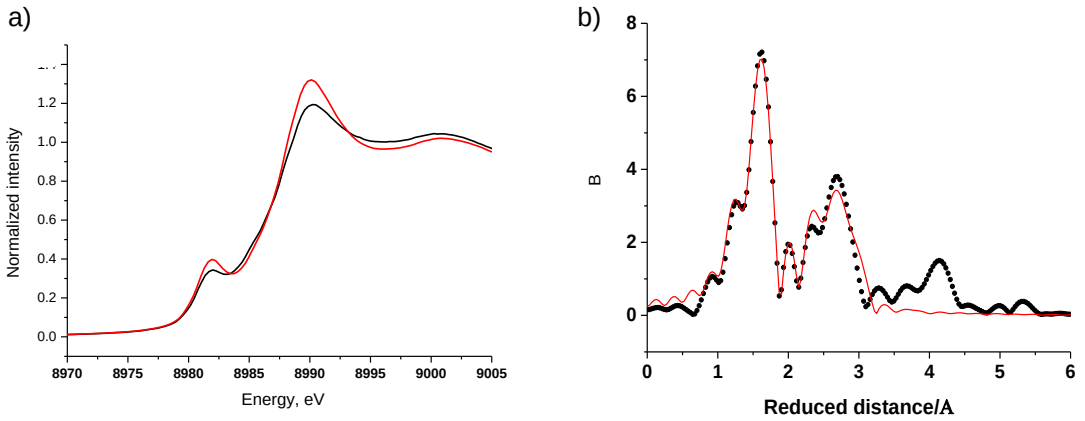

Figure VII.27. a) XANES region of complex **9** (red line) and **10** (black line). b) EXAFS of complex **10**, *black line* data, *red line* best fit.

At this point, DFT calculations were employed to determine the possible geometry and electronic structure of **10**, optimized with uB3LYP/TZVP level of theory. Thus, we firstly optimized the structure of $[Cu(^{Me}L2\text{-}N)]^+$ in all possible spin states (S = 0 or 1) and the most stable multiplicity, in this case the triplet, was selected, being 3 and 18 kcal·mol^{-1} more stable than the open and closed-shell singlets, respectively. The model consisted of a copper center in a strongly distorted tetrahedral geometry coordinated to the 4 nitrogen atoms (Figure VII.28a). The calculated metrical parameters for $[Cu(^{Me}L2\text{-}N)]^+$ were found to be in reasonable agreement with those determined by XAS for **10** (Table VII.5). Moreover, the experimentally observed FT-IR band at 426 cm^{-1} ($\Delta[^{15}N]$ = -8 cm^{-1}), which was tentatively assigned to a Cu-N vibration, was fully congruent with the computed frequency corresponding to this vibration for the model (427 cm^{-1}, $\Delta[^{15}N]$ = -6 cm^{-1}).

Interestingly, a Mulliken spin density analysis of the computed structure of $[Cu(^{Me}L2\text{-}N)]^+$ showed that the copper atom only located part of the spin density (ρ(Cu) = 0.4), and the other part was mainly located on the N_{aryl} atom (ρ(N_{aryl}) = 1.2) (Figure VII.28b). Such spin density distribution suggests the involvement of both $[Cu^{II}(^{Me}L2\text{-}N\bullet)]^+$ and $[Cu^{I}(^{Me}L2\text{-}N\bullet\bullet)]^+$ resonance forms in the electronic structure of **10**. A similar non-classical electronic structure has been previously suggested in oxocobalt species.[36] This electronic configuration was further confirmed by analysis of the spin natural orbitals (Figure VII.29), which showed one of the unpaired electrons in the p_y orbital of the N_{aryl} atom (42%) with a minor contribution of d_{yz} orbital of copper (6%) and the other SNO was distributed between the p_z orbital of the N_{aryl} atom (19%) and the d_{z2} orbital of copper (46%) plus a minor contribution of the other N atoms and the aromatic ring (<10%).

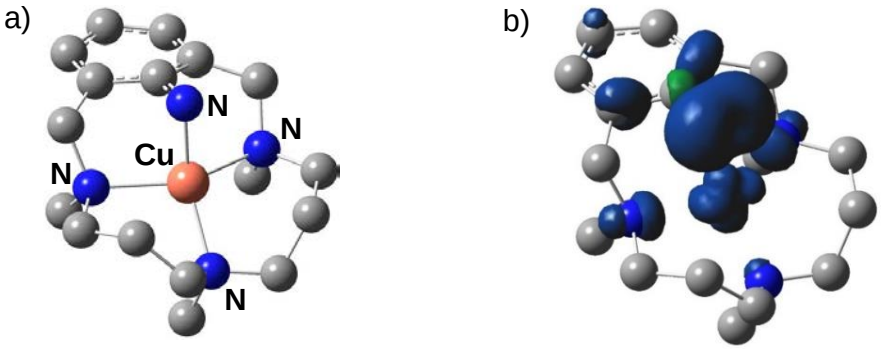

Figure VII.28. a) DFT computed structure of $[Cu(^{Me}L2\text{-}N)]^+$. b) Mulliken's spin density of the most relevant atoms for $[Cu(^{Me}L2\text{-}N)]^+$ (isovalue= 0.005).

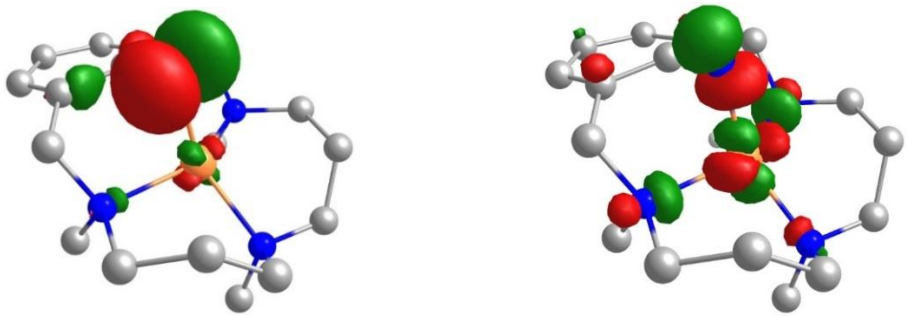

Figure VII.29. Spin-natural orbitals of $[Cu(^{Me}L2\text{-}N)]^+$ (isovalue = 0.062).

Table VII.5. Summary of the experimental characterization of **10** and comparison with theoretical model.

techniques	experimental data for compound 10	theoretical model $[Cu(^{Me}L2\text{-}N)]^+$
FT-IR	426 cm^{-1} ($\Delta[^{15}N]$ = -8 cm^{-1})	υ(Cu-N) 427 cm^{-1} ($\Delta[^{15}N]$ = -6 cm^{-1})
ESI-MS	major peak assigned to $\{[Cu(^{Me}L2\text{-}N)]\}^+$	monocharged molecule
μ_{eff}	2.14 μ_B (Evans' method)	expected μ_{eff} = 2.83 μ_B (*S* = 1)
X-band EPR	no signal related to **10** detected	*S* = 1 (even number of unpaired electrons)
XANES	the oxidation state of copper fits with +2	copper oxidation state between +2 and +1
EXAFS	4-coordinate Cu center (4 Cu-N ~2.04 Å)	4-coordinate Cu center (Cu-N_{aryl} 1.94 Å, Cu-N_{amine} 2.08-2.17 Å)

Self-decomposition of compound **10** was monitored by both ESI-MS (Figure VII.31b) and ^{1}H-NMR (Figure VII.31a). ESI-MS analysis of a one-day aged solution of **10** in CH_3CN at room temperature showed its molecular mass peak at *m/z* 351.14 accompanied by a major peak at *m/z* 289.24 corresponding to the loss of N_2 and protonation of $^{Me}L2\text{-}N_3$, suggesting the formation of a N-N bond (compound **11,** Figure VII.30). However, further evolution was observed and a new peak was observed after a few days at *m/z* 335.13. This mass value corresponds to the coordination of copper to an indazole-based ligand analogous to $^{H}L2^{in}$ in which one of the N-CH_3 bonds has been broken and a methane unit has been lost (compound **12**, Figure VII.30). The use of 50% ^{15}N-labeled **10** afforded partial labelling of mass peaks related to **11** and **12**.

On the other hand, ^{1}H-NMR monitoring of the decomposition of **10** correlated well with MS experiments and a set of broad signals related to **11** were observed in the first stages of the decomposition, while a second set of aromatic signals associated to **12** (70% yield) were evidenced after longer decomposition times (Figure VII.31a). The similarity of the aromatic ^{1}H-NMR pattern of this latter species with that observed for **9** is a clear indication that an indazole ring is formed in **12.** Particularly revealing are the down-field shifted singlet at 8.2 ppm and doublet at 7.7 ppm characteristic of indazole rings. Due to its triplet ground state, compound **10** was invisible by ^{1}H-NMR and it only caused a broadening of the bands related to **11** in the first stages of the decomposition. Analysis of the headspace of the solution of **12** was performed by GC-TCD, which clearly showed the release of methane further supporting the formation of the indazole ring in compound **12**.

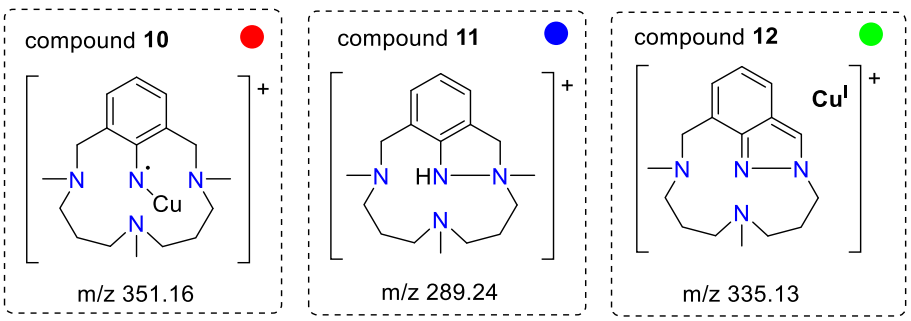

Figure VII.30. Schematic representation of the species observed by ESI-MS upon self-decomposition of compound **10**.

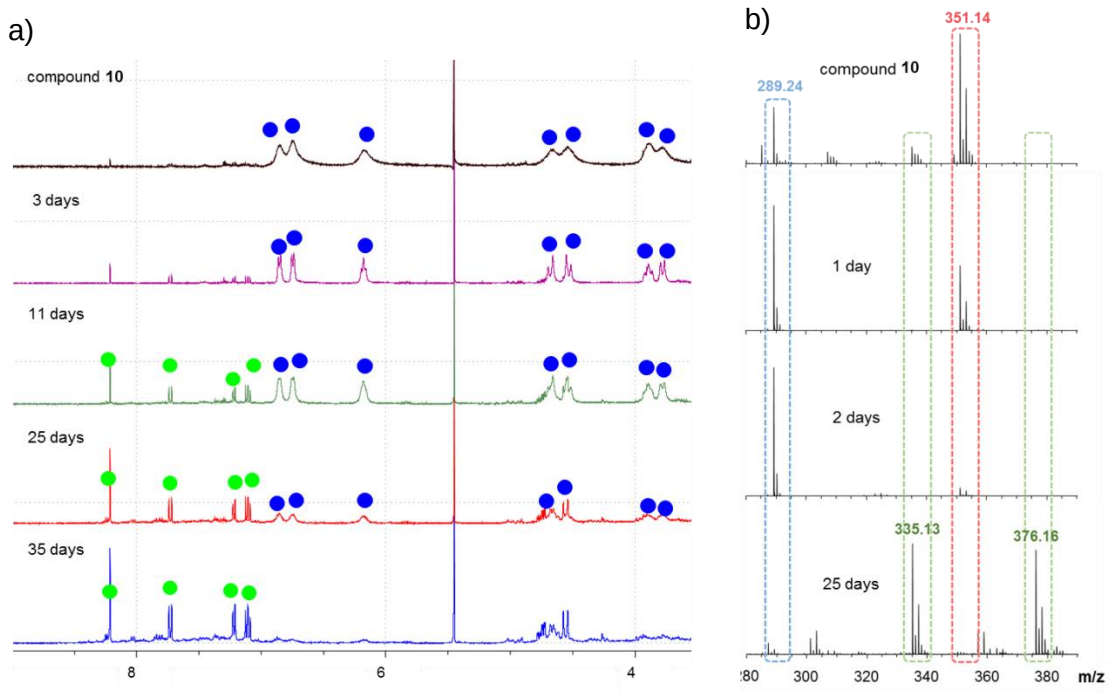

Figure VII.31. a) ^{1}H-NMR spectra over time (up to 35 days) of a solution of **10** formed by reaction of ^{Me}L2-N_3 with 1 equiv. [Cu^{I}(CH$_3$CN)$_4$](CF$_3$SO$_3$) in CD$_3$CN at room temperature under N_2. NMR signals belonging to **11** and **12** are marked with blue and green dots, respectively (see Figure VII.30 for structures). b) ESI-MS spectra over time (up to 25 days) of a solution of **10** in CH$_3$CN at room temperature under N_2 (see Figure VII.30 for an assignment of the mass peaks).

*VII.3.4. Kinetic analysis of the reaction of **10** toward organic substrates*

Remarkably, species **10** turned out to be reactive towards different substrates (Scheme VII.9 and Table VII.6). Phosphines were selected as substrates for direct nitrene-transfer reactions. UV-vis monitoring of this reaction indicated that the decay of the 710 and 980 nm bands associated to **10** became significantly accelerated by the addition of triphenylphosphine (PPh$_3$). Under conditions of excess substrate kinetic traces showed pseudo-first order behaviour and could be fitted to single exponential functions. The corresponding k_{obs} values were found to be linearly dependent on substrate concentration, affording a second-order rate constant (k) of 7.5 M^{-1}s^{-1} for the reaction towards PPh$_3$. Analysis of the final products were carried out. ESI-MS showed a peak at *m/z* 551.35 corresponding to nitrogen insertion to the phosphorous atom to form ^{Me}L2-N=PPh$_3$. As expected, ESI-MS of the same reaction starting from 50% ^{15}N-labeled **10** afforded a shift of 1 mass unit in ~50% of the reaction product (*m/z* 552.34), further confirming the formation of the nitrene-transfer product. ^{31}P-NMR of the final product showed a signal at 25.6 ppm, which is the typical region for N=P bonds (Figure VII.32a).[37] Moreover, ^{31}P-NMR of the reaction of 50% ^{15}N-labeled **10** with PPh$_3$ showed two signals: a singlet at 25.6 ppm together with a doublet at 25.3 ppm. The latter corresponds to the ^{15}N-labelled product due to the coupling between ^{31}P and ^{15}N (S = 1/2) (Figure VII.32a). The coupling constant of this doublet was $J_{N\text{-}P}$ = 38.2 Hz, which is in the typical range for N-P bonds.[38] Thus, all the experiments supported the formation of the nitrene-transfer product ^{Me}L2-N=PPh$_3$ which was formed in 41% yield with respect to copper as

determined by ^{31}P-NMR. More information about the mechanism operating in this transformation was gained through the initial observation that the reaction rates were highly dependent on the *para* substituent present in phenyl groups of the phosphine. Thus, we measured the second order rate constants corresponding to the reaction of **10** with a series of *para*-substituted triphenylphospine, *p*-X-triphenylphospine (X = Me, H and Cl). Plotting of log(k_X/k_H) for the different substrates against the corresponding Hammett parameter (σ_p) afforded a good correlation and a Hammett value with negative slope (ρ = -1.9), which is indicative of the electrophilic character of **10** (Figure VII.32b). Reaction of **10** with other phosphines was also performed. Interestingly, *k* values were found to be highly dependent on the substituent at the phosphorous atom. The reaction of **10** with a bulkier substrate such as tri(*o*-tolyl)phosphine (P(*o*-tol)$_3$) was much slower (0.052 $M^{-1}s^{-1}$) than with triphenylphospine. These results suggest that steric effects have a strong influence in the reaction of **10** towards phosphines.

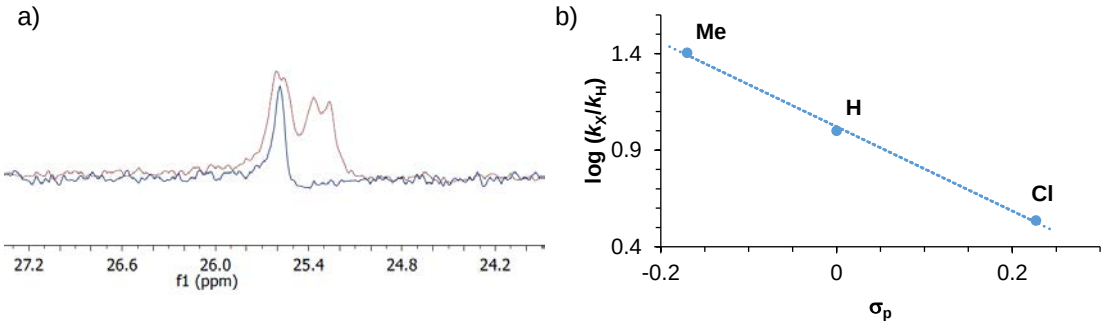

Figure VII.32. a) ^{31}P-NMR (blue line) and its 50% ^{15}N-labeled analogue (red line) of the reaction of **10** (or ^{15}N-**10**) with PPh_3 in CD_3CN at room temperature under N_2. b) Hammett plot, log(k_X/k_H) vs the Hammett parameter (σ_p), for the reaction of **10** against *para*-substituted-triphenylphospines in CH_3CN at room temperature under N_2.

Moreover, reaction of **10** with hydrocarbons bearing weak C-H bonds was also performed. As expected, we observed also a steric effect with hydrocarbons. The reaction with xanthene (k = 0.009 $M^{-1}s^{-1}$, BDE = 75.5 kcal·mol^{-1}) was slower than with 1,4-cyclohexadiene (k = 0.020 $M^{-1}s^{-1}$, BDE = 78 kcal·mol^{-1}). These results do not correlate with the bond dissociation energies of the corresponding C-H bonds but they do correlate with the fact that 1,4-cyclohexadiene is significantly less sterically hindered than xanthene. Furthermore, the kinetic isotope effect was determined by measurement of the reaction rates of **10** with xanthene and d_2-xanthene. A KIE of 5.4 was determined.

Table VII.6. Second-order rate constants (k, $M^{-1}s^{-1}$) for the reaction of **10** towards substrates together with product analyses and product yields.

Substrate	k, $M^{-1}s^{-1}$	^{31}P-NMR, ppm	ESI-MS, *m/z* (^{15}N)	Product yield, %
xanthene	0.009	-	469.31 (471.31)	44
1,4-cyclohexadiene	0.020	-	367.29	-
PPh_3	7.5	26	551.35 (552.34)	41
P^nBu_3	too fast	51	491.35	84
P(*o*-tol)$_3$	0.052	17	-	48

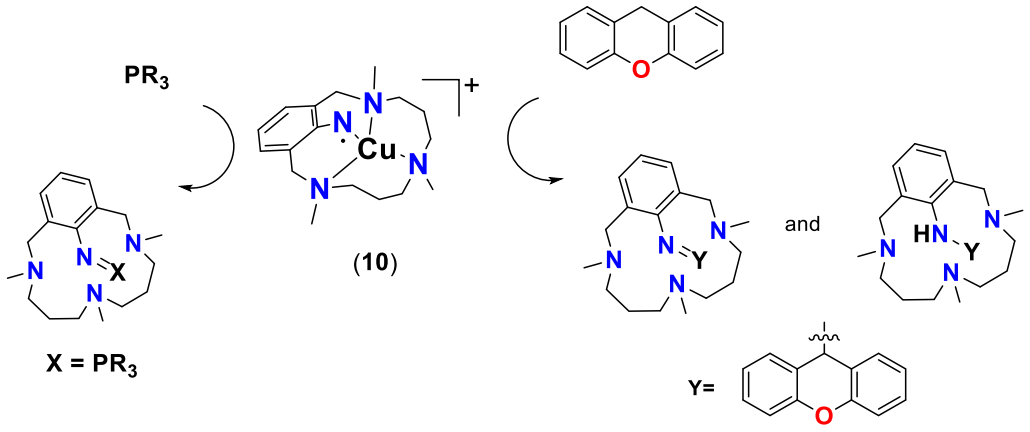

Scheme VII.9. Schematic representation of the nitrene-transfer products formed by reaction of **10** with phosphines and xanthene.

In summary, full characterization by experimental and DFT techniques indicate that compound **10** corresponds to the first example of a well-defined terminal imidocopper without the need of redox-innocent cations such as Sc^{3+}. This compound can be trapped at room temperature and it is competent to perform nitrogen-atom transfer to phosphines and hydrogen-atom abstraction from weak C-H bonds.

VII.4. References

[1] a) Patra, A. K.; Mukherjee, R., *Inorg. Chem*., **1999**, *38*, 1388. b) de Oliveira, F. T.; Chanda, A.; Banerjee, D.; Shan, X.; Mondal, S.; Que, L.; Bominaar, E. L.; Munck, E.; Collins, T. J., *Science,* **2007**, *315*, 835. c) Ghosh, M.; Singh, K. K.; Panda, C.; Weitz, A.; Hendrich, M. P.; Collins, T. J.; Dhar, B. B.; Sen Gupta, S., *J. Am. Chem. Soc*., **2014**, *136*, 9524. d) Taguchi, T.; Gupta, R.; Lassalle-Kaiser, B.; Boyce, D. W.; Yachandra, V. K.; Tolman, W. B.; Yano, J.; Hendrich, M. P.; Borovik, A. S., *J. Am. Chem. Soc*., **2012**, *134*, 1996. e) Lacy, D. C.; Gupta, R.; Stone, K. L.; Greaves, J.; Ziller, J. W.; Hendrich, M. P.; Borovik, A. S., *J. Am. Chem. Soc*., **2010**, *132,* 12188.

[2] Arbuse, A.; Font, M.; Martínez, M. A.; Fontrodona, X.; Prieto, M. J.; Moreno, V.; Sala, X.; Llobet, A., *Inorg. Chem.,* **2009**, *48*, 11098.

[3] Huang, D.; Holm, R. H., *J. Am. Chem. Soc.,* **2010**, *132*, 4693.

[4] Sharma, S. K.; Upreti, S.; Gupta,R., *Eur. J. Inorg. Chem.,* **2007**, 3247.

[5] Draksharapu, A.; Codolà, Z.; Gómez, L.; Lloret-Fillol, J.; Browne, W. R.; Costas, M., *Inorg. Chem.,* **2015**, *54*, 10656.

[6] Liu, W.; Groves, J. T., *J. Am. Chem. Soc.,* **2010**, *132*, 12847.

[7] a) Huang, Y. H.; Park, J. B.; Adams, M. W. W.; Johnson, M. K., *Inorg. Chem.,* **1993**, *32*, 375. b) Lee, C. M.; Chen, C. H.; Liao, F. X.; Hu, C. H.; Lee, G. H, *J. Am. Chem. Soc.,* **2010**, *132*, 9256. c) Yang, N.; Reiher, M.; Wang, M.; Harmer, J.; Duin, E. C., *J. Am. Chem. Soc.,* **2007**, *129*, 11028. d) Dey, M.; Telser, J.; Kunz, R. C.; Lees, N. S.; Ragsdale, S. W.; Hoffman, B. M., *J. Am. Chem. Soc,.* **2007**, *129*, 11030.

[8] Colpas, G. J.; Maroney, M. J.; Bagyinka, C.; Kumar, M.; Willis, W. S.; Suib, S. L.; Mascharak, P. K.; Baidya, N., *Inorg. Chem.*, **1991**, *30*, 920.

[9] a) Furenlid, L. R.; Renner, M. W.; Fujita, E., *Phys. B Phys. Condens. Matter,* **1995**, *208-209*, 739. b) Risch, M.; Klingan, K.; Heidkamp, J.;Ehrenberg, D.; Chernev, P.; Zaharieva, I.; Dau, H., *Chem. Commun,.* **2011**, *47*, 11912.

[10] Cong, Z.; Yanagisawa, S.; Kurahashi, T.; Ogura, T.; Nakashima, S.; Fujii, H., *J. Am. Chem. Soc.,* **2012**, *134*, 20617.

[11] a) Kau, L.; Spira-Solomon, D. L.; Penner-Hahn, J. E.; Hodgson, K. O.; Solomon, E. I., *J. Am. Chem. Soc.,* **1987**, *109*, 6433. b) Westre, T. E.; Kennepohl, P.; DeWitt, J. G.; Hedman, B.; Hodgson, K. O.; Solomon, E. I., *J. Am. Chem. Soc.,* **1997**, *119*, 6297.

[12] a) Gu, W.; Wang, H.; Wang, K., *Dalton Trans.*, **2014**, *43*, 6406. b) Colpas, G. J.; Maroney, M. J.; Bagyinka, C.; Kumar, M.; Willis, W. S.; Suib, S. L.; Baidya, N.; Mascharak, P. K., *Inorg. Chem*., **1991**, *30*, 920.

[13] Ray, K.; Debeer George, S.; Solomon, E. I.; Wieghardt, K.; Neese, F., *Chemistry,* **2007**, *13*, 2783.

[14] a) Yano, J.; Yachandra, V. K.; *Photosynth. Res*. **2009**, *102*, 241. b) Scott, R. A.; Eidsness, M. K., *Comments Inorg. Chem*., **1988**, *7*, 235.

[15] Ray, K.: Begum, A.; Weyhermuller, T.; Piligkos, S.; van Slageren, J.; Neese, F.; Wieghardt, K., *J. Am. Chem. Soc.,* **2005**, *127*, 4403.

[16] Sastri, C. V.; Seo, M. S.; Park, M. J.; Kim, K. M.; Nam, W., *Chem. Commun*., **2005**,1405.

[17] Manner, V. W.; Markle, T. F.; Freudenthal, J. H.; Roth, J. P.; Mayer, J. M., *Chem. Commun.,* **2008**, *246*, 256.

[18] a) Sastri, C. V.; Lee, J.; Oh, K.; Lee, Y. J.; Jackson, T. A.; Ray, K.; Hirao, H.; Shin, W.; Halfen, J. A.; Kim, J., *Proc. Natl. Acad. Sci. U. S. A.,* **2007**, *104*, 19181. b) Mayer, J. M., *Acc. Chem. Res.,* **1998**, *31*, 441.

[19] Pfaff, F. F.; Heims, F.; Kundu, S.; Mebs, S; Ray, K., *Chem. Commun*., **2012**, *48*, 3730.

[20]Nakazawa, J.; Terada, S.; Yamada, M.; Hikichi, S., *J. Am. Chem. Soc*., **2013**, *135*, 6010.

[21] Pirovano, P.; Farquhar, E. R.; Swart, M.; Fitzpatrick, A. J.; Morgan, G. G.; McDonald, A. R., *Chem. Eur. J.*, **2015**, *21,* 3785.

[22] Pirovano, P.; Farquhar, E. R.; Swart, M.; McDonald, A. R*., J. Am. Chem. Soc.,* **2016**, *138*, 14362.

[23] Corona, T., *Master thesis* **2013**.

[24] Cibian, M.; Derossi S. Hanan, G. S., *Dalton Trans*., **2011**, *40*, 1038.

[25] a) Halpern, J.; Chan, M. S.; Hanson, J.; Roche, T. S.; Topich, J. A., *J. Am. Chem. Soc*., **1975**, *97*, 1606. b) Will, S.; Lex, J.; Vogel, E.; Adamian, V. A.; Van Caemelbecke, E.; Kadish, K. M., *Inorg. Chem.,* **1996**, *35*, 5577. c) Hong, S.; Pfaff, F. F.; Kwon, E.; Wang, Y.; Seo, M. –S.; Bill, E.; Ray, K.; Nam, W., *Angew. Chem., Int. Ed*., **2014**, *53*, 10403. d) Levitin, I.; Sigan A. I.; Vol'pin, M. E, *J. Chem. Soc., Chem. Commun*., **1975**, 469.

[26] a) Hong, S.; Pfaff, F. F.; Kwon, E;. Wang, Y;. Seo, M;. Bill, E.; Ray, R.; Nam, W., *Angew. Chem., Int. Ed.,* **2014**, *53*, 10403. b) Ions, S. I. I. I.; Pfaff, F. F.; Kundu, S;. Risch, M.; Pandian, S.; Heims,

F.; Pryjomska-ray, I.; Haack, P.; Metzinger, R.; Bill, E., *Angew. Chem., Int. Ed.,* **2011**, *3*, 1711. c) Lacy, D. C.; Park, Y. J.; Ziller, J. W.; Yano, J.; Borovik, A. S., *J. Am. Chem. Soc*., **2012,** *134*, 17526.

[27] a) Klein J. E. M. N.; Que, L., in Encyclopedia of Inorganic and Bioinorganic Chemistry, John Wiley & Sons, Ltd, 2011. b) Chen, J.; Lee, Y. -M.; Davis, K. M.; Wu, X.; Seo, M. S.; Cho, K. –B.; Yoon, H.; Park, Y. J.; Fukuzumi, S.; Pushkar, Y. N.; Nam, W., *J. Am. Chem. Soc.*, **2013**, *135*, 6388. c) Hong, S.; So, H.; Yoon, H.; Cho, K. –B.; Lee, Y. –M.; Fukuzumi, S.; Nam, W., *Dalton Trans*., **2013**, *42*, 7842.

[28] a) Annaraj, J.; Suh, Y.; Seo, M. S.; Kim, S.O.; Nam, W., *Chem. Commun*., **2005**, 4529. b) Geiger, R. A.; Chattopadhyay, S.; Day, V. W.; Jackson, T. A., *Dalton Trans*., **2011**, *40*, 1707. c) Jo, Y.; Annaraj, J.; Seo, M. S.; Lee, Y. –M.; Kim, S. Y.; Cho, J.; Nam, W., *J. Inorg. Biochem.,* **2008**, *102*, 2155.

[29] a) Shin, K.; Kim. H.; Chang, S, *Acc. Chem. Res*, **2015**, *48*, 1040. b) Gephart, R. T.; Warren, T. H., *Organometallics,* **2012**, *31*, 7728. c) Badiei, Y. M.; Krishnaswamy, A.; Melzer, M. M.; Warren, T. H., *J. Am. Chem. Soc.,* **2006**, *128*, 15056. d) Badiei, Y. M.; Dinescu, A.; Dai, X.; Palomino, R. M.; Heinemann, F. W.; Cundari, T. R.; Warren, T. H., *Angew. Chem. Int. Ed.* **2008**, *47*, 9961.

[30] a) Kundu, S.; Miceli, E.; Farquhar, E.; Pfaff, F. F.; Kuhlmann, U.; Hildebrandt, P.; Braun, B.; Greco, C.; Ray, K., *J. Am. Chem. Soc.,* **2012**, *134*, 14710. b) Abram, S.-L.; Monte-Pérez, I.; Pfaff, F. F.; Farquhar, E. R.; Ray, K., *Chem. Commun.,* **2014**, *50*, 9852.

[31] a) Casitas, A.; Canta, M.; Solà, M.; Costas, M;. Ribas, X., *J. Am. Chem. Soc*., **2011**, *133*, 19386. b) Casitas, A. King, A. E.; Parella, T.; Costas, M.; Stahl, S. S.; Ribas, X., *Chem. Sci.,* **2010**, *1*, 326. c) Rovira, M.; Font, M.; Ribas, X., *ChemCatChem,* **2013**, *5*, 687. d) Rovira, M.; Font, M.; Acuña-Parès, F.; Parella, T.; Luis, J. M.; Lloret-Fillol, J.; Ribas, X., *Chem. Eur. J.,* **2014**, *20*, 10005. e) Huffman, L. M; Casitas, A; Font, M.; Canta, M.; Costas, M.; Ribas, X.; Stahl, S. S., *Chem. Eur. J.,* **2011**, *17*, 10643. f) Font, M.; Parella, T.; Costas, M.; Ribas, X., *Organometallics,* **2012**, *31*, 7976.

[32] a) Ribas, X.; Jackson, D. A.; Donnadieu, B.; Mahía, J.; Parella, T.; Xifra, R.; Hedman, B.; Hodgson, K. O.; Llobet, A.; Stack, T. D. P., *Angew. Chem. Int. Ed.,* **2002**, *41*, 2991. b) Casitas, A.; Canta, M.; Solà, M.; Costas, M;. Ribas, X., *J. Am. Chem. Soc*., **2011**, *133*, 19386.

[33] Marlin, D. S.; Olmstead, M. M.; Mascharak, P. K., *Inorg. Chem*., **2001**, *40*, 7003.

[34] Costas, M.; Ribas, X.; Poater, A.; López Valbuena, J. M.; Xifra, R.; Company, A.; Duran, M.; Solà, M.; Llobet, A.; Corbella, M.; Usln, M. A.; Mahía, J.; Solans, X.; Shan, X.; Benet-Buchholz, J., *Inorg. Chem.* **2006**, *45*, 3569.

[35] a) Evans, D. F.; *J. Chem. Soc.,* **1959**, 2003. b) Naklicki, M. L.; White, C. A.; Plante, L. L.; Evans, C. E. B.; Crutchley, R. J., *Inorg. Chem*., **1998**, *37*, 1880.

[36] Crandell, D. W.; Ghosh, S.; Berlinguette, C. P.; Baik, M.-H., *ChemSusChem,* **2015**, *8*, 844.

[37] Kundu, S., PhD Thesis; Department of Chemistry, Humboldt Universität zu Berlin (Germany), 2013.

[38] Gombler, W.; Kinas, R. W.; Stec, W. J., *Z. Naturforsch*, **1983**, *38*, 815.

Chapter VIII.

General Conclusions

VIII. GENERAL CONCLUSIONS

In the first part of this thesis a new dianionic unsymmetric tetradentate macrocyclic ligand (L1) that contains a 2,6-pyridinecarboxamidate motif has been designed as a platform for the stabilization of terminal high-valent metal-oxygen species. Ligand L1 was also regarded as a good platform to achieve N_2O activation because it forms metal complexes with highly electron rich metal centers, an essential requirement to achieve the transfer of electrons to N_2O and consequently its activation. Thus, results presented in **Chapter III** and **IV** highlight the stabilization and characterization of two terminal high-valent nickel-oxygen species that behave as strong oxidizing agents. In **Chapter V** we show the successful activation of nitrous oxide (N_2O) using the corresponding cobalt(II) complex.

Firstly, in **Chapter III** we prepared the nickel(II) complex of L1 (**1**) and studied its reactivity towards different oxidants: O_2, H_2O_2, N_2O, ROOH, peracids and NaOCl. Remarkably, compound **1** reacted with *meta*-chloroperbenzoic acid (*m*CPBA) at low temperature to form compound **2**, which was trapped and spectroscopically characterized. A combination of experimental and theoretical analyses suggested that a heterolytic O-O bond cleavage of a nickel(II)-peracid adduct occurred, thus giving rise to the formation of a high-valent nickel-oxygen species that was best formulated as a nickel(III)-oxyl complex [Ni(L1)(O)]. Secondly, in **Chapter IV** we studied the reaction of compound **1** with sodium (or calcium) hypochlorite in the presence of acetic acid at low temperature to form a highly reactive species (**4**). Compound **4** was characterized by UV-vis absorption, resonance Raman, EPR, XAS and cryospray mass analyses as well as DFT calculations, which indicated that this trapped species was best formulated as a nickel(III)-hypochlorite radical species with the general formula $[Ni(L1)(OCl)]^+$. Remarkably, the oxidation/chlorination of strong C-H bonds such as cyclohexane or *n*-hexane under catalytic conditions using compound **1** in combination with NaOCl and acetic acid was accomplished affording up to 34 turnovers of chlorocyclohexane and 7 turnovers of cyclohexanone. The higher reactivity of **2** and **4** towards C-H bonds, C=C bonds and sulfides compared to other reported well-defined terminal nickel-oxygen systems suggests that these two species might be relevant in nickel-catalyzed oxidation reactions. Thus, the dianionic ligand L1 serves as an excellent platform to favor the formation and stabilization of high-valent nickel species that behave as strong oxidants.

In **Chapter V** we describe the activation of N_2O using the cobalt(II) complex of L1 (**5**). This complex proved to be highly reactive with oxidants including N_2O. Indeed the reaction of **5** with N_2O occurred within 1 min under mild reactions conditions (T= 0 ºC, P= 1 atm). Moreover, the system was applied for the catalytic oxidation/deformylation of aldehydes. Unfortunately, the nature of the cobalt species resulting from N_2O activation and responsible for substrate oxidation could not be determined. Kinetic studies indicated that the reaction between **5** and N_2O occurred with a 1:1 stoichiometry with the generation of 1 equiv. N_2, which would be in

agreement with the involvement of a cobalt(IV) compound. This work is specially remarkable considering that the activation of this waste gas under mild conditions is highly challenging due to its chemical inertness. Furthermore, this work demonstrates that N_2O can be used as oxidant in chemical transformations through the mediation of particular metal complexes and it establishes the bases for further development in this direction.

In **Chapter VI** we focus our attention on the detection of mononuclear imidocopper species, which have long been postulated as the active species in copper-catalyzed amination and aziridination reactions. Detection and characterization of such species has remained elusive and only recently imidylcopper(II) species stabilized with redox-innocent metal ions such as Sc^{3+} have been reported. Thus, in **Chapter VI** we described the synthesis and spectroscopic characterization of the first example of a well-defined terminal imidylcopper(II) species (copper-nitrene radical) in the absence of a Lewis acid. Reaction of a copper(I) salt with an azide-containing macrocyclic ligand (^{Me}L2-N_3) afforded the stabilization of an imidilycopper(II) compound (**10**) at room temperature under an inert atmosphere. The methylation of the secondary amines of the ligand was crucial to slow down the main decomposition pathway corresponding to the N-N bond formation event (as observed in ligand ^{H}L2-N_3) and enable the stabilization of **10** even at room temperature. Interestingly, compound **10** could carry out nitrene-transfer reactions to organic substrates such as phosphines and perform hydrogen-atom abstraction from weak C-H bonds. The trapped species may be relevant in copper catalyzed C-N bond formation reactions.

Annex

A.1. Supplementary Information Chapter III

1.1. Synthesis of H_2L

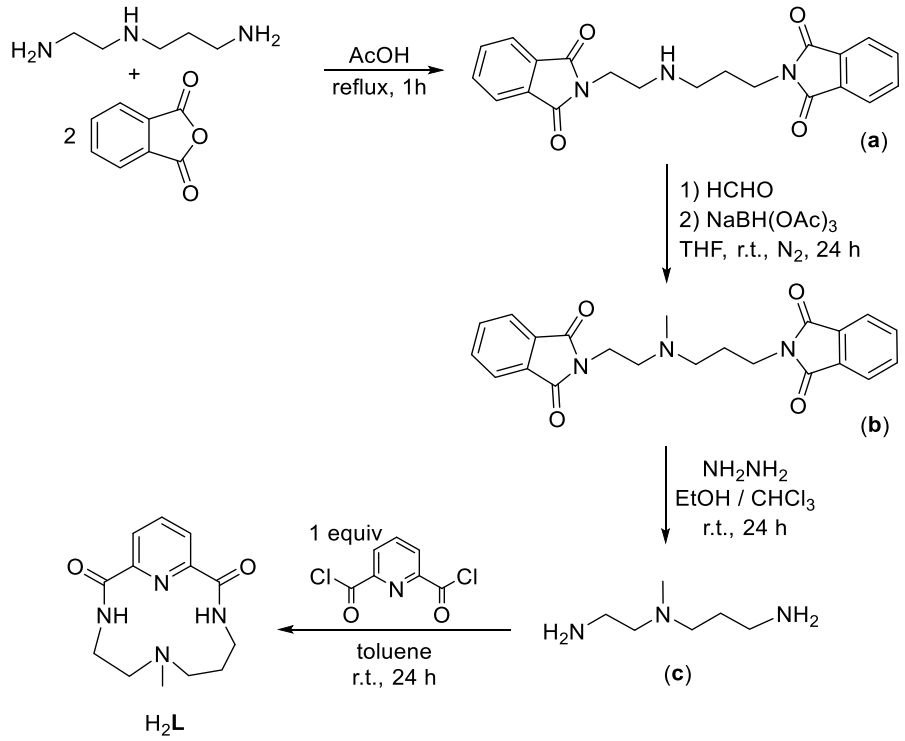

Scheme S1. Synthetic route for the preparation of H_2**L**.

Synthesis of a. Following the experimental procedure described in the literature,[1] a mixture of *N*-(2-aminoethyl)-1,3-propanediamine (15.04 g, 0.13 mol) and phthalic anhydride (37.91 g, 0.26 mol) in glacial acetic acid (185 mL) was refluxed for 1 h. Afterwards, the solvent was removed under reduced pressure and hot ethanol (280 mL) was added with stirring which caused the formation of a yellow solid. This product was filtered off and washed with cold ethanol. Finally, the pale yellow solid was dried under vacuum to obtain the desired product **a** as a pale yellow solid (47.83 g, 0.13 mol, 99%). ^{1}H-NMR ($CDCl_3$, 300 MHz, 298K) δ, ppm: 7.83 (m, 4H, Ar**H**), 7.71 (m, 4H, Ar**H**), 3.86 (t, J = 9.1 Hz, 2H, C**H**$_2$N), 3.74 (t, J = 8.1 Hz, 2H, C**H**$_2$N), 2.97 (t, J = 8.1 Hz, 2H, C**H**$_2$NH), 2.72 (t, J = 9.1 Hz, 2H, C**H**$_2$NH), 1.88 (quint, J = 9.1 Hz, 2H, CH_2C**H**$_2$$CH_2$). ^{13}C-NMR ($CDCl_3$, 75 MHz, 298K) δ, ppm: 175.77, 168.50, 168.31, 134.05, 132.03, 131.87, 123.32, 123.31, 58.03, 46.04, 44.99, 35.09, 26.36.

Synthesis of b. Compound **a** (16.32 g, 0.043 mol) and formaldehyde 38% (5.1 mL, 0.068 mol) were mixed in tetrahydrofuran (275 mL) at room temperature under nitrogen. Then, sodium triacetoxyborohydride (13.75 g, 0.065 mol) was added and the mixture was stirred at room temperature for 24 h. Afterwards, NaOH 2M (250 mL) was added and the mixture was extracted with dichloromethane (3 × 250 mL). The combined organic extracts were dried over anhydrous

$MgSO_4$, filtered and the solvent was removed under reduced pressure to yield a solid residue. This compound was suspended in diethyl ether and the resulting pale yellow solid was filtered and dried under vacuum. Compound **b** was obtained as a pale yellow solid (16.68 g, 0.043 mol, 99%). ^{1}H-NMR ($CDCl_3$, 400 MHz, 298K) δ, ppm: 7.81 (m, 4H, Ar**H**), 7.70 (m, 4H, Ar**H**), 3.78 (t, J = 7.0 Hz, 2H, C**H**$_2$N), 3.65 (t, J = 6.6 Hz, 2H, C**H**$_2$N), 2.65 (t, J = 6.6 Hz, 2H, C**H**$_2$NMe), 2.47 (t, J = 7.0 Hz, 2H, C**H**$_2$NMe), 2.29 (s, 3H, C**H**$_3$), 1.78 (quint, J = 7.0 Hz, 2H, CH_2C**H**$_2$$CH_2$). ^{13}C-NMR ($CDCl_3$, 100 MHz, 298K) δ, ppm: 168.34, 133.82, 132.19, 123.21, 54.56, 41.39, 36.06, 35.19, 25.72, 20.75.

Synthesis of c. A mixture of **b** (5.43 g, 0.014 mol) and hydrazine monohydrate (10.5 mL, 0.22 mol) in ethanol (310 mL) and chloroform (70 mL) was allowed to react at room temperature for 24 h. Afterwards, the white solid that had appeared along the reaction was filtered off, and the solvent from the filtrate was removed under reduced pressure. Chloroform (290 mL) was added to the resulting residue and the mixture was further stirred for 6 h and filtered again. Removal of the solvent from the filtrates afforded compound **c** as a yellow oil (1.49 g, 0.011 mol, 82%). ^{1}H-NMR ($CDCl_3$, 400 MHz, 298K) δ, ppm: 2.65 (m, 4H, C**H**$_2$NMe), 2.30 (m, 4H, C**H**$_2$$NH_2$), 2.11 (s, 3H, C**H**$_3$), 1.52 (quint, J = 7.0 Hz, 2H, CH_2C**H**$_2$$CH_2$). ^{13}C NMR ($CDCl_3$, 100 MHz, 298K) δ, ppm: 59.85, 55.27, 41.76, 39.88, 38.89, 30.09.

Synthesis of H_2L. 2,6-pyridinedicarbonyldichloride (2.40 g, 0.012 mol) was dissolved in toluene (400 mL) and **c** (1.57 g, 0.012 mol) dissolved in toluene (400 mL) was added dropwise over a period of 7 h. The resulting mixture was stirred at room temperature overnight and afterwards the solvent was removed. NaOH 2 M (40 mL) was added to the resulting residue and this aqueous mixture was extracted with dichloromethane (4 x 40 mL). The combined organic extracts were dried over $MgSO_4$, filtered and the solvent was removed under vacuum. The obtained white solid was purified by column chromatography over silica using CH_2Cl_2:CH_3OH 90:10 as the mobile phase. Product H_2**L** was obtained as a white solid (21%). ^{1}H-NMR ($CDCl_3$, 400 MHz, 243K) δ, ppm: 10.33 (m, 1H, N**H**), 9.81 (m, 1H, N**H**), 8.25-8.12 (m, 1H, Py**H**$_\beta$), 8.12-8.01 (m, 2H, Py**H**$_\alpha$+Py**H**$_{\beta'}$), 3.88 (m, 1H, C**H**$_2$$NH_2$), 3.65 (m, 1H, C**H**$_2$NH), 3.50 (m, 1H, C**H**$_2$NH), 3.29 (td, 1H, C**H**$_2$NH), 2.96 (td, 1H, C**H**$_2$NMe), 2.86 (m, 1H, C**H**$_2$NMe), 2.78 (m, 1H, C**H**$_2$NMe), 2.49 (dd, 1H, C**H**$_2$NMe), 2.24 (s, 3H, C**H**$_3$), 2.11 (m, 1H, CH_2C**H**$_2$$CH_2$), 1.84 (m, 1H, CH_2C**H**$_2$$CH_2$). ^{13}C-NMR ($CDCl_3$, 100 MHz, 243K) δ(ppm): 165.79 (**C**=O), 163.40 (**C**=O), 148.15 (Py**C**$_\alpha$), 146.90 (Py**C**$_\alpha$), 140.65 (Py**C**$_\gamma$), 122.95 (Py**C**$_\beta$), 122.80 (Py**C**$_\beta$), 58.65 (**C**H_2NMe), 58.50 (**C**H_2NMe), 40.73 (**C**H_3), 37.77 (**C**H_2NHCO), 37.06 (**C**H_2NHCO), 23.46 (CH_2**C**$H_2$$CH_2$). ESI-MS (*m/z*): 263.15 $[M+H]^+$ (100), 285.13 $[M+Na]^+$ (10), 547.27 $[2M+Na]^+$(10). Anal. Calcd. for $C_{13}H_{18}N_4O_2$: C, 59.53; H, 6.92; N, 21.36. Found: C, 59.61; H, 7.00; N, 21.18.

1.2. Full characterization of [Ni^{II}(L)] (1)

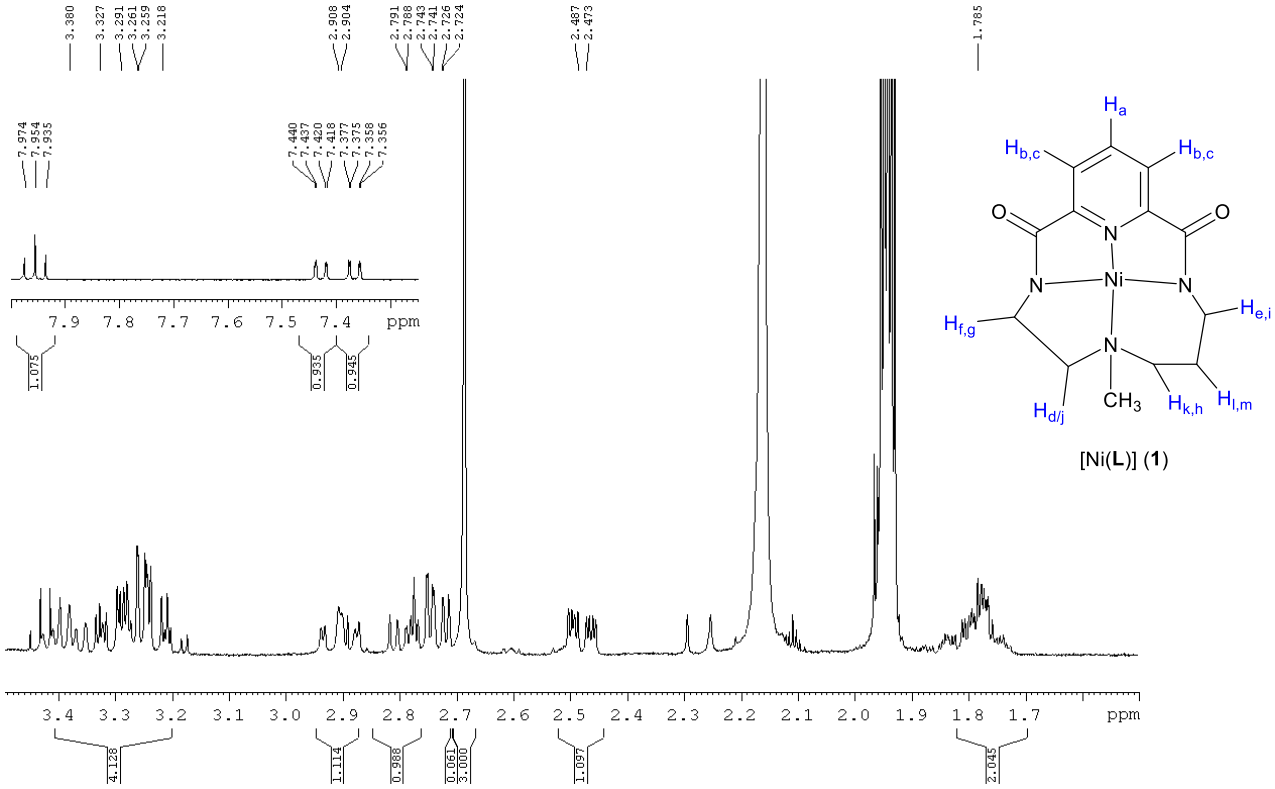

Figure S1. ^{1}H-NMR spectrum of [Ni^{II}(L)] (**1**) in CD_3CN at 298K (400 MHz).

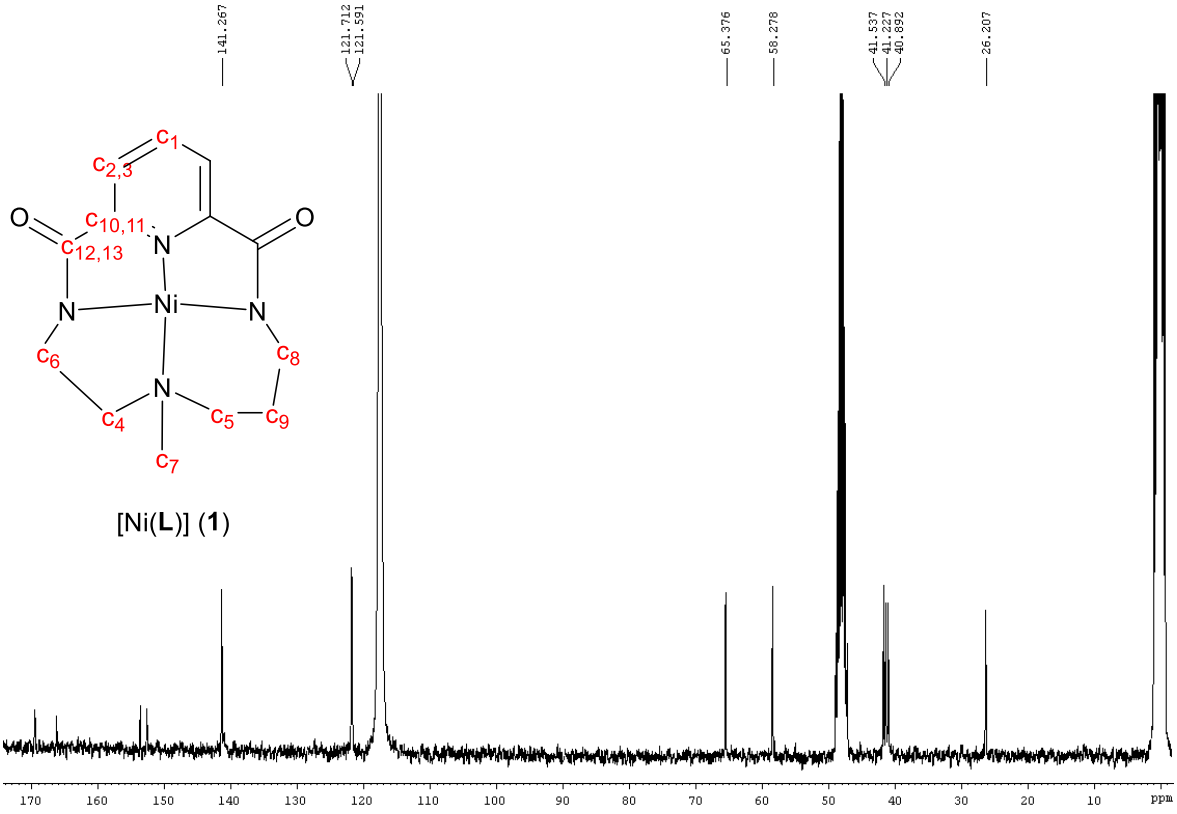

Figure S2. ^{13}C-NMR spectrum of [Ni^{II}(L)] (**1**) in CD_3CN at 298K (100 MHz).

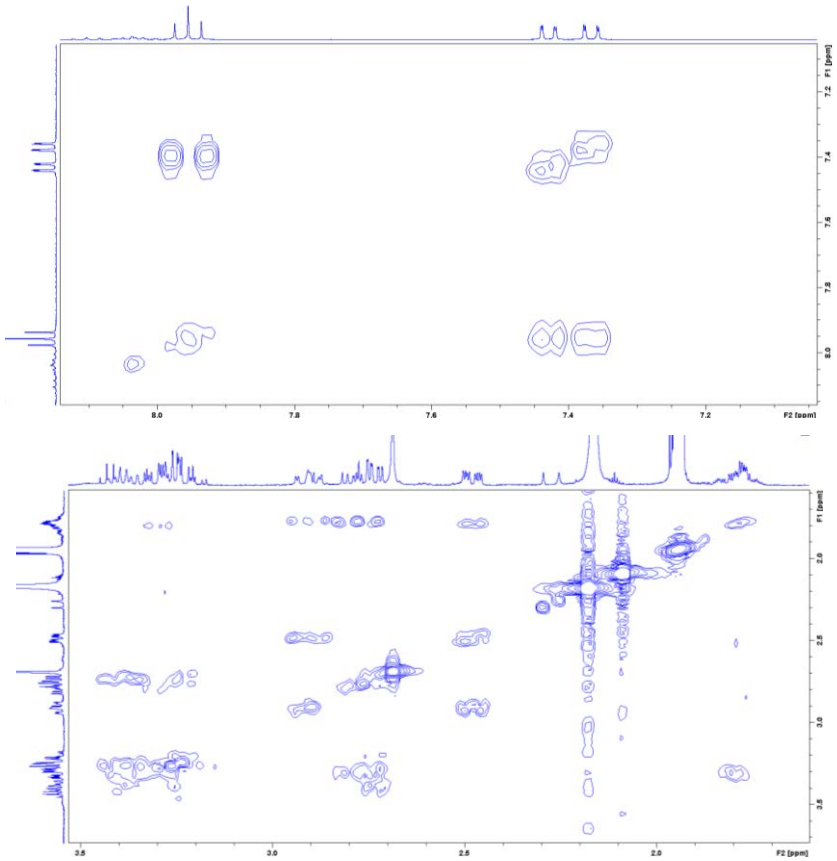

Figure S3. COSY (^{1}H-^{1}H) spectrum of [Ni^{II}(L)] (**1**) in CD_3CN at 298K (400 MHz).

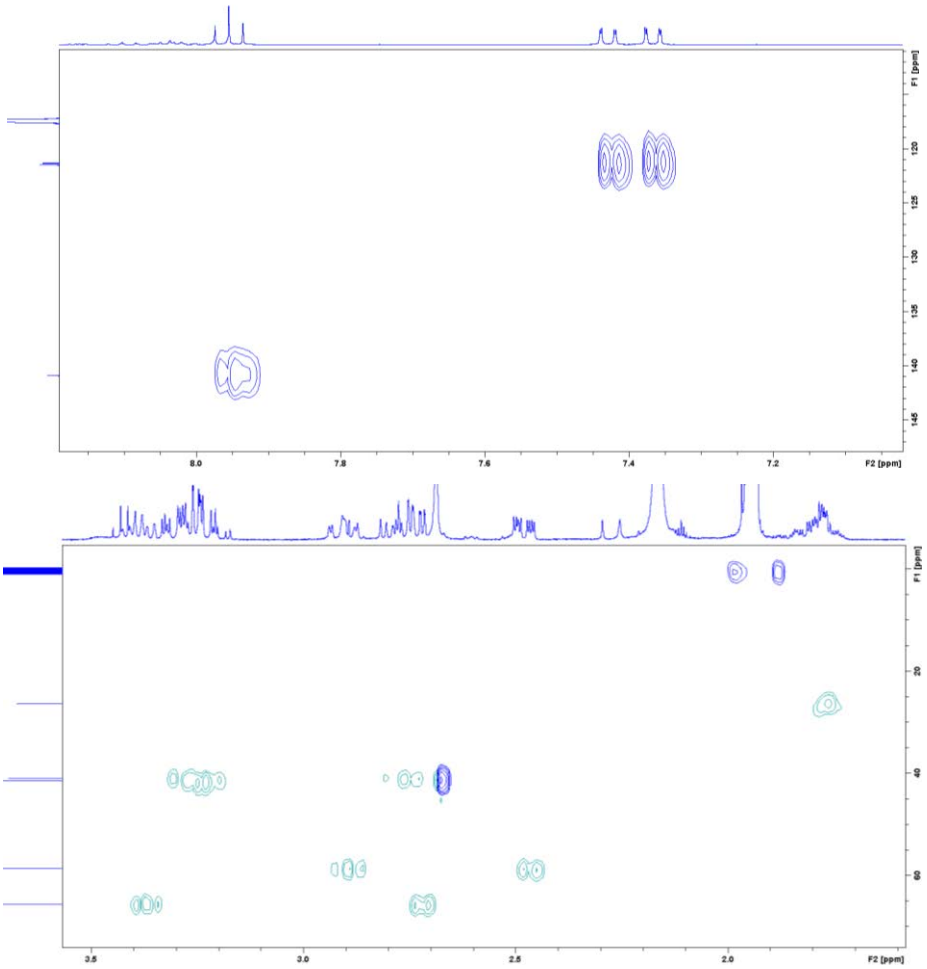

Figure S4. HSQC (^{1}H-^{13}C) spectrum of [Ni^{II}(L)] (**1**) in CD_3CN at 298K (400 MHz).

Red crystals of $C_{14}H_{16}F_3N_4NaNiO_5S$ were grown from slow diffusion of ethyl ether in a MeOH solution of the compound, and used for low temperature (100(2) K) X-ray structure determination. The measurement was carried out on a BRUKER SMART APEX CCD diffractometer using graphite-monochromated Mo *K*α radiation (λ = 0.71073 Å) from an X-ray tube. The measurements were made in the range 1.598 to 28.213° for θ. Half-sphere data collection was carried out with ω and φ scans. A total of 9796 reflections were collected of which 2264 [R(int) = 0.1250] were unique. Programs used: data collection, Smart;[2] data reduction, Saint+;[3] absorption correction, SADABS.[4,5] Structure solution and refinement was done using SHELXTL.[6,7] The structure was solved by direct methods and refined by full-matrix least-squares methods on F^2. The non-hydrogen atoms were refined anisotropically. The H-atoms were placed in geometrically optimized positions and forced to ride on the atom to which they are attached.

Table S1. Crystal Data for [Ni^{II}(L)] (**1**)

Empirical formula	C_{14} H_{16} F_3 N_4 Na Ni O_5 S
Formula weight	491.07
Temperature	100(2) K
Wavelength	0.71073 Å
Crystal system, space group	Orthorhombic, P m n a
Unit cell dimensions	a = 7.120(4) Å α = 90º b = 10.058(5) Å β = 90º c = 25.493(13) A γ = 90º
Volume	1825.6(17) A^3
Z, Calculated density	4, 1.787 Mg/m^3
Absorption coefficient	1.267 mm^{-1}
F(000)	1000
Crystal size	0.23 x 0.20 x 0.08 mm
Theta range for data collection	1.598 to 28.213º
Limiting indices	-8 ≤ h ≤ 9 -13 ≤ k ≤ 12 -29 ≤ l ≤ 33
Reflections collected / unique	9796 / 2264 [R(int) = 0.1250]
Completeness to theta = 28.10	99.8%
Absorption correction	Empirical
Max. and min. transmission	1.0 and 0.140929
Refinement method	Full-matrix least-squares on F^2
Data / restraints / parameters	2264 / 6 / 177
Goodness-of-fit on F^2	1.019
Final R indices [I>2sigma(I)]	R1 = 0.0811 wR2 = 0.1979
R indices (all data)	R1 = 0.1927 wR2 = 0.2588
Largest diff. peak and hole	1.75 d -0.825 $e.A^{-3}$

1.3. Reactivity of 2 with organic substrates

*1.3.1. Reaction of **2** with thioanisoles*

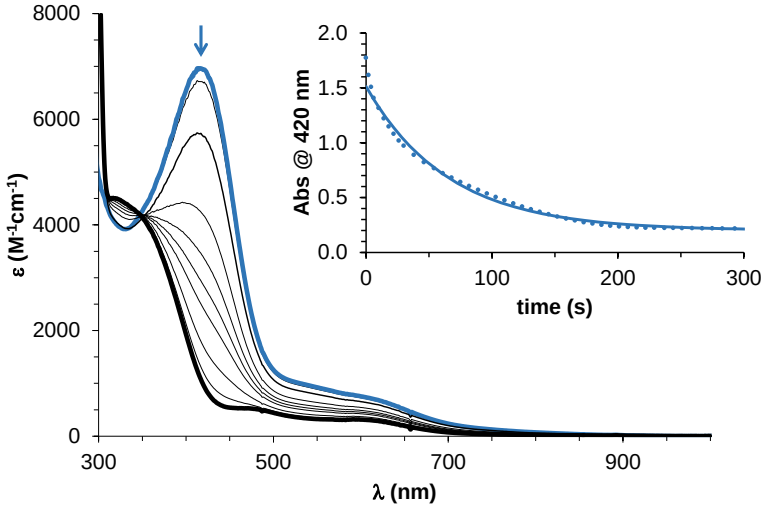

Figure S5. UV-vis spectral changes of a solution of **2** upon addition of 100 equiv. thioanisole. Experimental reaction conditions: 100 equiv. of thioanisole were added at once to a solution of **2** (0.24 mM) in CH_3CN at -30 ºC and the kinetics were monitored at 420 nm (inset).

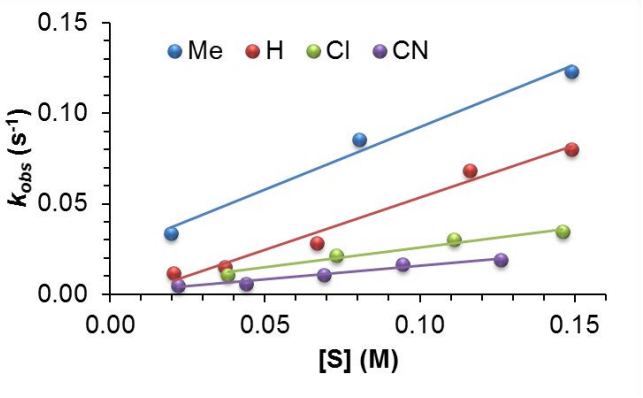

Figure S6. Plot of k_{obs} against substrate concentration for the reaction of **2** (0.24 mM) at -30 ºC with *p*-X-thioanisoles (the slope of each line corresponds to the second-order rate constant, *k*).

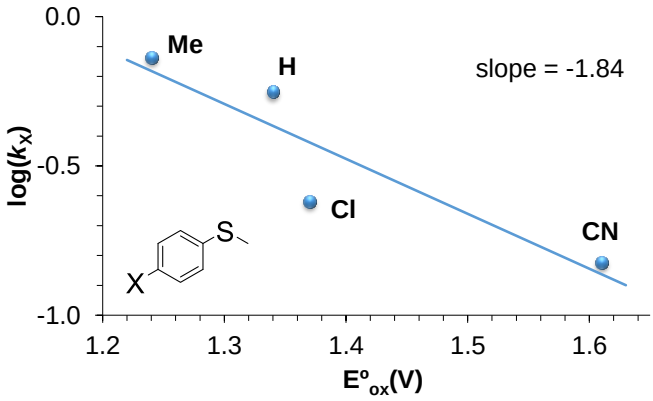

Figure S7. Plot of log(k_X) against the one-electron oxidation potentials of *p*-X-thioanisoles. A linear correlation with a slope of -1.84 is obtained.

1.3.2. Reaction of **2** with alkenes

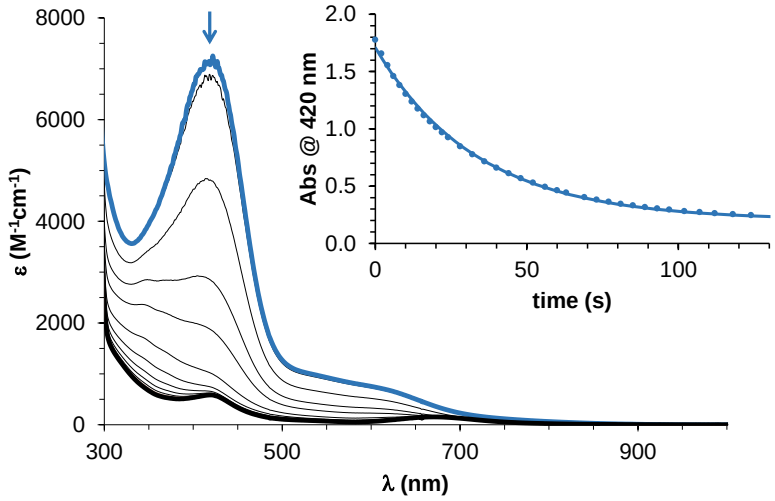

Figure S8. UV-vis spectral changes of a solution of **2** upon addition of 100 equiv. styrene. Experimental reaction conditions: 100 equiv. of styrene were added at once to a solution of **2** (0.24 mM) in CH_3CN at -30 ºC and the kinetics were monitored at 420 nm (inset).

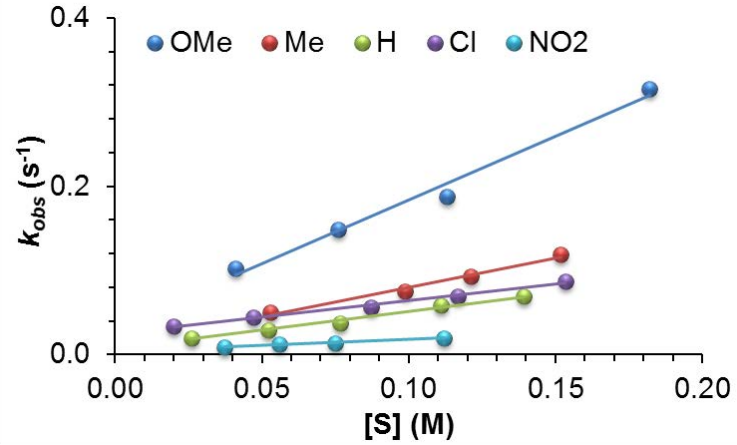

Figure S9. Plot of k_{obs} against substrate concentration for the reaction of **2** (0.24 mM) at -30 ºC with *p*-Y-styrenes (the slope of each line corresponds to the second-order rate constant, *k*).

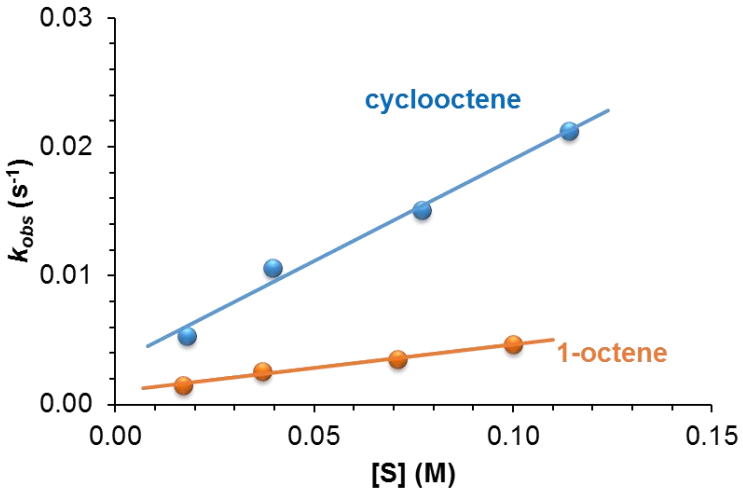

Figure S10. Plot of k_{obs} against substrate concentration for the reaction of **2** (0.24 mM) at -30 ºC with cyclooctene or 1-octene (the slope of each line corresponds to the second-order rate constant, *k*).

1.3.3. Reaction of **2** with phenols

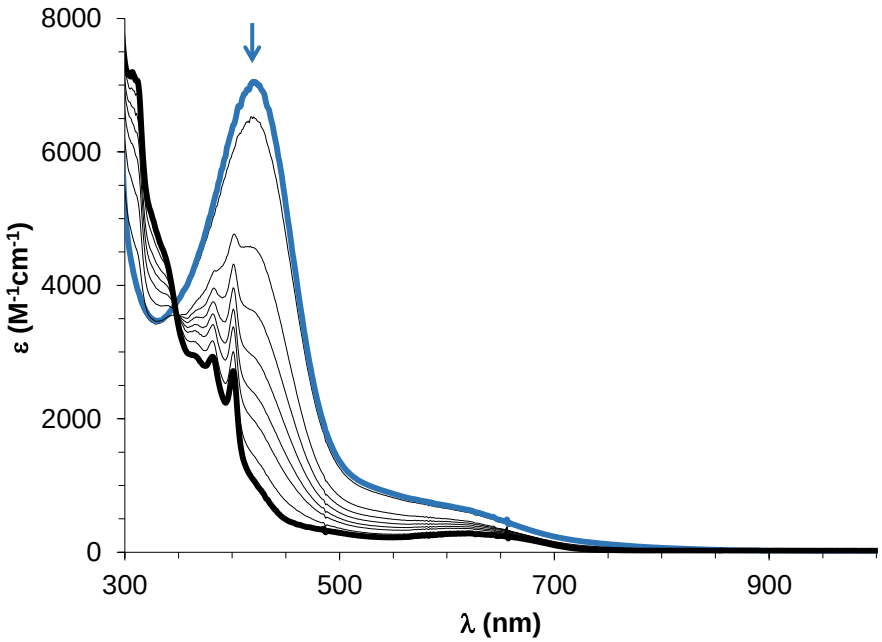

Figure S11. UV-vis monitoring of the reaction of **2** with 10 equiv. 2,4,6-tri-*tert*-butylphenol in CH_3CN at -30 ºC.

1.3.4. Reaction of **2** with weak C-H bonds

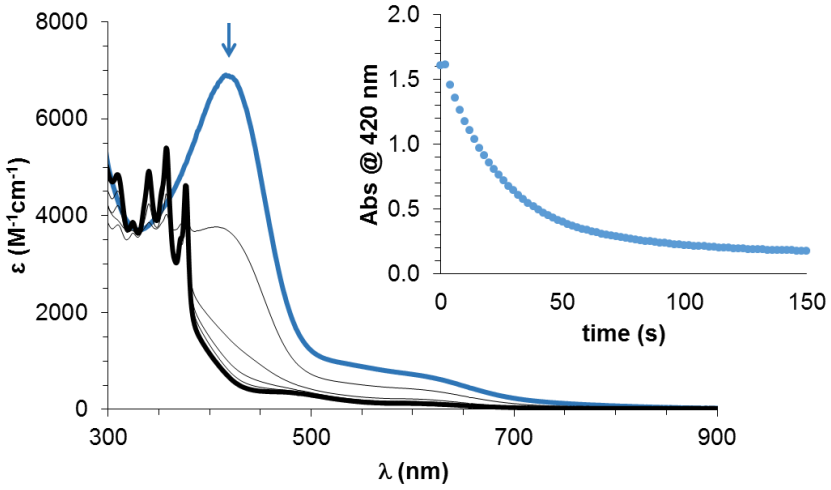

Figure S12. UV-vis spectral changes of a solution of **2** upon addition of 30 equiv. 9,10-dihydroanthracene. Experimental reaction conditions: 30 equiv. 9,10-dihydroanthracene were added at once to a solution of **2** (0.24 mM) in CH_3CN at -30 ºC and the kinetics were monitored at 420 nm (inset).

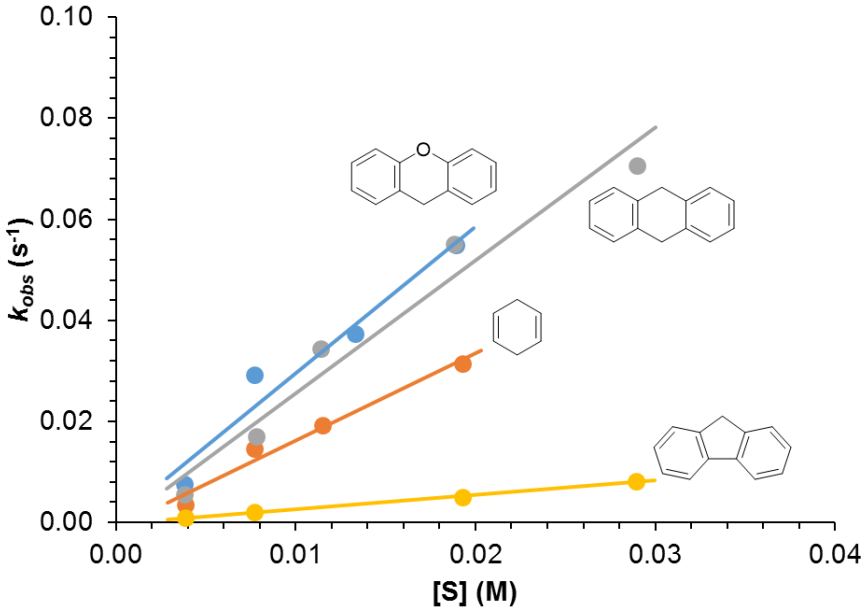

Figure S13. Plot of k_{obs} against substrate concentration for the reaction of **2** (0.24 mM) at -30 ºC with alkanes with activated C-H bonds (the slope of each line corresponds to the second-order rate constant, *k*).

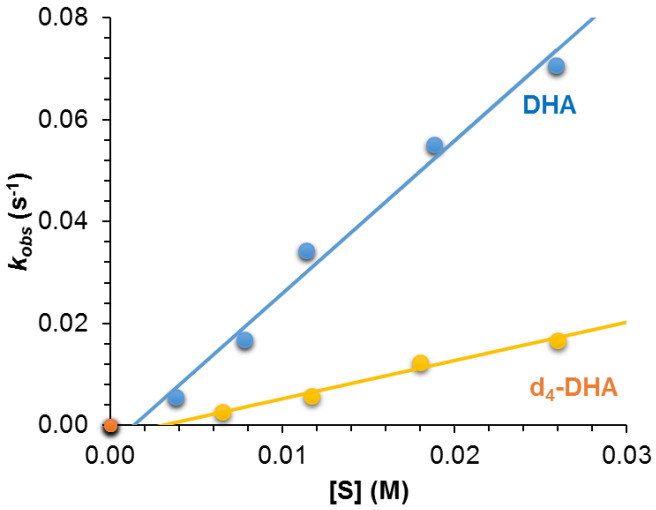

Figure S14. Plot of k_{obs} against substrate concentration for the reaction of **2** (0.24 mM) at -30 ºC with 9,10-dihydroanthracene (DHA) and deuterated 9,10-dihydroanthracene (d_4-DHA) (the slope of each line corresponds to the second-order rate constant, *k*). Kinetic isotope effect (KIE) is calculated by dividing the second-order rate constant for the oxidation of DHA by the second-order rate constant for the oxidation of d_4-DHA.

1.3.5. Reaction of **2** with strong C-H bonds

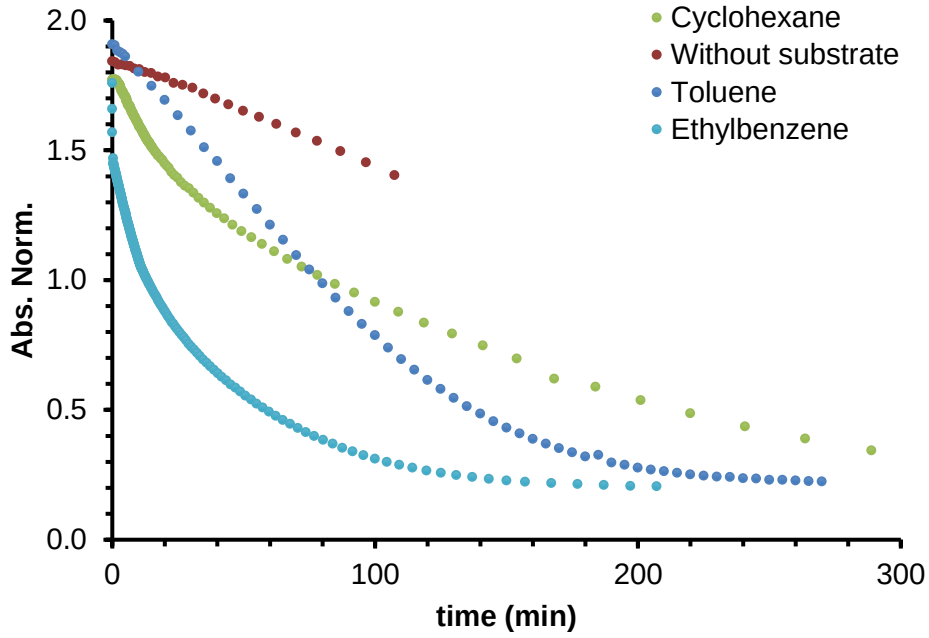

Figure S15. Kinetic trace at 420 nm of the decay of **2** upon reaction with 300 equiv. of cyclohexane, toluene or ethylbenzene in acetonitrile at -30 ºC.

Table S2. Yield (%) of the oxidation product of different substrates with **2** in acetonitrile at -30 ºC when the decay of 420 nm band was finished.

Substrate	Product	Yield (%) *sample (blank)*
cyclohexene	OH / O=	OH 8 (0) / O= 47 (0)
toluene	OH / O=	OH 1 (0) / O= 21 (0)
ethylbenzene	OH / O=	OH 2 (0) / O= 25 (0)
1-cyclooctene	Epoxide/aldehyde	137 (1) / 0 (0)
1-octene	Epoxide/aldehyde	46 (0) / 0 (0)
4-methylstyrene	Epoxide/aldehyde	140 (13) / 0 (0)
cis-2-octene	Epoxide/aldehyde	195 (106) / 34 (12)

Table S3. Second order rate constant (*k*) corresponding to the reaction of **2** with different substrates in CH_3CN at -30 ºC.

Substrate	***k*, $M^{-1}s^{-1}$**
xanthene	2.93
9,10-dihydroanthracene	2.62
1,4-cyclohexadiene	1.69
fluorene	0.28
1-cyclooctene	0.18
1-octene	0.044
4-methoxystyrene	1.51
4-methylstyrene	0.69
styrene	0.45
4-chlorostyrene	0.39
4-nitrostyrene	0.14
4-methylthioanisole	0.73
thianisole	0.56
4-chlorothioanisole	0.24
4-(methylthio)benzonitrile	0.15

1.4. Characterization of 2

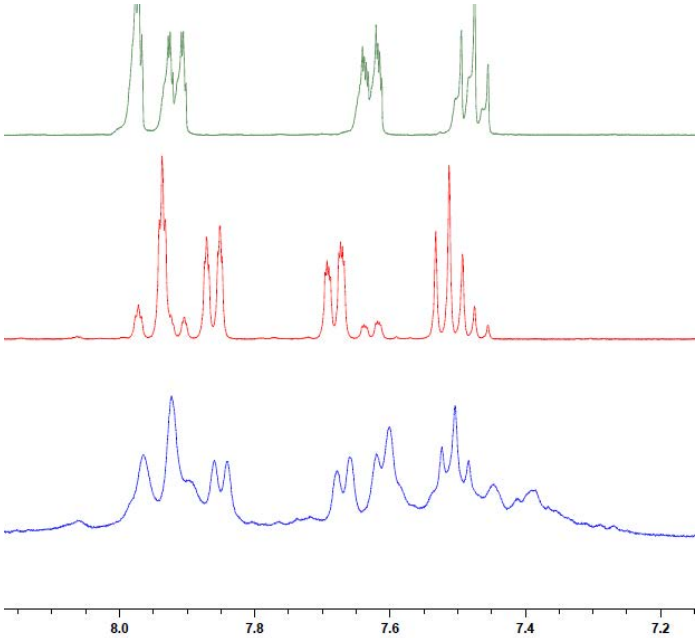

Figure S16. ^{1}H-NMR spectrum of the compound **2** (bottom) in comparison with H*m*CPBA (middle) and H*m*CBA (top) in CD_3CN at 243K (400 MHz).

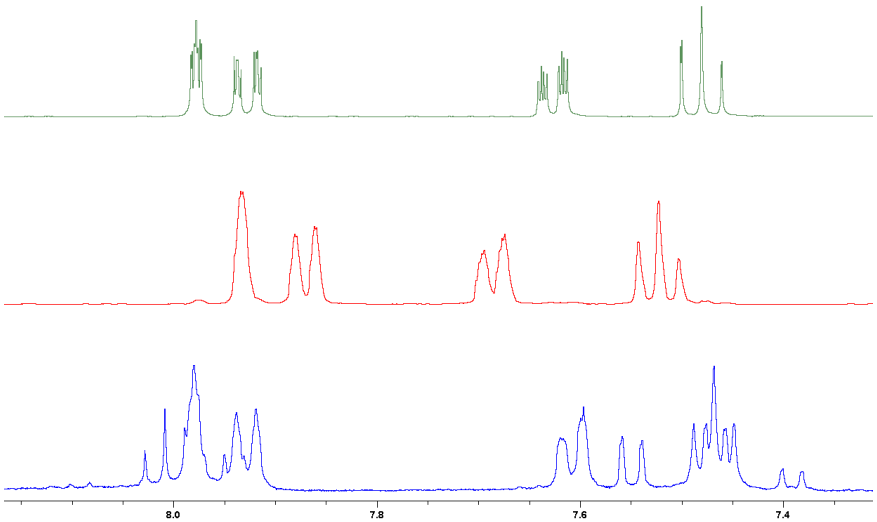

Figure S17. ^{1}H-NMR spectrum of the final reaction mixture after decomposition of **2** (bottom) in comparison with H*m*CPBA (middle) and H*m*CBA (top) in CD_3CN at 298K (400 MHz).

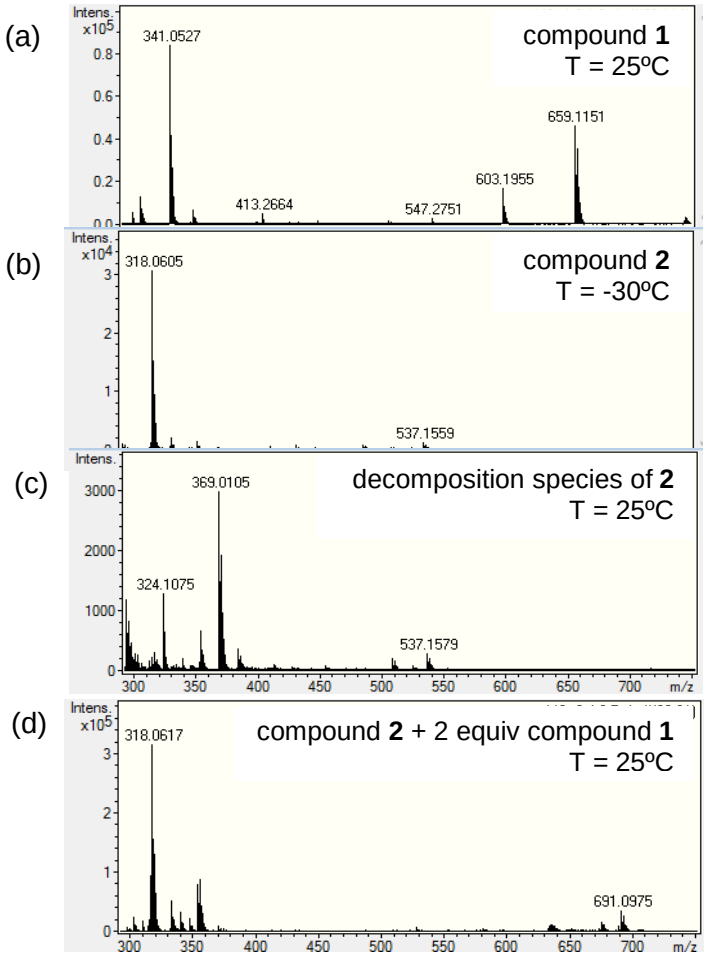

Figure S18. ESI-MS spectrum in CH_3CN of: (a) compound **1**; (b) compound **2** obtained by reaction of **1** with 3 equiv. H*m*CPBA at -30 ºC; (c) the final reaction mixture after decomposition of **2** at room temperature; (d) the reaction mixture obtained after reaction of compound **2** with 2 equiv. of **1** at room temperature.

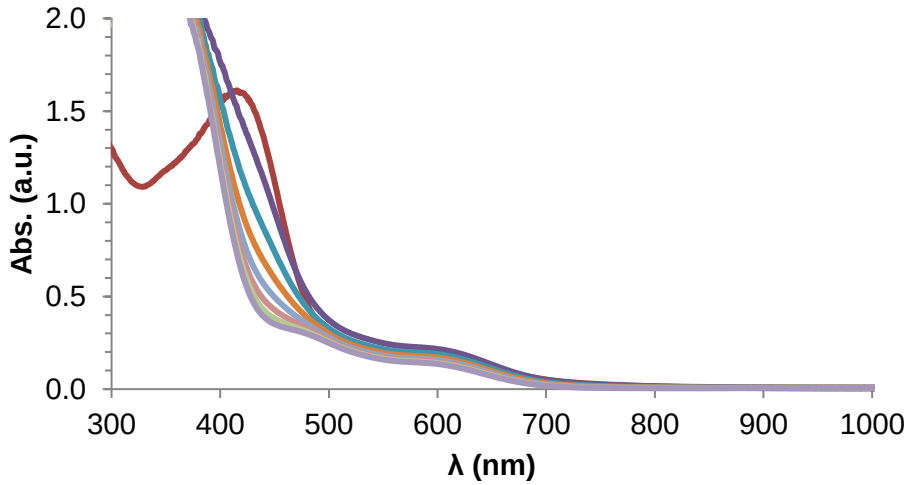

Figure S19. UV-vis spectral changes of a solution of **2** upon addition of 2 equiv. of [Ni^{II}(L)] (**1**) at room temperature.

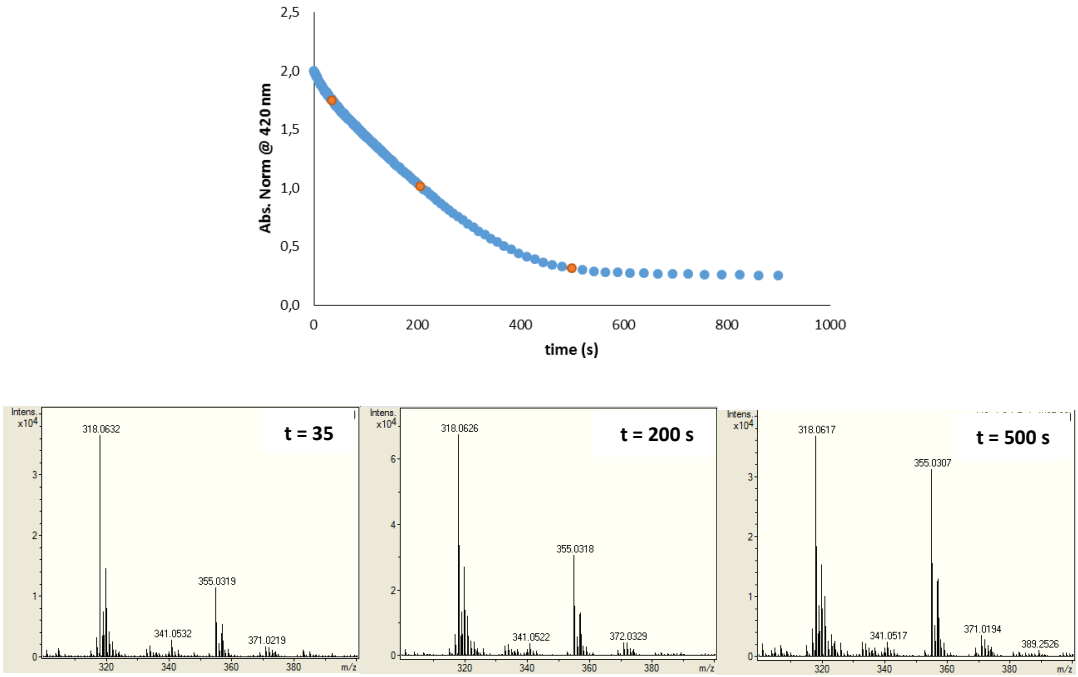

Figure S20. Top: UV-vis kinetic trace at 420 nm corresponding to the reaction of **2** with 100 equiv. 1-octene at -30 ºC in CH_3CN. Bottom: CSI-MS spectra of the reaction mixture taken at different times. $\{[Ni^{III}(L)]\}^+$: *m/z* = 318.06; $\{[Ni^{II}(L_{ox})]+Na\}^+$: *m/z* = 355.03. [$L_{ox}$ = $C_{13}H_{14}N_4O_3$].

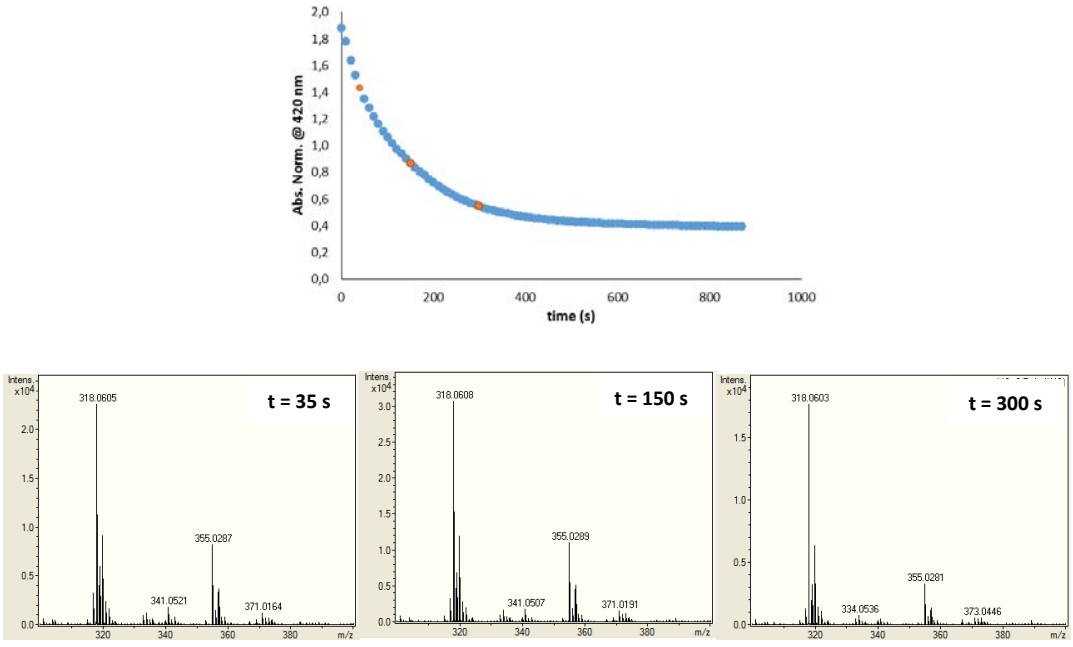

Figure S21. Top: UV-vis kinetic trace at 420 nm corresponding to the reaction of **2** with 10 equiv. 9,10-dihydroanthracene at -30 ºC in CH_3CN. Bottom: CSI-MS spectra of the reaction mixture taken at different times. $\{[Ni^{III}(L)]\}^+$: *m/z* = 318.06; $\{[Ni^{II}(L_{ox})]+Na\}^+$: *m/z* = 355.03. [$L_{ox}$ = $C_{13}H_{14}N_4O_3$].

1.4.1. EPR analysis

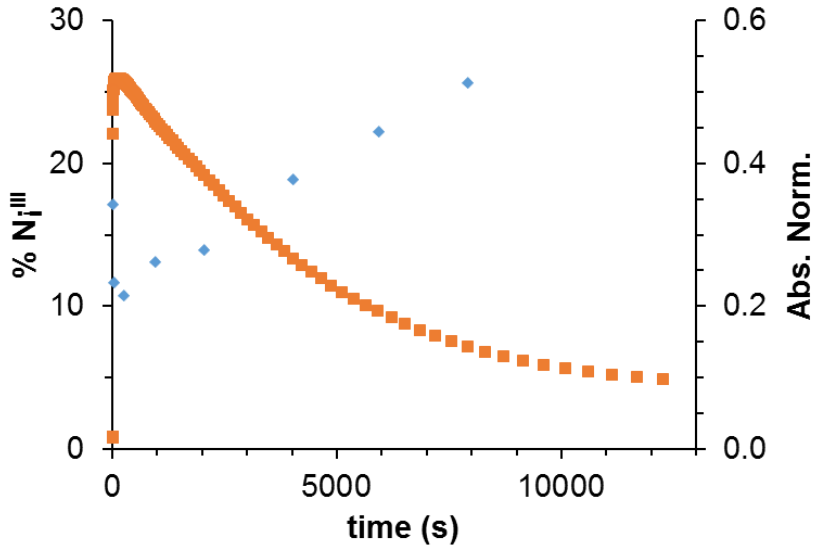

Figure S22. Orange dots: time-course of the self-decay of **2** generated by adding 3 equiv. H*m*CPBA to **1** (0.5 mM) in CH_3CN at -25 ºC followed by UV-vis absorption spectroscopy (λ = 580 nm). Blue dots: Total intensity of the Ni^{III} EPR signals corresponding to a major species (95%) at g_1= 2.03, g_2= 2.22, and g_3= 2.24 and a minor species (5%) with g_1= 2.02, g_2= 2.19 and g_3= 2.32 (Anisotropic broadening in MHz (H_1= 50; H_2= 180; H_3= 180)).

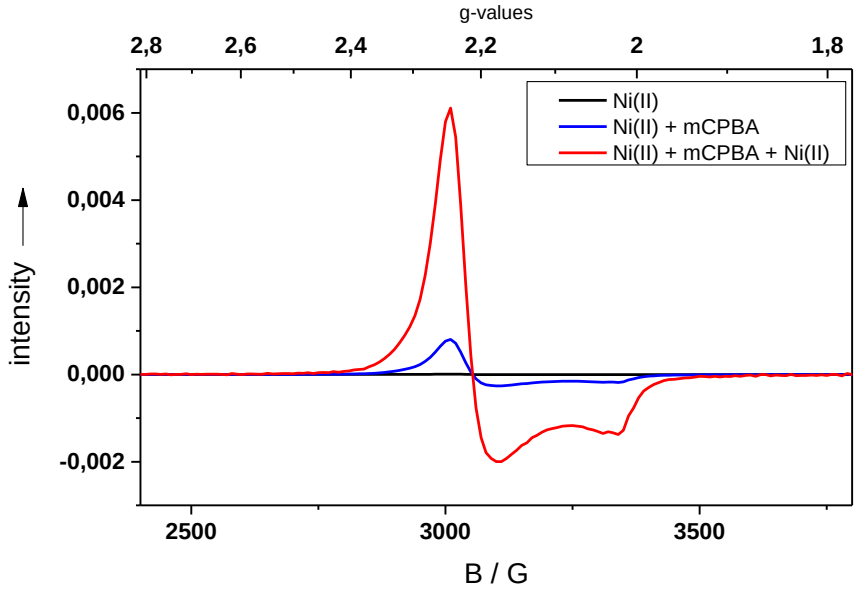

Figure S23. Black line: EPR spectrum of **1** in acetonitrile. Blue line. EPR spectrum of the reaction of **1** (0.94 mM) with 3 equiv. H*m*CPBA in CH_3CN at -30 ºC showing the formation of Ni^{III} products. The resultant solution when reacted with an additional 2.75 equiv. of **1** in acetonitrile at -30 ºC gave a higher yield of Ni^{III} in the EPR spectrum (red trace).

$$Ni(II) + HmCPBA \longrightarrow Ni(IV)=O + H^+$$

$$Ni(IV)=O + 2.75\ Ni(II) + 2H^+ \longrightarrow 2Ni(III)\text{-}OH + 1.75\ Ni(II)$$

$$\text{Total reaction: } 3.75\ Ni(II) + HmCPBA + H^+ \longrightarrow 2Ni(III)\text{-}OH + 1.75\ Ni(II)$$

Maximum possible yield of Ni(III) = (2/3.75) * 100 = 53.33%

Scheme S2. Balanced equation for the reaction of **2** with 2.75 equiv. **1**.

1.4.2. XAS analysis

Table S4. Table of single scattering EXAFS fits. Fits carried out in r-space (Δk = 2-12 $Å^{-1}$; Δr = 1-3.8 Å) with a Kaiser-Bessel window (dk 2), a *k*-weight = 3 and S_0 = 0.9. Up to three separate sets of Δr_{eff} and σ^2 for the nitrogen/oxygen atoms were explored with initial values of 0.0 Å and 0.003 $Å^2$ respectively, with a universal E_0 initially set to 8344.2 eV and ΔE_0 = 0 eV. (Fits highlighted in blue are statistically similar, relevant fits).

DESCRIPTION	FIT NUMBER	R_{FACTOR}	χ^2_v	χ^2	*No. var.*
NxNyNz	***-where x, y, z is the number of N/O atoms at 2.0, 1.8 and 1.9 A respectively***				
	-fits were carried out with fixed values of σ^2 = 0.003 and ΔE_0 = 0				
N2	2	0.462	31.445	518.533	1
N3	3	0.530	36.097	595.251	1
N4	4	0.821	55.912	922.006	1
N1N1	5	0.474	34.356	532.181	2
N2N1	6	0.569	41.280	639.438	2
N3N1	7	0.795	57.600	892.244	2
N1N2	8	0.329	23.835	369.214	2
N1N3	9	0.301	21.803	337.740	2
N1N4	10	0.491	35.602	551.480	2
N2N2	11	0.330	23.888	370.038	2
N3N2	12	0.462	33.462	518.334	2
N2N3	**13**	**0.209**	**15.172**	**235.018**	**2**
N2N4	14	0.302	21.880	338.922	2
N3N3	**15**	**0.253**	**18.352**	**284.279**	**2**
N1N1N1	16	0.324	25.108	363.817	3
N2N1N1	17	0.334	25.904	375.361	3
N3N1N1	18	0.476	36.865	534.190	3
N1N2N1	19	0.287	22.212	321.856	3
N1N3N1	20	0.216	16.700	241.980	3
N1N4N1	21	0.299	23.179	335.875	3
N1N1N2	22	0.274	21.239	307.764	3
N1N1N3	23	0.359	27.796	402.777	3
N2N2N1	24	0.205	15.914	230.591	3
N1N2N2	25	0.358	27.712	401.554	3
N2N1N2	26	0.203	15.718	227.753	3
N2N2N2	27	0.238	18.443	267.240	3
N1N3N2	28	0.238	18.469	267.616	3

Table S5. Table of multiple scattering EXAFS fits. Fits carried out in r-space (Δk = 2-12 Å^{-1}; Δr = 1-3.8 Å) with a Kaiser-Bessel window (dk 2), a *k*-weight = 3 and S_0 = 0.9. Up to three separate sets of Δr_{eff} and σ^2 for the nitrogen/oxygen and pyridine atoms were explored with initial values of 0.0 Å and 0.003 Å^2 respectively, with a universal E_0 initially set to 8344.2 eV and ΔE_0 = 0 eV. (Fits highlighted in blue are statistically similar, relevant fits).

DESCRIPTION	FIT NUMBER	R_{FACTOR}	χ^2_ν	χ^2	No. Var.
NxNy(Pyr)	***-where x, y, is the number of N/O atoms at 2.0, 1.8 respectively***				
	-Pyr indicates multiple scattering from pyridine included with a N-Ni bond length of 1.8				
	-fits were carried out with fixed values of σ^2 = 0.003 and ΔE_0 = 0				
N1N1(Pyr)	29	0.25	19.18	277.90	3
N1N2(Pyr)	30	0.20	15.17	219.82	3
N1N3(Pyr)	31	0.36	27.60	399.86	3
N2N1(Pyr)	32	0.27	20.96	303.77	3
N3N1(Pyr)	33	0.43	32.94	477.33	3
N2N2(Pyr)	34	0.13	9.80	142.05	3
N2N3(Pyr)	35	0.20	15.12	219.02	3
N3N2(Pyr)	36	0.19	14.94	216.45	3
N3N3(Pyr)	37	0.17	12.92	187.20	3
	-fits were carried out with fixed values of ΔE_0 = 0				
N2N2(Pyr)	38	0.08	9.06	95.00	7
N3N2(Pyr)	39	0.11	11.56	121.27	7
N2N3(Pyr)	40	0.10	11.04	115.76	7
	-fits were carried out with fixed values of ΔE_0 = 0 and with floating linked N/O σ^2s				
N2N2(Pyr)	**50**	**0.08**	**7.61**	**95.07**	**4**
N3N2(Pyr)	51	0.17	14.12	190.54	4
N2N3(Pyr)	52	0.17	13.77	183.76	4

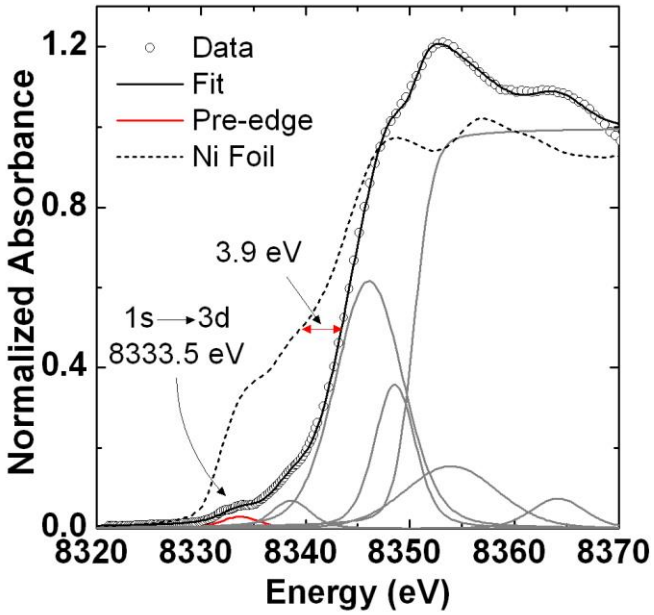

Figure S24. Ni K-edge XANES region for Ni foil and complex **2**. At ~8333.5 eV is the 1s → 3d feature. Furthermore a ~3.9 eV difference is observed in the rising edge of complex 2 *versus* Ni foil when using the half-height method, which is consistent with a Ni^{III} species.

1.5. Reaction of 1 with pernonanoic acid

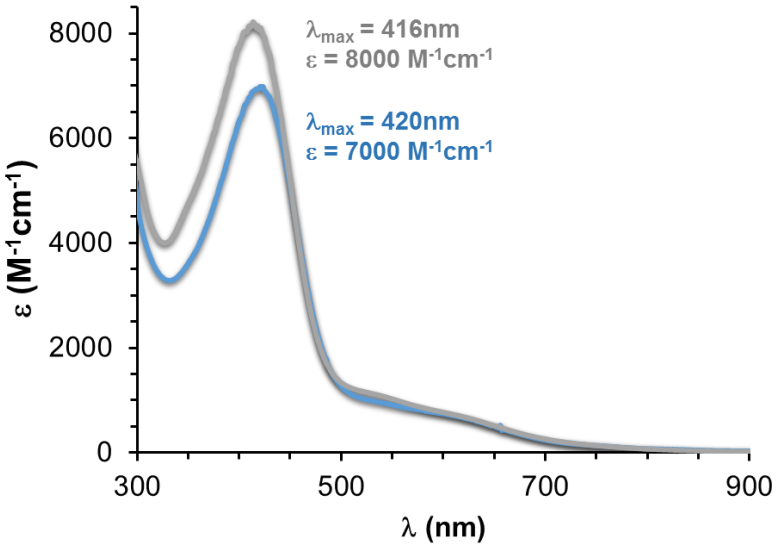

Figure S25. UV-vis spectrum of **2** (blue line) and the corresponding species obtained by mixing **1** with 3 equiv. pernonanoic acid in CH_3CN at -30 ºC (grey line).

1.6. DFT calculations

Table S6. Hirshfeld's charges of the most relevant atoms for each intermediate involved in the homolytic and heterolytic O-O bond cleavage mechanisms.

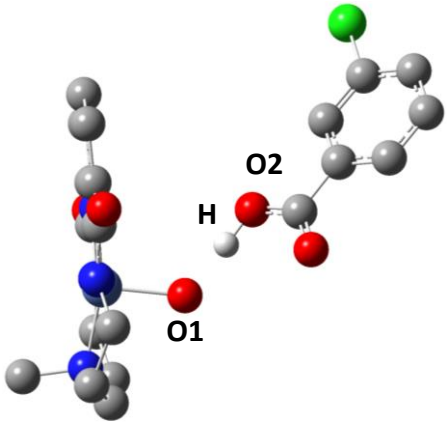

Atom/fragment	[Ni^{II}(L)]	[Ni^{II}(L)]-H*m*CPBA	TS-heterolytic	[Ni^{III}(L)(O•)]-H*m*CBA	[Ni^{III}(L)(O•)]	TS-homolytic
Ni	0.23	0.23	0.39	0.40	0.46	0.41
O1	-	-0.15	-0.29	-0.22	-0.42	-0.13
O2	-	-0.06	-0.22	-0.22	-	-0.09
H	-	0.15	0.32	0.11	-	0.14
H*m*CBA	-	0.01	-0.31	-0.35	-	-0.09

Table S7. Hirshfeld's spin density of the most relevant atoms for each intermediate involved in the homolytic and heterolytic O-O bond cleavage mechanisms.

Atom	[Ni^{II}(L)]	[Ni^{II}(L)]-H*m*CPBA	TS-heterolytic	[Ni^{III}(L)(O•)]-H*m*CBA	[Ni^{III}(L)(O•)]	TS-homolytic
Ni	0.00	0.00	0.00	0.79	0.66	1.49
O1	0.00	0.00	0.00	1.11	1.29	0.15
O2	0.00	0.00	0.00	0.00	-	0.16
H	0.00	0.00	0.00	0.01	-	0.01
H*m*CBA	0.00	0.00	0.00	0.02	-	0.17

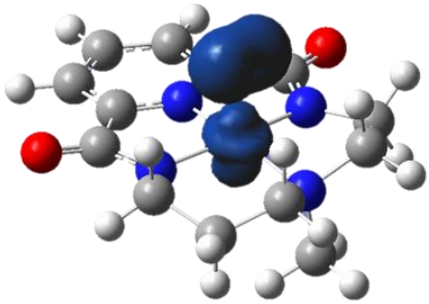

Figure S26. Isodensity surface (isovalue = 0.01) of the spin density for [Ni^{III}(L)(O•)] (**2**).

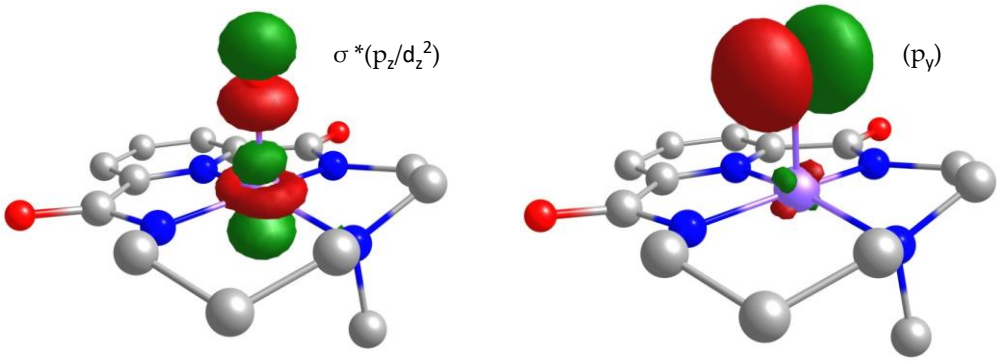

Figure S27. sitive occupation nu

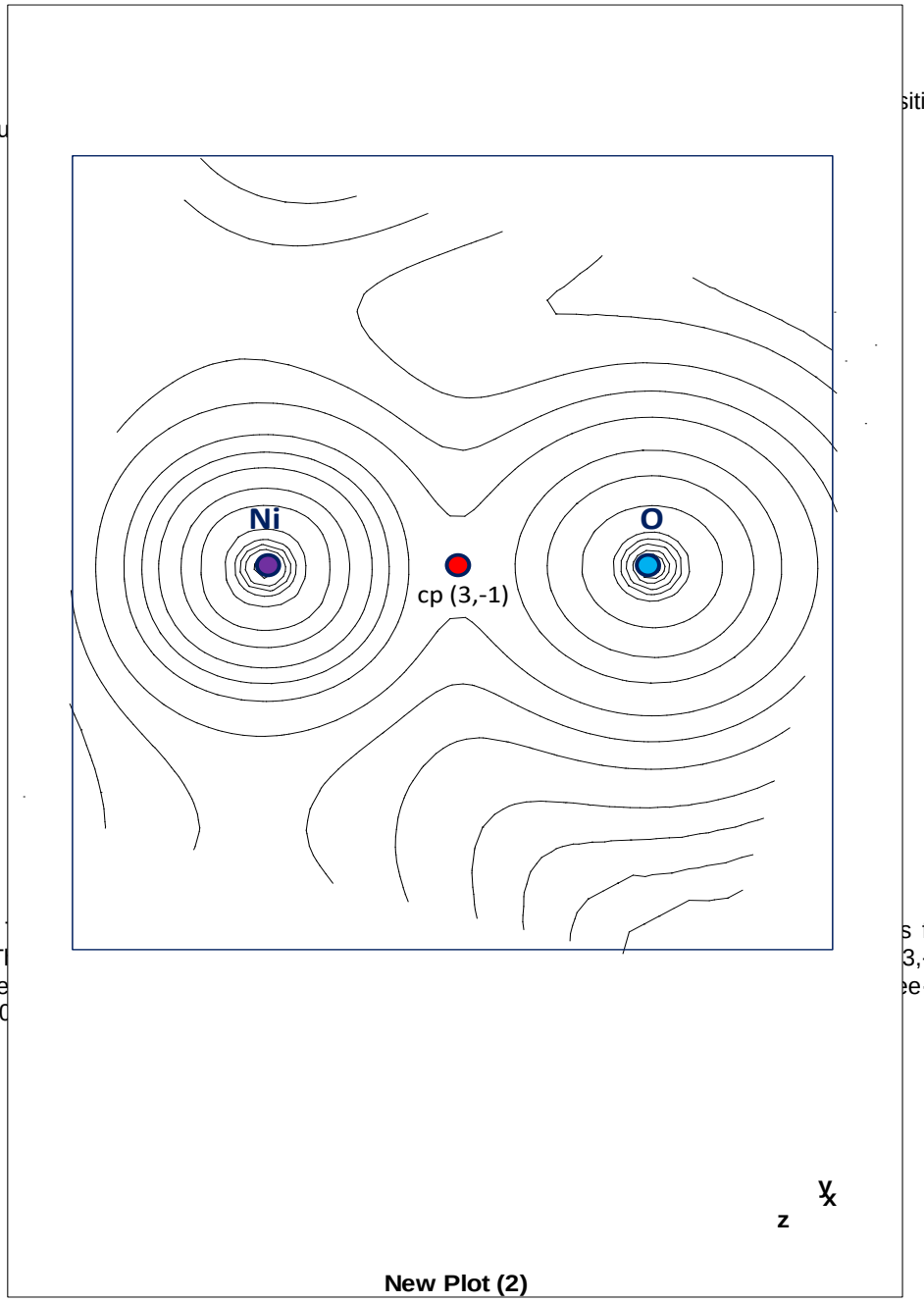

Figure S28. s for complex **2**. Tl 3,-1) properties are ee·Å^{-3} and *V(r)* = -0

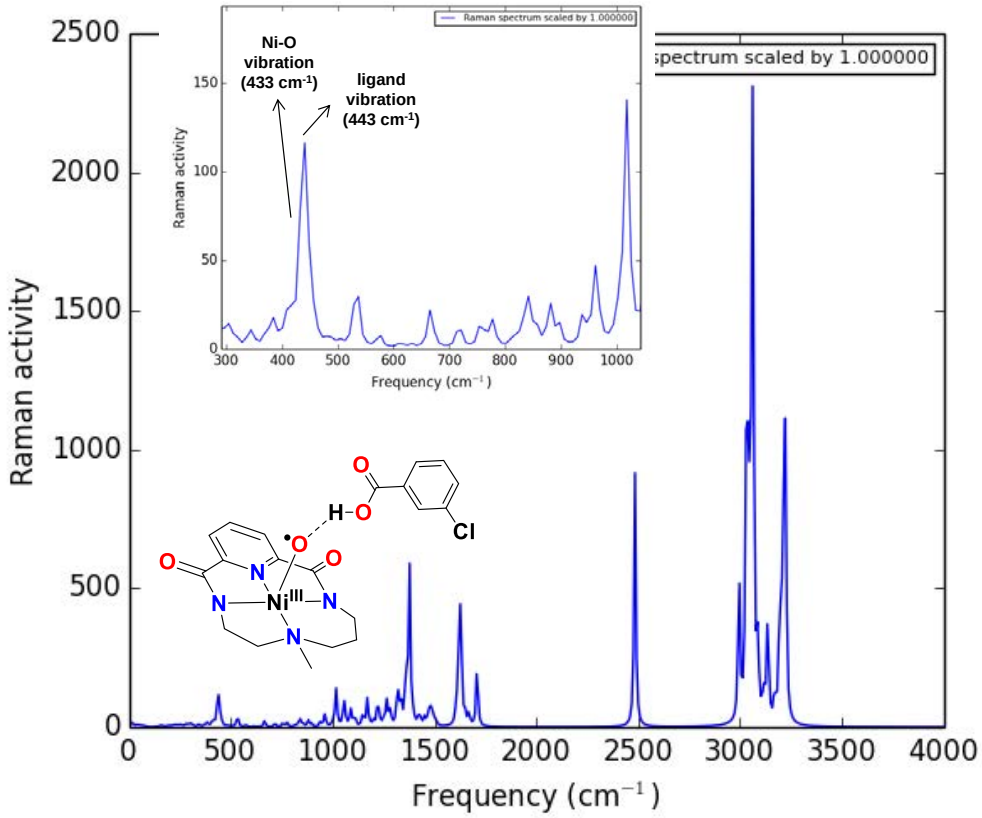

Figure S29. Calculated Raman of [Ni^{III}(L)(O•)]-H*m*CBA simulated at 77 K and with a laser excitation of 457 nm.

1.7. References

1) Arbuse, A.; Font, M.; Martínez, M. A.; Fontrodona, X.; Prieto, M. J.; Moreno, V.; Sala, X.; Llobet, A. *Inorg. Chem.* **2009**, *48*, 11098.

(2) *Bruker Advanced X-Ray Solutions SMART. Version 5.631*, 1997.

(3) *Bruker Advanced X-Ray Solutions. SAINT+*, *Version 6.36A*, 2001.

(4) Sheldrick, G. M. **1996**, Empirical Absorption Correction Program. Universität Göttingen.

(5) *Bruker Advanced X-Ray Solutions. SADABS*, *Version 2.10*, 2001.

(6) Sheldrick, G. M. **1997**, Program for Crystal Structure Refinement. Universität Göttingen.

(7) *Bruker Advanced X-Ray Solutions. SHELXL*, *Version 6.14*, 2000.

A.2. Supplementary Information Chapter IV

2.1. Spectroscopic characterization of 2

*2.1.1. Cyclic voltammetry and spectroelectrochemistry of **1***

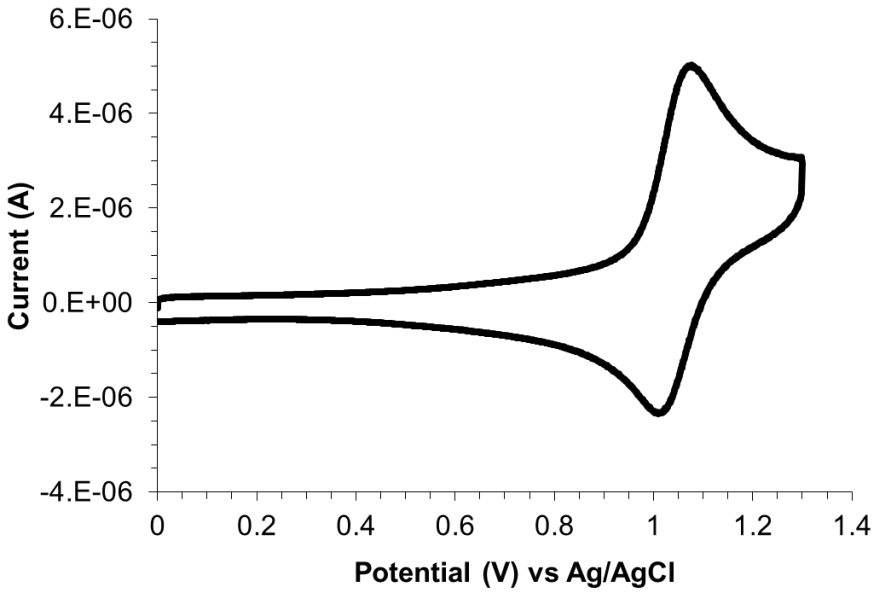

Figure S1. Cyclic voltammogram of **1** (0.2 mM) in CH_3CN with 0.1 M $TBAPF_6$ vs Ag/AgCl (Scan rate = 100 $mV \cdot s^{-1}$)

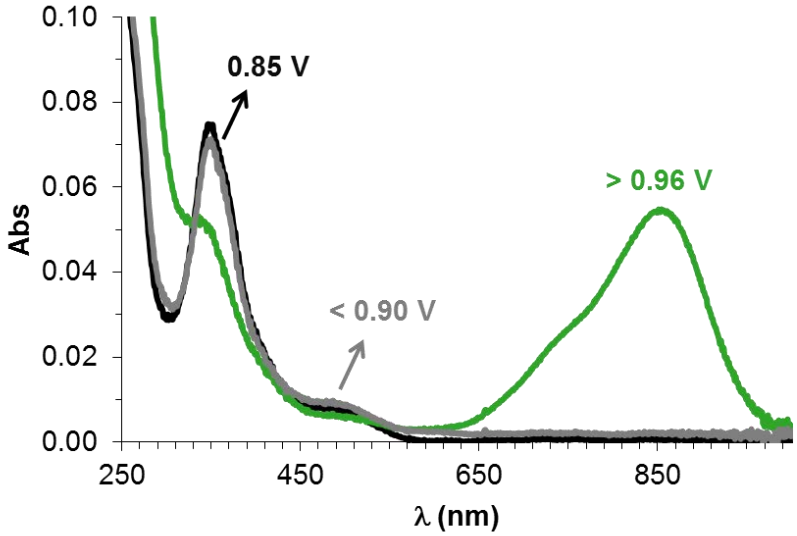

Figure S2. UV-vis spectroelectrochemistry of a solution of **1** (1 mM) in CH_3CN with 0.1 M $TBAPF_6$. Consecutive experimets were carried out at 0.75 V (black line), > 0.96 V (green line) and at < 0.90 V (grey line) vs Ag wire.

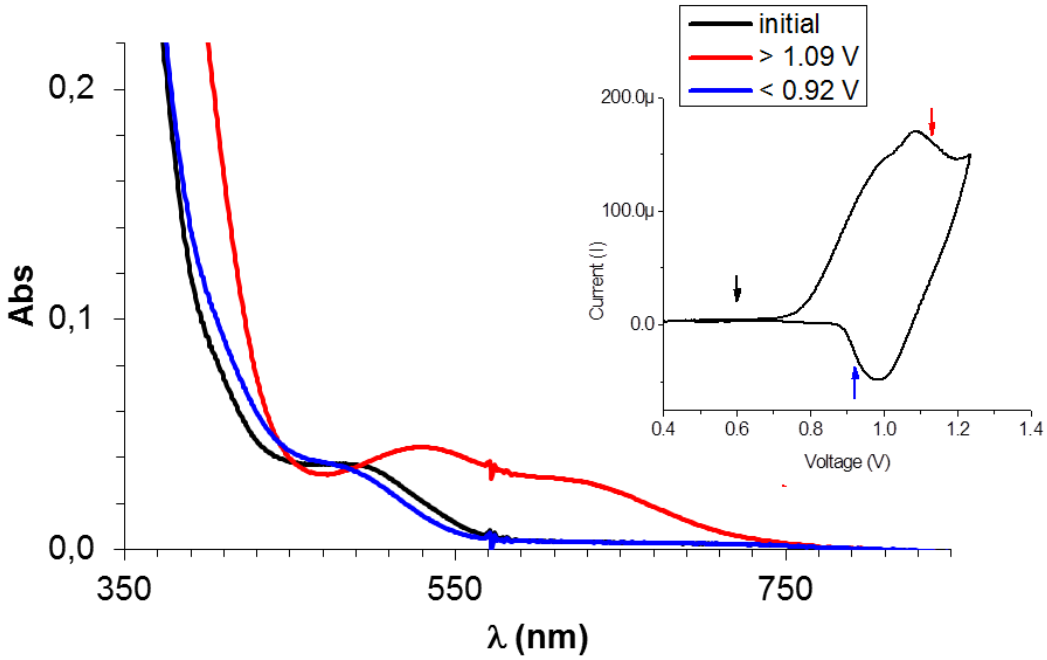

Figure S3. UV-vis spectroelectrochemistry of a solution of **1** (5 mM) in CH_3CN with 0.1 M $TBAPF_6$ in the presence of 5 equiv. acetic acid, 50 equiv. water and 5 equiv. NaCl with respect to **1**. Consecutive experimets were carried out at 0.75 V (black line), > 1.09 V (red line) and at < 0.92 V (blue line) vs Ag wire.

2.1.2. EPR spectroscopy of **2**

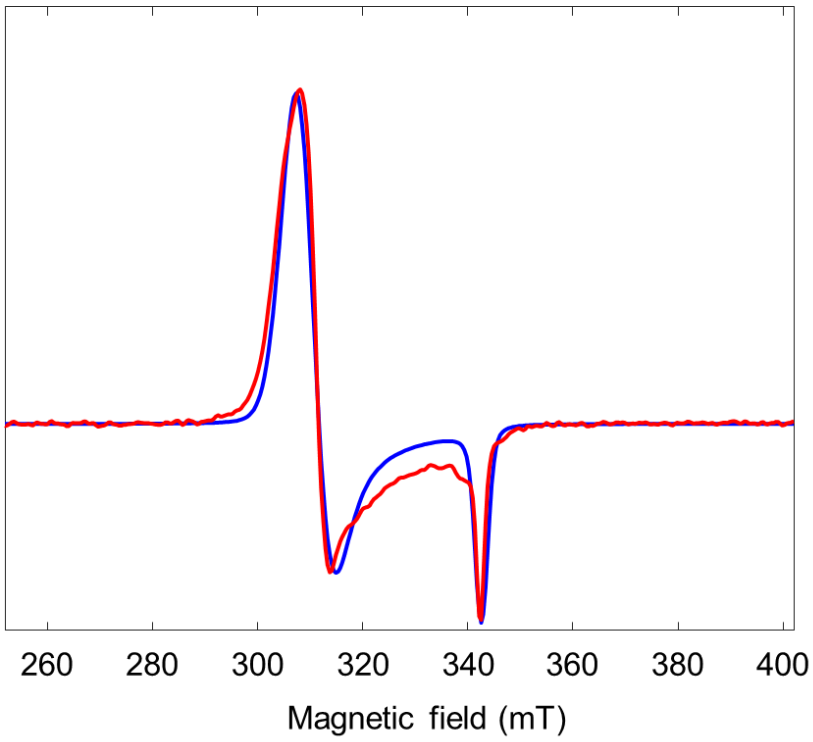

Figure S4. Red line: EPR spectrum of **2** in CH_3CN:H_2O 95:5 (v:v) generated by reaction of **1** with 3 equiv. NaOCl in the presence of 5 equiv. AcOH. Blue line: Simulated EPR spectrm with $g_{\perp}$=2.23 and $g_{//}$= 2.01 (anisotropic broadening: H_1= 220 MHz, H_2= 10 MHz).

2.1.3. CSI-MS analysis of **2**

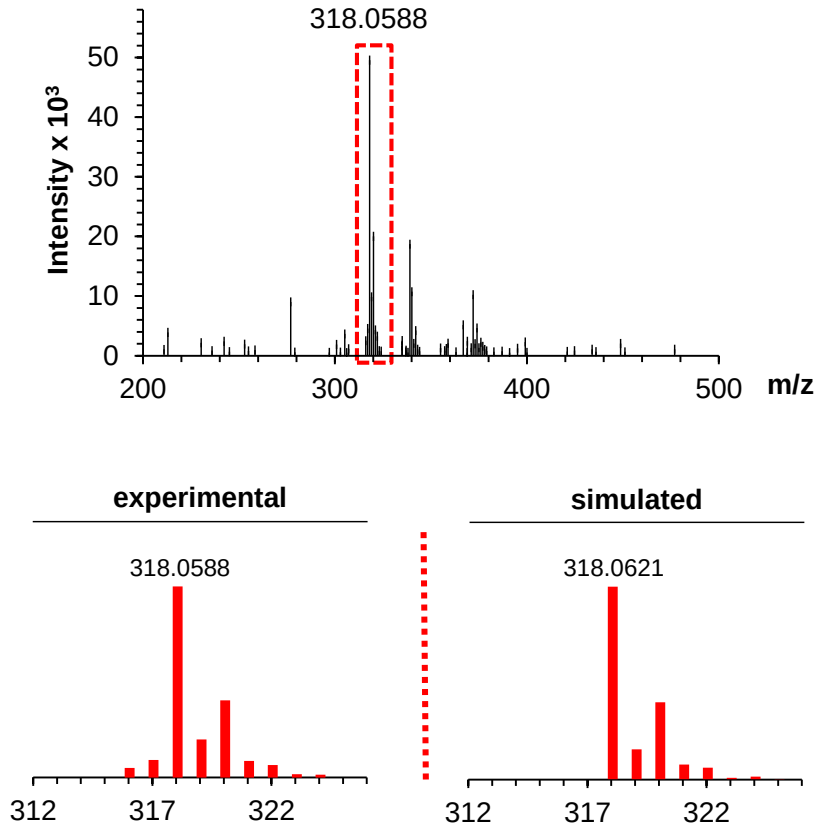

Figure S5. CSI-MS of **2** in $CH_3CN:H_2O$ 95:5 (v:v) at -30 ºC formed by reaction of **1** with 3 equiv. NaOCl in the presence of 5 equiv. AcOH in $CH_3CN:H_2O$ 95:5 at -30 ºC. The spectrum shows a major peak at *m/z* 318.0588 corresponding to $\{[Ni(L)]\}^+$.

2.2. Reaction of 3 towards organic substrates

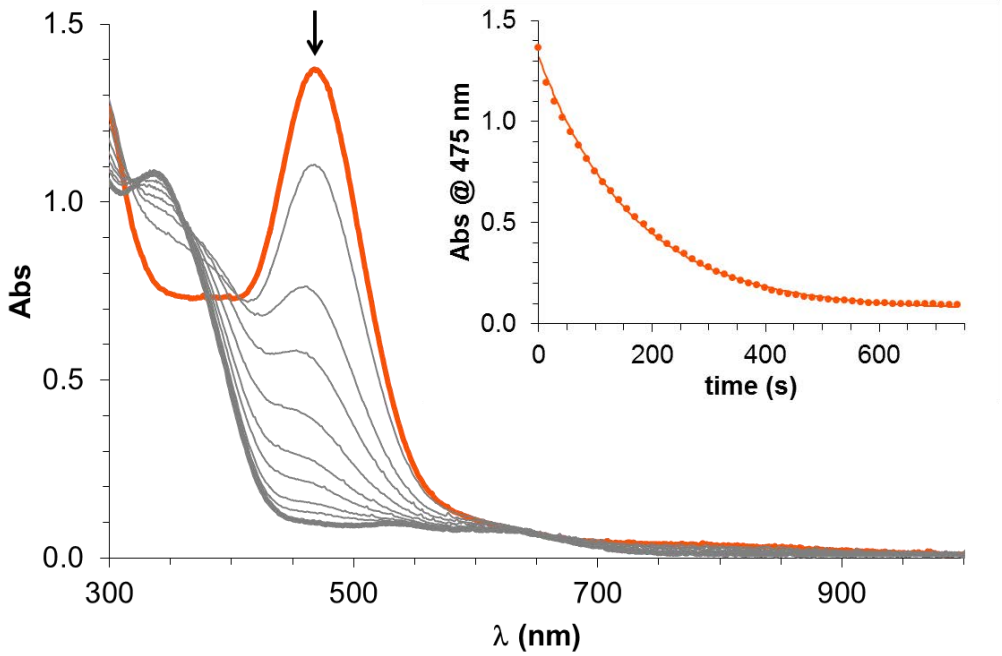

Figure S6. UV-vis spectral changes of a solution of **3** (0.2 mM **1**) upon addition of 500 equiv. 1-octene in $CH_3CN:H_2O$ 95:5 (v:v) at -30 ºC. Inset: kinetic trace at 475 nm which fits to a monoexponential decay function.

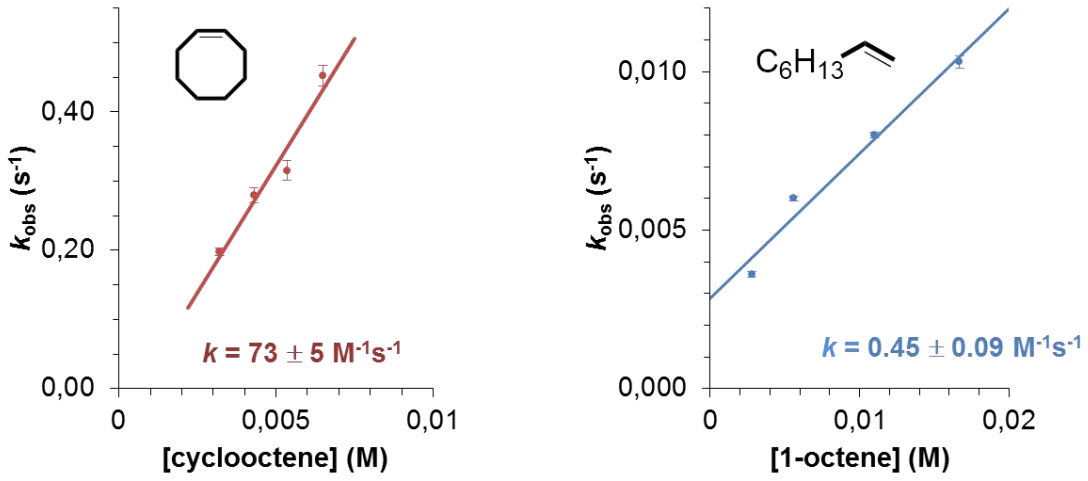

Figure S7. Plot of k_{obs} against substrate concentration for the reaction of **3** with cyclooctene (left) and 1-octene (right) in $CH_3CN:H_2O$ 95:5 (v:v) at -30 ºC. Compound **3** was generated by reaction of **1** with 5 equiv. NaOCl in the presence of 5 equiv AcOH in $CH_3CN:H_2O$ 95:5 (v:v) at -30 ºC.

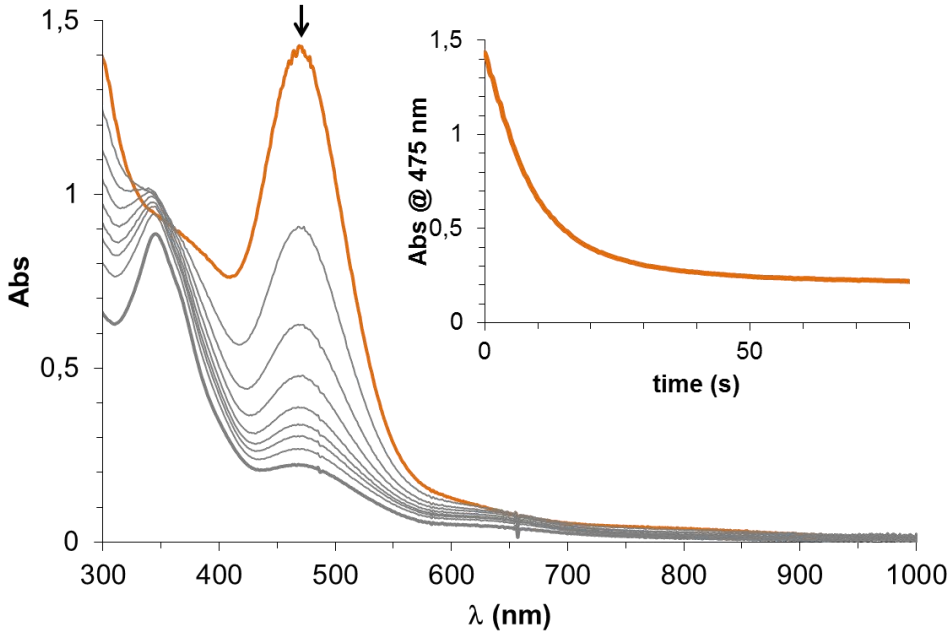

Figure S8. UV-vis spectral changes of a solution of **3** (0.2 mM **1**) upon addition of 100 equiv. cyclohexadiene in $CH_3CN:H_2O$ 95:5 (v:v) at -30 ºC. Inset: kinetic trace at 475 nm.

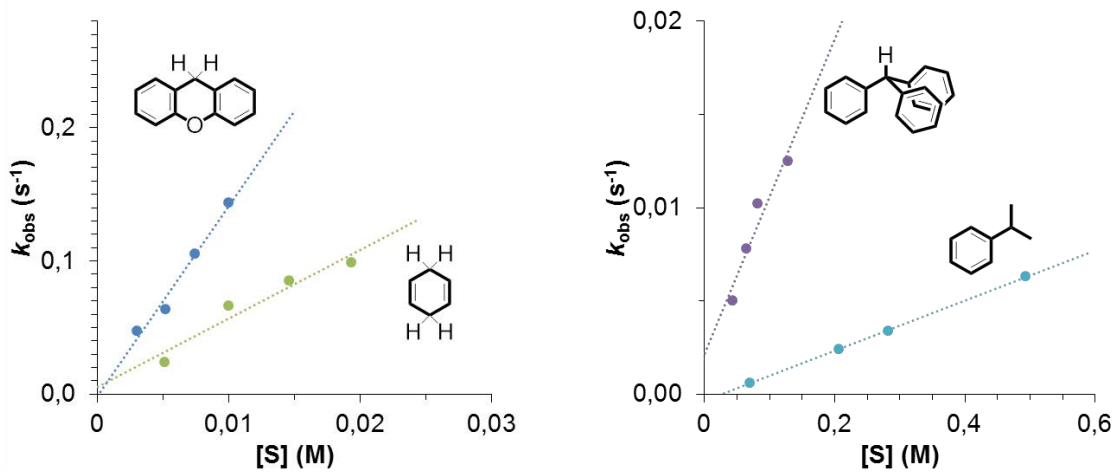

Figure S9. Plot of k_{obs} against substrate concentration for the reaction of **3** with xanthene, 1,4-cyclohexadiene, triphenylmethane and cumene in $CH_3CN:H_2O$ 95:5 (v:v) at -30 ºC. Compound **3** was generated by reaction of **1** with 5 equiv. NaOCl in the presence of 5 equiv. AcOH in $CH_3CN:H_2O$ 95:5 (v:v) at -30 ºC.

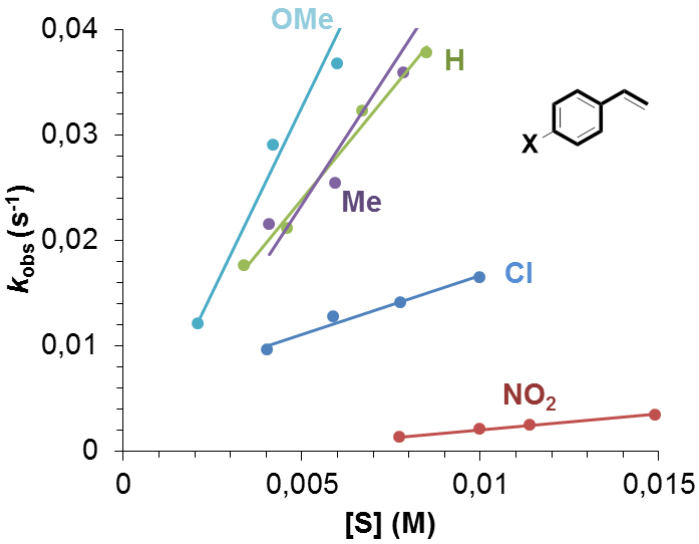

Figure S10. Plot of k_{obs} against substrate concentration for the reaction of **3** with *p*-substituted-styrenes in $CH_3CN:H_2O$ 95:5 (v:v) at -30 ºC. Compound **3** was generated by reaction of **1** with 5 equiv. NaOCl in the presence of 5 equiv. AcOH in $CH_3CN:H_2O$ 95:5 (v:v) at -30 ºC.

Table S1. Second-order rate constants (*k*) for the reaction of **3** with alkanes and alkenes in $CH_3CN:H_2O$ 95:5 (v:v) at -30 ºC. For alkanes, corrected second-order rate constants (*k*') are also shown.

substrate	*k*, $M^{-1}s^{-1}$	*k'*, $M^{-1}s^{-1}$ [a]	substrate	*k*, $M^{-1}s^{-1}$
xanthene	14±1	7	cyclooctene	73±5
9,10-dihydroanthracene	8.5±0.6	2.1	1-octene	0.45±0.9
1,4-cyclohexadiene	5.3±0.9	1.4	4-methoxystyrene	7±1
triphenylmethane	0.08±0.02	0.08	4-methylstyrene	5.2±0.8
cumene	0.0135±0.0001	0.013	styrene	4.1±0.6
ethylbenzene[b]	0.014±0.001	0.0070	4-chlorostyrene	1.1±0.1
toluene[b]	0.0037±0.0002	0.0012	4-nitrostyrene	0.30±0.02
cyclohexane[b]	0.0011±0.0001	0.00009		

[a]*k*': second-order rate constants corrected by the number of C-H bonds in the substrate. *k*' values are obtained by dividing the second-order rate constants (*k*) by the number of C-H bonds present in the substrate (1 for triphenylmethane and cumene; 2 for xanthene and ethylbenzene; 3 for toluene; 4 for 9,10-dihydroanthracene and cyclohexadiene; 12 for cyclohexane). [b]Due to extremely slow reactions, rate constants for the reaction of **3** with toluene and cyclohexane were determined from two replicates at a given substrate concentration (0.36 M).

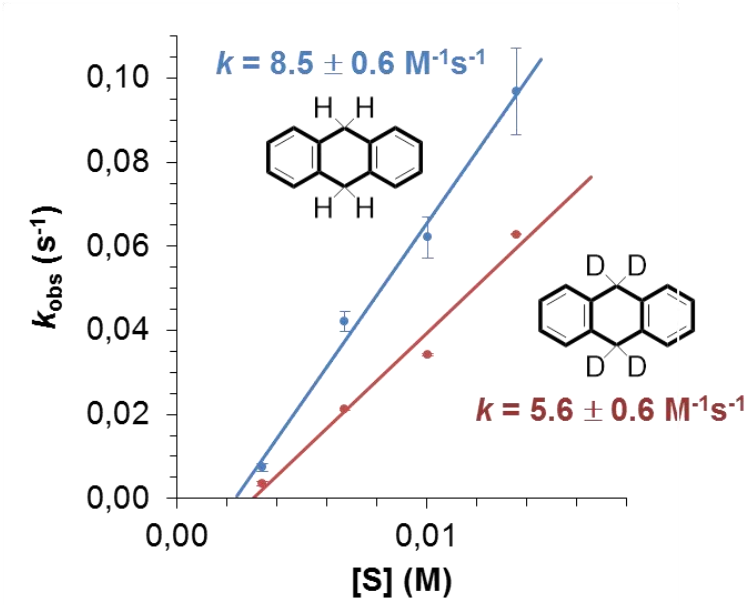

Figure S11. Plot of k_{obs} against substrate concentration for the reaction of **3** with 9,10-dihydroanthracene (blue line) and d_4-9,10-dihydroanthracene (red line) in CH_3CN:H_2O 95:5 (v:v) at -30 ºC. Compound **3** was generated by reaction of **1** with 5 equiv. NaOCl in the presence of 5 equiv. AcOH in CH_3CN:H_2O 95:5 (v:v) at -30 ºC.

Table S2. Oxidized products obtained in the reaction of **3** with different substrates in CH_3CN:H_2O 95:5 (v:v) at -30 ºC under N_2.[a]

substrate	products	$TON_{products}$ (blank)[b]
triphenylmethane	Ph_3C-OH	0.1 (0)
	Ph_3C-Cl	1.3 (0.5)
1-octene	epoxide	0.2 (0)
	allylic chlorination	0.5 (0.4)
thioanisole	sulfoxide	1.3 (0.3)

[a]To a solution of **3** (formed by reaction of **1** (0.2 mM) in MeCN:H_2O 95:5 (v:v) at -30ºC with 5 equiv AcOH and 5 equiv NaOCl under N_2) a 100 µL of a MeCN solution containing a known amount of the substrate were added in the UV-vis cuvette. The reaction was stopped by addition of $Na_2S_2O_3$ once the band at 475 nm had completely disappeared. Biphenyl (internal standard) was added and reaction mixture was then analyzed by GC-FID. See experimental section for more details. [b]$TON_{products}$ = turnover number of oxidized products with respect to nickel. In parentheses, turnover number of oxidized products formed in the blank experiments without nickel.

2.3. Spectroscopic characterization of 3

2.3.1. Resonance Raman of **3**

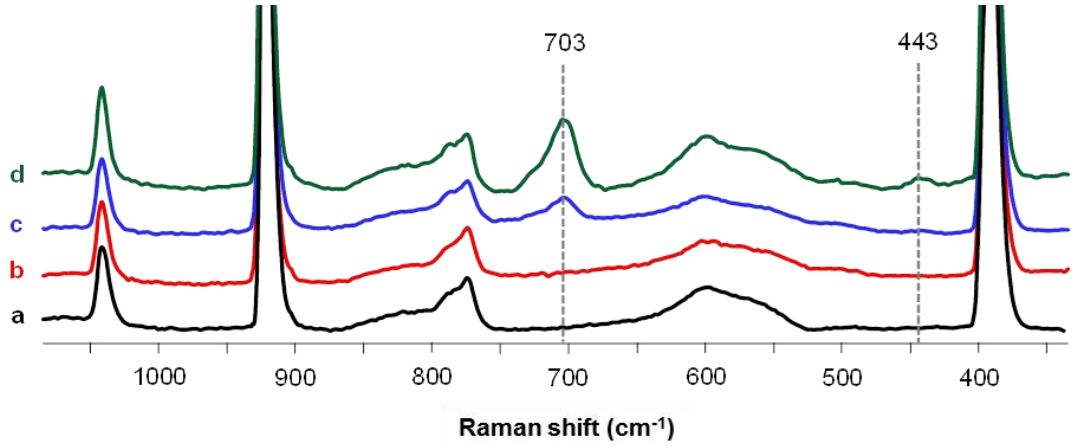

Figure S12. Resonance Raman spectra (λ_{exc} 473 nm) in frozen $CH_3CN:H_2O$ 95:5 (v:v) (77 K) of a solution of **1** (0.48 mM) in the presence of 5 equiv. AcOH (a) and upon addition of NaOCl at -30 ºC to form **2** (b), **3** (d) and an intermediate point corresponding to the transformation of **2** into **3** (c). Resonance enhanced features at 703 and 443 cm^{-1} only arise when chromophore **3** (λ_{max} = 475 nm) starts to appear after the formation **2** (λ_{max} = 550 and 650 nm).

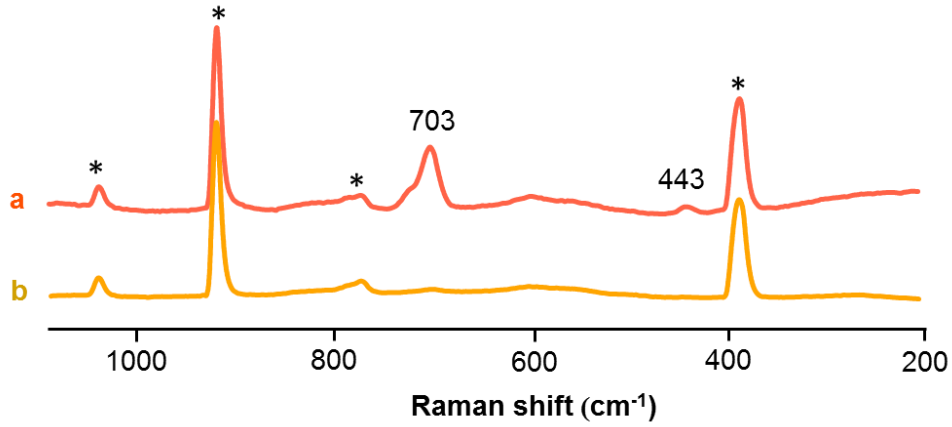

Figure S13. Resonance Raman (λ_{exc} = 473 nm) of compound **3** formed upon addition of 5 equiv. NaOCl to a solution of **1** (0.2 mM) in $CH_3CN:H_2O$ 95:5 (v:v) in the presence of 5 equiv. AcOH before (a) and after (b) addition of 50 equiv. 1-octene. *Bands of MeCN.

2.3.2. CSI-MS analyses of **3**

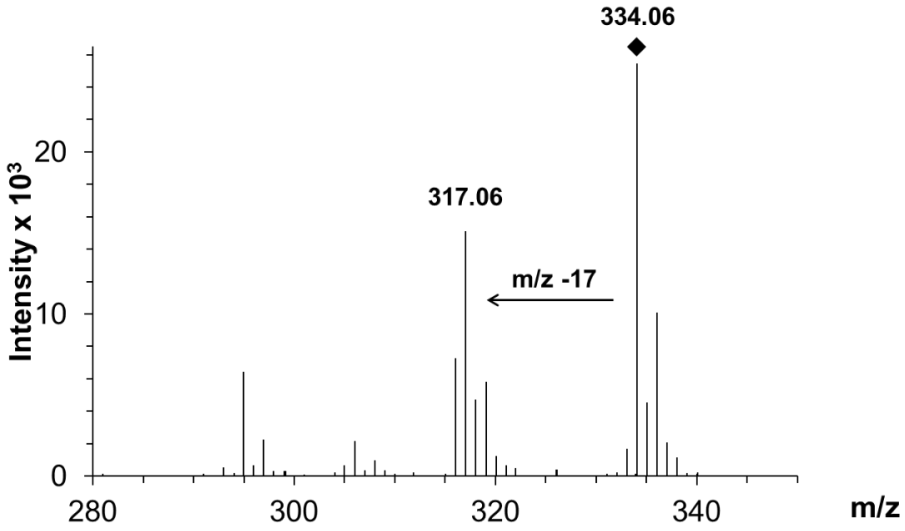

Figure S14. Collision induced dissociation (20 eV) of the peak at *m/z* 334.06 present in the reaction of **1** with 5 equiv. NaOCl in the presence of 5 equiv. AcOH $CH_3CN:H_2O$ 95:5 (v:v) at -30 ºC to form **3**.

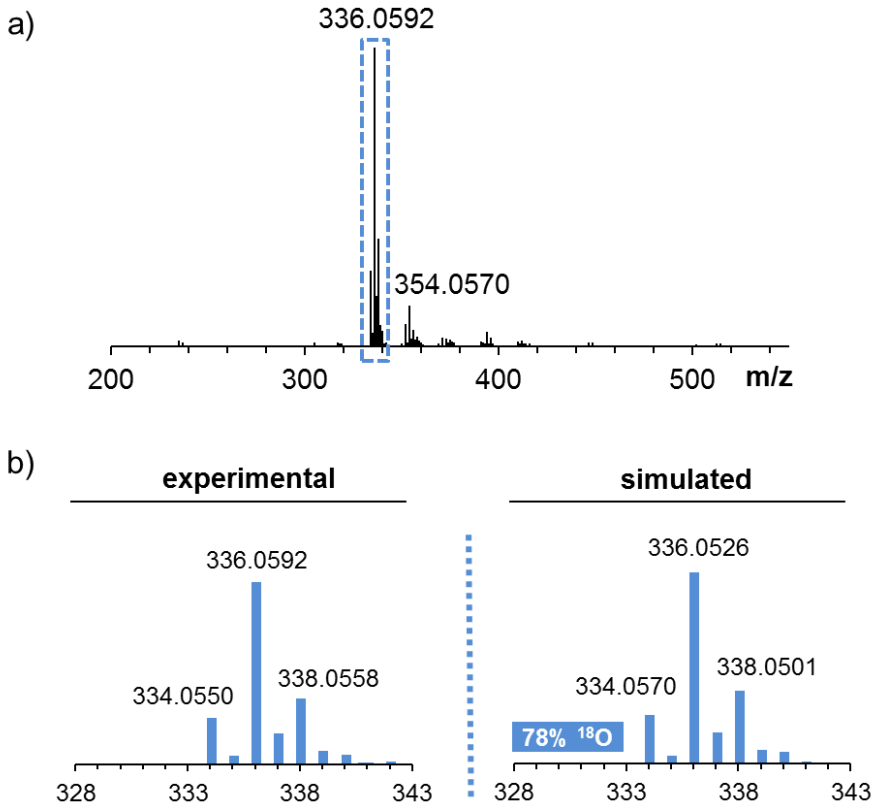

Figure S15. CSI-MS of partially ^{18}O-labeled **3** at -30 ºC formed by reaction of **1** with 5 equiv. partially ^{18}O-labeled NaOCl in the presence of 5 equiv. AcOH in $MeCN:H_2O$ 95:5 at -30 ºC. The spectrum shows a major peak at *m/z* 336.0592 corresponding to {[Ni(^{18}O)(L)]}. b) Experimental and simulated pattern for the peak at *m/z* 336.06.

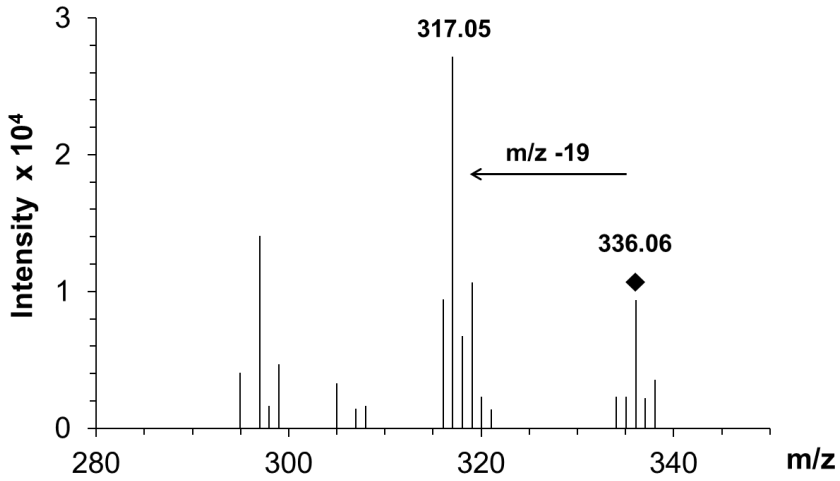

Figure S16. Collision induced dissociation (25 eV) of the peak at *m/z* 336.06 present in the reaction of **1** with 5 equiv. partially ^{18}O-labeled NaOCl in the presence of 5 equiv. AcOH in $CH_3CN:H_2O$ 95:5 (v:v) at -30 ºC to form **3**.

2.4. XAS analysis of 2 and 3

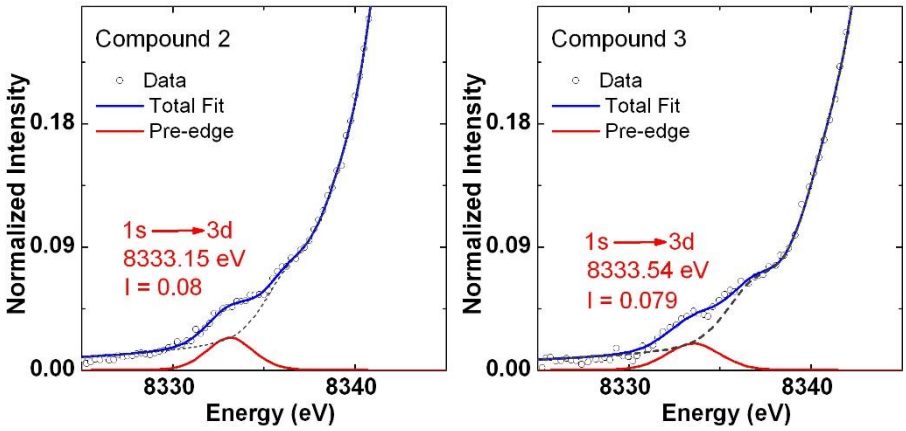

Figure S17. Ni K pre-edge XANES region for **2** and **3**, highlighting 1s → 3d transitions.

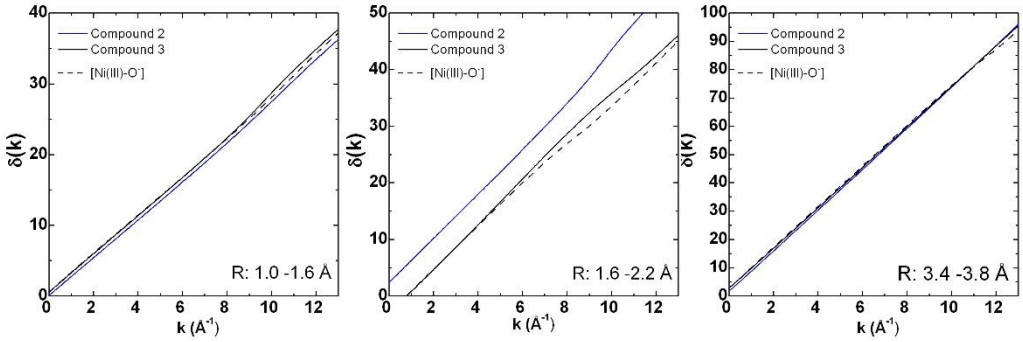

Figure S18. Phase comparison of back Fourier transformed EXAFS data for **2**, **3** and [Ni^{III}(O•)(L)] windowed in r-space regions: (left) 1.0-1.6 Å showing the same phase where only N/O scatterers are expected for all species; (center) 1.6-2.2 Å where compound **2** has a different phase from **3** and [Ni^{III}(O•)(L)], as would be expected due to the presence of a chloride ligand; (right) 3.4-3.8 Å where phase differences due to the presence of Ni-Ni scattering would be expected, and by comparison to [Ni^{III}(O•)(L)], not evident either in **2** or **3**.

Table S3. Selected EXAFS fits for **2**. Fits carried out in r-space (Δk = 2-13 Å^{-1}; Δr = 1-4 Å) with a Hanning window (dk 2), a *k*-weight = 2 and S_0 = 0.9. Bond distances and disorder parameters (Δr_{eff} and σ^2) were allowed to float having initial values of 0.0 Å and 0.003 Å^2 respectively, with a universal E_0 initially set to first inflection point of the rising edge and ΔE_0 = 0 eV. (Fits highlighted in blue are the best models; values highlighted in red are either statistically or physically erroneous; σ^2 reported as x10^3 Å^2).

							Ni-N/O*			Ni-N/O*			Ni-Cl			Ni--C			Ni--C-N--Ni			Ni--C-N--Ni			Ni--C			Ni--N-N--Ni			Ni--N-Ni-N--Ni			Ni--O-C--Ni			Ni--Ni		
FIT	Δk	Δr	*Var.*	R_{FACTOR}	χ^2_v	ΔE_0	N	r(Å)	σ^2	N	r(Å)	σ^2	N	r(Å)	σ^2	N	r(Å)	σ^2	N	r(Å)	σ^2	N	r(Å)	σ^2	N	r(Å)	σ^2	N	r(Å)	σ^2	N	r(Å)	σ^2	N	r(Å)	σ^2	N	r(Å)	σ^2
1	1-13.0	1-2.7	6	0.045	15.8	0	3	1.87(1)	2(1)	1	2.09(3)	2(1)	1	2.48(3)	6(4)	4	2.76(1)	7(6)																					
2	1-13.0	1-2.7	6	0.082	29.1	0	4	1.88(1)	4(2)	1	2.13(5)	4(2)	1	2.48(3)	4(4)	4		13(13)																					
3	1-13.0	1-2.7	6	0.053	18.9	0	3	1.86(1)	1(1)	1	2..06(3)	1(1)	2	2.47(2)	10(3)	4	2.76(1)	70(12)																					
4	1-13.0	1-2.7	6	0.049	17.3	0	2	1.85(1)	-2(1)	1	2.02(2)	-2(1)	2	2.50(4)	20(9)	4	2.75(1)	4(4)																					
5	1-13.0	1-2.7	6	0.086	22.7	0	3	1.87(1)	2(1)	1	2.11(4)	2(1)	-	-	-	4	2.77(1)	2(3)																					
6	1-13.0	1-2.7	6	0.129	33.7	0	3	1.87(1)	2(1)	2	2.12(2)	2(1)	-	-	-	4	2.76(1)	2(4)																					
7	1-13.0	1-4.0	6	0.069	10.2	0	3	1.87(1)	2(1)	1	2.08(3)	2(1)	1	2.50(3)	6(4)	8	2.73(1)	10(4)	8	2.96(1)	10(4)	4	3.08(1)	10(4)	1	3.23(1)	10(4)	4	3.78(1)	10(4)	4	3.80(1)	10(4)	4	3.98(1)	10(4)			
8	1-13.0	1-4.0	7	0.063	9.4	-1.15	3	1.86(1)	2(1)	1	2.07(3)	2(1)	1	2.50(4)	7(5)	8	2.72(1)	8(4)	8	2.96(1)	8(4)	4	3.08(1)	8(4)	1	3.22(1)	8(4)	4	3.77(1)	8(4)	4	3.79(1)	8(4)	4	3.97(1)	8(4)			
9	1-13.0	1-4.0	9	0.058	10.0	-0.99	3	1.86(1)	2(1)	1	2.07(3)	2(1)	1	2.50(3)	7(5)	8	2.73(1)	10(4)	8	2.96(1)	10(4)	4	3.08(1)	10(4)	1	3.22(1)	10(4)	4	3.77(1)	10(4)	4	3.79(1)	10(4)	4	3.97(1)	10(4)	1	3.79(13)	17(21)
Distances from DFT Geometry Optimized Structure							**3**	**1.86**		**1**	**1.93**		**1**	**2.4**		**8**	**2.76**	-	**8**	**2.96**	-	**4**	**3.09**		**1**	**3.21**		**4**	**3.75**		**4**	**3.76**		**4**	**3.95**		-	-	-

*Although EXAFS can not differentiate between O/N/C scattering paths, chemical intuition was used for description to facilitate comparison with theoretically derived structure

Table S4 Selected EXAFS fits for **3**. Fits carried out in r-space (Δk = 2-12.5 Å^{-1}; Δr = 1-4 Å) with a Hanning window (dk 2), a *k*-weight = 2 and S_0 = 0.9. Bond distances and disorder parameters (Δr_{eff} and σ^2) were allowed to float having initial values of 0.0 Å and 0.003 Å^2 respectively, with a universal E_0 initially set to the first inflection point of the rising edge and ΔE_0 = 0 eV. (Fits highlighted in blue are the best models; values highlighted in red are either statistically or physically erroneous; σ^2 reported as x10^3 Å^2).

							Ni-N/O*			Ni--C			Ni--C-N--Ni			Ni--C-N--Ni			Ni--C			Ni--N-N--Ni			Ni--N-Ni-N--Ni			Ni--O-C--Ni			Ni--Ni		
FIT	Δk	Δr	*Var.*	R_{FACTOR}	χ^2_v	ΔE_0	N	r(Å)	σ^2	N	r(Å)	σ^2	N	r(Å)	σ^2	N	r(Å)	σ^2	N	r(Å)	σ^2	N	r(Å)	σ^2	N	r(Å)	σ^2	N	r(Å)	σ^2	N	r(Å)	σ^2	N	r(Å)	σ^2
1	1-12.5	1-2.0	2	0.065	9.2	0	4	1.89(1)	1(1)																												
	1-12.5	1-2.0	2	0.053	7.5	0	5	1.89(1)	3(1)																												
2	1-12.5	1-2.0	2	0.061	8.7	0	6	1.89(1)	5(1)																												
3	1-12.5	1-2.6	4	0.036	4.3	0	5	1.89(1)	3(1)	8	2.76(3)	6(3)																									
4	1-12.5	1-4.0	4	0.093	4.9	0	6	1.89(1)	5(1)	8	2.76(2)	5(2)	8	3.02(2)	5(2)	4	3.11(2)	5(2)	1	3.24(2)	5(2)	4	3.79(2)	5(2)	4	3.84(2)	5(2)	4	4.01(2)	5(2)						
5	1-12.5	1-4.0	4	0.075	3.9	0	5	1.89(1)	3(1)	8	2.76(2)	5(2)	8	3.02(2)	5(2)	4	3.11(2)	5(2)	1	3.24(2)	5(2)	4	3.79(2)	5(2)	4	3.84(2)	5(2)	4	4.01(2)	5(2)						
6	1-12.5	1-4.0	6	0.063	3.8	0	5	1.89(1)	3(1)	8	2.77(2)	5(2)	8	3.02(2)	5(2)	4	3.11(2)	5(2)	1	3.25(2)	5(2)	4	3.79(2)	5(2)	4	3.85(2)	5(2)	4	4.01(2)	5(2)	1	3.77(5)	5(6)			
Distances from Geometry Optimized Structure							**5**	**1.93**	-	**8**	**2.77**	-	**8**	**2.97**	-	**4**	**3.10**	-	**1**	**3.21**	-	**4**	**3.77**	-	**4**	**3.78**	-	**4**	**3.97**	-	-	-	-			

*Although EXAFS can not differentiate between O/N/C scattering paths, chemical intuition was used for description to facilitate comparison with theoretically derived structure

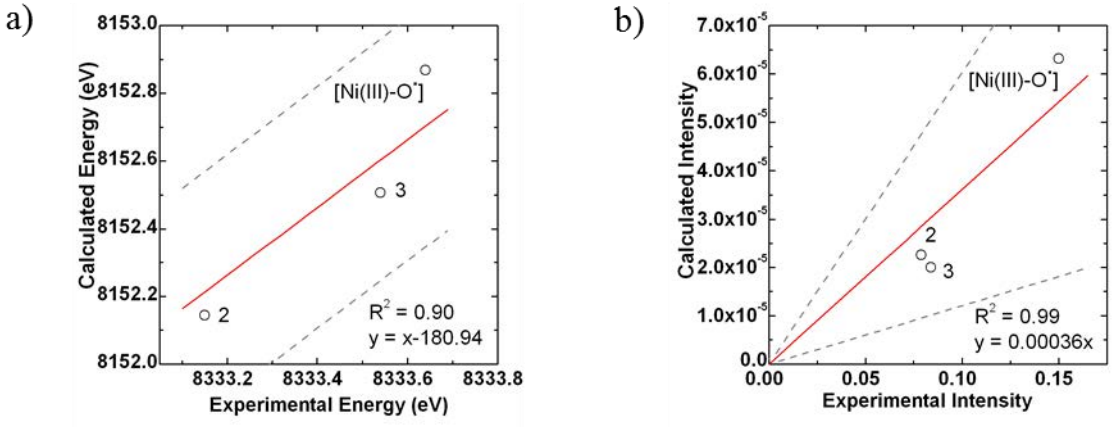

Figure S19. Correlation between calculated and experimental Ni K pre-edge energies (a) and intensities (b) for **2**, **3** and [Ni^{III}(O•)(L)].

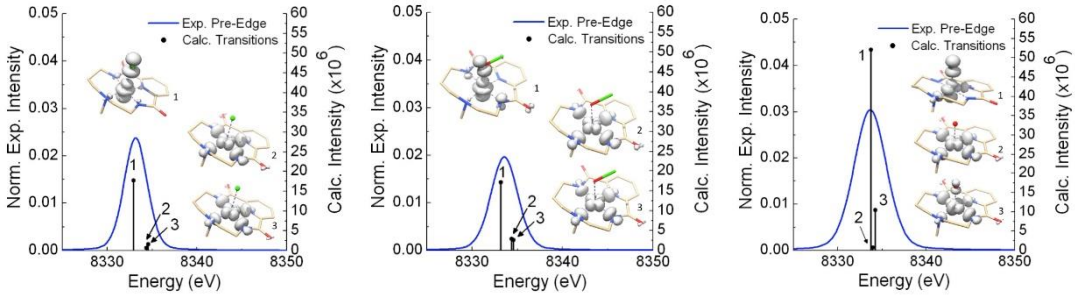

Figure S20. Overlay between experimental Ni K pre-edges and calculated transitions also showing their difference density maps for: **2** (left), **3** (center) and [Ni^{III}(O•)(L)] (right). Transitions were shifted by 180.94 eV to match experiment.

2.5. DFT calculations

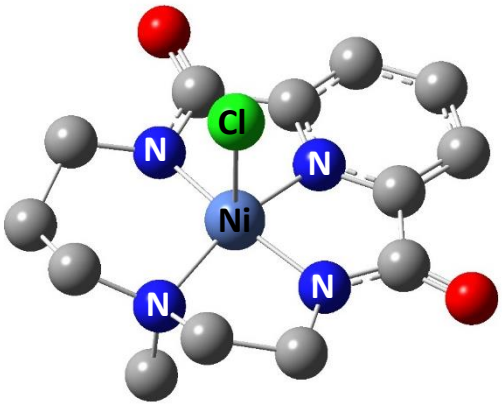

Figure S21. DFT computed structure of [Ni^{III}(L)(Cl)] (S =1/2).

2.5.1. Raman simulations

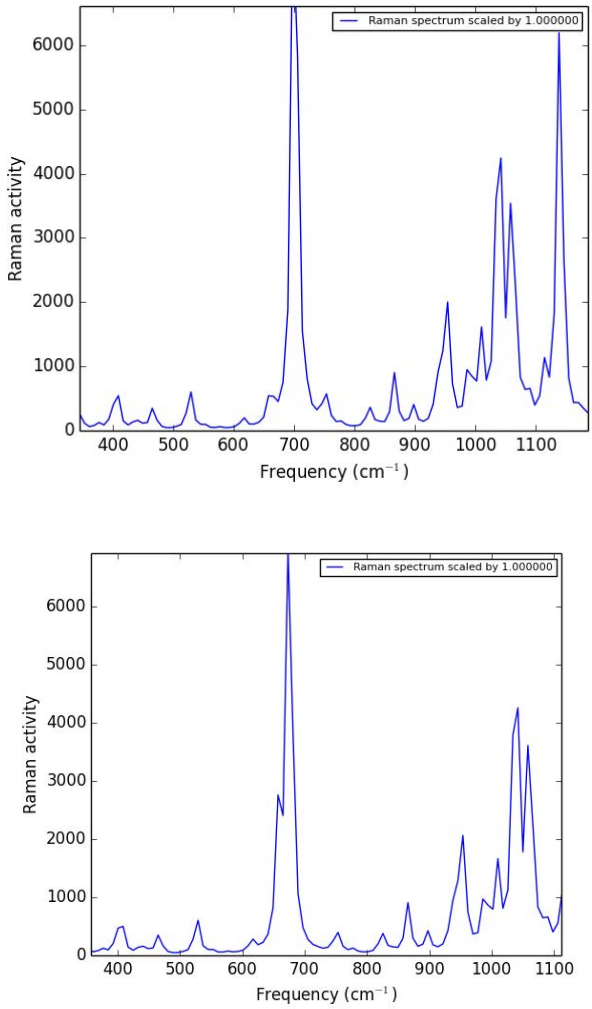

Figure S22. Calculated Raman spectra of $[Ni(OCl)(L)]^+$ (^{3}**A**) simulated at 77 K and with a laser excitation of 473 nm. Top: $[Ni(OCl)(L)]^+$. Bottom: $[Ni(^{18}OCl)(L)]^+$.

2.5.2. Thermodynamic data

Equations (1) to (3) correspond to the reactions for which the thermodynamics have been calculated.

$NaOCl + CH_3COOH \rightarrow NaOCOCH_3 + HOCl$	$\Delta G = -11$ kcal·mol^{-1}
$[Ni^{II}(L)]$ (1) + 2 HOCl → $[Ni^{III}(OCl)(L)]$ (^{2}B) + H_2O + Cl•	$\Delta G = +5.3$ kcal·mol^{-1}
$[Ni^{II}(L)]$ (1) + 2 HOCl + H^+ → $[Ni(OCl)(L)]^+$ (^{3}A) + H_2O + HCl	$\Delta G = -12.8$ kcal·mol^{-1}
$[Ni(OCl)(L)]^+$ (^{3}A) → $[Ni(O•)(L)]^+$ (^{4}C) - Cl•	$\Delta G = +43.1$ kcal·mol^{-1}

2.5.3. Spin density analysis

Table S5. Mulliken spin density of the most relevant atoms for each nickel species.

Atom	$[Ni^{II}(L)]^0$	$[Ni^{III}(L)]^+$	$[Ni^{III}(OCl)(L)]^0$	$[Ni(OCl)(L)]^+$	$[Ni(O)(L)]^+$
Ni	0.00	0.61	0.73	0.75	0.72
O	-	-	0.25	0.42	1.43
Cl	-	-	0.02	0.09	-
ligand L	-	-	-	0.68	0.88

A.3. Supplementary Information Chapter V

3.1. Materials and methods

3.1.1. Instrumentation

Reagents and solvents used were commercially available and purchased from Panreac, Scharlau and Aldrich. Preparation and handling of air-sensitive materials were carried out in a N_2 drybox (MBraun ULK 1000) with O_2 and H_2O concentrations < 1 ppm. Commercially available superdry N_2O (H_2O ≤ 8ppm/v) from Abelló-Linde and O_2 >99.5% pure from Praxair were purchased and used as received. H_2L ligand was prepared following procedures described in the literature [T. Corona, F. F. Pfaff, F. Acuña-Parés, A. Draksharapu, C. J. Whiteoak, V. Martin-Diaconescu, J. Lloret-Fillol, W. R. Browne, K. Ray and A. Company, *Chem. Eur. J.,* **2015**, *21*, 15029-15038].

Elemental analyses of C, H and N were performed with a Perkin Elmer EA2400 series II elemental analyzer. Mass spectra were performed by electrospray ionization in a high-resolution mass spectrometer Bruker micrOTOF QII (Q-TOF) with a quadrupole analyzer with positive and negative ionization modes. ^{1}H-NMR, ^{13}C-NMR, COSY and HSQC spectra were performed in a Bruker Ultrashield Avance III400 and Ultrashield DPX300 spectrometers. UV-Vis spectra were performed by a diode array spectrophotometer Agilent Cary 60 and low temperature control was maintained with a cryostat from Unisoku Scientific Instruments. X-Ray analyses were carried out on a Bruker AXS SMART APEX CCD diffractometer using Mo Kα monochromatic radiation (λ = 0.71073 Å). Cyclic voltammetries were performed using a potentiostat from CHInstruments with a three electrode cell. The working electrode is a glassy carbon disk from BAS (0.07 cm^2), the reference electrode is a Ag^0/Ag^+ and the auxiliary electrode is platinum wire. All voltammetries have been carried out with nBu$_4$NPF$_6$ (TBAP) as supporting electrolyte (0.1 M ionic strength) under N_2. GC analyses were carried out on an Agilent 7820A gas chromatograph (HP5 column, 30m) with a flame ionization detector. GC-MS spectral analyses were performed on an Agilent 7890A gas chromatograph interfaced with an Agilent 5975c mass spectrometer with Triple-axis detector. N_2 identification was carried out with an Agilent 7820A GC system equipped with three columns: washed molecular sieves 5Å, 2 m × 1/8 inch outside diameter (OD), Mesh 60/80 SS and Porapak Q, 4 m × 1/8 inch OD, Mesh 80/100 SS, and a thermal conductivity detector. Perpendicular mode X-band electron paramangetic responance (EPR) spectra were collected using a Bruker ESP 300E spectrometer. All EPR spectra were recorded at 77K with the following experimental parameters: frequency, 9.39 GHz; power 0.3 mW; modulation amplitude, 32 G; time constant, 20.48 s; conversion time, 80 s.

3.1.2. Synthesis of cobalt complexes

Synthesis of the [$Co^{II}(CF_3SO_3)_2(CH_3CN)_2$]. In a 100 mL Schlenk flask, $CoCl_2$ (4.9 g, 0.038 mmol) was dissolved with 30 mL of dry CH_3CN. Then, about Me_3SiOTf (14.5 mL, 0.080 mmol) was added to the solution under a N_2 atmosphere and allowed to stir at room temperature for 24 hours. A red colored solution appeared with a pale red precipitate. Then, the solvent was removed completely with a rotary evaporator. The resulting solid was dissolved again in CH_3CN (10 mL) and slow diethyl ether diffusion at room temperature over the resultant solution afforded a pink powder solid (12.7 g, 0.029 mmol, 76%). Anal. Calcd for $C_6H_6CoF_6N_2O_6S_2 \cdot 2H_2O$: C, 15.16; N, 5.90; H, 2.12%. Found: C, 15.13; N, 5.65; H, 2.16%.

Synthesis of [Co^{II}(L)]·KCF_3SO_3 (**1**·KCF_3SO_3). In the glove box, a solution of $[Co(CH_3CN)_2(CF_3SO_3)_2]$ (16.7 mg, 0.038 mmol) in anhydrous CH_3CN (0.5 mL) was added dropwise to a vigorously stirred solution of H_2**L** (9.8 mg, 0.038 mmol) in anhydrous CH_3CN (0.5 mL). After a few seconds the solution turned orange. Addition of 2 equiv $K[N(SiMe_3)_2]$ (15.2 mg, 0.076 mmol) caused a clear color change to dark red. After stirring for 3 hours, the solution was filtered through silica and concentrated. Slow diethyl ether diffusion over the resulting solution afforded, in a few days, dark red powder (co-crystallization with KCF_3SO_3) (11.0 mg, 0.022 mmol, 58%). ESI-MS (*m/z*): 319.0590 $[Co+L]^+$, 342.0476 [**1**+Na]$^+$, 358.0238 [**1**+K]$^+$. CV (CH_3CN vs SCE) $E_{1/2}$= 0.17 V. μ_{eff} =1.69 μ_B (Evans' method).

Synthesis of [Co^{III}(L)(acac)] (**2**). A solution of $[Co(acac)_3]$ (24.8 mg, 0.060 mmol) in CH_3CN (0.5 mL) was added dropwise to a vigorously stirred solution of H_2**L** (15.8 mg, 0.060 mmol) in CH_3CN (0.5 mL). After a few seconds the solution turned dark green. Addition of 2 equiv $K[N(SiMe_3)_2]$ (24.0 mg, 0.120 mmol) caused a clear color change to dark brown. After stirring for 3 hours, the solution was filtered through silica and evaporated. Then, it was dissolved with methanol and slow diethyl ether diffusion over the resulting solution afforded, in a few days, dark brown crystals. ESI-MS (*m/z*): 319.0 $[Co^{III}+L]^+$ 337.0 $[Co^{III}+L+H_2O]^+$, 419.0 [**2**+H]$^+$. Anal. Calcd for $C_{18}H_{23}CoN_4O_4 \cdot 1H_2O$: C, 49.55; N, 12.84; H, 5.77%. Found: C, 49.28; N, 12.81; H, 5.38 %. ^{1}H-NMR (CD_3CN, 400 MHz, 298K) δ, ppm: 8.1 (t, J = 7.7 Hz, 1H, Ar**H$_a$**), 7.79 (d, J = 7.7 Hz, 2H, Ar**H$_b$**), 4.14-4.05 (m, 1H, **H$_c$**), 4.05-3.95(m, 1H, **H$_d$**), 3.60-3.49 (m, 1H, **H$_e$**), 3.31-3.20 (m, 1H, **H$_f$**), 3.19-3.08 (m, 1H, **H$_g$**), 2.81-2.70 (m, 1H, **H$_h$**), 2.25(s, 3H, L-C**H$_3$**), 1.92-1.85 (m, 1H, **H$_i$**), 1.79-1.70 (m, 1H, **H$_j$**), 1.70-1.59 (m, 2H, **Hk/l**), 1.50 (s, 3H, acac-C**H$_{3m}$**), 1.22 (s, 3H, acac-C**H$_{3n}$**). ^{13}C-NMR (CD_3CN, 100 MHz, 298K) δ, ppm: 206.65, 140.14, 123.34, 123.05, 99.11, 65.23, 59.98, 46.11, 44.50, 40.06, 29.90, 26.91, 25.34.

3.2. Characterization of 1

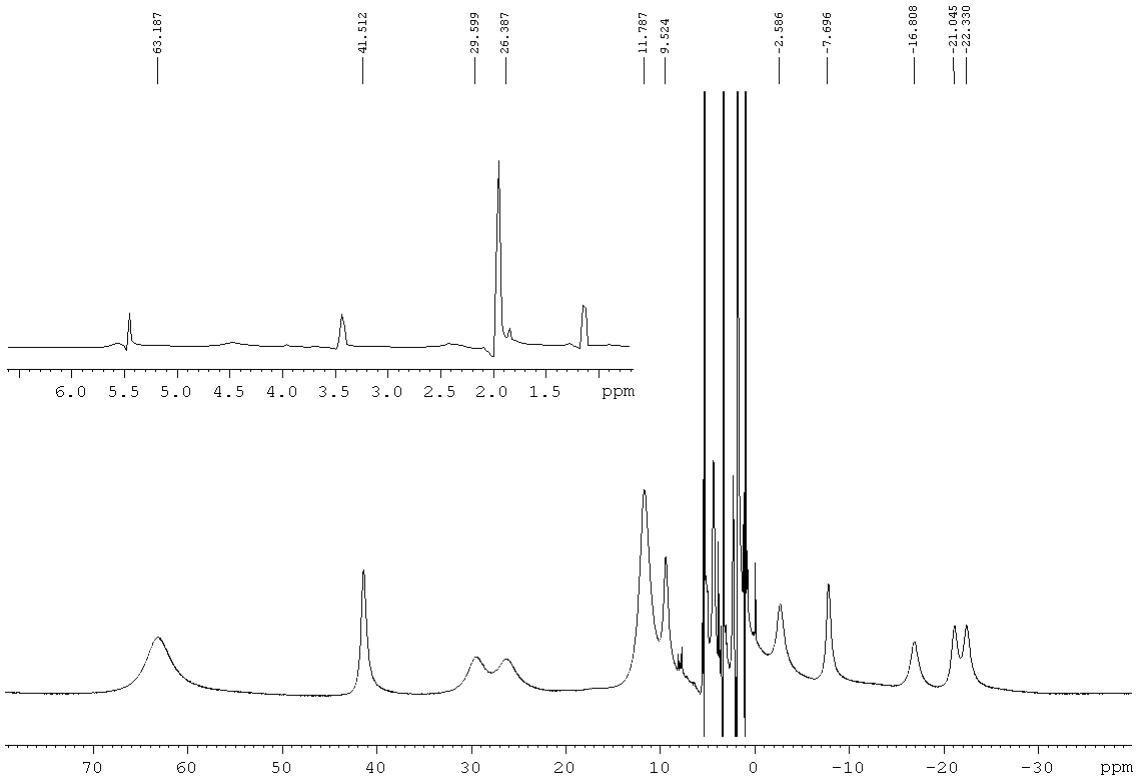

Figure S1. ^{1}H-NMR spectrum of **1** in CD_3CN at 298K (400 MHz).

Table S1. Chemical shift, relaxation time and integration of the ^{1}H-NMR spectrum of **1** in CD_3CN at 298K (400 MHz).

Chemical shift (ppm)	Relaxation time (ms)	Integration (H)
64.47	1.8	2
41.66	16	2
29.87	0.6	1
26.74	0.7	1
11.83	0.8	3
9.54	3.3	1
-2.63	2.1	2
-7.75	2.1	1
-16.92	1.9	1
-21.16	6.1	1
-22.47	5.7	1

Table S2. Crystal Data for $[Co^{II}(L)]\cdot NaBF_4$ (**1**·$NaBF_4$).

Empirical formula	$C_{13}\ H_{16}\ B\ Co\ F_4\ N_4\ Na\ O_2$
Formula weight	429.03
Temperature	143(2) K
Wavelength	0.71073 Å
Crystal system, space group	Monoclinic, P 21
Unit cell dimensions	a = 9.991(3) Å α = 90 º b = 6.986(2) Å β = 112.856(5) º c = 12.879(4) Å γ = 90 º
Volume	828.4(4) A^3
Z, Calculated density	2, 1.720 Mg/m^3
Absorption coefficient	1.121 mm^{-1}
F(000)	434
Crystal size	0.30 x 0.12 x 0.08 mm
Theta range for data collection	2.211 to 24.991 º
Limiting indices	-10 ≤ h ≤ 11 -8 ≤ k ≤ 8 -14 ≤ l ≤ 15
Reflections collected / unique	3905 / 2514 [R(int) = 0.0401]
Completeness to theta = 28.21	96.3 %
Absorption correction	Empirical
Max. and min. transmission	1.0 and 0.417707
Refinement method	Full-matrix least-squares on F^2
Data / restraints / parameters	2514 / 145 / 271
Goodness-of-fit on F^2	1.264
Final R indices [I>2sigma(I)]	R1 = 0.0989 wR2 = 0.2662
R indices (all data)	R1 = 0.1192 wR2 = 0.3121
Largest diff. peak and hole	1.828 and -1.722 $e.A^{-3}$

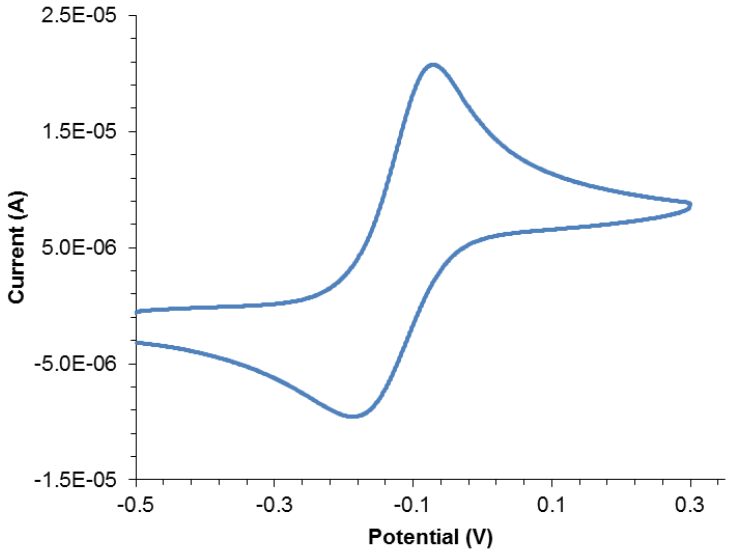

Figure S2. Cyclic voltammetry of **1** in anhydrous CH_3CN at 298 K under N_2 vs Ag/Ag^+.

3.3. Characterization of 2

Table S3. Crystal Data for $[Co^{III}(L)(acac)]\cdot H_2O$ (**2**·H_2O).

Empirical formula	$C_{18}\ H_{25}\ Co\ N_4\ O_5$
Formula weight	436.34
Temperature	100(2) K
Wavelength	0.71073 Å
Crystal system, space group	Triclinic, P -1
Unit cell dimensions	a = 8.0011(15) Å α = 92.10(3) º b = 9.657(19) Å β = 102.94(3) º c = 12.97(2) Å γ = 105.15(3) º
Volume	938(3) A^3
Z, Calculated density	2, 1.545 Mg/m^3
Absorption coefficient	0.954 mm^{-1}
F(000)	456
Crystal size	0.08 x 0.15 x 0.20 mm
Theta range for data collection	1.6 to 28.4 º
Limiting indices	-9 ≤ h ≤ 10 -11 ≤ k ≤ 12 -16 ≤ l ≤ 15
Reflections collected / unique	5488 / 4040 [R(int) = 0.067]
Completeness to theta = 28.39	97.6
Absorption correction	Empirical
Max. and min. transmission	1.0 and 0.298558
Refinement method	Full-matrix least-squares on F^2
Data / restraints / parameters	4040/ 3 / 305
Goodness-of-fit on F^2	1.019
Final R indices [I>2sigma(I)]	R1 = 0.0730 wR2 = 0.1763
R indices (all data)	R1 = 0.1047 wR2 = 0.1980
Largest diff. peak and hole	1.339 and -0.811 $e.A^{-3}$

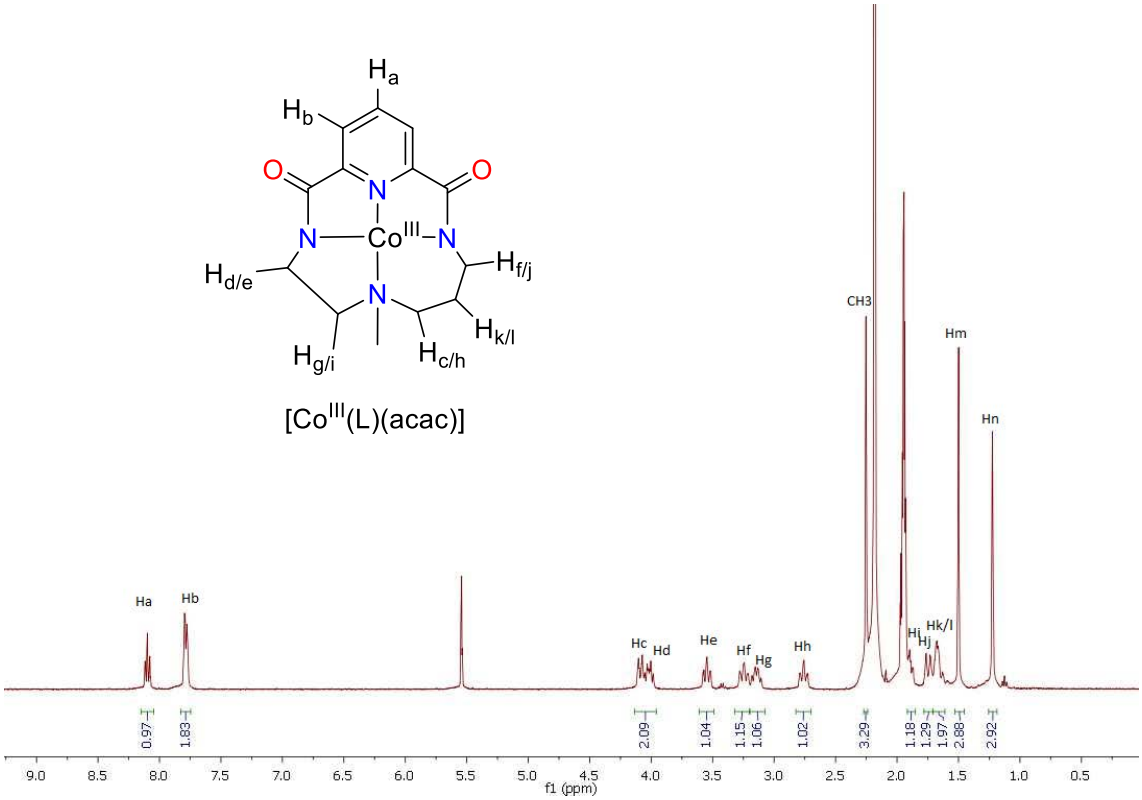

Figure S3. ^{1}H-NMR spectrum of **2** in CD_3CN at 298K (400 MHz).

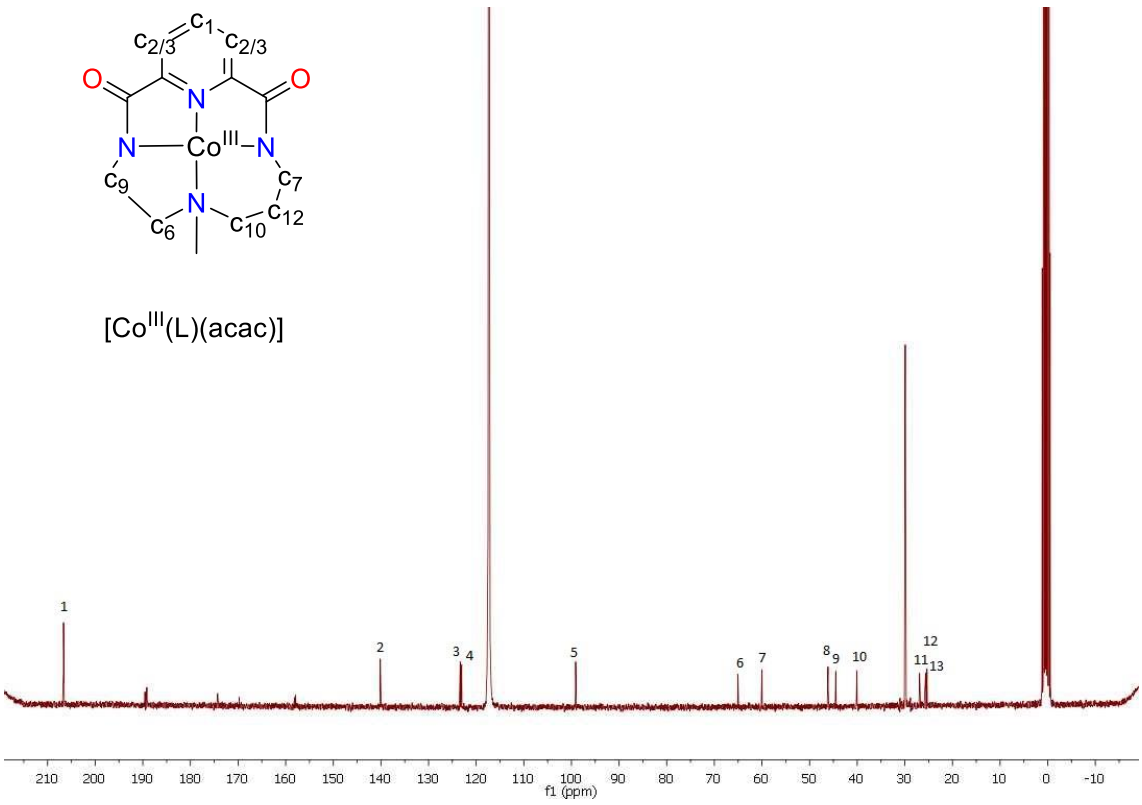

Figure S4. ^{13}C-NMR spectrum of **2** in CD_3CN at 298K (100 MHz).

3.4. Reaction of 1 with N_2O

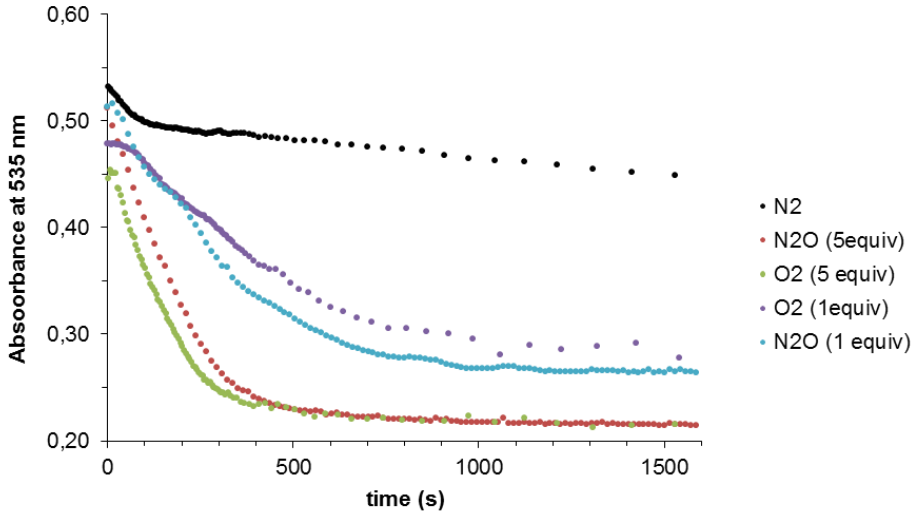

Figure S5. Kinetics traces at 535 nm of the reaction of **1** (0.5 mM) with different amounts of oxidant (N_2O or O_2) in anhydrous CH_3CN at 273K together with a blank experiment with N_2.

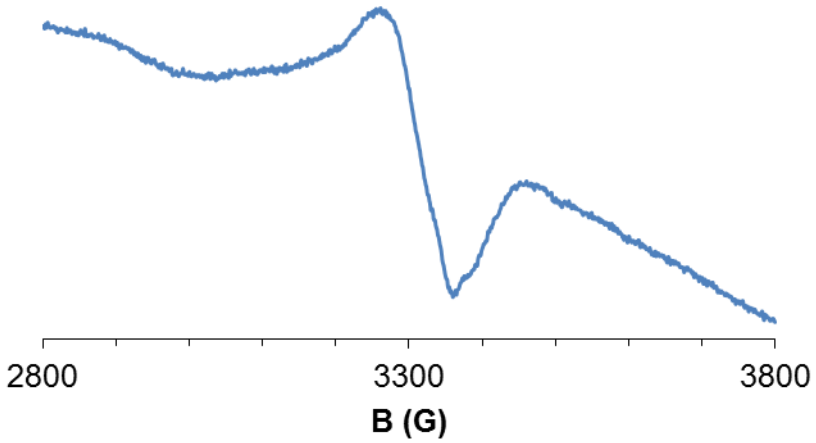

Figure S6. EPR spectrum of the reaction mixture obtained after decay of compound **1** (2 mM) upon reaction with excess N_2O in CH_3CN at 273K.

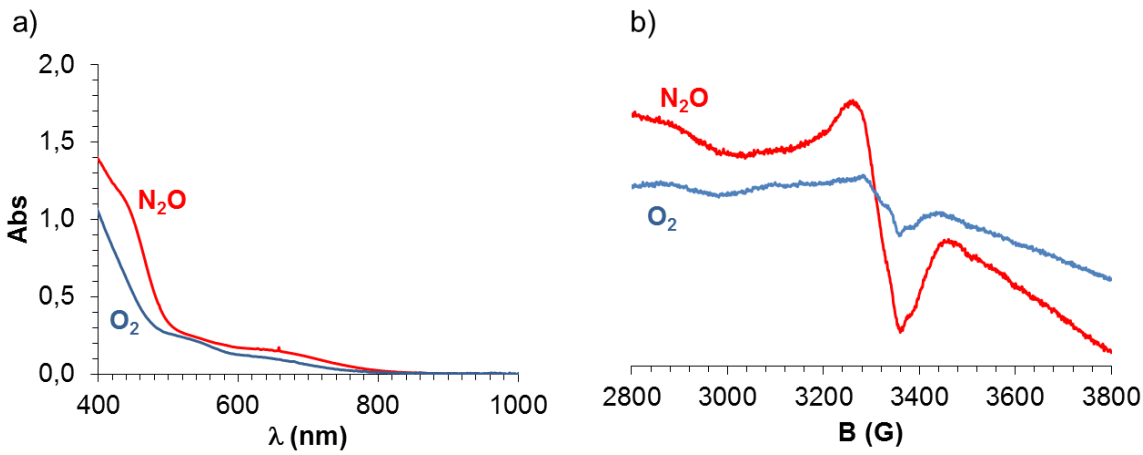

Figure S7. a) UV-vis spectra of the reaction mixture obtained after decay of compound **1** (0.5 mM) upon reaction with excess N_2O or O_2 in CH_3CN at 273 K. b) EPR spectra of the reaction mixture obtained after decay of compound **1** (2 mM) upon reaction with excess N_2O or O_2 in CH_3CN at 273 K.

Kinetic analysis of the reaction of 1 with N_2O. In a typical experiment, 2.5 mL of a 0.5 mM solution of **1** in anhydrous CH_3CN were placed in a UV-Vis cuvette (1.25 µmol of **1**). The quartz cell was capped with a septum and taken out of the glovebox, placed in the Unisoku cryostat of the UV-Vis spectrophotometer and cooled down at 273 K. After reaching thermal equilibrium a UV-Vis spectrum of the starting complex was recorded. Then, a known amount of N_2O was injected into the cell using a syringe through the septum and the process was monitored by UV-Vis. The decay of the characteristic absorption band at λ_{max} = 535 nm associated to **1** occurred in a few minutes. The reaction order with respect to **1** and N_2O was determined as follows:

a) Reaction order with respect to N_2O: under conditions of excess N_2O (5-100 equiv with respect to **1**) reactions showed pseudo-first-order behaviour so that the observed reaction rates (k_{obs}) were linearly dependent on the amount of N_2O (Figure 3a).

b) Reaction order with respect to **1**: the initial rates method was applied to determine the reaction order with respect to **1** by performing a series of experiments at different initial concentrations of **1** (0.1-0.8 mM) using a fixed amount of N_2O (0.13 mmol) (Figure S8).

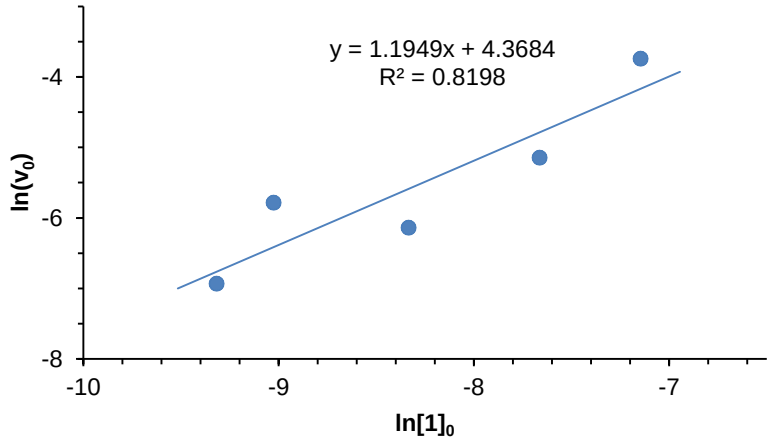

Figure S8. Plot of ln(initial rates) in front of ln[**1**]$_0$ corresponding to the reaction of **1** with N_2O (0.13 mmol N_2O) in CH_3CN at 273 K ([**1**]$_0$ = initial concentration of **1**).

Quantification of N_2 released during the reaction of 1 with N_2O. 10 mg of compound **1** (20 µmol) were dissolved in 5 mL anhydrous acetone under Ar in an encapsulated glass vial of 11 mL (capped with a septum). The vial was placed in an ice bath and under vigorous stirring excess N_2O (750 µL, 34 µmol) was injected through the septum. After 30 min, a 50 µL aliquot was extracted from the headspace and analyzed by GC-TCD. The amount of liberated N_2 was calculated by interpolation in a calibration curve (Figure S9. Standard samples were prepared as follows: 5 mL anhydrous acetone were placed in an encapsulated glass vial of 11 mL (capped with a septum) under Ar. This vial was placed in an ice bath and under vigorous stirring, 750 µL N_2O were injected through the septum. Afterwards, a known amount of N_2 (100–1250 µL, 4–56 µmol) was also introduced into the vial. After 30 min, 50 µL aliquots were extracted from the headspace of each standard sample and analyzed by GC-TCD. See the Instrumentation section above for a description of the GC-TCD columns.

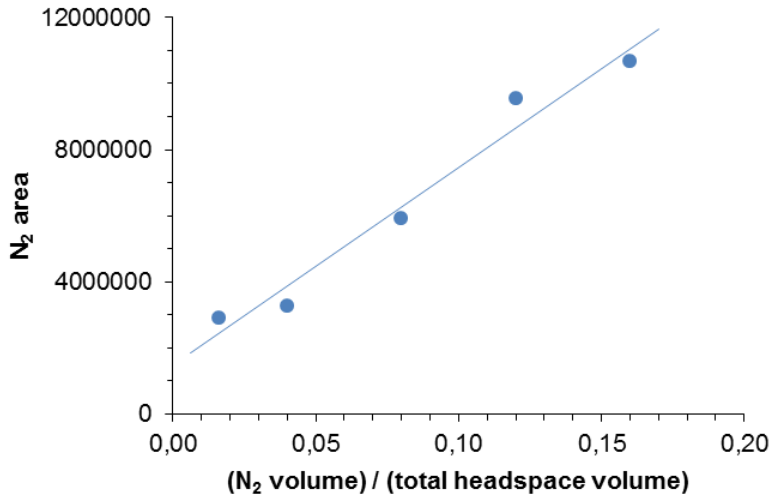

Figure S9. Calibration curve for the determination of N_2 released in the reaction of **1** with N_2O.

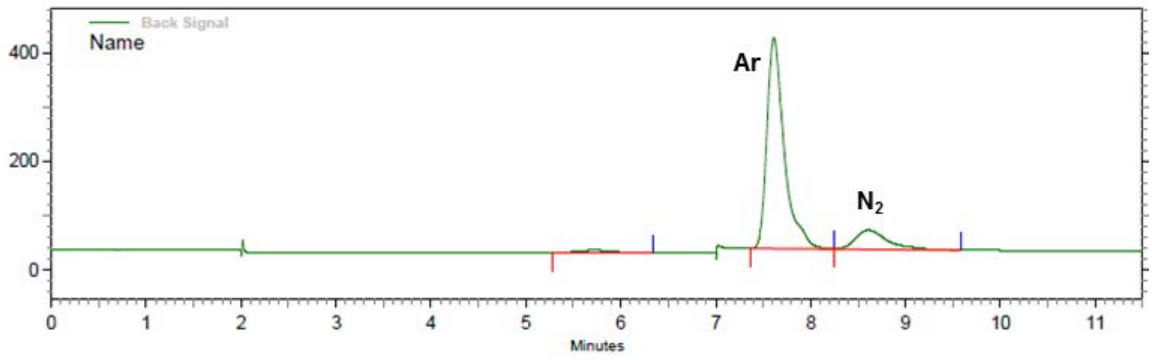

Figure S10. Gas chromatogram (GC-TCD) for the quantification of the N_2 released in the reaction of **1** with N_2O.

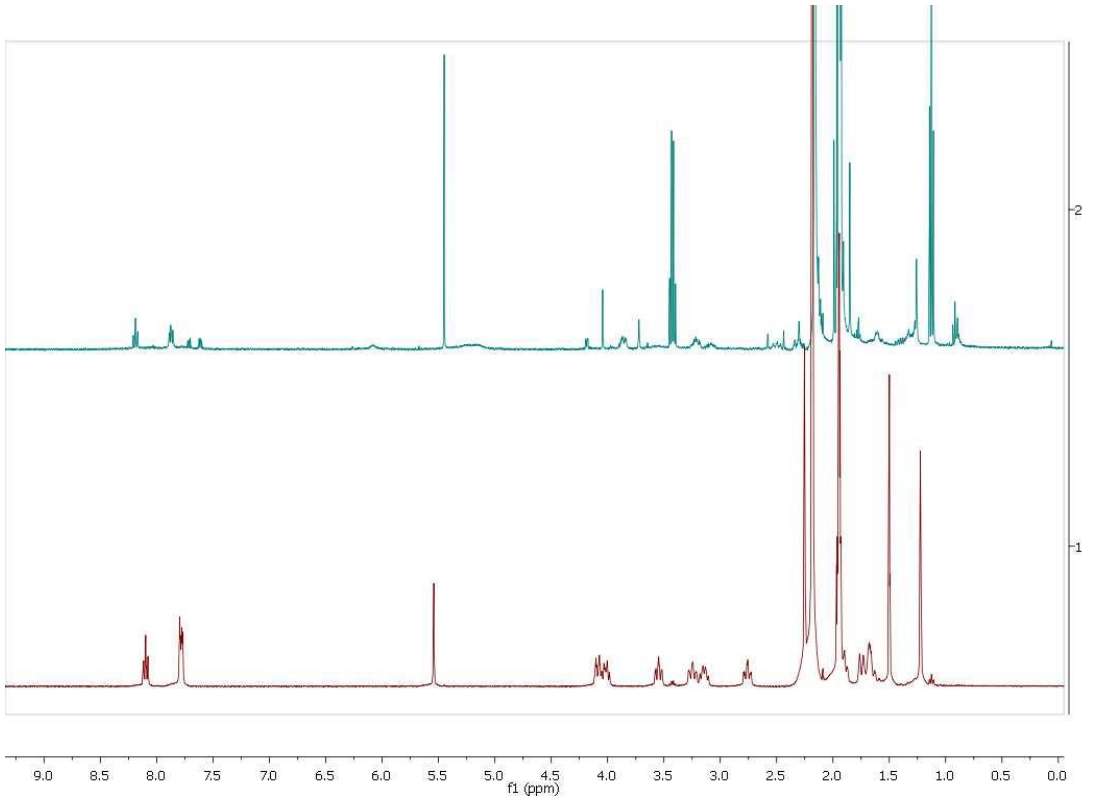

Figure S11. Top: ^{1}H-NMR spectrum of decomposed species after reaction of **1** with N_2O in CD_3CN at 298K. Bottom: ^{1}H-NMR spectrum of **2** in CD_3CN at 298 K.

Analysis of the reaction of 1 with N_2O with cyclohexanecarboxaldehyde. In the glove box, a solution of cyclohexanecarboxaldehyde (0.2 mL, 50 equiv.) in anhydrous CH_3CN was added to a stirred solution of **1** (1 equiv.) in anhydrous CH_3CN (2.5 mL). Afterwards, nitrous oxide was injected into the reaction vessel using a balloon. The resulting mixture was stirred at room temperature for a given time. Biphenyl was added as internal standard and the cobalt complex was removed by passing the solution through a short path of silica. The products were then eluted with ethyl acetate and analyzed by GC-FID. The organic products were identified by comparison with authentic compounds. All reactions were run in triplicate and the results are the average of the three replicates.

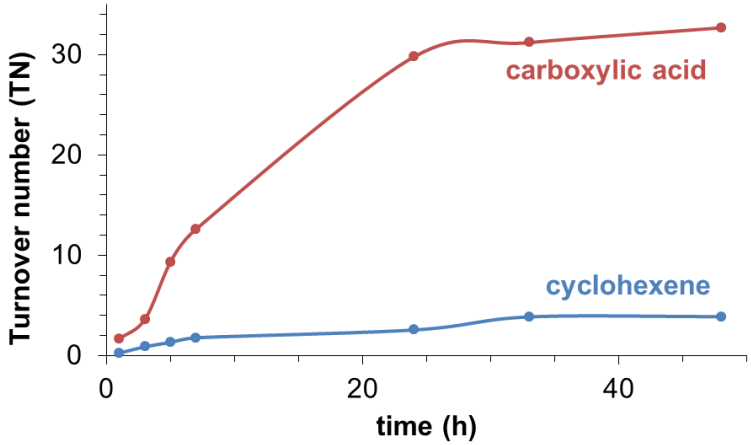

Figure S12. Evolution of cyclohexanecarboxylic acid and cyclohexene production in the reaction of **1** with cyclohexanecarboxaldehyde in the presence of N_2O in CH_3CN. A blank experiment without **1** afforded only 0.5 TN cyclohexene and 4.8 TN cyclohexanecarboxylic acid after 48 hours of reaction.

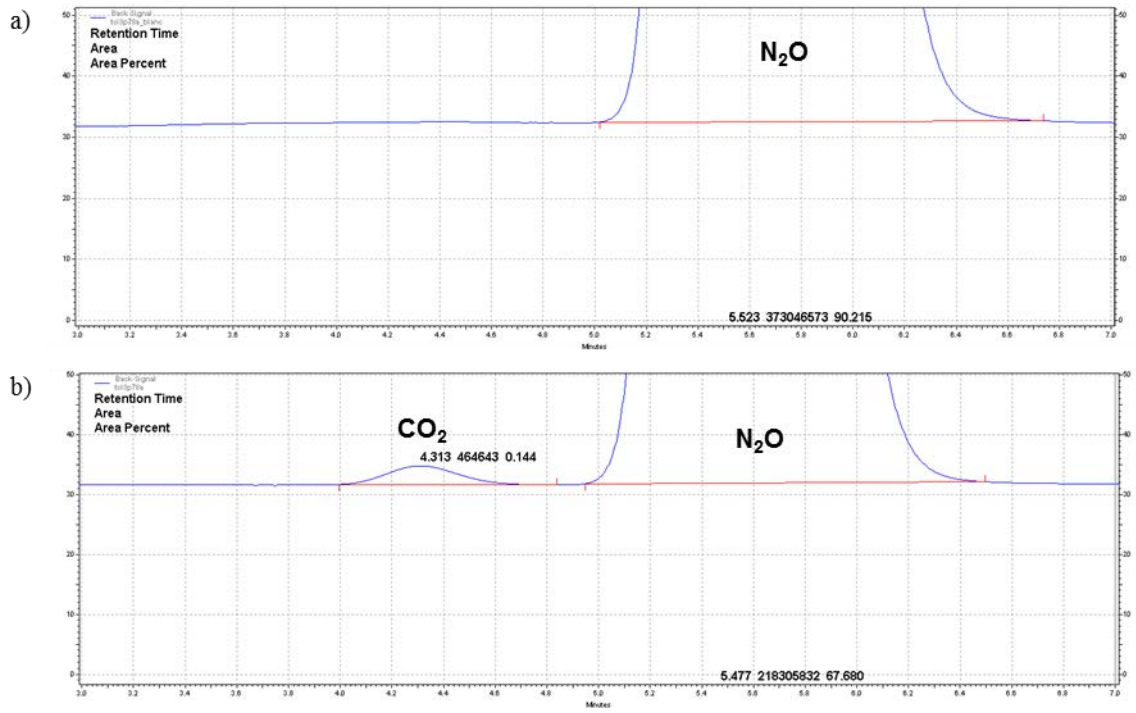

Figure S13. Gas chromatogram (GC-TCD) for the qualitative evaluation of CO_2 release in the reaction of **1** with N_2O in CH_3CN at 273K (b) together with a blank experiment in the absence of **1** (a).

A.4. Supplementary Information Chapter VI

4.1. Materials and methods

Reagents and solvents used were commercially available and purchased from Carl ROTH and Aldrich. Preparation and handling of air-sensitive materials were carried out in a N_2 drybox (OMNI-Lab 2 (VAC) or MBraun ULK 1000) with O_2 and H_2O concentrations < 1 ppm.

Mass spectra were performed by electrospray ionization in a high-resolution mass spectrometer Bruker micrOTOF QII (Q-TOF) with a quadrupole analyser with positive and negative ionization modes with a Bruker Cryospray ionization source or by electrospray ionization in an Agilent-1200 mass spectrometer.

UV-vis absorption spectra were performed by a diode array spectrophotometer Agilent Cary 60 and low temperature control was maintained with a cryostat from Unisoku Scientific Instruments EPR spectra were recorded with an ESP 300 X-Band EPR spectrometer from Bruker with a TE011 super high Q microwave resonator. Samples were cooled to 77 K with a liquid nitrogen Dewar. Spin quantifications were calculated on the basis of double integrals of the recorded spectra in comparison to a measured Cu^{II}-standard with a given concentration. Sample tubes were filled higher than the cavity dimension to guarantee an equally filled cavity for all measured samples. Spin quantifications were additionally corrected for volume errors resulting in slight differences in tube diameter. EPR simulation was performed with EASYSPIN.[1]

NMR spectra were recorded in a Bruker AV 500 NMR spectrometer or in a Bruker Ultrashield Avance III400 spectrometer.

Methane detection was carried out with an Agilent 7820A GC system equipped with three columns: washed molecular sieves 5Å, 2 m × 1/8 inch outside diameter (OD), Mesh 60/80 SS and Porapak Q, 4 m × 1/8 inch OD, Mesh 80/100 SS, and a thermal conductivity detector.

IR spectra were measured on an ATR unit connected to a Bruker Vector 22 spectrometer under inert atmosphere.

XAS data was collected at the Stanford Synchrotron Radiation Lightsource (SSRL) on beamline 2-2, with the SPEAR3 storage ring operating at 3 GeV and 500mA in top-off mode throughout data collection. Data was collected in unfocused mode using a Si(111) double crystal monochromator for energy selection, which was detuned by 30% to remove contaminating higher harmonics. Samples were maintained at approx. 20K using a He Displex cryostat. XAS spectra were obtained in fluorescence with a 13 element solid-state germanium detector (10 working elements, Ge2, Ge7, and Ge13 nonfunctional). A photodiode placed before I_0 was used to obtain a Cu metal foil reference via scattering, with the first inflection of the Cu metal spectrum set to 8979.0 eV. Data was generally obtained on 1x5 mm (VxH) spots, with individual scans monitored for evidence of photoreduction. No radiation damage was observed, as judged by the lack of any observable changes in the pre-edge and edge features. Data were collected with 10 eV steps before the edge (1 sec integration time), 0.3 eV steps in pre-edge and edge regions (2 sec integration time), and in 0.05k steps over k = 1.62 $Å^{-1}$ to 15 $Å^{-1}$ (integration time increased in k_2-weighted fashion from 2 to 9 sec over range of scan). XAS data was inspected, averaged and normalized using Athena, while EXAFS simulations were conducted using

Artemis.[2] EXAFS simulations were performed on k^3-weighted data, with the amplitude reduction factor S_0^2 fixed at 0.9 and ΔE_0 allowed to float at a single common value for all shells. Coordination numbers were varied in integer increments during the simulations, with r and σ^2 allowed to freely float. Cu phase functions were calculated using FEFF6L. Atomic coordinates of the FEFF input files were taken from the DFT model of complex **3**.

Crystal structure determination: Data collection was performed at 100 K on a Stoe IPDS 2Θ diffractometer using Mo-K_α radiation (λ = 0.71073 Å); radiation source was a sealed tube generator with graphite monochromator. Multi-scan (PLATON[3]) absorption correction for **2**. The structure was solved by direct methods (SHELXS-97[4]) and refined by full matrix least-squares procedures based on F^2 with all measured reflections (SHELXL-97[4]). All non-hydrogen atoms were refined anisotropically. H atoms were introduced in their idealized positions and refined as riding except for the N bonded ones which were located in the Fourier electron density map.

4.2. Computational details

Density functional theory (DFT) calculations were performed with the Gaussian09 program package.[5] The geometry of **3** $[Cu(^{Me}L\text{-}N)]^+$ was optimized with the uB3LYP exchange-correlation functional[6, 7] and the TZVP basis set.[8] Copper species were considered in all possible spin states without symmetry constraints. The acetonitrile solvation effects were included in geometry optimizations through the SMD polarizable continuum model.[9]
IR spectra intensities of **3** were simulated at 298 K. The IR spectrum was also modelled with the ^{15}N isotope $[Cu(^{Me}L\text{-}^{15}N)]^+$ compound, to determine the shift in the Cu-N bond stretching frequency due to the isotopic labelling. Mulliken spin densities were computed to rationalize the electronic structure of the copper-nitrene intermediate. The atomic orbital contribution to the SNOs was evaluated with the Multiwfn 3.3.6 software.

4.3. Synthesis and characterization of ^{H}L-N$_3$ and ^{Me}L-N$_3$

L-Br and ^{Me}L-Br were prepared as previously reported.[10, 11]

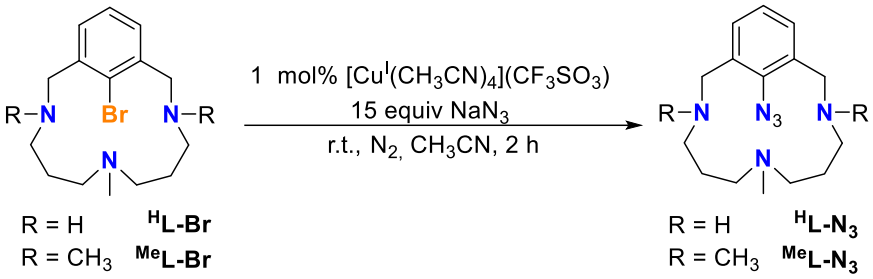

Scheme S1. Synthesis of ^{H}L-N$_3$ and ^{Me}L-N$_3$ by reaction of ^{H}L-Br and ^{Me}L-Br with an excess NaN$_3$ and 1 mol% [Cu^{I}(CH$_3$CN)$_4$](CF$_3$SO$_3$) as catalyst.

Synthesis of ^{H}L-N$_3$. Into the glovebox, ligand ^{H}L-Br (0.0068g, 21 µmol) was dissolved in acetonitrile (1 mL) and this solution was transferred to a vial containing 15 equiv NaN$_3$ (0.020 g, 0.31 mmol). Then, 1 mol% [Cu^{I}(CH$_3$CN)$_4$](CF$_3$SO$_3$) was added (addition of 0.1 mL of a 2.7 mM stock solution in acetonitrile). The colourless solution became slightly red indicating that oxidative addition occurred to afford the red-colored aryl-Cu^{III}-Br complex. The resulting mixture was stirred at room temperature for 2 hours and afterwards the solvent was removed. H$_2$O with NH$_3$ drops (~ 2 mL) were added to the resulting residue and this aqueous mixture was extracted with dichloromethane (3 x 2 mL). The combined organic extracts were dried over MgSO$_4$, filtered and the solvent was removed under vacuum. Ligand ^{H}L-N$_3$ was obtained as a yellow oil (95%). ^{1}H-NMR (CDCl$_3$, 400 MHz, 298K) δ, ppm: 7.10 (d, J = 7.6 Hz, 2H, Ar**H**), 7.01 (dt, J = 7.6 Hz, 1H, Ar**H**), 4.42 (d, J = 14 Hz, 2H, Ar-C**H**$_2$), 3.52 (d, J = 14 Hz, 2H, Ar-C**H**$_2$), 2.63-2.51 (m, 2H, N-C**H**$_2$), 2.39-2.28 (m, 2H, N-C**H**$_2$), 2.05-1.96 (m, 2H, N-C**H**$_2$), 1.86 (s, 3H, C**H**$_3$), 1.53-1.37 (m, 4H, NCH$_2$-C**H**$_2$-CH$_2$N). ESI-MS (*m/z*): 289.21 (100) [^{H}L-N$_3$ + H]$^{+}$. FT-IR (v, cm^{-1}): 2262 (N$_3$).

Synthesis of ^{Me}L-N$_3$. Into the glovebox, ligand ^{Me}L-Br (0.0074 g, 21 µmol) was dissolved in acetonitrile (1 mL) and this solution was transfered to a vial containing 15 equiv NaN$_3$ (0.022 g, 0.34 mmol). Then, 1 mol% [Cu^{I}(CH$_3$CN)$_4$](CF$_3$SO$_3$) was added (addition of 0.1 mL of a 2.7 mM stock solution in acetonitrile). The colourless solution became dark green indicating that oxidative addition occurred to afford the aryl-Cu^{III}-Br complex. The resulting mixture was stirred at room temperature for 1 hour and afterwards the solvent was removed. H$_2$O with NH$_3$ drops (~2 mL) were added to the resulting residue and this aqueous mixture was extracted with dichloromethane (3 x 2 mL). The combined organic extracts were dried over MgSO$_4$, filtered and the solvent was removed under vacuum. Ligand ^{Me}L-N$_3$ was obtained as a yellow oil (91%). ^{1}H-NMR (CDCl$_3$, 400 MHz, 298K) δ, ppm: 7.11 (d, J = 7.2 Hz, 2H, Ar**H**), 6.98 (dt, J = 7.2 Hz, 1H, Ar**H**), 4.07 (d, J = 12 Hz, 2H, Ar-C**H**$_2$), 3.01 (d, J = 12 Hz, 2H, Ar-C**H**$_2$), 2.55-2.50 (m, 2H, NH-C**H**$_2$), 2.36 (s, 6H, C**H**$_3$), 2.35-2.28 (m, 2H, N$_{CH3}$-C**H**$_2$), 1.80 (s, 3H, C**H**$_3$), 1.78-1.65 (m, 4H,

NCH_2-C**H**$_2$-CH_2N), 1.55-1.35 (m, 2H), 1.35-1.15 (m, 2H). ESI-MS (*m/z*): 317.26 (100) [^{Me}L-N_3 + H]$^+$. IR: 2261 cm^{-1}.

By analogy to previously reported C_{aryl}-heteroatom bond formation reactions using ^{H}L-Br,[10, 11] formation of ^{H}L-N_3 and ^{Me}L-N_3 presumably occurs through a 2e$^-$ Cu^I/Cu^{III} catalytic cycle involving oxidative addition, ligand-exchange and reductive elimination steps (Scheme S2).

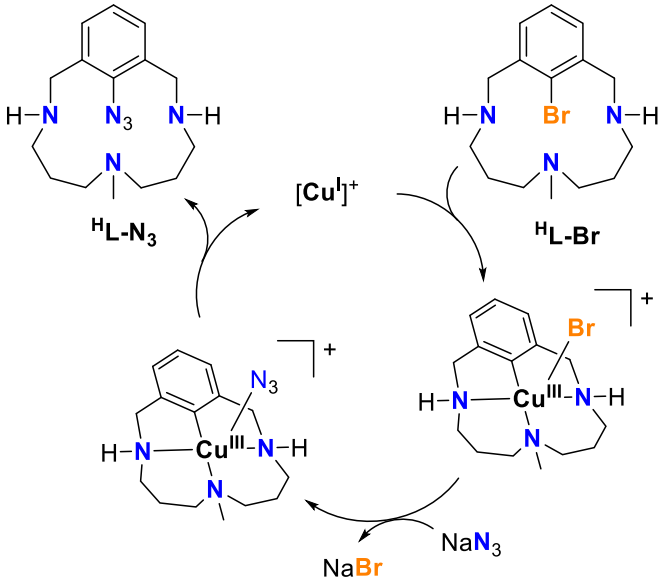

Scheme S2. Cu^I/Cu^{III} catalytic cycle for the synthesis of ^{H}L-N_3 from ^{H}L-Br.

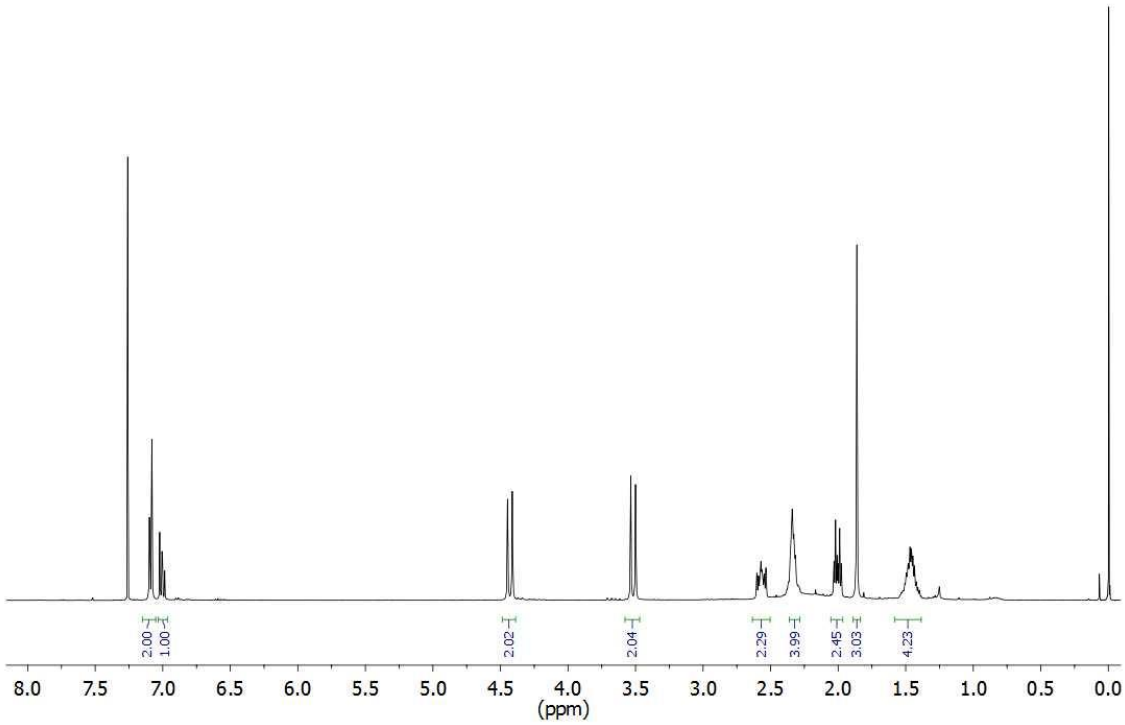

Figure S1. ^{1}H-NMR spectrum of ^{H}L-N$_3$ in CDCl$_3$ at 298K (400 MHz).

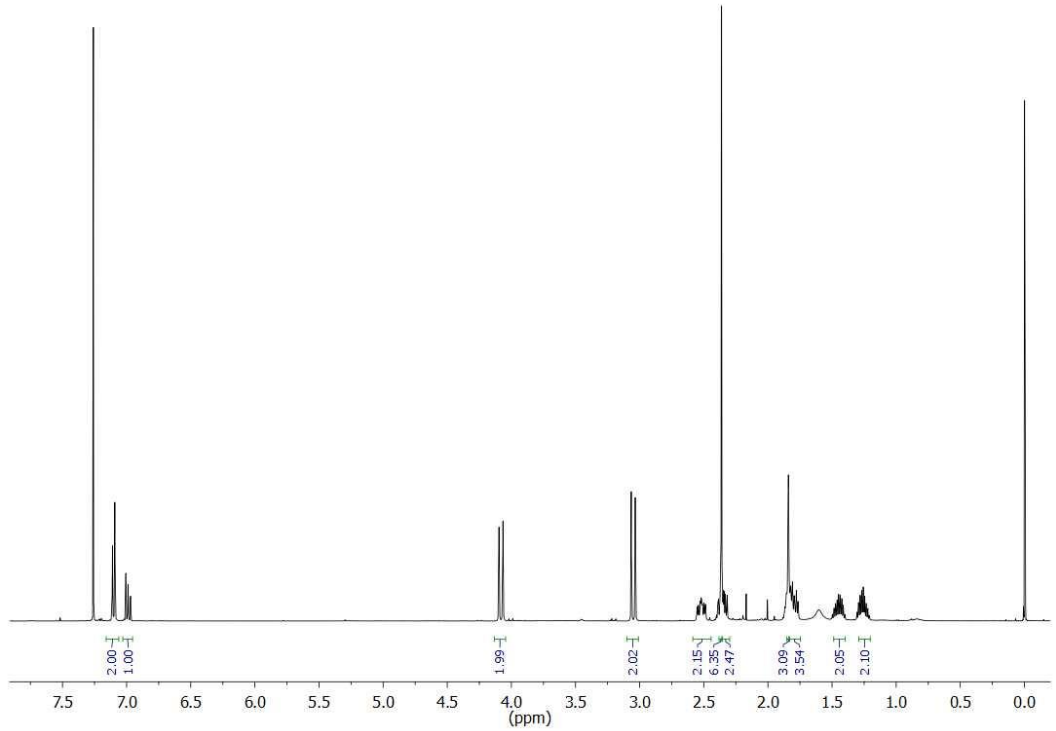

Figure S2. ^{1}H-NMR spectrum of ^{Me}L-N$_3$ in CDCl$_3$ at 298K (400 MHz).

4.4. Synthesis and characterization of compound 2

UV-vis monitoring of the reaction of ^{H}L-N$_3$ with Cu^{I} to form compounds 1 and 2. In a typical experiment, 2.5 mL of a 1.4 mM solution of ^{H}L-N$_3$ (3.5 µmols) in acetonitrile were placed in a 1 cm path-length cuvette. The quartz cell was placed in the Unisoku cryostat of the UV-vis spectrophotometer set at 298K. After reaching thermal equilibrium an UV-vis absorption spectrum of the starting ^{H}L-N$_3$ was recorded. Then, 150 µL of a 31 mM solution of [Cu^{I}(CH$_3$CN)$_4$](CF$_3$SO$_3$) (4.6 µmols, 1.5 equiv) in acetonitrile were added. Initially, a transient species with a band at ~380 nm was formed but it quickly evolved to form compound **2** with a characteristic absorption band at λ_{max} [ε, M^{-1}cm^{-1}] = 550 nm [1000]. Compound **2** was fully formed within 500 s (Figure S3).

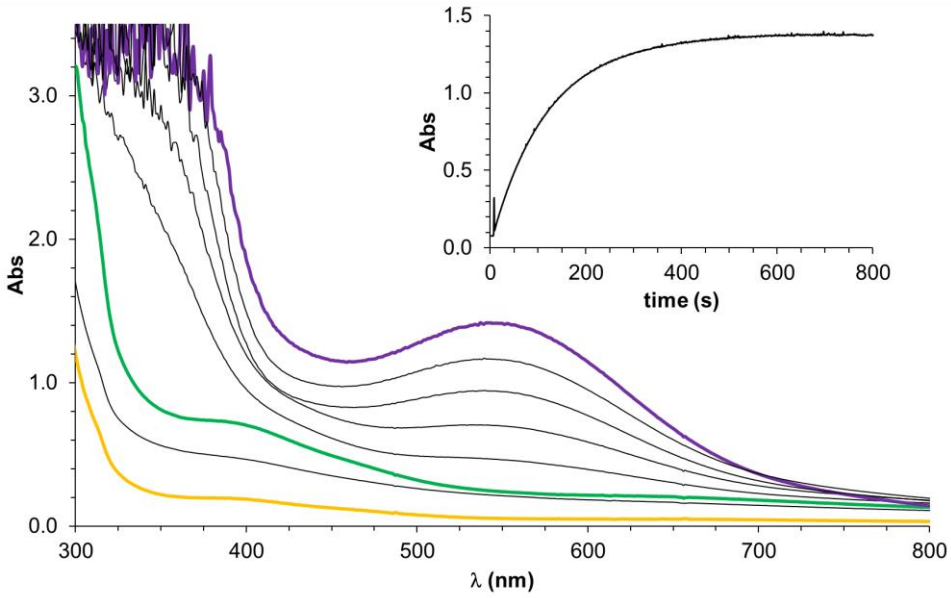

Figure S3. UV-vis absorption spectroscopic changes observed upon reaction of ^{H}L-N$_3$ (yellow line) with 1.5 equiv. of [Cu^{I}(CH$_3$CN)$_4$](CF$_3$SO$_3$) in CH$_3$CN at 25ºC under Ar to form **1** (green line), which evolves to compound **2** (purple line). Inset: kinetic trace at λ = 550 nm.

Synthesis and isolation of compound 2. Into the glovebox, ligand ^{H}L-N$_3$ (35 µmol) was dissolved in acetonitrile (3 mL) and then [Cu^{I}(CH$_3$CN)$_4$](CF$_3$SO$_3$) (13 mg, 35 µmol) dissolved in the minimum amount of acetonitrile was added. The resulting mixture was stirred at room temperature for 15 min to afford a purple solution. Slow diethyl ether diffusion over the resulting solution at room temperature afforded 9.5 mg of compound **2** as purple crystals suitable for X-ray diffraction (yield 56%). ^{1}H-NMR and ESI-MS of compound **2** are depicted in Figures S4 and S5, respectively.

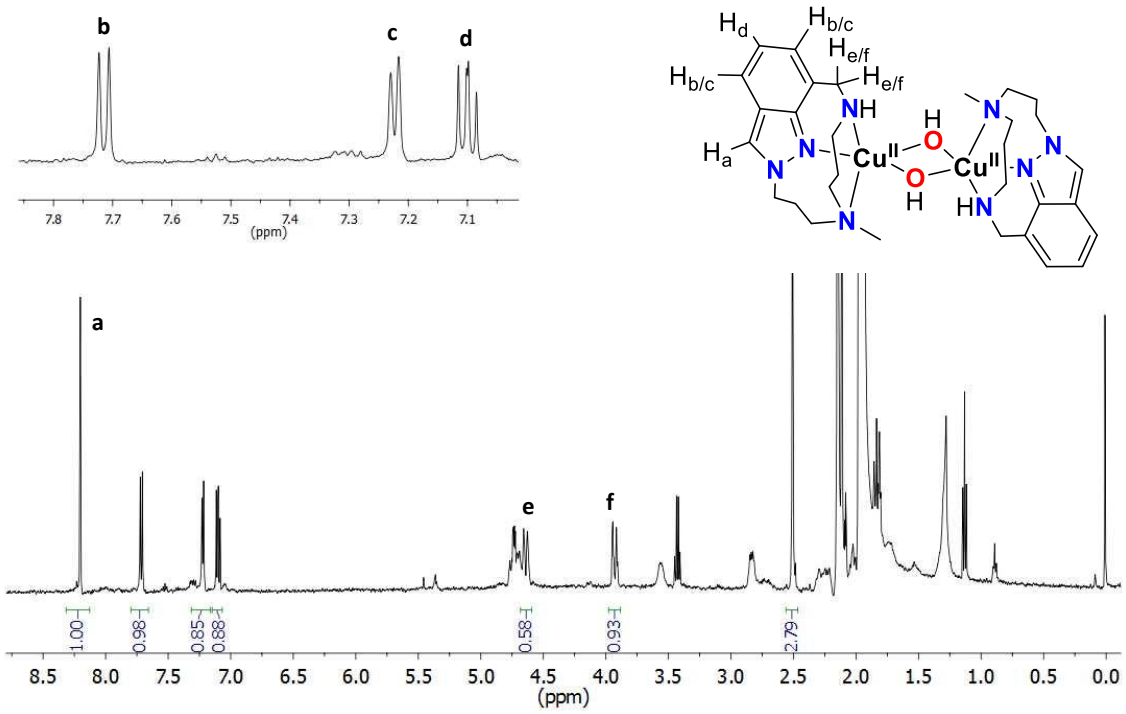

Figure S4. ^{1}H-NMR spectrum of **2** in CD_3CN at 298K (500 MHz).

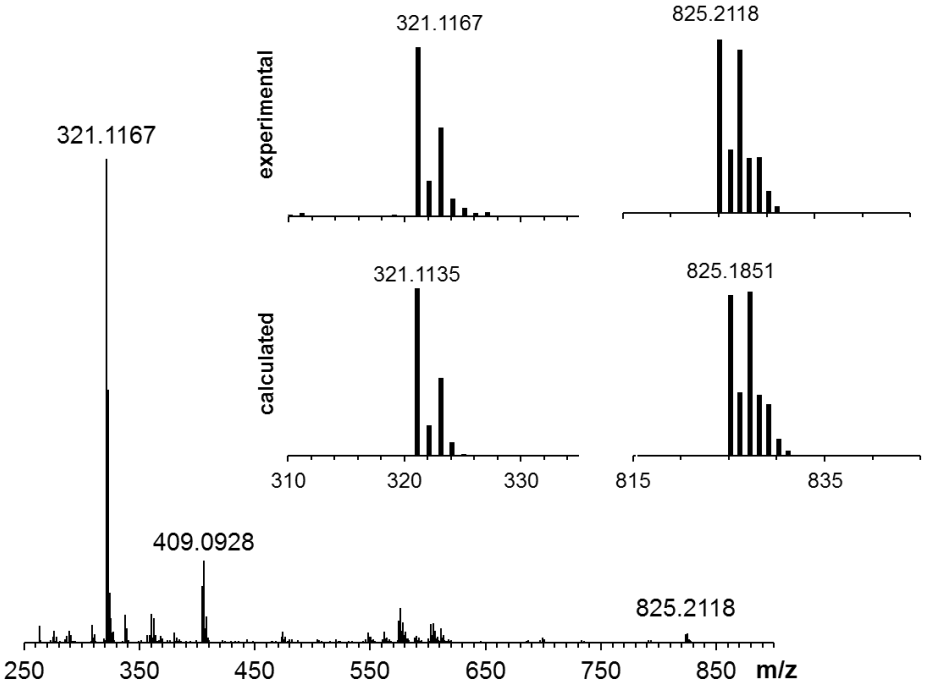

Figure S5. ESI-MS spectrum (3 eV) of isolated compound **2** in CH_3CN at 25 ºC under N_2. Inset: experimental pattern and simulation of the most relevant peaks in the MS spectrum of **2**. The peak at *m/z* 321.1167 corresponds to $[Cu^{I}(L^{in})]^{+}$ while the peak at *m/z* 825.2118 corresponds to the molecular peak $[Cu^{II}_2(OH)_2(L^{in})_2(CF_3SO_3)]^{+}$.

Table S1. Crystal data for **2**.

Formula weight	975.97
Temperature	100(2) K
Wavelength	0.71073 Å
Crystal system, space group	orthorombic, $P2_1\ 2_1\ 2_1$
Unit cell dimensions	a = 10.9034(3) Å α = 90º
	b = 18.9785(6) Å β = 90º
	c = 19.5583(7) Å γ = 90º
Volume	4047.2 A^3
Density (calculated)	1.602 g/cm^3
Z, Calculated density	4
Absorption coefficient	1.240 mm^{-1}
F(000)	2008
Crystal size	0.24 x 0.12 x 0.05 mm
Theta range for data collection	2.343 to 25.066º
Limiting indices	$-12 \leq h \leq 12, -20 \leq k \leq 22, -22 \leq l \leq 23$
Reflections collected / unique	16697 / 7126 [R(int) = 0.0723]
Completeness to Θ	99.8% (Θ = 25.00º)
Refinement method	Full-matrix least-squares on F^2
Data / restraints / parameters	7126 / 0 / 532
Goodness-of-fit on F^2	1.031
Final R indices [$I>2\sigma(I)$]	R1 = 0.0484 wR2 = 0.1343
R indices (all data)	R1 = 0.0577 wR2 = 0.1424
Largest diff. peak and hole	0.757 and -0.372 $e.A^{-3}$

Table S2. Selected bond lengths (Å) and angles (º) for **2**.

Cu1 O1	1.925(5)	O1 Cu1 O2	76.94(19)
Cu1 O2	1.942(5)	O1 Cu1 N5	100.9(2)
Cu1 N5	1.988(5)	O2 Cu1 N7	90.5(2)
Cu1 N7	2.025(5)	N5 Cu1 N7	87.4(2)
Cu1 N8	2.298(6)	O1 Cu1 N8	96.1(2)
Cu1 Cu2	3.0353(10)	O2 Cu1 N8	107.0(2)
Cu2 O2	1.934(5)	N5 Cu1 N8	94.4(2)
Cu2 O1	1.945(5)	N7 Cu1 N8	96.2(2)
Cu2 N1	1.991(5)	O2 Cu2 O1	76.66(19)
Cu2 N3	2.019(5)	O2 Cu2 N1	101.2(2)
Cu2 N4	2.298(6)	O1 Cu2 N3	90.5(2)
		N1 Cu2 N3	87.4(2)
		O2 Cu2 N4	95.6(2)
		O1 Cu2 N4	106.8(2)
		N1 Cu2 N4	94.8(2)
		N3 Cu2 N4	96.6(2)
		Cu1 O1 Cu2	103.3(2)
		Cu2 O2 Cu1	103.1(2)

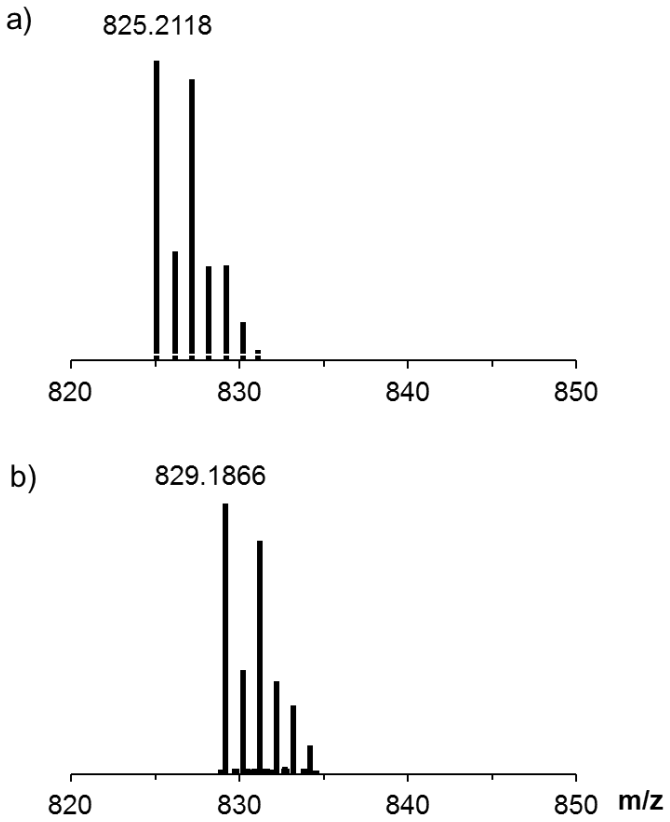

Figure S6. ESI-MS of compound **2** before (a) and after (b) addition of 10 equiv. $H_2{}^{18}O$ in CH_3CN at 25 ºC under N_2. The molecular peak at *m/z* 825.21 shifts 4 units (*m/z* 829.20) due to exchange of the hydroxo ligands with $H_2{}^{18}O$.

4.5. Synthesis and characterization of compound 1

UV-vis monitoring of the reaction of ^{H}L-N$_3$ with Cu^{I} to form compound 1. In a typical experiment, 2.5 mL of a 1.4 mM solution of ^{H}L-N$_3$ (3.5 µmols) in acetone were placed in a 1 cm path-length cuvette. The quartz cell was placed in the Unisoku cryostat of the UV-vis spectrophotometer and cooled down to 223K. After reaching thermal equilibrium an UV-vis absorption spectrum of the starting ^{H}L-N$_3$ was recorded. Then, 150 µL of a 31 mM solution of [Cu^{I}(CH$_3$CN)$_4$](CF$_3$SO$_3$) (4.6 µmols, 1.5equiv) in acetonitrile were added. The formation of a band at λ_{max} [ε, M^{-1}cm^{-1}] = 380 nm [615], 790 nm [65] was observed. **1** was fully formed within 1000 s.

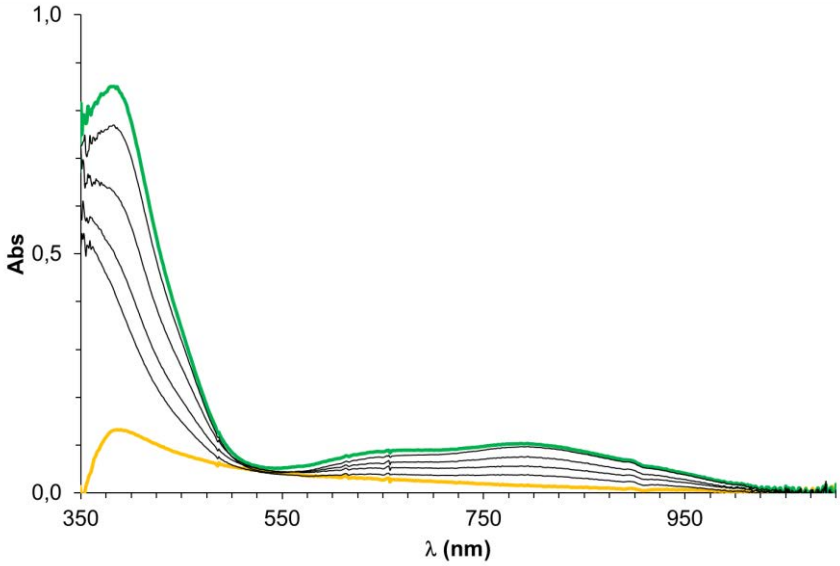

Figure S7. UV-vis absorption spectroscopic changes observed upon the reaction of ^{H}L-N$_3$ (yellow line) with 1.5 equiv. of [Cu^{I}(CH$_3$CN)$_4$](CF$_3$SO$_3$) in acetone at -50 ºC under Ar to form **1** (green line) in 15 min.

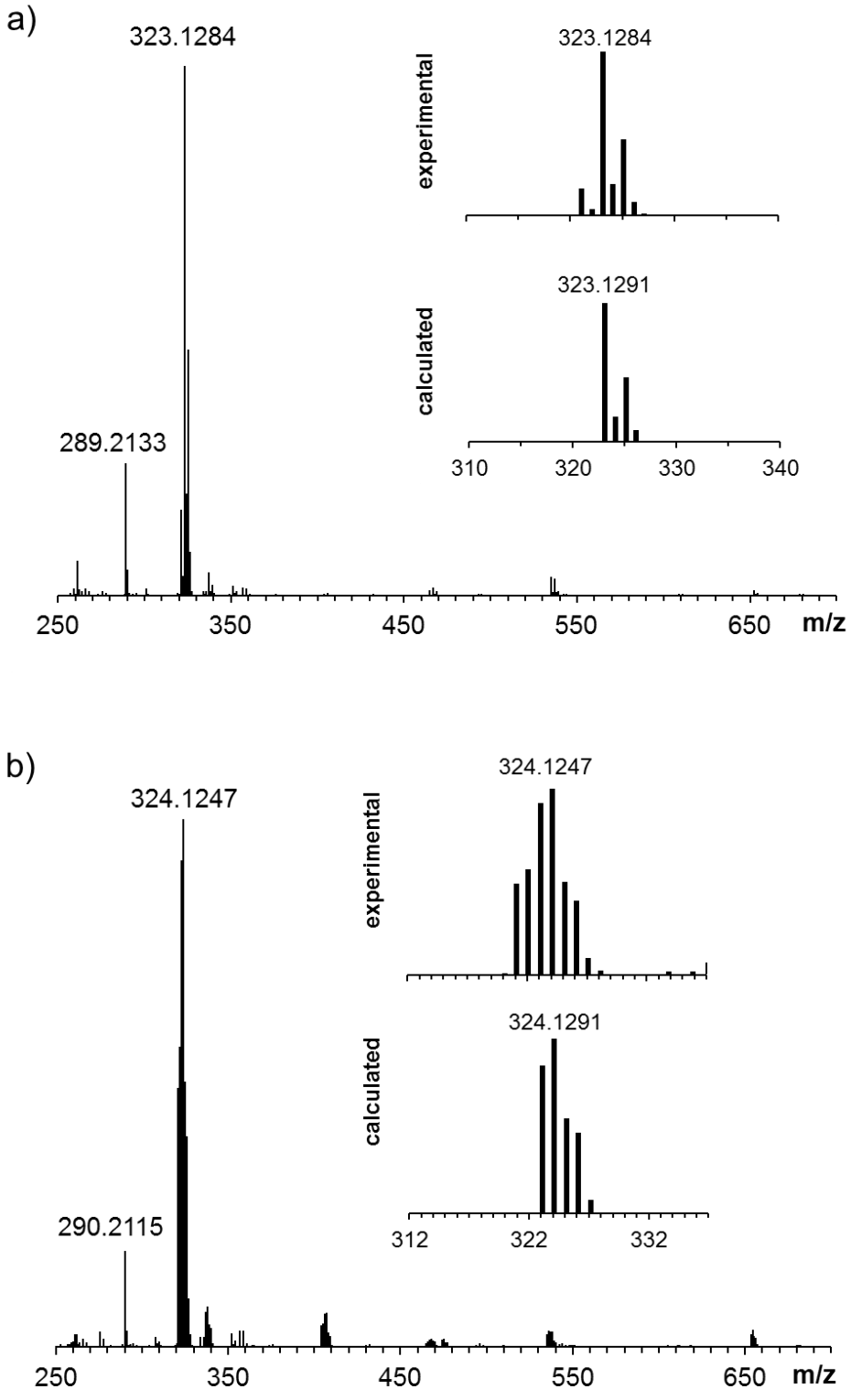

Figure S8. CSI-MS spectra of compound **1** (a) and its 50% ^{15}N-labeled analogue (b) in acetone at -50 ºC under N_2. Insets: simulated and experimental molecular peaks of **1** (inset a) and its 50% ^{15}N-labeled analogue (inset b). The discrepancy between experimental and calculated patterns is due to the presence of the decomposition product of **1**. Thus, the ion peak at *m/z* 321.13 (^{14}N) or 322.13 (^{15}N) corresponds to $[Cu(L^{in})]^+$, which derives from the decomposed species **2**.

4.6. Generation of compound 3 and XAS analysis

UV-vis monitoring of the reaction of ^{Me}L-N$_3$ with Cu^{I} to form compound 3. In a typical experiment, 2.5 mL of a 1.26 mM solution of ^{Me}L-N$_3$ (3.1 µmols) in acetonitrile were placed in a 1 cm path-length cuvette. The quartz cell was placed in the Unisoku cryostat of the UV-vis spectrophotometer set at 298K. After reaching thermal equilibrium an UV-vis absorption spectrum of the starting ^{Me}L-N$_3$ was recorded. Then, 100 µL of a 31 mM solution of [Cu^{I}(CH$_3$CN)$_4$](CF$_3$SO$_3$) in acetonitrile were added (3.1 µmols, 1 equiv). The formation of a band at λ_{max} [ε, M^{-1}cm^{-1}] = 360 nm [1200], 710 nm [200] and 980 nm [150] was observed. **3** was fully formed immediately by irradiation every second.

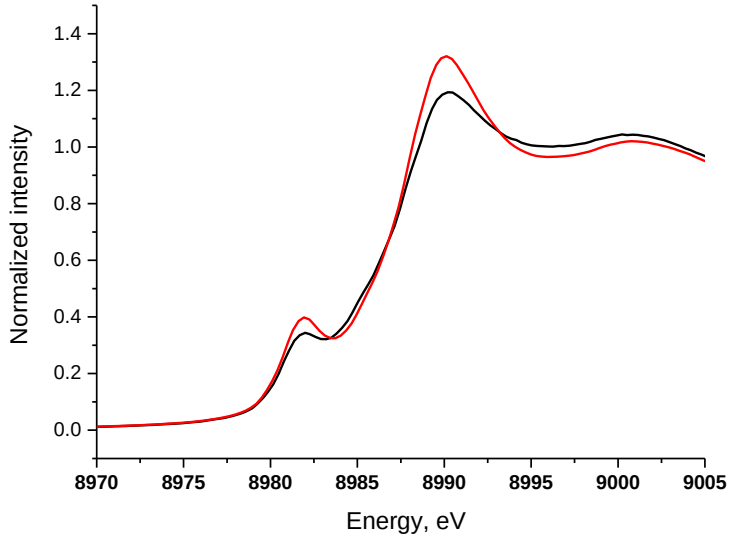

Figure S9. XANES of compounds **2** (red trace) and **3** (black trace) at 20K.

Table S3. Summary of EXAFS fitting for **3**. Bold line represents the best fit for the system (fit 6). Fourier transform range: 2 - 12 Å^{-1}. The fit was optimized in R space with a k-weight of 3. The fitting range is 1.0-2.0 and 1.0-3.0 for fits 1-3 and 4-6, respectively.

Fit	**N**	**R [Å]**	**σ [Å]**	**N**	**R [Å]**	**σ [Å]**	**N**	**R [Å]**	**σ [Å]**	R_F
1	3	2.01	0.002							.026
2	4	2.01	0.005							.009
3	5	2.00	0,007							.035
4	4	2.01	0.006							.181
5	4	2.04	0.005	2	2.43	0.006				.162
6	**4**	**2.04**	**0.007**	**2**	**2.44**	**0.006**	**12**	**3.23**	**0.009**	.007
DFT	4	2.08		2	2.53		12	3.45		

Table S4. Summary of EXAFS fitting for **2**. Bold line represents the best fit for the system (fit 7). Fourier transform range: 2 - 12 $Å^{-1}$. The fit was optimized in R space with a k-weight of 3. The fitting range is 1.0-2.0 and 1.0-3.15 for fits 1-4 and 5-7, respectively.

Fit	**N**	**R [Å]**	**σ [Å]**	**N**	**R [Å]**	**σ [Å]**	**N**	**R [Å]**	**σ [Å]**	**N**	**R [Å]**	**σ [Å]**	**R_F**	reduced chi-square
1	2	1.97	0.003										.051	87
2	4	1.97	0.008										.020	34
3	4	1.99	0.007	1	2.10	0.001							.019	29
4	5	2.18	0.004										.267	38
5	4	1.99	0.008	1	2.13	0.008							.120	52
6	4	1.99	0.008	1	2.13	0.008	1	2.91	0.007				.040	25
7	**4**	**1.99**	**0.008**	**1**	**2.13**	**0.008**	**1**	**2.93**	**0.007**	**6**	**3.30**	**0.007**	**.014**	20
DFT	4	1.97		1	2.29		1	3.03						

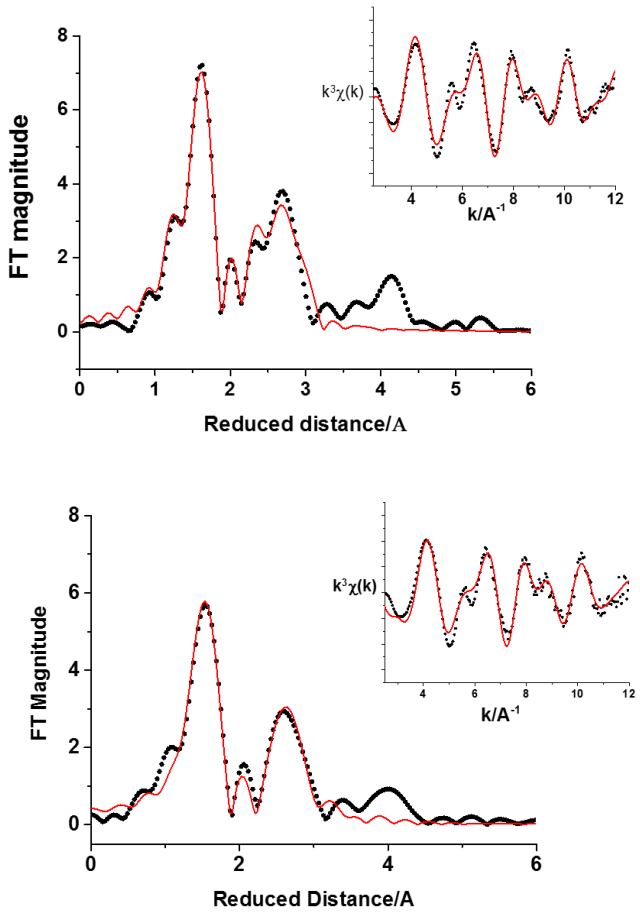

Figure S10. Top: Fourier transform EXAFS spectra of **3** (dotted line) and the best fit (red line); the inset shows the EXAFS data on a wave vector scale weighted by k^3 with respective representation. Bottom: Fourier transform EXAFS spectra of **2** (dotted line) and the best fit (red line); the inset shows the EXAFS data on a wave vector scale weighted by k^3 with respective representation.

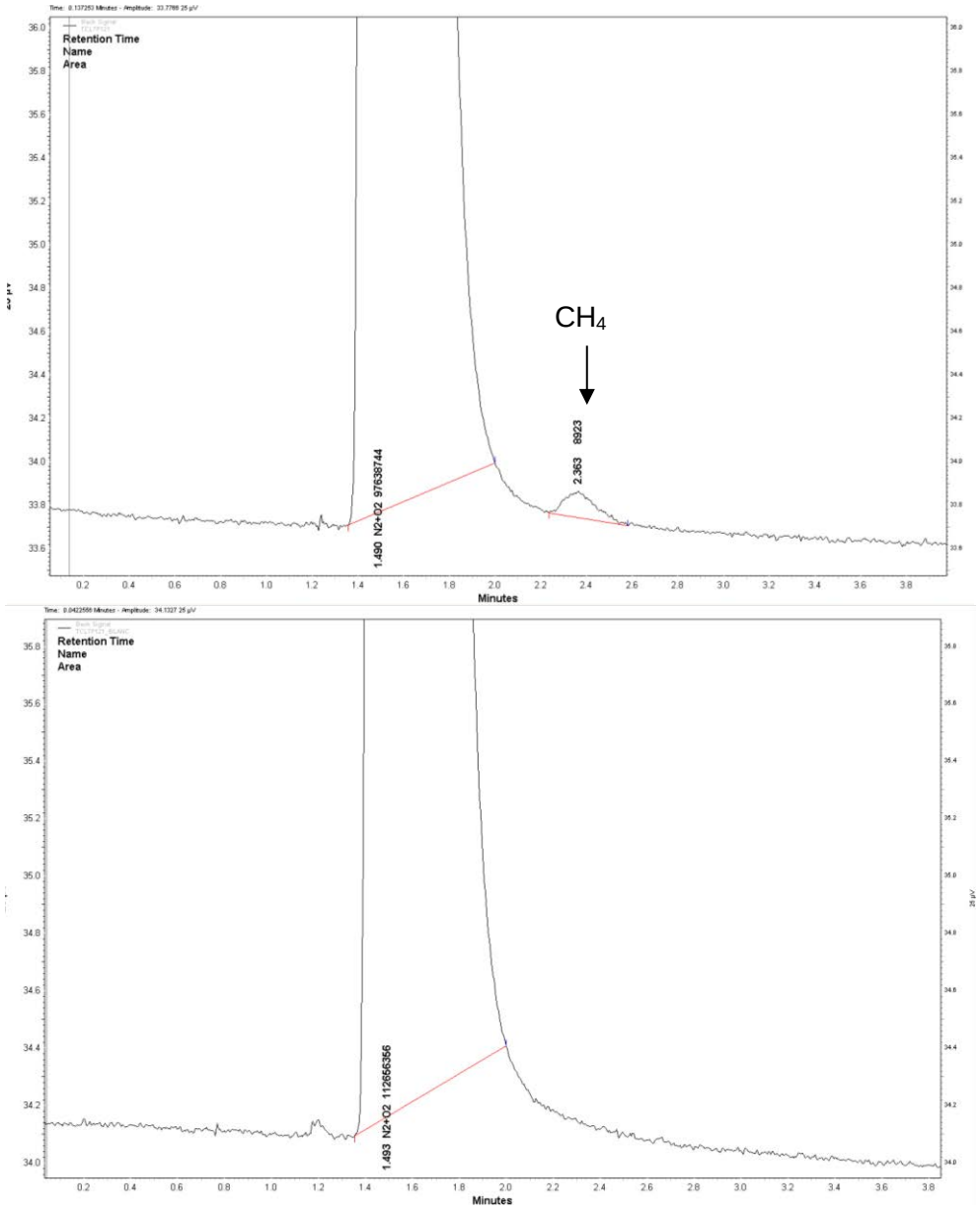

Figure S11. Gas chromatogram (GC-TCD) for the detection of methane released during the reaction of ^{Me}L-N_3 with 1 equiv. [$Cu^{I}(CH_3CN)_4$](CF_3SO_3) in CH_3CN at 50 ºC after 7 days (top). For comparison, a blank experiment under analogous conditions without copper is also depicted (bottom).

4.7. Reaction of 3 with substrates

Analysis of the reaction of 3 with substrates. Once **3** was fully formed, 150 µL of a solution containing the corresponding equivalents of the desired substrate were added in the cuvette. The decay of the band at λ = 710 nm was monitored by UV-vis spectroscopy. After complete decay of this band, the resulting solution was analyzed by NMR and ESI-MS. Trimethoxybenzene (TMB) and triphenylphosphine oxide were used as internal standards in ^{1}H-NMR and ^{31}P-NMR analyses, respectively.

Table S5. Second-order rate constants (k_2, $M^{-1}s^{-1}$) for the reaction of **3** towards substrates together with product analysis and product yields.

Substrate	k_2 ($M^{-1}s^{-1}$)	^{31}P-NMR product (ppm)	ESI-MS m/z product (^{15}N)	Product yield (%)
xanthene	0.009	-	469.31 (471.31)	44
1,4-cyclohexadiene	0.020	-	367.29	-
PPh_3	7.5	26	551.35 (552.34)	41
P^nBu_3	too fast	51	491.35	84
$P(o\text{-}tol)_3$	0.052	17	-	48

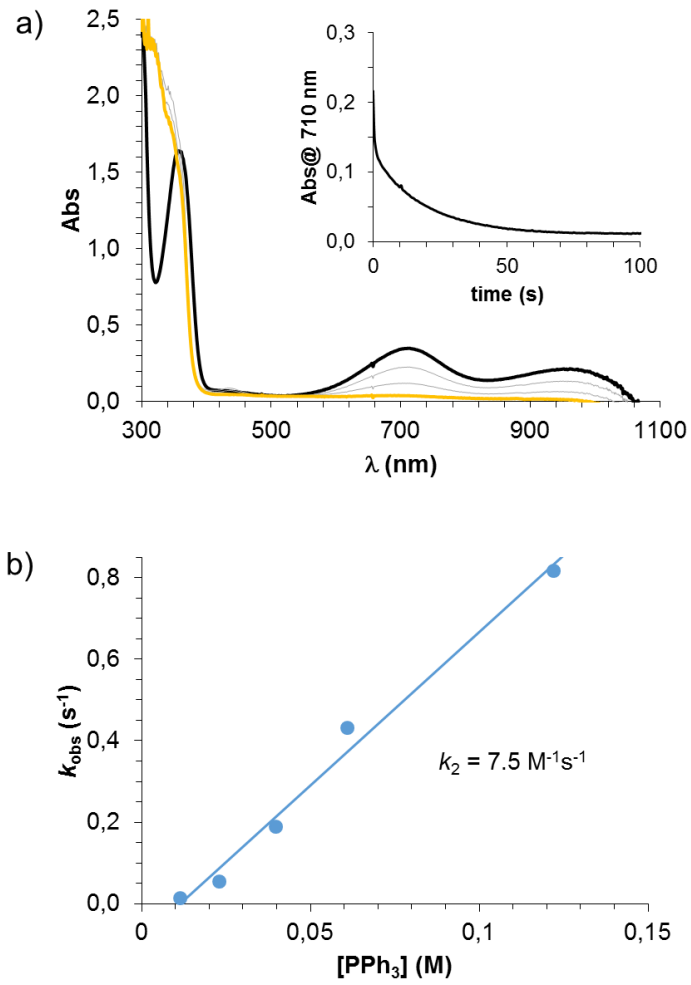

Figure S12. a) UV-vis spectral changes of a solution of **3** upon addition of 15 equiv. PPh_3. Experimental reaction conditions: 15 equiv. PPh_3 were added at once to a solution of **3** (1.2 mM) in CH_3CN at 25 ºC under Ar and the kinetics were monitored at 710 nm (inset). b) Plot of k_{obs} against substrate concentration for the reaction of **3** (1.2 mM) with triphenylphosphine (PPh_3) in CH_3CN at 25 ºC under Ar.

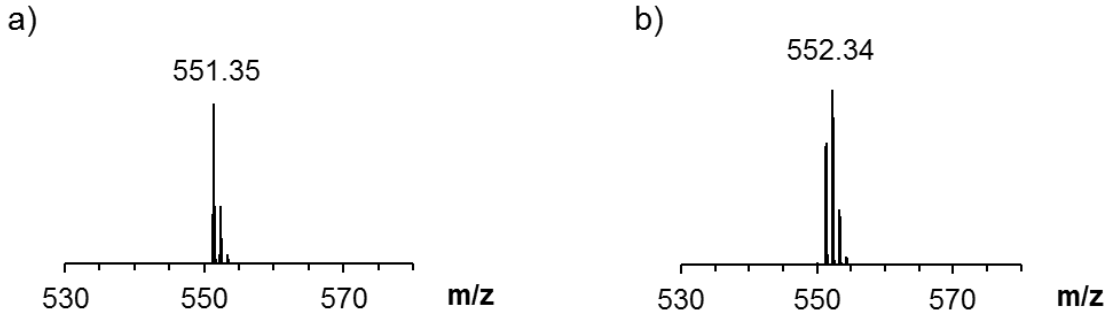

Figure S13. ESI-MS spectrum of the product formed upon reaction of **3** with 5 equiv. PPh_3 at 25 ºC in CH_3CN (a) and the analogous spectrum starting from 50% ^{15}N-labeled **3** (b).

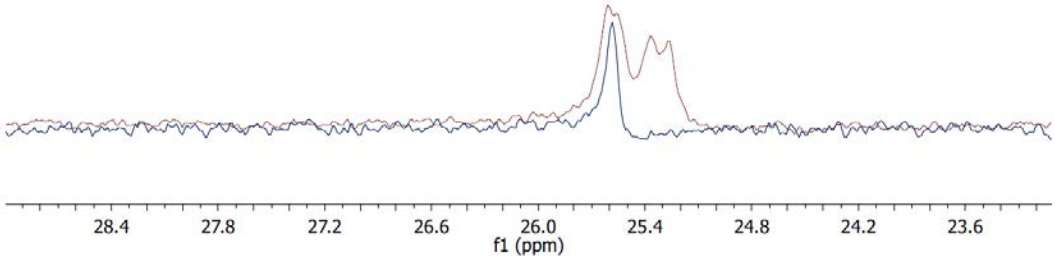

Figure S14. ^{31}P-NMR spectrum of the product formed upon reaction of **3** with 5 equiv. PPh_3 at 25 ºC in CD_3CN (blue line) and the analogous spectrum starting from 50% ^{15}N-labeled **3** (purple line).

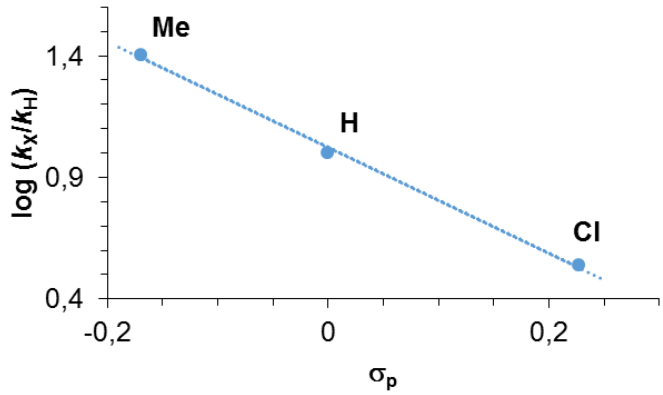

Figure S15. Hammett plot for the reaction of **3** with *para*-substituted triphenylphospines (X = Me, H and Cl) in CH_3CN at 25 ºC.

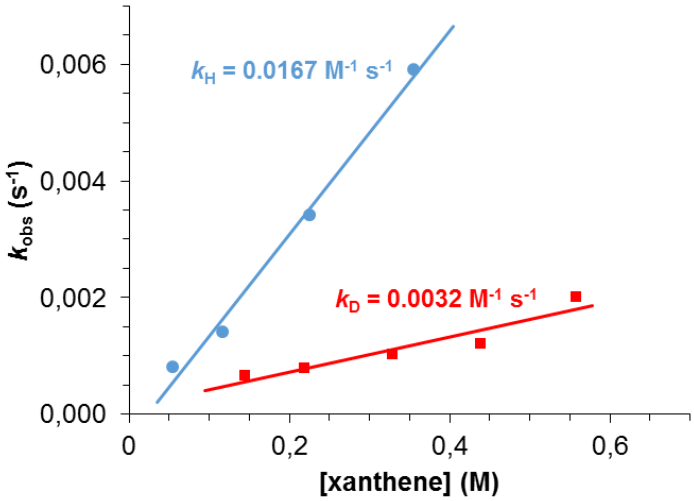

Figure S16. Plot of k_{obs} against substrate concentration for the reaction of **3** with xanthene (blue line) and d_2-xanthene (red line) in CH_3CN at 25 ºC.

4.8. DFT calculations

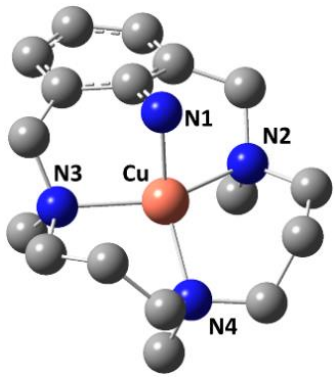

Cu1 N1	1.94	N1 Cu N2	86.3
Cu1 N2	2.16	N1 Cu N3	88.1
Cu1 N3	2.17	N3 Cu N4	100.2
Cu1 N4	2.08	N2 Cu N4	104.2

Figure S17. DFT optimized structure of **3** and selected bond lengths (Å) and angles (º) for this compound.

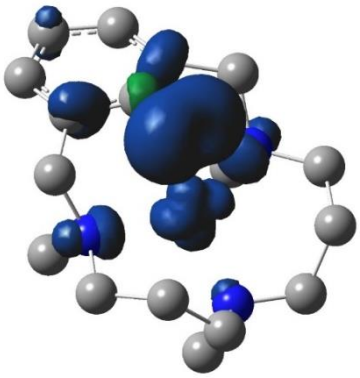

atom	spin density
Cu	0.4
N_{aryl}	1.2
$C_{benzene}$	0.2
N_{CH3}	0.2

Figure S18. Mulliken's spin density of the most relevant atoms for the intermediate **3**, isovalue= 0.005.

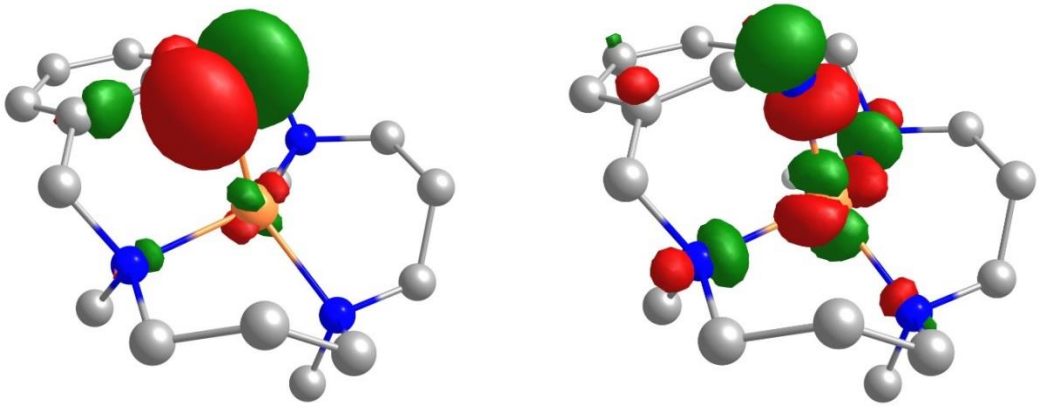

Figure S19. Spin-natural orbitals (SNO) corresponding to **3** (isovalue = 0.062).

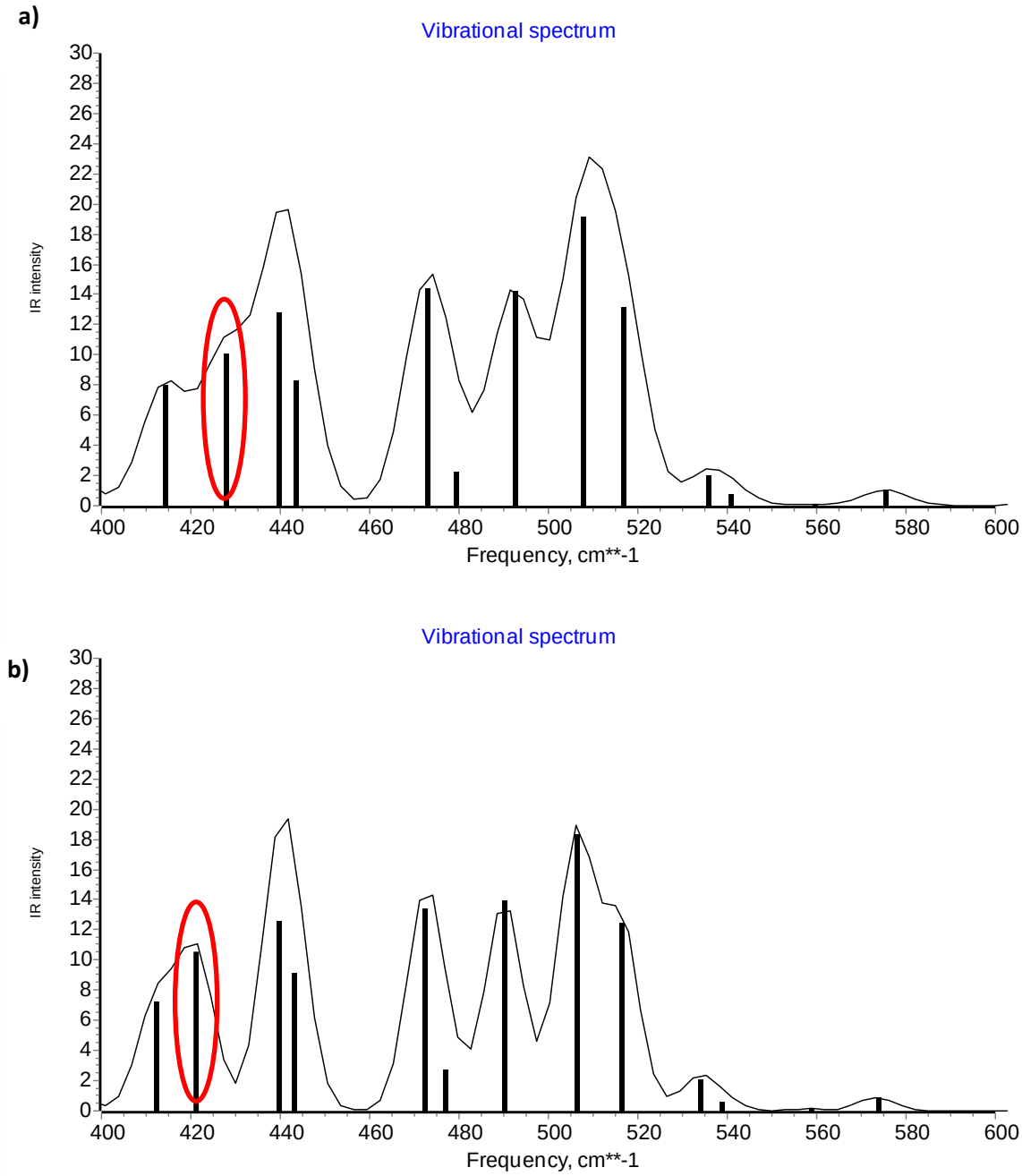

Figure S20. Calculated IR spectrum of compound **3** (a) and its ^{15}N-labeled analogue (b) simulated at 298K.

4.9. References

[1] Stoll, S.; Schweiger, A., *J. Magn. Reson.,* **2006**, *178*, 42.

[2] Demeter, Version 0.9.17, http://bruceravel.github.io/demeter/.

[3] Spek, A. L., *J. Appl. Cryst.,* **2003**, *36*, 7.

[4] Sheldrick, G. M. A., *Acta Cryst. A,* **2008**, *64*, 112.

[5] Frisch, M. J.; Trucks, G. W.; Schlegel, H. B.; Scuseria, G. E.; Robb, M. A.; Cheeseman, J. R.; Scalmani, G.; Barone, V.; Mennucci, B.; Petersson, G. A.; Nakatsuji, H.; Caricato, M.; Li, X.; Hratchian, H. P.; Izmaylov, A. F.; Bloino, J.; Zheng, G.; Sonnenberg, J. L.; Hada, M.; Ehara, M.; Toyota, K.; Fukuda, R.; Hasegawa, J.; Ishida, M.; Nakajima, T.; Honda, Y.; Kitao, O.; Nakai, H.; Vreven, T.; Montgomery, J. A.; Peralta, J. E.; Ogliaro, F.; Bearpark, M.; Heyd, J. J.; Brothers, E.; Kudin, K. N.; Staroverov, V. N.; Kobayashi, R.; Normand, J.; Raghavachari, K.; Rendell, A.; Burant, J. C.; Iyengar, S. S.; Tomasi, J.; Cossi, M.; Rega, N.; Millam, M. J.; Klene, M.; Knox, J. E.; Cross, J. B.; Bakken, V.; Adamo, C.; Jaramillo, J.; Gomperts, R; Stratmann,R. E.; Yazyev, O.; Austin, A. J.; Cammi, R.; Pomelli, C.; Ochterski, J. W.; Martin, R. L.; Morokuma, K.; Zakrzewski, V. G.; Voth, G. A.; Salvador, P.; Dannenberg, J. J.; Dapprich, S.; Daniels, A. D.; Farkas, O.;. Foresman, J. B.; Ortiz, J. V.; Cioslowski, J.; Fox, D. J., Gaussian, Inc., Wallingford CT, **2009**.

[6] Becke, A. D., *J. Chem. Phys.,* **1993**, *98*, 1372.

[7] Becke, A. D., *J. Chem. Phys.,* **1993**, *98*, 5648.

[8] Schaefer, A.; Huber, C.; Ahlrichs, R., *J. Chem. Phys.,* **1994**, *100*, 5829.

[9] Marenich, A. V.; Cramer, C. J.; Truhlar, D. G., *J. Phys. Chem. B,* **2009**, *113*, 6378.

[10] Ribas, X.; Jackson, D. A.; Donnadieu, B.; Mahía, J.; Parella, T.; Xifra, R.; Hedman, B.; Hodgson, K. O.; Llobet, A.; Stack, T. D. P., *Angew. Chem. Int. Ed.,* **2002**, *41*, 2991.

[11] Casitas, A.; Canta, M.; Solà, M.; Costas, M.; Ribas, X., *J. Am. Chem. Soc.* **2011**, *133*, 19386.